

**Energy Reconstruction  
of Electron Neutrino Events  
and  $\nu_\mu \rightarrow \nu_e$  Appearance Search  
in the OPERA Detector**

**Dissertation**

zur Erlangung des Doktorgrades  
an der Fakultät für  
Mathematik, Informatik und Naturwissenschaften  
Fachbereich Physik  
der Universität Hamburg

vorgelegt von

**Annika Hollnagel  
aus Braunschweig**

Hamburg  
2018

**Gutachter der Dissertation:**

Prof. Dr. Caren Hagner  
Prof. Dr. Michael Wurm

**Zusammensetzung der Prüfungskommission:**

Prof. Dr. Caren Hagner  
Prof. Dr. Michael Wurm  
Prof. Dr. Dieter Horns  
Prof. Dr. Gudrid Moortgat-Pick  
Dr. Björn Wonsak

**Vorsitzender der Prüfungskommission:**

Prof. Dr. Dieter Horns

**Datum der Disputation:**

20.06.2018

**Vorsitzender Fach-Promotionsausschuss PHYSIK:**

Prof. Dr. Wolfgang Hansen

**Leiter des Fachbereichs PHYSIK:**

Prof. Dr. Michael Potthoff

**Dekan der Fakultät MIN:**

Prof. Dr. Heinrich Graener

**Energy Reconstruction of Electron Neutrino Events  
and  $\nu_\mu \rightarrow \nu_e$  Appearance Search in the OPERA Detector**

- Abstract -

OPERA is a long-baseline neutrino oscillation experiment studying the high-energy CNGS muon neutrino beam. Detector and beam were specifically designed to enable the observation of  $\tau$  neutrino appearance via  $\nu_\mu \rightarrow \nu_\tau$  oscillations on an event-by-event basis.

The OPERA detector is a hybrid apparatus, consisting of a kton-scale target, made from lead and high-resolution nuclear emulsions, that is equipped with electronic detector elements and followed by a magnetic spectrometer. While the contamination of the CNGS  $\nu_\mu$  beam with  $\tau$  neutrinos is negligible and enables a background-free  $\nu_\tau$  appearance search, the contribution from  $\nu_e$  and  $\bar{\nu}_e$  is  $\mathcal{O}(1\%)$ . Nonetheless, the sub-leading channel of  $\nu_\mu \rightarrow \nu_e$  oscillations can be studied. Using the nuclear emulsion event reconstruction to identify  $\nu_e$  CC interactions, the electronic detector information can be exploited to improve the signal-to-noise ratio.

Within the framework of this thesis, an estimation of the original electron neutrino energy using the electronic detector of OPERA is developed that allows to discriminate against beam-induced background. It is then applied to a search for  $\nu_\mu \rightarrow \nu_e$  oscillations in the 2008 - 2009 data sample collected with OPERA. The results of the oscillation analysis, both in the standard 3-flavour scenario and regarding nonstandard oscillations, are presented.

**Energierückbau von Elektron Neutrino-Ereignissen  
und  $\nu_\mu \rightarrow \nu_e$  Appearance-Suche im OPERA Detektor**

- Zusammenfassung -

OPERA ist ein Long-Baseline-Neutrinooszillationsexperiment, welches den hochenergetischen CNGS Myon-Neutrinostrahl untersucht. Sowohl Detektor als auch Neutrinostrahl wurden dafür entwickelt, die Beobachtung von  $\tau$ -Neutrino Appearance durch  $\nu_\mu \rightarrow \nu_\tau$  Oszillationen auf Einzelereignisbasis zu ermöglichen.

Der OPERA-Detektor ist eine hybride Apparatur, bestehend aus einem kton-schweren Target aus Blei und Fotoemulsionen, welches mit elektronischen Detektorelementen bestückt ist und von einem magnetischen Spektrometer gefolgt wird. Während die Kontamination des CNGS-Strahls mit  $\tau$ -Neutrinos vernachlässigbar ist, liegt der Beitrag von  $\nu_e$  und  $\bar{\nu}_e$  bei etwa 1%. Dennoch kann der untergeordnete  $\nu_\mu \rightarrow \nu_e$ -Oszillationskanal untersucht werden. Unter Verwendung der Fotoemulsions-Ereignisrekonstruktion zur Identifikation von  $\nu_e$  CC-Interaktionen können die Informationen der elektronischen Detektoren ausgenutzt werden, um das Signal-Rausch-Verhältnis zu verbessern.

Im Rahmen dieser Arbeit wurde eine Abschätzung der ursprünglichen Energie der Elektron-Neutrinos entwickelt, welche die elektronischen Detektoren von OPERA verwendet um den strahlinduzierten Hintergrund zu reduzieren. Diese wird anschließend auf eine  $\nu_\mu \rightarrow \nu_e$  Appearance-Suche in den 2008 - 2009 von OPERA gesammelten Daten angewandt. Die Ergebnisse der Oszillationsanalyse, sowohl im 3-Flavour Standard-Szenario als auch im Hinblick auf Nichtstandard-Oszillationen, werden vorgestellt.



# Contents

<b>1</b>	<b>Introduction</b>	<b>1</b>
<b>2</b>	<b>Neutrino Physics</b>	<b>3</b>
2.1	Historical Overview: Neutrino Oscillations . . . . .	4
2.1.1	Early Discussion of Neutrino Oscillations . . . . .	4
2.1.2	Number of Lepton Families . . . . .	4
2.1.3	SNO and the Solar Neutrino Problem . . . . .	5
2.1.4	SK and the Atmospheric Neutrino Anomaly . . . . .	6
2.2	Neutrinos and the Standard Model of Particle Physics . . . . .	8
2.2.1	Quantum Chromo Dynamics: $SU(3)$ . . . . .	9
2.2.2	GWS Model of Electroweak Unification: $SU(2)_L \otimes U(1)_Y$ . . . . .	9
2.3	Neutrino Interactions with Matter . . . . .	11
2.3.1	Elastic and Quasi-Elastic Scattering . . . . .	11
2.3.2	Resonant Scattering . . . . .	13
2.3.3	Deep-Inelastic Scattering . . . . .	14
2.3.4	Total Charged Current Cross Sections . . . . .	16
2.4	Flavour Mixing in the Neutrino Sector . . . . .	19
2.4.1	Neutrino Oscillations in Vacuum . . . . .	19
2.4.2	Matter Effects . . . . .	22
2.4.3	Global Best Fit Parameters . . . . .	24
2.5	Open Questions . . . . .	25
2.5.1	Neutrino Mass Ordering . . . . .	25
2.5.2	CP Violation . . . . .	26
2.5.3	Sterile Neutrinos . . . . .	26
2.5.4	Absolute Mass Scale . . . . .	27
2.5.5	Dirac or Majorana . . . . .	28
<b>3</b>	<b>Electromagnetic Showers</b>	<b>29</b>
3.1	Bremsstrahlung . . . . .	29
3.2	Pair Production . . . . .	30
3.3	Radiation Length . . . . .	31
3.4	Electromagnetic Cascades . . . . .	31

<b>4</b>	<b>The OPERA Experiment</b>	<b>33</b>
4.1	Physical Motivation & Experimental Requirements . . . . .	33
4.2	Predecessors to OPERA . . . . .	36
4.2.1	DONuT . . . . .	36
4.2.2	CHORUS & NOMAD . . . . .	37
4.3	The CNGS Neutrino Beam . . . . .	41
4.3.1	CNGS Facility & Beam Properties . . . . .	42
4.3.2	Monte Carlo Simulation . . . . .	44
4.3.3	CNGS Performance . . . . .	46
4.4	The OPERA Detector . . . . .	48
4.4.1	Target Area . . . . .	49
4.4.2	Spectrometer . . . . .	55
4.4.3	Veto System . . . . .	59
4.4.4	DAQ & Overall Event Trigger . . . . .	59
4.5	The OpRelease Software Framework . . . . .	60
4.5.1	OpNegn . . . . .	60
4.5.2	OpData & OpRData . . . . .	60
4.5.3	OpGeom . . . . .	60
4.5.4	OpSim, OpDigit, OpEmuIO . . . . .	61
4.5.5	OpRec & OpEmuRec . . . . .	61
4.5.6	OpCarac . . . . .	62
4.5.7	OpBrickFinder . . . . .	62
4.6	Event Reconstruction in OPERA . . . . .	63
4.6.1	Electronic Detector Event Reconstruction . . . . .	63
4.6.2	Electronic Detector - Emulsion Cloud Chamber Interface . . . . .	63
4.6.3	Emulsion Cloud Chamber Event Reconstruction . . . . .	66
4.7	$\nu_\mu \rightarrow \nu_\tau$ Appearance Search . . . . .	68
4.7.1	General Event Topology . . . . .	68
4.7.2	Standard Analysis Chain . . . . .	69
4.7.3	Backgrounds . . . . .	71
4.7.4	Decay Channels & Kinematical Cuts . . . . .	75
4.7.5	Discovery of $\nu_\mu \rightarrow \nu_\tau$ Oscillations . . . . .	77
4.7.6	Outlook: Final Analysis . . . . .	79
<b>5</b>	<b><math>\nu_e</math> Event Reconstruction</b>	<b>81</b>
5.1	General Event Topology . . . . .	81
5.2	Electromagnetic Showers in OPERA . . . . .	82
5.2.1	ED Reconstruction . . . . .	82
5.2.2	CS Shower Hints & Extended Scanning Volume . . . . .	83
5.2.3	ECC Reconstruction & Rejection of Backgrounds . . . . .	84
5.3	Monte Carlo Simulation . . . . .	86
5.3.1	Neutrino Event Generator . . . . .	86
5.3.2	Detector Geometry Description . . . . .	87
5.3.3	Detector Simulation . . . . .	88
5.3.4	Quality Cuts . . . . .	88

5.3.5	Location of $\nu_e$ Candidate Bricks . . . . .	90
5.4	Energy Estimation for $\nu_e$ Events . . . . .	91
5.4.1	Energy Reconstruction in the OPERA TT . . . . .	91
5.4.2	ED $\nu_e$ Energy Estimation . . . . .	93
5.5	Outlook . . . . .	99
<b>6</b>	<b><math>\nu_\mu \rightarrow \nu_e</math> Oscillation Analysis</b>	<b>101</b>
6.1	Data Sample . . . . .	101
6.1.1	$\nu_e$ Detection Efficiency . . . . .	102
6.1.2	$\nu_e$ Event Selection & Backgrounds . . . . .	103
6.2	$\nu_e$ Appearance Search . . . . .	105
6.2.1	Background from Beam Contamination . . . . .	106
6.2.2	Reconstructed Energy . . . . .	106
6.2.3	$\nu_e$ Appearance Search: Standard 3-Flavour Scenario . . . . .	108
6.2.4	$\nu_e$ Appearance Search: Nonstandard Oscillations . . . . .	111
6.3	Outlook . . . . .	113
<b>7</b>	<b>Conclusion</b>	<b>115</b>
<b>A</b>	<b>Appendix</b>	<b>117</b>
A.1	3-Flavour Neutrino Oscillations in Vacuum . . . . .	117
A.1.1	$\nu_\mu \rightarrow \nu_\mu$ Survival Probability . . . . .	117
A.1.2	$\nu_\mu \rightarrow \nu_\tau$ Appearance Probability . . . . .	118
A.1.3	$\nu_\mu \rightarrow \nu_e$ Appearance Probability . . . . .	119
	<b>List of Abbreviations</b>	<b>121</b>
	<b>List of Tables</b>	<b>125</b>
	<b>List of Figures</b>	<b>127</b>
	<b>Bibliography</b>	<b>131</b>





# Chapter 1

## Introduction

Many aspects of the Standard Model of particle physics have been explored and confirmed to a very high degree of detail. Yet due to its low interaction cross sections, the neutrino still retains a certain aspect of mystery.

The neutrino was originally presumed to be a massless particle. However, measurements of neutrino flavour transitions have shown that its mass eigenstates of time propagation are distinct from the flavour eigenstates of weak interaction - and that not all of them can be of the same value.

Numerous experiments, using both man-made and natural sources, have since measured the disappearance or appearance of certain flavours of neutrinos via various oscillation channels. While the disappearance of muon neutrinos in presumed  $\nu_\mu \rightarrow \nu_\tau$  oscillations was detected already in 1998 [98], the actual observation of  $\tau$  neutrino appearance was still missing to complete the picture.

The OPERA detector was specifically built to detect the appearance of  $\tau$  neutrinos in the CNGS pure muon neutrino beam on an event-by event basis. In 2010, its success was confirmed by the detection of a first  $\nu_\tau$  candidate event in the detector [12].

Though not optimised for a study of the sub-leading oscillation channel of  $\nu_\mu \rightarrow \nu_e$  oscillations, OPERA is well suited to identify  $\nu_e$  CC interactions. Given the relatively large value of the respective mixing angle  $\theta_{13}$  recently reported by reactor experiments [35, 28, 5], a search for  $\nu_e$  appearance was attempted.

Within the framework of this thesis, an energy estimation of  $\nu_e$  CC interactions using the Electronic Detector of OPERA is developed. The energy spectra of oscillated electron neutrinos and those from the prompt CNGS beam contamination differ. The reconstructed  $\nu_e$  energy can thus be used to separate a possible oscillation signal from the CNGS beam-induced background.

The results are applied to both a 3-flavour  $\nu_\mu \rightarrow \nu_e$  oscillation analysis and a nonstandard 'sterile' neutrino search [16]. New limits on the parameter space of nonstandard oscillations are provided.

Following this introduction, Chapter 2 will give a summary of neutrino physics<sup>1</sup>. After providing some historical background, the neutrino's role within the Standard Model of particle physics is explained. Neutrino interactions and cross sections are described, as is the theoretical framework of neutrino oscillations. The chapter concludes with a brief overview of open questions.

As the topology of electromagnetic showers is of great importance for the reconstruction of  $\nu_e$  Charged Current (CC) interactions in OPERA, Chapter 3 will provide a short review of their general properties and kinematics.

In Chapter 4, the OPERA experiment will be explained. Following its physical motivation and a summary of predecessor experiments, the CNGS neutrino beam and the OPERA detector are described. An outline of the software framework and event reconstruction methods is given. The presentation of the experiment's principal  $\nu_\mu \rightarrow \nu_\tau$  appearance search brings the chapter to a close.

The main contribution to the OPERA  $\nu_\mu \rightarrow \nu_e$  oscillation analysis conducted within the framework of this thesis is summarised in Chapter 5. The general  $\nu_e$  CC interaction topology in OPERA is explained, including the procedures for electromagnetic shower search and background rejection. A description of the MC simulation of  $\nu_e$  events in the OPERA detector is given. It is followed by the detailed explanation of the developed energy estimation, its performance and application to real  $\nu_e$  candidates.

Chapter 6 presents the first  $\nu_\mu \rightarrow \nu_e$  oscillation search conducted with OPERA. After detailing the analysed data sample, efficiencies, and backgrounds, the energy calibration described in the previous chapter is applied to introduce selection cuts on the reconstructed  $\nu_e$  energy. The results of a 3-flavour analysis and a search for nonstandard oscillations are presented, both profiting from the improved signal-to-noise ratio.

---

<sup>1</sup>For a much more comprehensive review, see e.g. [163].

## Chapter 2

# Neutrino Physics

This chapter will give a brief overview of the history of the neutrino (Section 2.1), its relation to the Standard Model of particle physics (Section 2.2), and its properties. The focus will be on neutrino oscillations (Section 2.4), also addressed are neutrino interactions and cross sections (Section 2.3) as well as select open questions (Section 2.5).

Proposed in 1930 by W. Pauli with his famous letter [141], the neutrino was introduced to explain the continuous energy spectrum of radioactive  $\beta$  decay (see Figure 2.1) that had first been observed in 1914 by J. Chadwick in decays of  $^{214}\text{Pb}$  and  $^{214}\text{Bi}$  [70].

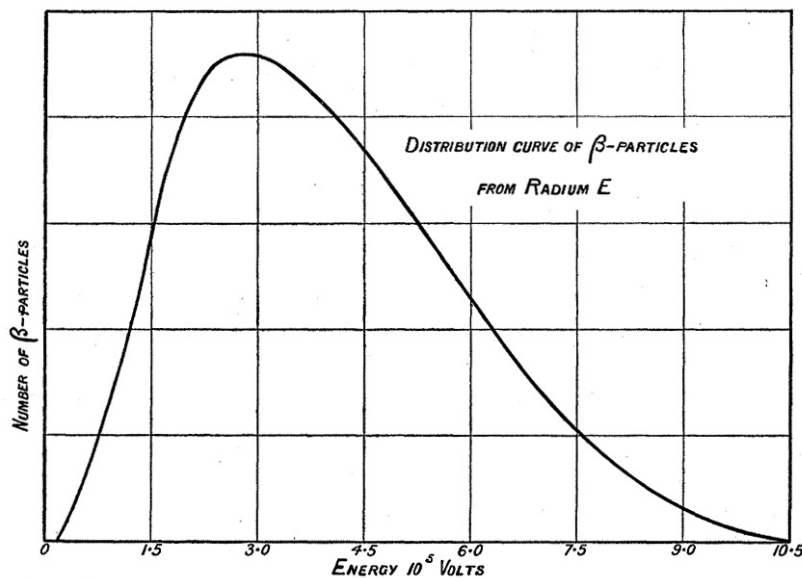


**Figure 2.1:** Continuous  $\beta$  decay spectrum observed in measurements of 'Radium E' ( $^{210}\text{Bi}$ ), energy in units of (electron)'Volts' [84].

The electrically neutral spin 1/2-neutrino was intended to ensure both the conservation of angular momentum<sup>1</sup> and energy via the three-body decay:

$$M(A, Z) \rightarrow D(A, Z + 1) + e^- + \bar{\nu}_e \quad (2.1)$$

<sup>1</sup>Required by the recently-formulated quantum-mechanical spin statistics of fermions and bosons.

with  $M(A, Z)$  and  $D(A, Z + 1)$  being the mother and daughter nuclei,  $A$  and  $Z$  the nucleon and proton numbers, or:



where  $n^0$  and  $p^+$  denote the neutron and proton, respectively. While the electron  $e^-$  can be measured, the weakly interacting electron anti-neutrino  $\bar{\nu}_e$  usually escapes undetected.

It took more than 20 years until the neutrino could be directly observed via inverse  $\beta$  decay:



Using liquid scintillator to detect the delayed coincidence signal of positron  $e^+$  annihilation and  $n^0$  capture by Cd in an aqueous solution of CdCl<sub>2</sub>, F. Reines & C. L. Cowan finally succeeded in observing  $\bar{\nu}_e$  from the Savannah River Plant in 1956 [146, 77, 147].

## 2.1 Historical Overview: Neutrino Oscillations

The importance of the neutrino for our current understanding of nature is prominently illustrated by the 2015 physics Nobel prize that was awarded to T. Kajita of SK and A. McDonald of SNO, honouring the experimental discovery of neutrino oscillations.

### 2.1.1 Early Discussion of Neutrino Oscillations

Neutrino oscillations were first discussed in 1957 by B. Pontecorvo as  $\nu \leftrightarrow \bar{\nu}$  oscillations, in analogy to the recently discovered mixing in neutral  $K$  mesons [143].

In 1962, Lederman *et. al.* established the existence of at least two types of neutrinos with their  $\nu_\mu$  beam experiment at Brookhaven National Laboratory (BNL) [79] by observing the  $\nu_\mu$  and showing that  $\nu_\mu$  and  $\nu_e$  are not indistinguishable.

Z. Maki, M. Nakagawa and S. Sakata then started discussing the possibility of neutrino two-flavour mixing [130], which was later improved upon by B. Pontecorvo and V. N. Gribov [144, 104], and culminates in today's PMNS mixing matrix (s. Chapter 2.4.1).

### 2.1.2 Number of Lepton Families

While the  $\tau$  lepton was discovered as the third charged lepton in 1975 by M. Perl *et. al.* at the Stanford Linear Accelerator Center (SLAC) SPEAR facility [142], it took another 25 years until the  $\nu_\tau$  could finally be observed by the DONuT experiment (see Chapter 4.2.1) [119].

Before, the GWS theory of electro-weak interaction had already incorporated neutrinos, albeit as massless particles (see Chapter 2.2). In 1989, the measurement of the  $Z^0$  total decay width at the ALEPH Large Electron Positron Collider (LEP) experiment determined the number of active light<sup>1</sup> neutrino species to be about 3 [81].

---

<sup>1</sup>I.e.  $m_\nu \leq m_{Z^0}/2 \approx 91.2/2 \text{ GeV}$ .

### 2.1.3 SNO and the Solar Neutrino Problem

The so-called *solar neutrino problem* started in 1960. A deficit in the solar neutrino flux measured by R. Davis Jr.'s Homestake experiment was detected when compared to the theoretical calculations of J. Bahcall [80]. In the electron neutrino capture reaction:



only about one third of the rate expected from the solar  $\beta$  decay:



was observed, while helioseismological measurements agreed well with Standard Solar Model (SSM) predictions [52].

The simultaneous detection of all neutrino flavours could finally be conducted in 2001 with the Sudbury Neutrino Observatory (SNO) experiment [26]. Using a water Cerenkov detector with a target of heavy water ( $\text{D}_2\text{O}$ ), the following interactions became observable:



with  $d^+$  denoting the deuteron and  $l = e, \mu, \tau$  being the respective lepton flavour.

While the CC reaction is possible only for electron neutrinos, the Neutral Current (NC) elastic (EL) interactions are sensitive to all active neutrino flavours<sup>1</sup>.

A reduced  ${}^8\text{B}$  solar electron neutrino flux  $\phi_e$  was measured, but it was compensated for by the increased flux of muon and tau neutrinos  $\phi_{\mu\tau}$  [27]:

$$\phi_e = 1.76_{-0.05}^{+0.05}(\text{stat.})_{-0.05}^{+0.09}(\text{syst.}) \times 10^6 \text{ cm}^{-2} \text{ s}^{-1} \quad (2.9)$$

$$\phi_{\mu\tau} = 3.41_{-0.45}^{+0.45}(\text{stat.})_{-0.45}^{+0.48}(\text{syst.}) \times 10^6 \text{ cm}^{-2} \text{ s}^{-1} \quad (2.10)$$

$$\phi_{NC} = 5.09_{-0.43}^{+0.44}(\text{stat.})_{-0.43}^{+0.46}(\text{syst.}) \times 10^6 \text{ cm}^{-2} \text{ s}^{-1} \quad (2.11)$$

The total NC neutrino flux  $\phi_{NC}$  proved to be consistent with the predictions from the SSM (see Figure 2.2).

Though this measurement provides evidence for neutrino flavour transformation, it must be attributed not to neutrino flavour oscillations (described in Chapter 2.4.1), but to the adiabatic flavour transition in the Sun due to the MSW effect [150] (see Chapter 2.4.2).

---

<sup>1</sup>In the case of EL scattering however, lower cross sections apply to  $\nu_\mu$  and  $\nu_\tau$  than to  $\nu_e$ .

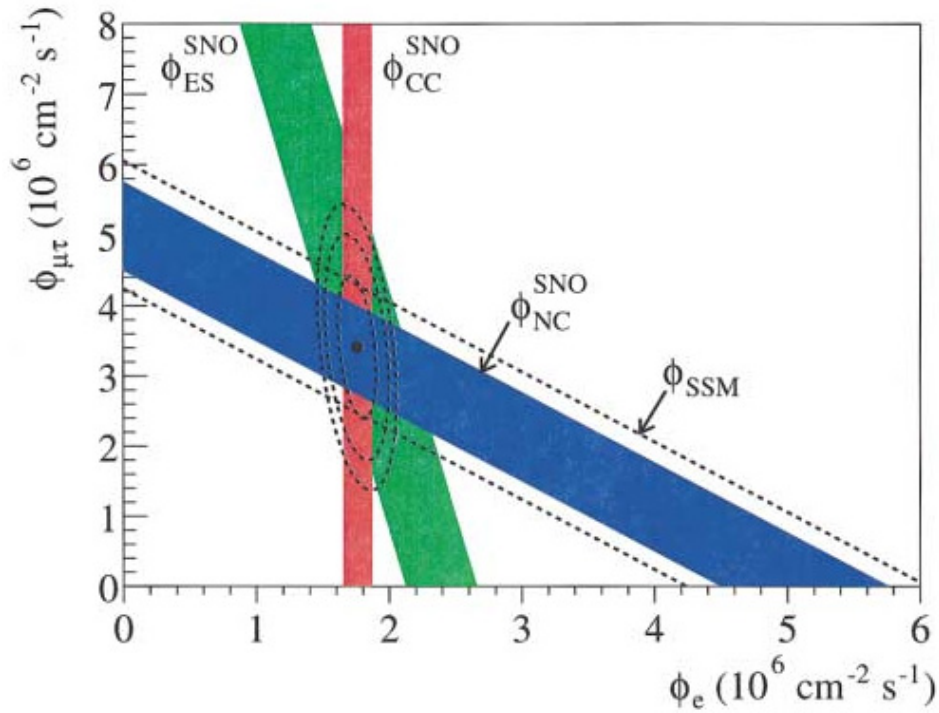


**Figure 2.2:**  $^8\text{B}$  solar neutrino flux measured by SNO. The diagonal bands of both the measured NC interactions  $\phi_{NC}^{SNO}$  and SSM prediction  $\phi_{SSM}$  intersect with the measured fluxes  $\phi_{ES}^{SNO}$  and  $\phi_{CC}^{SNO}$  of NC EL and  $\nu_e$  CC interactions at the fit values for  $\phi_e$  and  $\phi_{\mu\tau}$  within  $\pm 1\sigma$  [27].

### 2.1.4 SK and the Atmospheric Neutrino Anomaly

In 1998, the Super-Kamiokande (SK) collaboration presented an analysis of atmospheric  $\nu_\mu$ , reporting evidence for a *disappearance* of muon neutrinos that could be explained with the two-flavour oscillations of  $\nu_\mu \leftrightarrow \nu_\tau$  [98].

The *atmospheric neutrino anomaly* had persisted since the Irvine-Michigan-Brookhaven (IMB) experiment's indication of a deficit in the expected atmospheric  $\nu_\mu$  flux [109]. From the production of electron and muon neutrinos in the atmosphere, dominated by the decays of pions <sup>1</sup>, a ratio of:

$$\frac{N_\mu}{N_e} = \frac{N_{\nu_\mu + \bar{\nu}_\mu}}{N_{\nu_e + \bar{\nu}_e}} \approx 2 \quad (2.12)$$

is expected, with  $N_{\nu_\mu + \bar{\nu}_\mu}$  being the number of muon neutrino and anti-neutrino events and  $N_{\nu_e + \bar{\nu}_e}$  being the number of electron neutrino and anti-neutrino events. A deviation:

$$R = \frac{(N_\mu/N_e)_{\text{data}}}{(N_\mu/N_e)_{\text{MC}}} = 0.65 \pm 0.05(\text{stat.}) \pm 0.08(\text{syst.}) \quad (2.13)$$

of observed (data) vs. expected (MC) events was measured by the SK water Cerenkov detector. The observed asymmetry  $A = (U - D)/(U + D)$  of upgoing ( $U$ ) and downgoing ( $D$ )  $\mu$ -like events can be explained by  $\nu_\mu \leftrightarrow \nu_\tau$  oscillations, see Figure 2.3.

<sup>1</sup>I.e.  $\pi^+ \rightarrow \mu^+ + \nu_\mu$  followed by  $\mu^+ \rightarrow e^+ + \bar{\nu}_\mu + \nu_e$  and charge conjugate (c.c.).

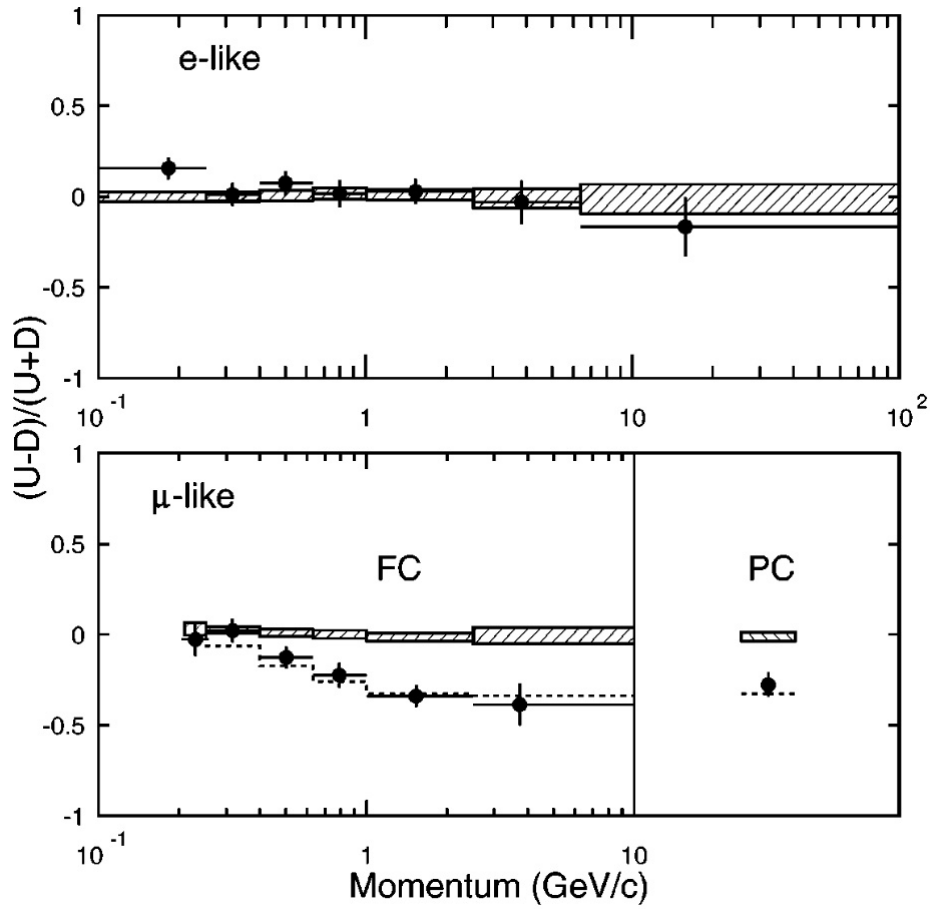


**Figure 2.3:**  $(U - D)/(U + D)$  asymmetry as a function of momentum for  $e$ -like and  $\mu$ -like interactions in SK. For fully contained events (FC), the momentum can be reconstructed, for partially contained events (PC), a mean energy of 15 GeV is assumed. The hatched region represents the MC expectation without neutrino oscillations, while the dotted line shows the expectation for  $\nu_\mu \leftrightarrow \nu_\tau$  two-flavour oscillations at  $\sin^2 2\theta = 1.0$  and  $\Delta m^2 = 2.2 \times 10^{-3} \text{ eV}^2$  [98].

Using the CNGS muon neutrino beam, in 2012 the OPERA experiment could demonstrate the *appearance* of  $\tau$  neutrinos on an event-by-event basis (see Chapter 4.7.5), thus firmly establishing the picture of neutrino oscillations.

## 2.2 Neutrinos and the Standard Model of Particle Physics

The current state of knowledge on the elementary particles and their interactions is summarised by the so-called Standard Model. Here, only a brief and phenomenological summary will be given - for a more comprehensive description see e.g. [105].

The Standard Model of particle physics is a gauge theory based on the mathematical framework of local  $SU(3) \otimes SU(2) \otimes U(1)$  invariance with spontaneously broken symmetry. Three different types of fields are described: The gauge fields, the fermion mass fields, and the Higgs field.

The twelve gauge fields are the generators of the three symmetry groups. They represent the vector bosons (spin 1) mediating the corresponding forces of electromagnetic, weak, and strong interactions.

Quarks  $q$  and leptons  $l$  are described by the twelve two-component spinor fermion fields (spin  $\frac{1}{2}$ ). These particles are arranged in three generations of identical structure (see Table 2.1 for an overview of their properties). While leptons only interact via electromagnetic and weak interactions, the quarks are subject to all three interaction types, including the strong interaction.

The masses of the elementary particles are introduced via the so-called Higgs field. After its proposal by P. Higgs *et al.* in 1964 [85, 110], the corresponding scalar gauge boson  $h$  (spin 0) was long sought for and could finally be observed in 2012 by the ATLAS and CMS experiments at the Large Hadron Collider (LHC) [1, 71].

**Table 2.1:** Properties of quarks and leptons. Shown are the three generations of left-handed doublets ( $L$ ) and right-handed singlets ( $R$ ) of elementary fermions  $l = e, \mu, \tau$  and their quantum numbers of weak hypercharge  $Y$ , weak isospin  $I$  and its third component  $I_3$ , and electric charge  $Q$ . The index  $i = R, G, B$  denotes the colour charge of QCD.  $q_u = u, c, t$  are *up-type* quarks,  $q_d = d, s, b$  are *down-type* quarks. The weak interaction quark eigenstates  $q'$  are mixed states w.r.t. the strong interaction eigenstates  $q$ :  $(d', s', b') = U_{CKM} \cdot (d, s, b)^T$  [65, 118]. Anti-particles feature the same additive quantum numbers as particles, but with reversed signs.

	I	II	III	$Y$	$I$	$I_3$	$Q$
Leptons	$\begin{pmatrix} \nu_e \\ e \end{pmatrix}_L$	$\begin{pmatrix} \nu_\mu \\ \mu \end{pmatrix}_L$	$\begin{pmatrix} \nu_\tau \\ \tau \end{pmatrix}_L$	-1	$+\frac{1}{2}$	$+\frac{1}{2}$ $-\frac{1}{2}$	0 -1
	$e_R$	$\mu_R$	$\tau_R$	-2	0	0	-1
Quarks	$\begin{pmatrix} u_i \\ d'_i \end{pmatrix}_L$	$\begin{pmatrix} c_i \\ s'_i \end{pmatrix}_L$	$\begin{pmatrix} t_i \\ b'_i \end{pmatrix}_L$	$+\frac{1}{3}$	$+\frac{1}{2}$	$+\frac{1}{2}$ $-\frac{1}{2}$	$+\frac{2}{3}$ $-\frac{1}{3}$
	$u_{i,R}$	$c_{i,R}$	$t_{i,R}$	$+\frac{4}{3}$	0	0	$+\frac{2}{3}$
	$d_{i,R}$	$s_{i,R}$	$b_{i,R}$	$-\frac{2}{3}$	0	0	$-\frac{1}{3}$

The accuracy of the Standard Model has been tested and established by many experiments to a very high degree. However, in its simplest form it treats neutrinos as massless particles<sup>1</sup>.

<sup>1</sup>In contrast to the case for gluons and photons, this is not strictly required by gauge invariance.



An extension of the Standard Model, allowing for neutrino masses and thus neutrino vacuum oscillations (see Section 2.4.1), should also make it possible to observe neutrinos of positive and anti-neutrinos of negative helicity (see Section 2.2.2).

### 2.2.1 Quantum Chromo Dynamics: SU(3)

Quantum Chromo Dynamics (QCD) is the non-Abelian<sup>1</sup> gauge theory of strong interaction, based on the local symmetry group  $SU(3)$ . It may be treated separately from  $SU(2)_L \otimes U(1)_Y$ , as the gauge bosons of strong and electroweak interactions do not mix.

The generators of the strong interaction are the eight massless and electrically neutral gluons  $g$  that couple to colour charge.

With the gluons themselves being carriers of colour (and anti-colour), their self-coupling leads to an amplification of the strong interaction with growing distance. This makes the creation of new quark anti-quark pairs energetically favourable to greater dislodgement of two individual quarks. As a result, the colour-charged quarks are confined inside colour-neutral hadrons (mesons  $q\bar{q}$  or baryons  $qqq$ ). Only at very high energies, they may be studied as asymptotically free particles.

### 2.2.2 GWS Model of Electroweak Unification: $SU(2)_L \otimes U(1)_Y$

Sometimes also called Quantum Flavour Dynamics (QFD), the Glashow Weinberg Salam (GWS) model of electroweak unification combines electromagnetic and weak interactions. It was invented in the 1960s [100, 157, 149] and later extended to also include the hadronic sector and quark flavour mixing [65, 118].

Electroweak interactions are described by the symmetry groups  $SU(2)_L \otimes U(1)_Y$  with their respective generators of weak isospin  $I$  and weak hypercharge  $Y$ .

The four physical gauge bosons  $W^\pm$ ,  $Z^0$ , and  $\gamma$  of electroweak theory result from the mixing of the gauge fields  $W_1^\mu$ ,  $W_2^\mu$ ,  $W_3^\mu$  of  $SU(2)_L$  with coupling constant  $g$ , and  $B^\mu$  of  $U(1)_Y$  with coupling constant  $g'$ :

$$W^{\pm\mu} = \frac{1}{\sqrt{2}}(W_1^\mu \pm iW_2^\mu) \quad (2.14)$$

$$\begin{pmatrix} Z^\mu \\ A^\mu \end{pmatrix} = \begin{pmatrix} \cos \theta_W & -\sin \theta_W \\ \sin \theta_W & \cos \theta_W \end{pmatrix} \times \begin{pmatrix} W_3^\mu \\ B^\mu \end{pmatrix} \quad (2.15)$$

where  $\theta_W$  represents the electroweak mixing angle:

$$\cos \theta_W = g/\sqrt{g^2 + g'^2} \quad \text{and} \quad \sin \theta_W = g'/\sqrt{g^2 + g'^2} \quad (2.16)$$

The physical mixed states of charged vector bosons  $W^\pm$  mediate the weak Charged Current (CC) using coupling constant  $g_{CC}$ :

$$g_{CC} = \frac{g}{2\sqrt{2}} \quad (2.17)$$

---

<sup>1</sup>The generators of such groups do not commute, causing the mediator particles to themselves carry charge.

$Z^\mu$  and  $A^\mu$  are identified with the neutral physical vector bosons  $Z^0$  and  $\gamma$ . The weak Neutral Current is mediated by  $Z^0$ , its coupling constant  $g_{NC}$  being:

$$g_{NC} = \frac{1}{2} \sqrt{g^2 + g'^2} = \frac{e}{2 \sin \theta_W \cos \theta_W} \quad (2.18)$$

$\gamma$  couples to electric charge<sup>1</sup>  $Q$  and mediates the electromagnetic interaction via coupling constant  $e$ :

$$e = \frac{g \cdot g'}{\sqrt{g^2 + g'^2}} = g \cdot \sin \theta_W = g' \cdot \cos \theta_W \quad (2.19)$$

The coupling constant  $g$  is the same for leptons of all flavours (*lepton universality*).

As the gauge field triplet  $W_1^\mu, W_2^\mu, W_3^\mu$  of  $SU(2)_L$  exclusively couple to left-handed fermions and right-handed anti-fermions<sup>2</sup> - thus maximally violating parity invariance - so do the physical mixed states of charged vector bosons  $W^\pm$ .  $Z^0$  and  $\gamma$ , as mixed states of  $W_3^\mu$  and the singlet  $B^\mu$ , on the other hand affect fermions regardless of chirality.

For the left-handed components of the fermion fields  $\Psi_L$  (see also Table 2.1):

$$\Psi_L = \begin{pmatrix} \Psi(1) \\ \Psi(2) \end{pmatrix}_L \quad \text{i.e.} \quad \Psi_L = \begin{pmatrix} \nu_l \\ l \end{pmatrix}_L \quad \text{or} \quad \Psi_L = \begin{pmatrix} q_u \\ q'_d \end{pmatrix}_L \quad (2.20)$$

CC interactions mediated by  $W^\pm$  describe transitions  $\Psi(1) \leftrightarrow \Psi(2)$  and thus a change of the weak isospin third component  $I_3$  of  $\pm 1$ . Contrary to that, NC interactions via  $Z^0$  imply  $\Psi(i) \leftrightarrow \Psi(i)$  ( $i = 1, 2$ ), conserving  $I_3$ .

The masses of the physical gauge bosons are introduced via the scalar Higgs field  $\Phi$  [85, 110]:

$$\Phi = \frac{1}{\sqrt{2}} \begin{pmatrix} \Phi_1 + i\Phi_2 \\ \Phi_3 + i\Phi_4 \end{pmatrix} \quad \text{and} \quad \Phi_0 = \frac{1}{\sqrt{2}} \begin{pmatrix} 0 \\ v \end{pmatrix} \quad (2.21)$$

where  $v^2 > 0$  renders the vacuum expectation value  $\Phi_0$  nonzero.

By coupling to  $\Phi$ , the weak isospin rotation symmetry of the massless gauge fields  $W_i^\mu$  is spontaneously broken. This leads to non-diagonal mass terms for the gauge fields in the Lagrangian energy density<sup>3</sup>, resulting in the masses of  $W^\pm$  and  $Z^0$ :

$$M_W = \frac{gv}{2} \quad (2.22)$$

$$M_Z = \frac{v}{2} \sqrt{g^2 + g'^2} = \frac{M_W}{\cos \theta_W} \quad (2.23)$$

while the photon  $\gamma$  remains massless ( $M_A = 0$ ).

<sup>1</sup>Electric charge  $Q$ , weak hypercharge  $Y$ , and weak Isospin  $I$  are related via  $Q = I_3 + Y/2$ .

<sup>2</sup>Chirality is determined by the sign of a particle's helicity  $H = s \cdot p/|p|$ . If  $H > 0$ , the particle is called *right-handed* ( $R$ ), if  $H < 0$ , the particle is called *left-handed* ( $L$ ). Massless particles are thus always left-handed, while massless anti-particles are always right-handed.

<sup>3</sup>In field theory, the Lagrange function  $L = T - V$  of classical dynamics converts into an integral over the Lagrangian energy density, summarising the dynamics of a system.

## 2.3 Neutrino Interactions with Matter

As the interaction of neutrinos with matter can only occur via the weak interaction, the respective cross sections are extremely small. Their understanding is an essential part of any neutrino experiment and a very active field of research [140, 137].

Neutrino - nucleus interactions can in principle be described by the Standard Model electroweak theory. However, they require not only radiative corrections, but also such for initial and final states, nuclear corrections, and several other effects [96, 91]. The complexity and secondary particle multiplicity increases with the neutrino energy, and various approximations exist that work well in one energy range but not others.

Depending on the neutrino's energy, the most important neutrino - nucleus interactions at OPERA are elastic (EL) and quasi-elastic (QE) scattering, resonant (RES) pion production, and deep-inelastic scattering (DIS) processes. In the following, the scattering of neutrinos on free protons or neutrons, or on hypothetically free isoscalar nucleons<sup>1</sup> will be considered, thus neglecting nuclear effects if not specifically stated otherwise.

Especially in the absence of a near detector, experiments have to employ reliable Monte Carlo (MC) simulations for calculating interaction rates and energy spectra. The default OPERA event generator is NEGN (see Chapter 4.5.1) which is based on a static FORTRAN software design. A more modern and flexible approach is provided by GENIE, enabling the reweighting of events to reflect changes of input parameters<sup>2</sup> [37, 36].

### 2.3.1 Elastic and Quasi-Elastic Scattering

At energies below  $\sim 2$  GeV, Neutral Current (NC) elastic (EL) scattering and Charged Current (CC) quasi-elastic (QE) scattering dominate.

These are the lowest-multiplicity neutrino - nucleus interactions where the neutrino scatters off an entire nucleon (i.e. a neutron  $n^0$  or a proton  $p^+$ ) rather than its constituent partons [96].

#### Neutral Current Elastic Scattering

The EL scattering of neutrinos and anti-neutrinos on nucleons via NC interactions is summarised by the following equations:

$$\nu_l + n^0 \rightarrow \nu_l + n^0 \qquad \bar{\nu}_l + n^0 \rightarrow \bar{\nu}_l + n^0 \qquad (2.24)$$

$$\nu_l + p^+ \rightarrow \nu_l + p^+ \qquad \bar{\nu}_l + p^+ \rightarrow \bar{\nu}_l + p^+ \qquad (2.25)$$

with  $l = e, \mu, \tau$  describing the lepton flavour. As there is no charged lepton in the final state, the flavour of the scattering neutrino cannot be identified.

<sup>1</sup>Isoscalar nuclei contain the same number of protons and neutrons.

<sup>2</sup>Instead of re-generating an entire MC sample, events are reweighted for changes of input parameters. Modified cross sections will usually affect both normalisation and shape of the event distribution, while an adjusted hadronisation model will change its shape only [91].

### Charged Current Quasi-Elastic Scattering

In CC QE neutrino - nucleon scattering a target neutron is converted to a proton, while in anti-neutrino - nucleon scattering a target proton is converted to a neutron:

$$\nu_l + n^0 \rightarrow l^- + p^+ \qquad \bar{\nu}_l + p^+ \rightarrow l^+ + n^0 \qquad (2.26)$$

The final states are characterised by the charged lepton  $l = e, \mu, \tau$  which carries most of the neutrino's kinetic energy [140]. It can be used to identify the incoming neutrino's flavour.

A Feynman diagram for the CC QE scattering of electron neutrinos on neutrons is shown in Figure 2.4.

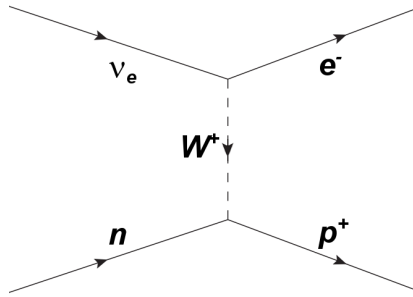


**Figure 2.4:**  $\nu_e + n^0$  CC QE scattering.

CC QE scattering defines the energy threshold  $E_{thr}$  for the production of charged leptons in neutrino interactions [96, 91]:

$$\nu_e + n^0 \rightarrow e^- + p^+ \qquad (2.27)$$

$$\bar{\nu}_e + n^0 \rightarrow e^+ + p^+ \qquad E_{thr} = 1.806 \text{ MeV} \qquad (2.28)$$

$$\nu_\mu + n^0 \rightarrow \mu^- + p^+ \qquad E_{thr} = 0.110 \text{ GeV} \qquad (2.29)$$

$$\bar{\nu}_\mu + p^+ \rightarrow \mu^+ + n^0 \qquad E_{thr} = 0.113 \text{ GeV} \qquad (2.30)$$

$$\nu_\tau + n^0 \rightarrow \tau^- + p^+ \qquad E_{thr} = 0.3454 \text{ GeV} \qquad (2.31)$$

$$\bar{\nu}_\tau + p^+ \rightarrow \tau^+ + n^0 \qquad E_{thr} = 0.3462 \text{ GeV} \qquad (2.32)$$

depending on the respective lepton flavour. As the simplest nuclear interaction, Equation 2.28 describes the inverse beta decay.

CC QE neutrino scattering is only possible on neutrons, while CC QE anti-neutrino scattering exclusively occurs on protons. Cross sections are commonly computed for isoscalar nuclei, requiring the application of corrections in the case of non-isoscalar target material.

A precise measurement of the neutrino and anti-neutrino CC QE cross sections may be able to answer the question of Charge-Parity (CP) violation (see Section 2.5.2) in the leptonic sector [96].

### 2.3.2 Resonant Scattering

In resonant (RES) scattering, the neutrino excites the struck nucleon. The produced short-lived baryon resonance quickly decays via the strong force, creating most often a single pion and nucleon final state [96].

This inelastic interaction dominates at intermediate neutrino energies around several GeV.

The cross sections for the scattering off free nucleons are commonly evaluated using a phenomenological description by Rein and Sehgal [145].

#### Neutral Current Resonant Scattering

There are four channels for NC RES single pion production:

$$\begin{aligned} \nu_l + n^0 &\rightarrow \nu_l + b^* & \bar{\nu}_l + n^0 &\rightarrow \bar{\nu}_l + b^* \\ &\hookrightarrow p^+ + \pi^- & &\hookrightarrow p^+ + \pi^- & (2.33) \\ &\hookrightarrow n^0 + \pi^0 & &\hookrightarrow n^0 + \pi^0 & (2.34) \end{aligned}$$

$$\begin{aligned} \nu_l + p^+ &\rightarrow \nu_l + b^* & \bar{\nu}_l + p^+ &\rightarrow \bar{\nu}_l + b^* \\ &\hookrightarrow p^+ + \pi^0 & &\hookrightarrow p^+ + \pi^0 & (2.35) \\ &\hookrightarrow n^0 + \pi^+ & &\hookrightarrow n^0 + \pi^+ & (2.36) \end{aligned}$$

with  $b^*$  being the excited nucleon and  $l = e, \mu, \tau$  the respective lepton flavour.

In neutrino oscillation experiments,  $\nu_\mu$ -induced NC RES pion production constitutes an important background to  $\nu_\mu \rightarrow \nu_e$  searches. A corresponding Feynman diagram is shown in Figure 2.5.

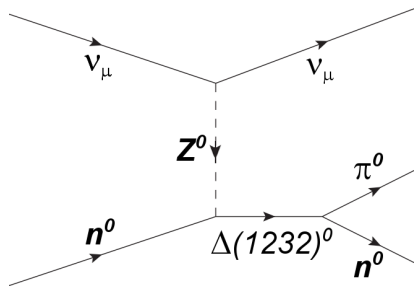


**Figure 2.5:**  $\nu_\mu + n^0$  NC RES scattering with  $\Delta(1232)^0$  production.

### Charged Current Resonant Scattering

CC RES single pion production is summarised by the following equations:

$$\begin{aligned} \nu_l + n^0 &\rightarrow l^- + b^* & \bar{\nu}_l + p^+ &\rightarrow l^+ + b^* \\ &\hookrightarrow p^+ + \pi^0 & &\hookrightarrow p^+ + \pi^- \end{aligned} \quad (2.37)$$

$$\hookrightarrow n^0 + \pi^+ \quad \hookrightarrow n^0 + \pi^0 \quad (2.38)$$

$$\begin{aligned} \nu_l + p^+ &\rightarrow l^- + b^* & \bar{\nu}_l + n^0 &\rightarrow l^+ + b^* \\ &\hookrightarrow p^+ + \pi^+ & &\hookrightarrow n^0 + \pi^- \end{aligned} \quad (2.39)$$

The created charged leptons  $l = e, \mu, \tau$  can be used to identify the neutrino flavour, but the reconstruction of its energy is often complicated by final state interactions (FSI) of the produced pions [96].

At low energies, RES neutrino - nucleon interactions are dominated by the production of the  $\Delta(1232)$  resonance. Figure 2.6 shows the respective Feynman diagram for CC RES scattering of muon neutrinos on protons.

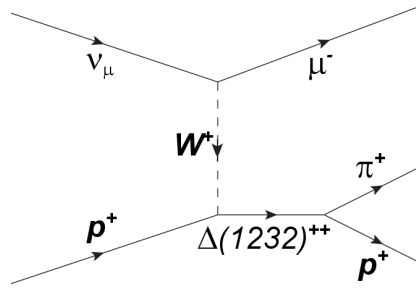


**Figure 2.6:**  $\nu_\mu + p^+$  CC RES scattering with  $\Delta(1232)^{++}$  production.

Increasing the neutrino energy will result in the excitation of higher-order resonances, producing final states with multiple pions [140].

### 2.3.3 Deep-Inelastic Scattering

At high energies  $\gtrsim 10$  GeV, the deep-inelastic scattering (DIS) of neutrinos on individual quarks probes the inner structure of the nucleon [96].

DIS of neutrinos on free nucleons is well understood by theory and can be described by the incoherent sum of elastic interactions with the nucleon constituents [91]. The final states are characterised by a neutral or charged lepton, and an outgoing system of hadrons.

#### Neutral Current Deep-Inelastic Scattering

The NC DIS of neutrinos and anti-neutrinos on a nucleon  $N = n^0, p^+$  is described by:

$$\nu_l + N \rightarrow \nu_l + X \quad \bar{\nu}_l + N \rightarrow \bar{\nu}_l + X \quad (2.40)$$

with  $l = e, \mu, \tau$  being the neutrino flavour and  $X$  the outgoing hadronic system.

### Charged Current Deep-Inelastic Scattering

Analogue to the NC processes, CC DIS neutrino - nucleon interactions are summarised by:

$$\nu_l + N \rightarrow l^- + X \qquad \bar{\nu}_l + N \rightarrow l^+ + X \qquad (2.41)$$

with a charged lepton  $l = e, \mu, \tau$  in the final state. The estimation of the incoming neutrino's energy requires not only momentum measurement for the lepton, but also the containment and reconstruction of the hadronic shower [140].

The pseudo-Feynman diagram of electron neutrino - nucleon CC DIS is shown in Figure 2.7.

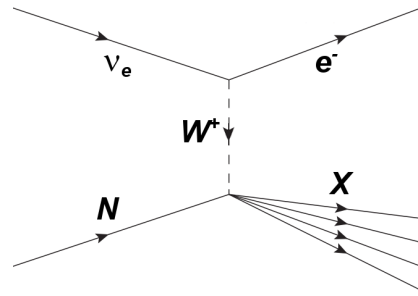


**Figure 2.7:**  $\nu_e + N$  CC DIS scattering.  $X$  symbolises the outgoing hadronic system.

### DIS Charm Production

The deep-inelastic scattering of neutrinos on nucleons may create charmed particles via NC or CC interactions.

At the energies relevant to the OPERA experiment, the contribution from NC DIS associated charm anti-charm production, shown in Figure 2.8a, is negligible [91].

The production of charmed particles in CC DIS interactions (see Figure 2.8b) however constitutes an important background to the  $\nu_\mu \rightarrow \nu_\tau$  oscillation search that will be described in Chapter 4.7.3.

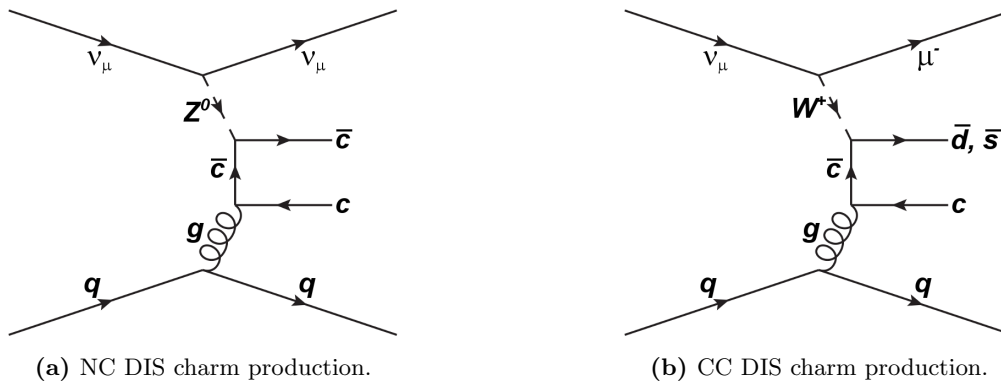


**Figure 2.8:** DIS charm production in boson-gluon fusion. (a) NC associated charm production. (b) CC single charm production.

### 2.3.4 Total Charged Current Cross Sections

The total cross sections for neutrino interactions with matter can in principle be evaluated by summing up all individual exclusive cross sections for the respective final states. Missing accurate theoretical descriptions, however, the total CC cross sections  $\sigma_{total}$  are usually estimated using the incoherent sum:

$$\sigma_{total} = \sigma_{QE} \oplus \sigma_{RES} \oplus \sigma_{DIS} \quad (2.42)$$

of the above-described dominating contributions from QE, RES, and DIS interactions [91].

The global experimental data on neutrino cross sections are severely limited by low statistics, and their combination is further complicated by the use of different target materials.

The scattering of neutrinos on free nucleons can only be measured using hydrogen or deuterium targets, and the current knowledge is based on bubble chamber measurements at low neutrino energies  $\mathcal{O}(1 \text{ GeV})$ .

Experimental data on RES scattering are provided by liquid scintillator or bubble chamber detectors and mostly limited to low-multiplicity pion final states.

Results from experiments employing heavier target materials are corrected so that they describe the  $\nu + N$  scattering on hypothetically free nucleons, with:

$$\sigma_N = \frac{\sigma_n + \sigma_p}{2} \quad (2.43)$$

i.e. for isoscalar target nuclei with the same number of protons and neutrons.

The only existing high-statistics data in the neutrino energy range of interest for OPERA around  $1 \text{ GeV} - 200 \text{ GeV}$  are from studies of  $\nu_\mu$  and  $\bar{\nu}_\mu$  scattering. These are mainly measurements of neutrino DIS in iron-based calorimeter detectors.



### Total $\nu_\mu$ and $\bar{\nu}_\mu$ CC Cross Sections

Comparisons of the available experimental data on the total  $\nu_\mu$  and  $\bar{\nu}_\mu$  CC cross sections with a calculation based on GENIE [91] are shown in Figures 2.9 and 2.10.

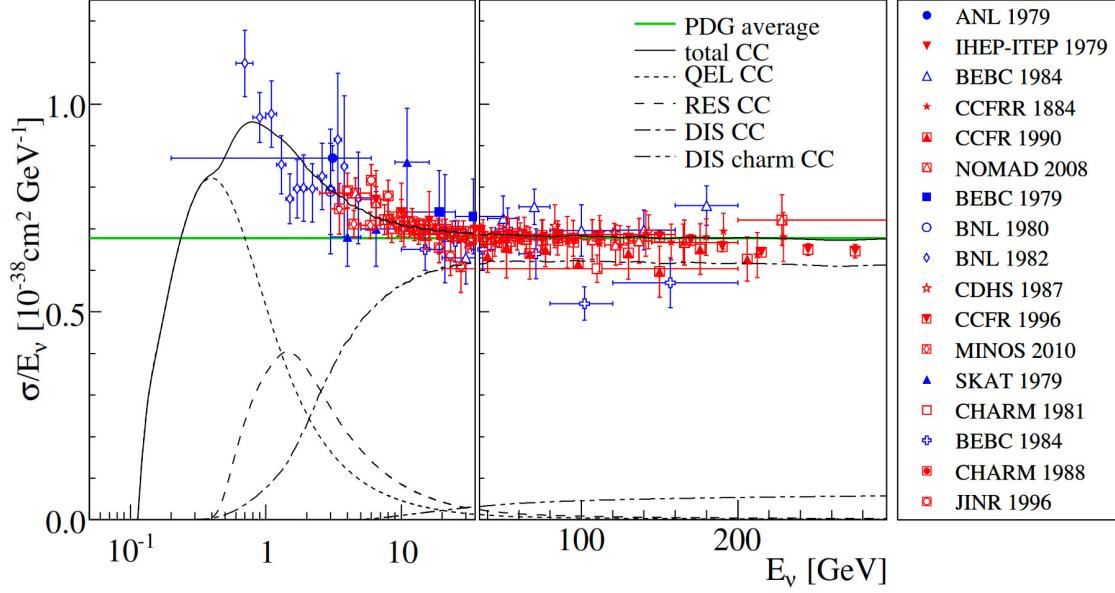


**Figure 2.9:** Total  $\nu_\mu + N$  CC cross section and contributions from QE, RES, and DIS interactions. Comparison of the calculation conducted in [91] with data from various experiments.

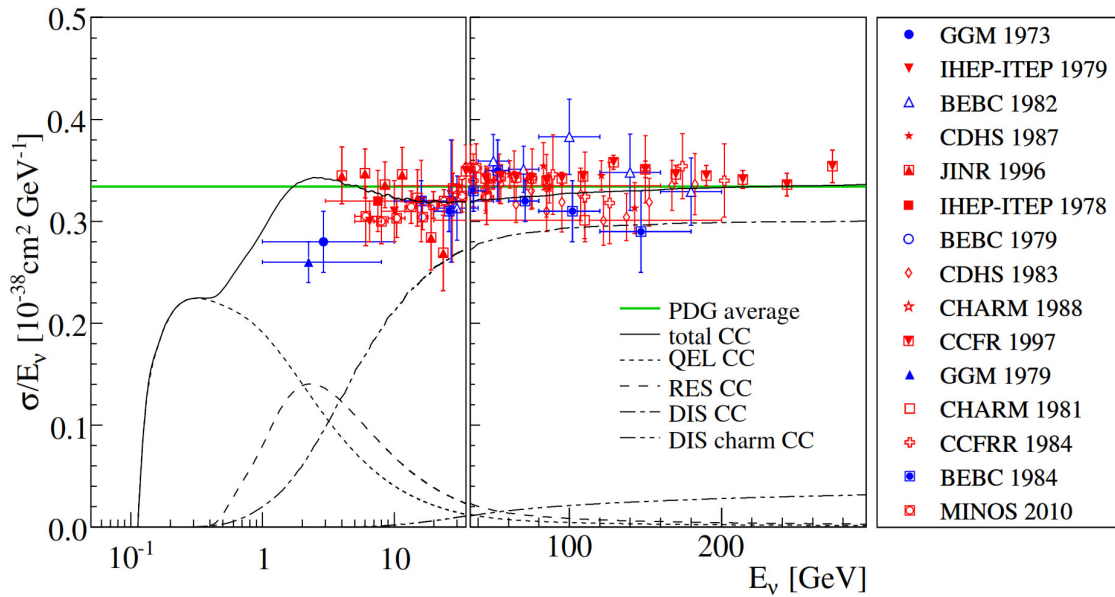


**Figure 2.10:** Total  $\bar{\nu}_\mu + N$  CC cross section and contributions from QE, RES, and DIS interactions. Comparison of the calculation conducted in [91] with data from various experiments.

At the average CNGS neutrino energies of  $\sim 20$  GeV (see Chapter 4.3.2), the total CC cross section for both  $\nu_\mu$  and  $\bar{\nu}_\mu$  interactions is dominated by DIS. RES scattering becomes relevant in the intermediate range of 0.5 GeV – 10 GeV, while QE scattering dominates at energies  $\lesssim 1$  GeV where the OPERA detection efficiency is very low.

### Total $\nu_e$ CC Cross Section

Intermediate-energy measurements of the total  $\nu_e$  CC cross section have been conducted by the Gargamelle experiment [60], and more recently by NOvA [64] and T2K [4]. They are shown in Figure 2.11, compared to the prediction from GENIE.

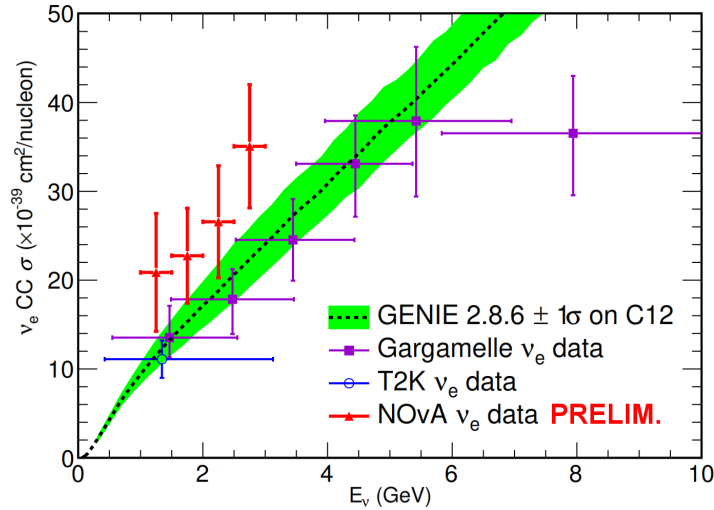


**Figure 2.11:** Total  $\nu_e + N$  CC cross section [64]. Comparison of the data from NOvA, T2K, and Gargamelle with a calculation using GENIE.

### Total $\nu_\tau$ CC Cross Section

The only existing data on the  $\tau$  neutrino cross section<sup>1</sup> are the 9  $\nu_\tau$  candidate events detected at DONuT (see Chapter 4.2.1) [120]. In Figure 2.12, the DONuT result can be seen, compared to a GENIE calculation of the total average ( $\nu_\tau + \bar{\nu}_\tau$ ) CC cross section [91].

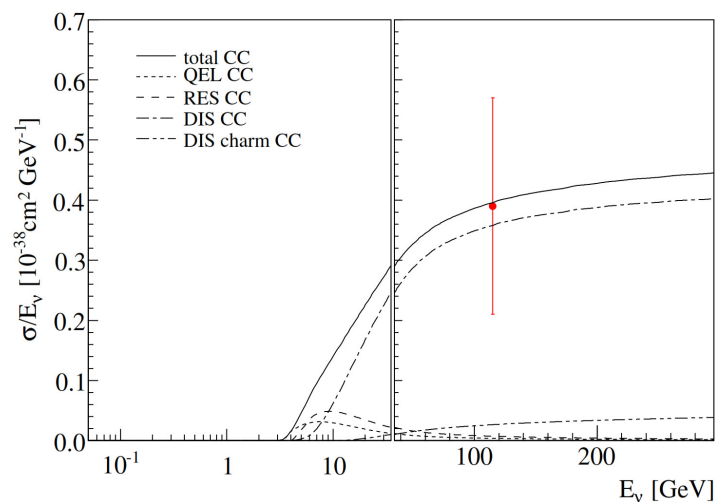


**Figure 2.12:** Total average ( $\nu_\tau + \bar{\nu}_\tau$ ) CC cross section and contributions from QE, RES, and DIS interactions [91]. Comparison of the calculation conducted with GENIE and data from DONuT [120].

<sup>1</sup>Apart from the measurement conducted by OPERA [21].

## 2.4 Flavour Mixing in the Neutrino Sector

Neutrino oscillations are the flavour-changing *periodic* transitions of a neutrino of generation  $\alpha$  into another neutrino of generation  $\beta$ :

$$\nu_\alpha \leftrightarrow \nu_\beta \quad (2.44)$$

with  $\alpha \neq \beta$ , thus violating lepton number conservation. Such processes are enabled by the neutrinos themselves being *massive*<sup>1</sup> particles.

Matter effects in the medium the neutrinos traverse may have similar effects, but have to be distinguished from oscillations (see Section 2.4.2).

### 2.4.1 Neutrino Oscillations in Vacuum

Neutrinos are produced and detected in weak interaction processes as orthonormal flavour eigenstates  $|\nu_\alpha\rangle$  of the lepton number operator  $L_\alpha$ :

$$L_\alpha|\nu_\beta\rangle = \delta_{\alpha\beta}|\nu_\beta\rangle \quad (2.45)$$

These differ from the orthonormal mass eigenstates  $|\nu_i\rangle$  of the mass operator  $M$ :

$$M|\nu_i\rangle = m_i\delta_{ij}|\nu_i\rangle \quad (2.46)$$

Assuming three generations of neutrinos,  $\alpha, \beta = e, \mu, \tau$  and  $i, j = 1, 2, 3$ .

Flavour and mass eigenstates are related via the complex unitary<sup>2</sup>  $n \times n$  mixing matrix  $U$  and may be expressed as linear combinations of each other:

$$|\nu_\alpha\rangle = \sum_i U_{\alpha i}^* |\nu_i\rangle \quad |\bar{\nu}_\alpha\rangle = \sum_i U_{\alpha i} |\bar{\nu}_i\rangle \quad (2.47)$$

$$|\nu_i\rangle = \sum_\alpha U_{\alpha i} |\nu_\alpha\rangle \quad |\bar{\nu}_i\rangle = \sum_\alpha U_{\alpha i}^* |\bar{\nu}_\alpha\rangle \quad (2.48)$$

Only the mass eigenstates  $|\nu_i\rangle$  are solutions to Schrödinger's Equation. In their rest frame, the time evolution is described by:

$$i \frac{\partial}{\partial \tau_i} |\nu_i(\tau_i)\rangle = H^V |\nu_i(\tau_i)\rangle \quad (2.49)$$

with  $\tau_i$  being the time of the neutrino mass eigenstate and  $H^V$  the Hamiltonian in vacuum.

The equation is solved by a plane wave using the mass  $m_i$  of the neutrino eigenstate:

$$|\nu_i(\tau_i)\rangle = e^{-im_i\tau_i} |\nu_i(0)\rangle \quad (2.50)$$

A Lorentz transformation  $m_i\tau_i = E_i t - p_i L$  to the lab frame yields:

$$|\nu_i(L, t)\rangle = e^{-i(E_i t - p_i L)} |\nu_i(0)\rangle \quad (2.51)$$

<sup>1</sup>While the Standard Model of particles physics assumes neutrinos to be massless, the introduction of neutrino masses does not violate any fundamental gauge symmetry.

<sup>2</sup> $U^\dagger U = \mathbf{1}$ ,  $\sum_i U_{\alpha i} U_{\beta i}^* = \delta_{\alpha\beta}$ ,  $\sum_\alpha U_{\alpha i} U_{\alpha j}^* = \delta_{ij}$ .

with  $p_i$  and  $E_i$  being the momentum and energy of the mass eigenstate  $|\nu_i\rangle$  in the lab frame. The distance travelled  $L$  and the elapsed time  $t$  are defined by experiment parameters and do not depend on  $|\nu_i\rangle$ .

Assuming small values of  $m_i \sim 0$ , and taking into account that the energy  $E_i = E$  of all coherently contributing mass eigenstates must be the same [117], the momentum of a mass eigenstate  $|\nu_i\rangle$  is given by:

$$p_i = \sqrt{E_i^2 - m_i^2} \quad (2.52)$$

$$\simeq E - \frac{m_i^2}{2E} \quad (2.53)$$

Using Equations 2.47 and 2.51, the time evolution of a neutrino flavour eigenstate  $|\nu_\alpha\rangle$  may now be expressed as:

$$|\nu_\alpha(t, E)\rangle = \sum_i U_{\alpha i}^* e^{-iE(t-L) - i\frac{m_i^2 L}{2E}} |\nu_i(0)\rangle \quad (2.54)$$

The transition probability for a neutrino of initial flavour  $\alpha$  to final flavour  $\beta$  is given by the square of the absolute time-dependent transition amplitude:

$$P_{\nu_\alpha \rightarrow \nu_\beta}(t, E) = |\langle \nu_\beta(t) | \nu_\alpha(0) \rangle|^2 \quad (2.55)$$

$$= \left| \sum_i U_{\alpha i}^* U_{\beta i} e^{-iE(t-L) - i\frac{m_i^2 L}{2E}} \right|^2 \quad (2.56)$$

$$= \sum_i \sum_j (U_{\alpha i}^* U_{\beta i} U_{\alpha j} U_{\beta j}^*) e^{-i(m_i^2 - m_j^2) \frac{L}{2E}} \quad (2.57)$$

using the unitarity condition  $\langle \nu_\beta | \nu_\alpha \rangle = \delta_{\alpha\beta}$ . The term  $E(t-L)$  can be neglected, as it is common to all interfering mass eigenstates [117].

Finally substituting  $\Delta m_{ij}^2 = m_i^2 - m_j^2$  and separating real and imaginary parts, the oscillation probability  $P_{\nu_\alpha \rightarrow \nu_\beta}$  for neutrinos becomes:

$$\begin{aligned} P_{\nu_\alpha \rightarrow \nu_\beta}(L, E) &= \delta_{\alpha\beta} - 4 \sum_{i>j} \mathcal{R}(U_{\alpha i}^* U_{\beta i} U_{\alpha j} U_{\beta j}^*) \sin^2 \left( \Delta m_{ij}^2 \frac{L}{4E} \right) \\ &\quad \pm 2 \sum_{i>j} \mathcal{I}(U_{\alpha i}^* U_{\beta i} U_{\alpha j} U_{\beta j}^*) \sin \left( \Delta m_{ij}^2 \frac{L}{2E} \right) \end{aligned} \quad (2.58)$$

Assuming CPT invariance, the transition probability  $P_{\bar{\nu}_\alpha \rightarrow \bar{\nu}_\beta}$  for anti-neutrinos is given by the  $-$  sign in the last line, while for neutrinos the  $+$  sign is applied. In the case of CP conservation, the imaginary part is rendered zero, and the oscillation probabilities for neutrinos and anti-neutrinos are the same:

$$P_{\nu_\alpha \rightarrow \nu_\beta}(L, E) = P_{\bar{\nu}_\alpha \rightarrow \bar{\nu}_\beta}(L, E) \quad (2.59)$$

As is obvious from Equation 2.58, such neutrino flavour oscillations in vacuum are only possible if  $\Delta m_{ij}^2 = m_i^2 - m_j^2 \neq 0$ , i.e. if not all neutrino mass eigenstates  $|\nu_i\rangle$  are of the same value.

Their observation in experiments thus contradicts the Standard Model assumption of neutrinos being massless particles.

### 3-Flavour Neutrino Oscillation Formalism

The case of three generations of neutrinos, which is favoured by the global experimental data, can be described by three orthonormal neutrino flavour eigenstates  $|\nu_l\rangle$  and three mass eigenstates  $|\nu_i\rangle$  with  $l = e, \mu, \tau$  and  $i = 1, 2, 3$ .

The Pontecorvo Maki Nakagawa Sakata (PMNS) matrix  $U$  then becomes a  $3 \times 3$  mixing matrix:

$$U_3 = \begin{pmatrix} U_{e1} & U_{e2} & U_{e3} \\ U_{\mu 1} & U_{\mu 2} & U_{\mu 3} \\ U_{\tau 1} & U_{\tau 2} & U_{\tau 3} \end{pmatrix} \quad (2.60)$$

$$= \begin{pmatrix} 1 & 0 & 0 \\ 0 & c_{23} & s_{23} \\ 0 & -s_{23} & c_{23} \end{pmatrix} \times \begin{pmatrix} c_{13} & 0 & s_{13}e^{-i\delta_{CP}} \\ 0 & 1 & 0 \\ -s_{13}e^{i\delta_{CP}} & 0 & c_{13} \end{pmatrix} \times \begin{pmatrix} c_{12} & s_{12} & 0 \\ -s_{12} & c_{12} & 0 \\ 0 & 0 & 1 \end{pmatrix} \times \begin{pmatrix} e^{i\epsilon_1/2} & 0 & 0 \\ 0 & e^{i\epsilon_2/2} & 0 \\ 0 & 0 & 1 \end{pmatrix} \quad (2.61)$$

showing the usual parameterisation by three mixing angles  $\theta_{ij}$  and three complex phases  $\delta_{CP}, \epsilon_1, \epsilon_2$ . The abbreviations  $s_{ij} \equiv \sin \theta_{ij}$  and  $c_{ij} \equiv \cos \theta_{ij}$  are used.

$\delta_{CP}$  is the CP-violating Dirac phase that, if nonzero, would imply a different behaviour of neutrinos and anti-neutrinos (compare Equation 2.58). It may be probed by precision measurements of the other oscillation parameters (see Section 2.5.2).

The so-called Majorana phases  $\epsilon_1$  and  $\epsilon_2$  cannot be measured at neutrino oscillation experiments, but are relevant to studies of the neutrino nature w.r.t. it being a Dirac<sup>1</sup> or Majorana<sup>2</sup> particle (see Section 2.5.5).

Assuming that neutrinos are Dirac particles, i.e.  $\epsilon_1 = \epsilon_2 = 0$ , the mixing matrix  $U$  reduces to:

$$U_3 = \begin{pmatrix} 1 & 0 & 0 \\ 0 & c_{23} & s_{23} \\ 0 & -s_{23} & c_{23} \end{pmatrix} \times \begin{pmatrix} c_{13} & 0 & s_{13}e^{-i\delta_{CP}} \\ 0 & 1 & 0 \\ -s_{13}e^{i\delta_{CP}} & 0 & c_{13} \end{pmatrix} \times \begin{pmatrix} c_{12} & s_{12} & 0 \\ -s_{12} & c_{12} & 0 \\ 0 & 0 & 1 \end{pmatrix} \quad (2.62)$$

$$= \begin{pmatrix} c_{12}c_{13} & s_{12}c_{13} & s_{13}e^{-i\delta_{CP}} \\ -s_{12}c_{23} - c_{12}s_{23}s_{13}e^{i\delta_{CP}} & c_{12}c_{23} - s_{12}s_{23}s_{13}e^{i\delta_{CP}} & s_{23}c_{13} \\ s_{12}s_{23} - c_{12}c_{23}s_{13}e^{i\delta_{CP}} & -c_{12}s_{23} - s_{12}c_{23}s_{13}e^{i\delta_{CP}} & c_{23}c_{13} \end{pmatrix} \quad (2.63)$$

The mixing angles are usually represented by the Euler angles  $\theta_{12}, \theta_{23}, \theta_{13}$  with  $0 \leq \theta_{ij} \leq \pi/2$ . The complex phase  $\delta$ , with  $-\pi \leq \delta \leq +\pi$ , is only nonzero if neutrino oscillations violate CP invariance.

Of the three squared mass differences  $\Delta m_{ij}^2 = m_i^2 - m_j^2$  only two are linearly independent:

$$\Delta m_{31}^2 = \Delta m_{21}^2 + \Delta m_{32}^2 \quad (2.64)$$

The full three-flavour oscillation probabilities for  $\nu_\mu \rightarrow \nu_\mu$ ,  $\nu_\mu \rightarrow \nu_\tau$ , and  $\nu_\mu \rightarrow \nu_e$  transitions in vacuum are given in Appendix A.1.

<sup>1</sup>Dirac particle: A fermion that is not identical with its anti-particle, i.e.  $\nu \neq \bar{\nu}$ .

<sup>2</sup>Majorana particle: A fermion that is identical with its anti-particle, i.e.  $\nu \equiv \bar{\nu}$ .

## 2-Flavour Approximation

Given the degeneracy of the neutrino squared mass differences  $|\Delta m_{32}^2| \approx |\Delta m_{31}^2| \gg \Delta m_{21}^2$  and the distinct mixing angles  $\theta_{ij}$  (see Section 2.4.3), many neutrino oscillation experiments make use of an effective 2-flavour approximation.

The mixing matrix  $U$  reduces to a  $2 \times 2$  matrix that can be parameterised as a rotation matrix:

$$U_2 = \begin{pmatrix} \cos \theta & \sin \theta \\ -\sin \theta & \cos \theta \end{pmatrix} \quad (2.65)$$

using a single rotation angle  $\theta$ .

The 2-flavour oscillation probability is then given by [117]:

$$P_{\nu_\alpha \rightarrow \nu_\beta}(L, E) = \sin^2(2\theta) \cdot \sin^2\left(\frac{\Delta m^2 L}{4E}\right) \quad (2.66)$$

$$\simeq \sin^2(2\theta) \cdot \sin^2\left(1.27 \Delta m^2 [\text{eV}^2] \frac{L[\text{km}]}{E[\text{GeV}]}\right) \quad (2.67)$$

While the mixing angle  $\theta$  determines the amplitude of the sinusoidal oscillation, its frequency is defined by the term  $\Delta m^2 L/4E$ .

Oscillations are observable for values of  $\Delta m^2 L/4E \gtrsim 1$  [117]. Long-baseline experiments with typical ratios of  $L/E \gtrsim 100 \text{ m/MeV}$  are thus sensitive to squared mass differences  $\Delta m^2 \lesssim 10^{-2} \text{ eV}^2$ . Short-baseline neutrino oscillation experiments operating at  $L/E \lesssim 10 \text{ m/MeV}$  can probe  $\Delta m^2 \gtrsim 10^{-1} \text{ eV}^2$ .

As only one squared mass difference is present in the equation, the vacuum 2-flavour oscillation approximation cannot provide a measurement of the sign of  $\Delta m^2$ . The propagation in matter of  $\nu_e$  on the one hand, and  $\nu_\mu$  and  $\nu_\tau$  on the other hand, however may provide insight on the neutrino Mass Ordering due to the different accessible CC or NC interaction channels and resulting potentials.

With no imaginary contributions from the complex Dirac phase<sup>1</sup>, 2-flavour neutrino oscillation measurements are insensitive to CP violation.

### 2.4.2 Matter Effects

The above-described phenomenological formalism is valid only for neutrino oscillations in vacuum. When crossing matter, weak interaction processes have to be taken into account that introduce additional potentials to the Hamiltonian (compare Equation 2.49):

$$H^V \rightarrow H^M = H^V + V_{NC}^n + V_{NC}^p + V_{NC}^e + V_{CC}^e \quad (2.68)$$

with  $H^M$  being the Hamiltonian in matter in the neutrino flavour basis. The leading-order expressions for the matter potentials  $V_{NC}^n, V_{NC}^p, V_{NC}^e, V_{CC}^e$  are listed in Table 2.2.

<sup>1</sup>The leptonic phase  $\delta_{CP}$  only appears in the 3-neutrino framework.

**Table 2.2:** Additional leading-order potentials for neutrino oscillations in matter [126].  $G_F$  is the Fermi constant,  $\theta_W$  the Weinberg angle,  $N^x$  the local number density for the respective interaction target  $x$ . The upper signs apply to neutrinos, the lower signs to anti-neutrinos.

Neutrino flavour	Target	Matter potential
$\nu_e, \nu_\mu, \nu_\tau$	$n^0$	$V_{NC}^n = \mp G_F N^n / \sqrt{2}$
$\nu_e, \nu_\mu, \nu_\tau$	$p^+$	$V_{NC}^p = \pm G_F N^p / \sqrt{2} \cdot (1 - 4 \sin^2 \theta_W)$
$\nu_e, \nu_\mu, \nu_\tau$	$e^-$	$V_{NC}^e = \mp G_F N^e / \sqrt{2} \cdot (1 - 4 \sin^2 \theta_W)$
$\nu_e$	$e^-$	$V_{CC}^e = \pm G_F N^e \sqrt{2}$

Since the NC contributions  $V_{NC}^n$ ,  $V_{NC}^p$ , and  $V_{NC}^e$  affect all neutrino flavours equally, they will not change the oscillation probability and can be omitted. The term  $V_{CC}^e$ , however, constitutes an additional CC interaction potential that is only present for electron neutrinos.

In the 2-flavour approximation, the Hamiltonian in matter can thus be expressed as [117]:

$$H_2^M = H^V + V_{CC}^e \quad (2.69)$$

$$= \frac{1}{4E} \begin{pmatrix} -(\cos(2\theta) - x) & \sin(2\theta) \\ \sin(2\theta) & \cos(2\theta) - x \end{pmatrix} \quad (2.70)$$

with the parameter  $x \equiv \frac{V_{CC}^e/2}{\Delta m^2/4E} = \frac{E2\sqrt{2}G_F N^e}{\Delta m^2}$  illustrating the impact of the matter effect w.r.t. the oscillation induced by the neutrino squared mass difference  $\Delta m^2$  [117].

Using the effective squared mass difference  $\Delta m_M^2$  and mixing angle  $\theta_M$  in matter:

$$\Delta m_M^2 \equiv \Delta m^2 \sqrt{\sin^2(2\theta) + (\cos(2\theta) - x)^2} \quad (2.71)$$

$$\sin^2(2\theta_M) \equiv \frac{\sin^2(2\theta)}{\sin^2(2\theta) + (\cos(2\theta) - x)^2} \quad (2.72)$$

the Hamiltonian in matter becomes:

$$H_2^M = \frac{\Delta m_M^2}{4E} \begin{pmatrix} -\cos(2\theta_M) & \sin(2\theta_M) \\ \sin(2\theta_M) & \cos(2\theta_M) \end{pmatrix} \quad (2.73)$$

The resulting 2-flavour neutrino oscillation probability in matter:

$$P_{\nu_\alpha \rightarrow \nu_\beta}^M(L, E) = \sin^2(2\theta_M) \cdot \sin^2\left(\frac{\Delta m_M^2 L}{4E}\right) \quad (2.74)$$

is identical to the expression for vacuum neutrino oscillations (compare Equation 2.66) except for the fact that the vacuum values of  $\Delta m^2$  and  $\theta$  have been replaced with their effective matter counterparts  $\Delta m_M^2$  and  $\theta_M$ .

If the neutrinos cross matter of varying electron density, MSW resonance effects may occur that significantly boost the oscillation probability of electron neutrinos [135, 158]. This is the case e.g. for neutrinos originating from the Sun, prominently measured by the SNO experiment (see Section 2.1.3).

For the main OPERA analysis of  $\nu_\mu \rightarrow \nu_\tau$  oscillations, matter effects can be neglected.

### 2.4.3 Global Best Fit Parameters

The current state of knowledge on 3-flavour neutrino oscillations is summarised in Table 2.3 by listing the global best fit parameters taken from [67].

**Table 2.3:** Global best fit parameters for 3-flavour neutrino oscillations with  $\delta m^2 = \Delta m_{21}^2$  and  $\Delta m^2 = m_3^2 - (m_2^2 + m_1^2)/2$  [67]. The fit to  $\delta m^2$  and  $\sin^2(\theta_{12})$  is basically insensitive to the MO.

Parameter	Best-fit ( $\pm 1\sigma$ ) for Mass Ordering			
	any	NO	IO	
$\delta m^2$	$7.37^{+0.17}_{-0.16}$			$\times 10^{-5} \text{ eV}^2$
$ \Delta m^2 $	$2.525^{+0.042}_{-0.030}$	$2.525^{+0.042}_{-0.030}$	$2.505^{+0.034}_{-0.032}$	$\times 10^{-3} \text{ eV}^2$
$\sin^2(\theta_{12})$	$2.97^{+0.17}_{-0.16}$			$\times 10^{-1}$
$\sin^2(\theta_{13})$	$2.15 \pm 0.07$	$2.15 \pm 0.07$	$2.16^{+0.08}_{-0.09}$	$\times 10^{-2}$
$\sin^2(\theta_{23})$	$4.25^{+0.21}_{-0.15}$	$4.25^{+0.21}_{-0.15}$	$5.89^{+0.16}_{-1.72}$	$\times 10^{-1}$
$\delta$	$1.38^{+0.23}_{-0.20}$	$1.38^{+0.23}_{-0.20}$	$1.31^{+0.32}_{-0.19}$	$\pi$

The values of squared mass differences measured by solar and atmospheric neutrino oscillation experiments differ by approximately two orders of magnitude. They are often treated in a 2-flavour formalism and commonly identified as:

$$\Delta m_{sol}^2 = \Delta m_{21}^2 \quad (2.75)$$

$$\Delta m_{atm}^2 \approx |\Delta m_{31}^2| \approx |\Delta m_{32}^2| \quad (2.76)$$

While the sign of  $\Delta m_{21}^2$  has been measured in solar neutrino experiments that are subject to matter effects, the sign of  $\Delta m_{31}^2$  is not yet known. Depending on this, the neutrino Mass Ordering (MO) may be either *normal* or *inverted* (see Figure 2.13).

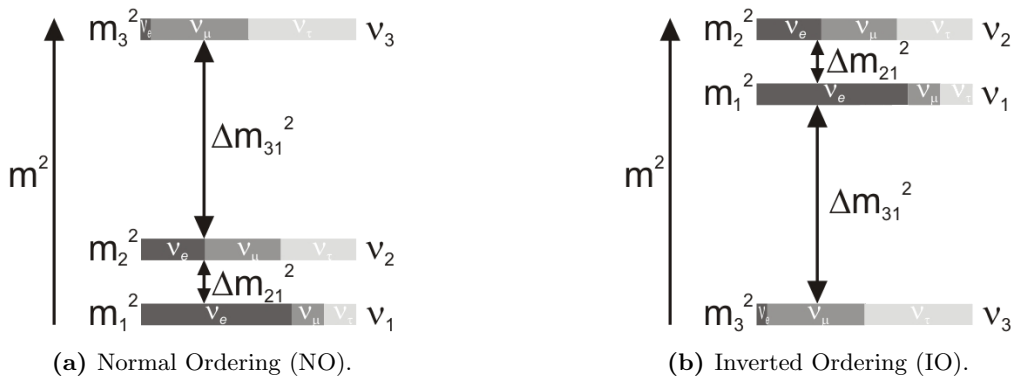


**Figure 2.13:** Neutrino Mass Ordering. (a) Normal Ordering and (b) Inverted Ordering, depending on the sign of  $\Delta m_{31}^2$ .

The Normal Ordering (NO) is described by values of  $m_1 < m_2 < m_3$ , while in the Inverted Ordering (IO)  $m_3 < m_1 < m_2$ . The quasi-degenerate case of  $m_1 \approx m_2 \approx m_3$  has already been excluded by oscillation experiments.

The existence and magnitude of the possible CP-violating phase  $\delta_{CP}$  is still largely unknown.



## 2.5 Open Questions

The 3-flavour framework of neutrino oscillations was firmly established with the discovery of  $\tau$  neutrino appearance in  $\nu_\mu \rightarrow \nu_\tau$  oscillations by OPERA [20] and the measurement of the last mixing angle  $\theta_{13}$  by reactor experiments [35, 28, 5].

Now entering an era of precision measurements, new experiments might soon provide insight into some of the yet-unresolved questions of neutrino physics.

### 2.5.1 Neutrino Mass Ordering

With the sign of  $\Delta m_{31}^2$ , the neutrino Mass Ordering (MO) is still unknown and may be realised as either Normal Ordering (NO) or Inverted Ordering (IO) (see Section 2.4.3). Different experimental approaches exist to determine it [140].

Detectors studying long-baseline accelerator neutrino beams (NOvA, T2K) or the oscillations of atmospheric neutrinos (PINGU ORCA) aim to compare the oscillations of  $\nu_\mu \rightarrow \nu_e$  and  $\bar{\nu}_\mu \rightarrow \bar{\nu}_e$ . The additional potentials for electron neutrinos in matter (see Section 2.4.2) will affect the oscillation probabilities of neutrinos and anti-neutrinos differently. Depending on the value of the likewise undetermined CP-violating phase  $\delta_{CP}$ , measurements from experiments at different baselines may need to be combined to disentangle the effect of both parameters.

Medium-baseline reactor experiments like JUNO on the other hand will conduct a precise measurement of the  $\bar{\nu}_e$  spectrum [34]. Depending on the MO realised in nature, the survival probability of  $\bar{\nu}_e \rightarrow \bar{\nu}_e$  is characteristically modulated (see Figure 2.16).

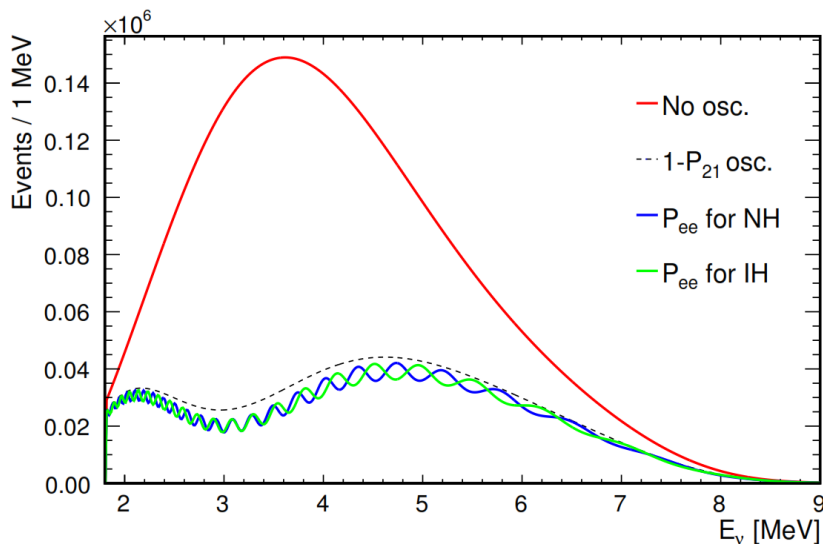


**Figure 2.14:** Measurement of the neutrino MO at JUNO [128]. NO and IO create different modulations on the  $\bar{\nu}_e \rightarrow \bar{\nu}_e$  oscillation probability.

### 2.5.2 CP Violation

While Charge-Parity (CP) violation in the quark sector has been a well-established fact since the observation of the decay of  $K_L^0 \rightarrow \pi^+ + \pi^-$  in 1964 [73], its existence in the leptonic sector is still not known.

CP violation would imply different oscillation probabilities of neutrinos and anti-neutrinos (see Section 2.4.1). Given the relatively large value of  $\theta_{13}$ , it may thus be probed by oscillation experiments using high-intensity accelerator beams (NOvA, T2K) or neutrino factories<sup>1</sup>.

Experiments must take care to disentangle the effect of  $\delta_{CP}$  from that of the neutrino Mass Ordering which may either increase or obscure the resulting change in oscillation probabilities.

The detection of leptonic CP violation would provide insight into the matter-antimatter asymmetry of the universe.

### 2.5.3 Sterile Neutrinos

Anomalous results from neutrino oscillation measurements that cannot be explained by the standard 3-flavour neutrino oscillation parameters (see Section 2.4.3) give rise to the idea of a possible 'sterile' neutrino state.

Figure 2.15 shows the results from LSND, MiniBooNE, and KARMEN in an effective 2-flavour approximation [24, 25, 45]. The favoured squared mass difference is  $\gtrsim 1 \text{ eV}^2$ .

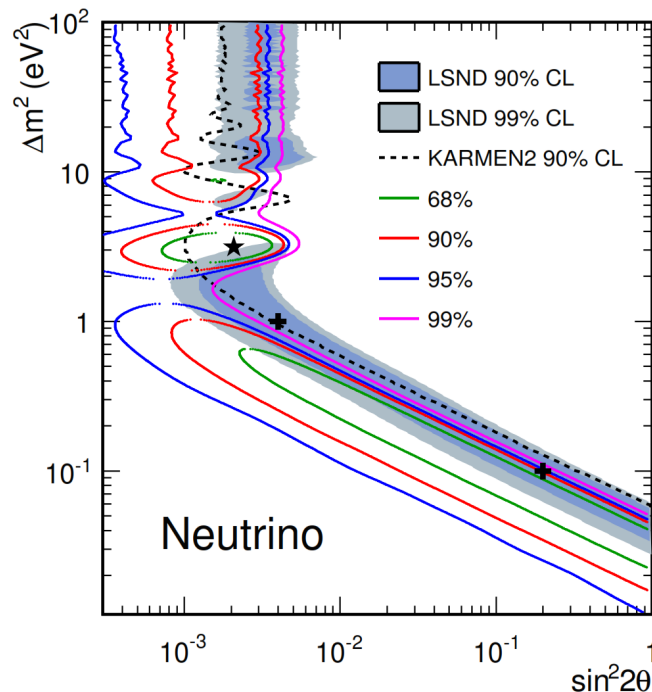


**Figure 2.15:** Combined plot showing the indications for nonstandard neutrino oscillations from LSND, MiniBooNE, and KARMEN [25].

<sup>1</sup>Neutrino factories create high-intensity neutrino beams via the decay-in-flight of muons from storage rings [44].

Similar indications arise from radioactive source experiments SAGE and GALLEX [2, 115] or the reactor anti-neutrino anomaly [134].

The measurements can be explained in '3+1' or '3+2' scenarios that combine 3 'active' lepton flavours of neutrinos with one or two 'sterile' neutrino states that are not subject to the weak interaction. This solution is attractive w.r.t. the heavier sterile neutrino being a candidate for the lightest supersymmetric particle in a  $\nu$ MSM extension of the Standard Model. Comprehensive fits able to reconcile all experimental results are however still missing.

Future experiments, such as SHiP [38], will probe the existence of heavy neutral leptons and thus provide answers to the 'sterile neutrino' puzzle.

#### 2.5.4 Absolute Mass Scale

Neutrino oscillation experiments are able to give insight concerning the squared mass *differences* between the mass eigenstates (see Section 2.4) - but not their absolute *scale*.

The present best limits on the average  $\bar{\nu}_e$  mass at 95% C.L. were obtained in the Mainz and Troitsk experiments by analysing the endpoint of the tritium beta decay spectrum [123, 47]:

$$m_{\bar{\nu}} < 2.30 \text{ eV} \quad (\text{Mainz}) \quad (2.77)$$

$$m_{\bar{\nu}} < 2.12 \text{ eV} \quad (\text{Troitsk}) \quad (2.78)$$

As a direct successor, KATRIN is currently in commissioning and will reach a sensitivity of 0.2 eV [39]. Other proposed experiments (Project8, PTOLEMY) will also study tritium, but follow different experimental approaches.

An upper limit on the average  $\nu_e$  mass was measured studying the X-ray spectrum of electron capture in  $^{163}\text{Ho}$  [151]:

$$m_{\nu} < 225 \text{ eV} \quad \text{at 95\% C.L.} \quad (2.79)$$

Future projects (ECHO, HOLMES, NuMECS) using  $^{163}\text{Ho}$  aim to make use of calorimetric methods.

From another angle, cosmological observations made by PLANCK provide an upper limit on the sum of neutrino masses [10]:

$$\sum_i m_i < 0.23 \text{ eV} \quad \text{at 95\% C.L.} \quad (2.80)$$

However, this result is largely model-dependent and difficult to compare with direct measurements.

### 2.5.5 Dirac or Majorana

Unlike the other Dirac fermions described by the Standard Model, neutrinos carry *no* additive quantum numbers with a non-zero value. This gives rise to the possibility of the neutrino being identical to its own anti-particle, and thus a Majorana particle.

The fundamental nature of the neutrino may be probed by the search for *neutrinoless double beta decay*, as is conducted by experiments like GERDA or C0BRA. If neutrinos are Majorana particles and have a non-vanishing mass<sup>1</sup>, neutrinoless double beta decay should be possible in isotopes that undergo standard  $2\nu$  double beta decay.

A key parameter of the measurement is given by the effective Majorana mass [140]:

$$\langle m \rangle \equiv \sum_i U_{ei}^2 m_i \quad (2.81)$$

with the neutrino mixing matrix  $U$  containing the Majorana phases  $\epsilon_1$  and  $\epsilon_2$  (see Section 2.4.1). Figure 2.16 shows  $|\langle m \rangle|$  as a function of the lightest neutrino mass  $m_{min}$ . Depending on the Mass Ordering, different regions of the parameter space are allowed.

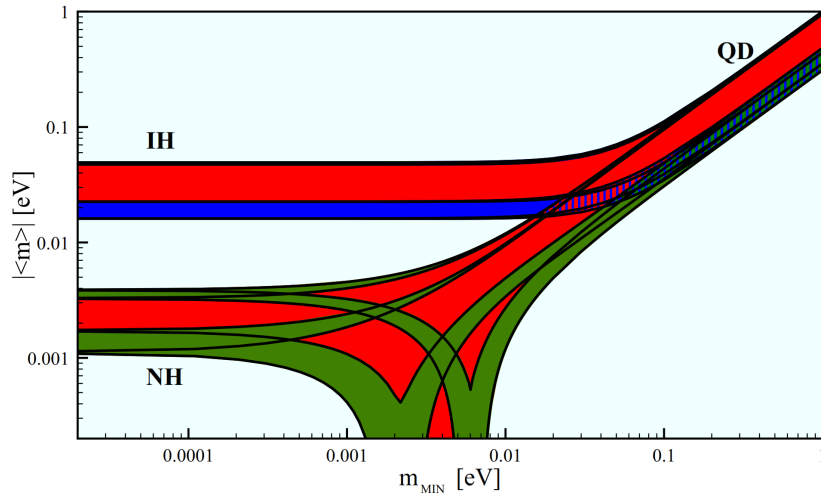


**Figure 2.16:** Effective Majorana mass  $|\langle m \rangle|$  as a function of the lightest neutrino mass  $m_{min}$ , using the global best fit of oscillation parameters [140]. The separate bands show  $2\sigma$  ranges for Normal Ordering (NO), Inverted Ordering (IO), or a Quasi-Degenerate (QD) case.

<sup>1</sup>A helicity flip is needed for the anti-neutrino created in one beta decay to be absorbed as a neutrino in the other beta decay.

## Chapter 3

# Electromagnetic Showers

The detection of  $\nu_e$  CC interactions in OPERA is based on the reconstruction of the electromagnetic (e.m.) showers initiated by the created electrons.

The most important processes, namely bremsstrahlung (Section 3.1) and  $e^+e^-$  pair production (Section 3.2), and characteristics of radiation length (Section 3.3) and electromagnetic cascades (Section 3.4) will be summarised in the following.

### 3.1 Bremsstrahlung

The fractional energy loss of electrons and positrons in lead is shown in Figure 3.1. At high energies, the energy loss of  $e^\pm$  in dense matter will occur primarily via bremsstrahlung, while interactions at energies  $\lesssim 10$  MeV are dominated by ionisation processes<sup>1</sup>. The low-energy contributions from Bhabha and Møller scattering or positron annihilation can largely be neglected at the energies relevant to the OPERA experiment.

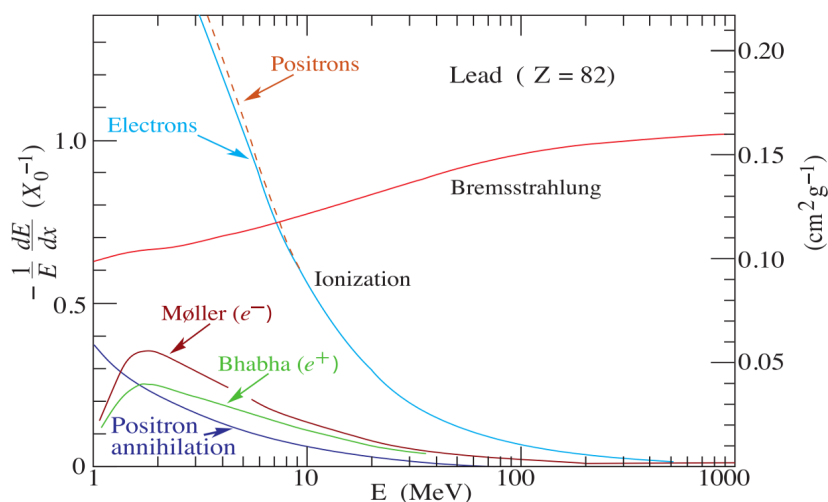
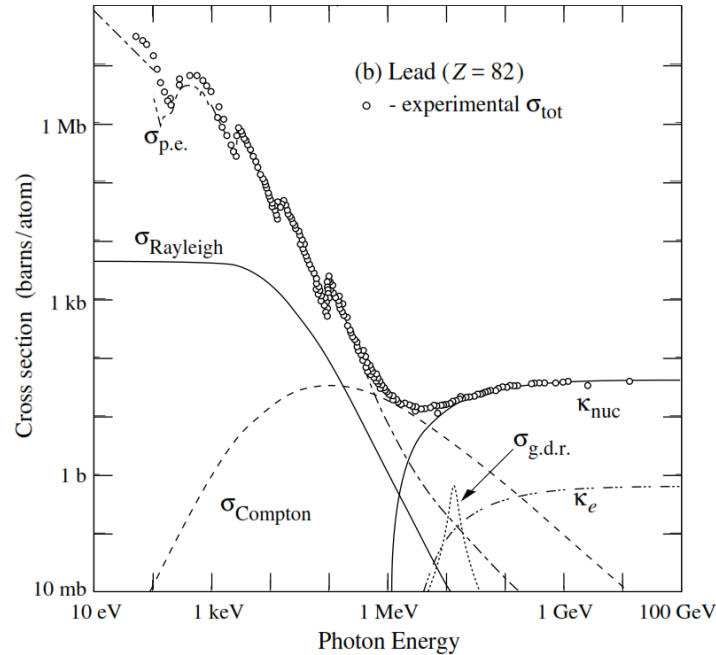


**Figure 3.1:** Fractional energy loss of  $e^\pm$  per  $X_0$  in Pb as a function of particle energy [140]. The energy loss via bremsstrahlung rises nearly linearly with energy and dominates for  $E \gtrsim 10$  MeV.

<sup>1</sup>Due to density effects, the ionisation energy loss in absorbers made of gases, liquids, or solids substantially differs.

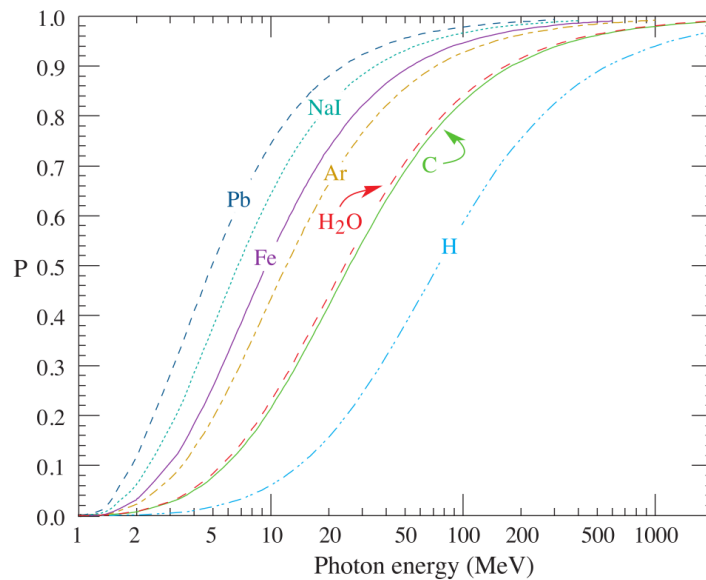
### 3.2 Pair Production

Figure 3.2 shows the cross section of high-energy  $\gamma$  in lead. While the photoelectric effect dominates up to incident photon energies of  $\lesssim 1$  MeV, the energy loss at higher energies occurs primarily via  $e^+e^-$  pair production.



**Figure 3.2:** Total cross section of  $\gamma$  in Pb and contributions from different processes [140]. At energies greater than a few MeV, the cross section is dominated by  $e^+e^-$  pair production in the nuclear field ( $\kappa_{nuc}$ ).

A comparison of the energy-dependent probabilities for  $e^+e^-$  pair production by photons in different absorber materials is given in Figure 3.3.



**Figure 3.3:** Probability of  $e^+e^-$  pair production for  $\gamma$  in different target materials [140].

### 3.3 Radiation Length

The radiation length  $X_0$  characterises both bremsstrahlung and  $e^+e^-$  pair production and defines the scale for electromagnetic cascades in a given absorber material [140].

It describes the mean distance after which high-energy  $e^\pm$  will have lost all but a fraction  $1/e$  of their energy, and also indicates  $7/9$  of the mean free path that a high-energy photon will travel before producing an  $e^+e^-$  pair.

The radiation length is usually measured in  $\text{g cm}^{-2}$  and can be estimated as [33]:

$$X_0 = \frac{7.164 \text{ g cm}^{-2} A}{Z(Z+1) \ln(287/\sqrt{Z})} \quad (3.1)$$

with  $A$  and  $Z$  being mass and atomic numbers of the absorber material nuclei.

For a mixture or compound of different materials, the effective radiation length  $X_{eff}$  is approximated by [140]:

$$\frac{1}{X_{eff}} = \sum_j \frac{w_j}{X_j} \quad (3.2)$$

with  $w_j$  being the weight fraction and  $X_j$  the radiation length for element  $j$ .

### 3.4 Electromagnetic Cascades

Inside thick absorbers, high-energy  $e^\pm$  or  $\gamma$  will create cascades of further  $e^\pm$  and  $\gamma$  with decreasing energies via a combination of bremsstrahlung and pair production processes.

The longitudinal development of these electromagnetic (e.m.) showers depends on the initial energy  $E_0$  of the incident particle and scales with the radiation length  $X_0$  inside the absorber.

After the initial shower development during the first two radiation lengths, a  $\Gamma$  distribution can be used to describe the mean longitudinal profile of the energy deposition [140]:

$$\frac{dE}{dt} = E_0 b \frac{(bt)^{a-1} e^{-bt}}{\Gamma(a)} \quad (3.3)$$

The scale variable  $t = x/X_0$  measures the traveled distance in units of  $X_0$  with a shower length of  $X_s = X_0/b$ . The ancillary parameters  $a$  and  $b$  depend on both  $E_0$  and the atomic number  $Z$ .

The longitudinal profile of an e.m. cascade initiated by a 30 GeV-electron in iron is shown in Figure 3.4.

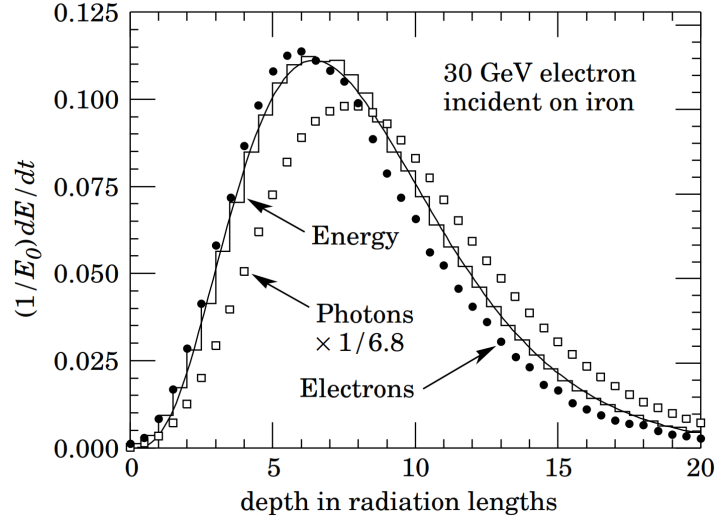


**Figure 3.4:** Longitudinal profile of an e.m. cascade inside an iron sampling calorimeter with a cutoff energy of 1.5 MeV [140]. The incident electron energy is 30 GeV.

The critical energy is defined as the energy where both ionisation loss per  $X_0$  and energy loss via bremsstrahlung are equal to the electron's energy:

$$E_c \sim E/X_0 \sim |dE/dx|_{brems} \quad (3.4)$$

After falling below  $E_c$ ,  $e^+$  and  $e^-$  are more likely to lose their energy via ionisation and excitation, halting the development of the e.m. cascade.

The transverse development of e.m. cascades can be described by the Moliere radius [140]:

$$R_M = X_0 \frac{E_s}{E_c} \quad (3.5)$$

with  $E_s \sim 21$  MeV.

For material compounds, it may be calculated as:

$$\frac{1}{R_M} = \frac{1}{E_s} \sum \frac{w_j E_{cj}}{X_j} \quad (3.6)$$

with the weight fraction  $w_j$ , and  $X_j$  and  $E_{cj}$  being radiation length and critical energy for element  $j$ .

A cylinder of radius  $R_M$  will contain about 90% of the deposited energy, while a radius of  $3.5R_M$  encompasses  $\sim 99\%$ . The distributions are characterised by a narrow core that broadens as the shower develops and can be described by the sum of two Gaussians [140].



## Chapter 4

# The OPERA Experiment

The acronym Oscillation Project with Emulsion tRacking Apparatus (OPERA) stands for Oscillation Project with Emulsion tRacking Apparatus. OPERA is a long-baseline neutrino oscillation experiment. Its detector is located at the Laboratori Nazionali del Gran Sasso (LNGS) underground laboratory in Central Italy and studies the CERN Neutrinos to Gran Sasso (CNGS)  $\nu_\mu$  beam at a distance of 730 km from its source at the Conseil Européen pour la Recherche Nucléaire (CERN) Super Proton Synchrotron (SPS) accelerator [107].

After a short explanation of the physical motivation and experimental requirements (Section 4.1), predecessor experiments are briefly discussed (Section 4.2). This chapter will then give details on the CNGS neutrino beam (Section 4.3) and the OPERA detector (Section 4.4) before explaining event reconstruction in OPERA (Section 4.6). It concludes with a presentation of the results from the main  $\nu_\mu \rightarrow \nu_\tau$  oscillation analysis (Section 4.7).

### 4.1 Physical Motivation & Experimental Requirements

In 1998, SK observed a deficit in the atmospheric muon neutrino flux that was dependent on the zenith angle, thus presenting evidence for  $\nu_\mu \rightarrow \nu_\tau$  oscillations in disappearance mode (see Section 2.1.4) [98]. To complement this analysis<sup>1</sup>, OPERA was designed as an appearance experiment to provide a direct measurement of tau neutrinos created via  $\nu_\mu \rightarrow \nu_\tau$  oscillations in a  $\nu_\mu$  beam [107].

Aiming for the detection of  $\tau$  leptons from  $\nu_\tau$  CC interactions on an event-by-event basis, the OPERA detector needs to provide both a kton-scale target mass and micrometric spatial resolution for resolving the signal topology (see Section 4.7.1). The design is thus based on a hybrid structure similar to that of predecessor experiments DONuT and CHORUS (see Section 4.2). It combines a passive lead target and high-resolution nuclear emulsions with electronic detector elements [6].

To enable a quasi background-free measurement of oscillated  $\tau$  neutrinos, the CNGS  $\nu_\mu$  beam must be free of any contamination with prompt  $\nu_\tau$ .

---

<sup>1</sup>Only the direct observation of  $\nu_\mu \rightarrow \nu_\tau$  appearance can unequivocally establish the picture of 3-flavour neutrino oscillations over other concepts such as decoherence or the oscillation into sterile neutrinos.

The total number  $N_{osc}^{\nu_\tau}$  of oscillated  $\tau$  leptons to be observed by OPERA is given by:

$$N_{osc}^{\nu_\tau} = N_A \cdot N_{p.o.t.} \cdot M \cdot \int \Phi^{\nu_\mu}(E) \cdot P_{\nu_\mu \rightarrow \nu_\tau}(E) \cdot \sigma_{CC}^{\nu_\tau}(E) \cdot \epsilon_{det}^{\nu_\tau}(E) dE \quad (4.1)$$

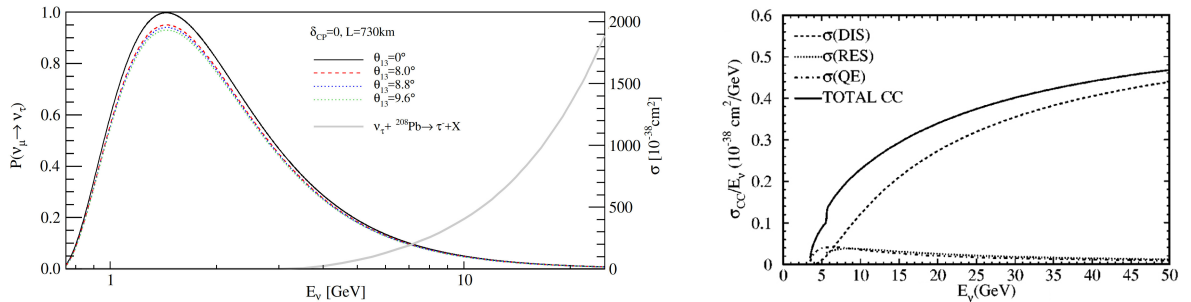
with  $N_A$  being the Avogadro constant,  $N_{pot}$  the number of protons on target, and  $M$  the detector target mass. The unoscillated  $\nu_\mu$  flux  $\Phi^{\nu_\mu}$  (see Chapter 4.3.2), the oscillation probability  $P_{\nu_\mu \rightarrow \nu_\tau}$ , the total  $\nu_\tau$  CC cross section  $\sigma_{CC}^{\nu_\tau}$ , and the  $\nu_\tau$  detection efficiency  $\epsilon_{det}^{\nu_\tau}$  are all dependent on the neutrino energy  $E_\nu$ .

The full 3-flavour parameterisation for  $\nu_\mu \rightarrow \nu_\tau$  oscillations in vacuum is given by Equation A.3 in Appendix A.1.2. Assuming  $\delta_{CP} = 0$  and taking into account the dominance of  $\nu_\mu \rightarrow \nu_\tau$  oscillations due to  $\Delta m_{32}^2 \gg \Delta m_{21}^2$  and a small value of  $\theta_{13} \sim 0$ , a 2-flavour approximation can be made (compare Equation 2.67, Section 2.4.1):

$$P_{\nu_\mu \rightarrow \nu_\tau}^{2flavour}(E) \simeq \sin^2(\theta_{23}) \cdot \sin^2 \left( 1.27 \cdot \Delta m_{32}^2 [\text{eV}^2] \cdot \frac{L[\text{km}]}{E[\text{GeV}]} \right) \quad (4.2)$$

for baselines  $L \sim \mathcal{O}(1000 \text{ km})$  and neutrino energies  $E_\nu \sim \mathcal{O}(\text{GeV})$ .

Figure 4.1a shows the energy-dependent  $\nu_\mu \rightarrow \nu_\tau$  oscillation probability for the fixed CNGS baseline of  $L = 730 \text{ km}$ . It is maximised for energies of  $E_\nu \sim 1.5 \text{ GeV}$ . To enable the production of  $\tau$  leptons in  $\nu_\tau$  CC reactions, the neutrino energy however must not be lower than the  $\tau$  production threshold of  $E_{thr} = 3.454 \text{ GeV}$  (see Chapter 2.3.1). The total  $\nu_\tau$  CC cross section on an isoscalar<sup>1</sup> target is shown in Figure 4.1b.



(a) 3-flavour  $\nu_\mu \rightarrow \nu_\tau$  oscillation probability vs.  $E_\nu$  [91].

(b) Total  $\nu_\tau$  CC cross section [139].

**Figure 4.1:**  $\nu_\mu \rightarrow \nu_\tau$  oscillation probability and total  $\nu_\tau$  CC cross section vs. neutrino energy  $E_\nu$ . (a)  $P_{\nu_\mu \rightarrow \nu_\tau}^{3flavour}(E)$  for different values of  $\theta_{13}$ ,  $\sin^2(2\theta_{23}) = 1$ ,  $\Delta m_{23}^2 = 2.5 \times 10^{-3} \text{ eV}^2$ ,  $\delta_{CP} = 0$ , and the OPERA baseline of  $L = 730 \text{ km}$ . The total  $\nu_\tau$  CC cross section in lead is superimposed. The oscillation probability is maximal for  $\theta_{13} = 0$  and reduced by  $\sim 7\%$  for large values of  $\theta_{13} = 9^\circ$ . (b) Total  $\nu_\tau$  CC cross section on an isoscalar target with a  $\tau$  production threshold of  $E_{thr} = 3.454 \text{ GeV}$  and noticeable contributions from QE and RES at  $E_\nu \gtrsim 5 \text{ GeV}$ .

The product of oscillation probability  $P_{\nu_\mu \rightarrow \nu_\tau}(E)$  and cross section  $\sigma_{CC}^{\nu_\tau}(E)$  can be seen in Figure 4.2. It exhibits a maximum around a neutrino energy of  $E_\nu \sim 10 \text{ GeV}$ .

<sup>1</sup>For non-isoscalar target material, corrections have to be applied to take into account the CC DIS coupling of  $\nu$  to  $d$  quarks and of  $\bar{\nu}$  to  $u$  quarks.

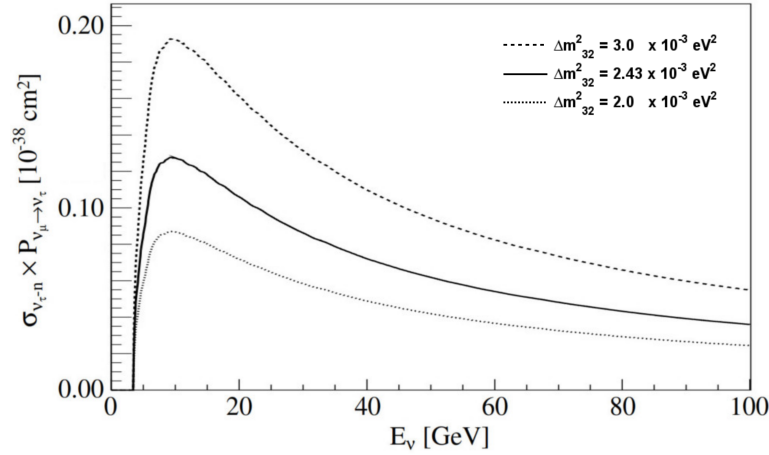


**Figure 4.2:**  $P_{\nu_{\mu} \rightarrow \nu_{\tau}}^{2\text{flavour}}(E) \times \sigma_{CC}^{\nu_{\tau}}(E)$  for different values of  $\Delta m_{32}^2$ ,  $\sin^2(2\theta_{23}) = 1$ , and the OPERA baseline of  $L = 730 \text{ km}$  [91].

Further taking into account a  $\nu_{\tau}$  detection efficiency that is slowly rising with energy, the chosen value of  $\langle E_{\nu} \rangle = 17.9 \text{ GeV}$  that is provided by the CNGS on-axis beam<sup>1</sup> optimises the experiment's sensitivity to  $\nu_{\mu} \rightarrow \nu_{\tau}$  oscillations.

With the OPERA detector location at the LNGS underground laboratory<sup>2</sup> and the neutrino source at CERN, the CNGS baseline is fixed to  $L = 730 \text{ km}$ .

Figure 4.3 shows the  $\nu_{\mu} \rightarrow \nu_{\tau}$  oscillation probability for the OPERA average neutrino energy of  $E_{\nu} = 17.9 \text{ GeV}$  against the baseline  $L$ . As is evident, the realised ratio of  $L/E$  does not match the first maximum of the oscillation. While a longer baseline would increase the oscillation probability, the greater divergence of the neutrino beam would result in an even lower flux of oscillated  $\nu_{\tau}$ .

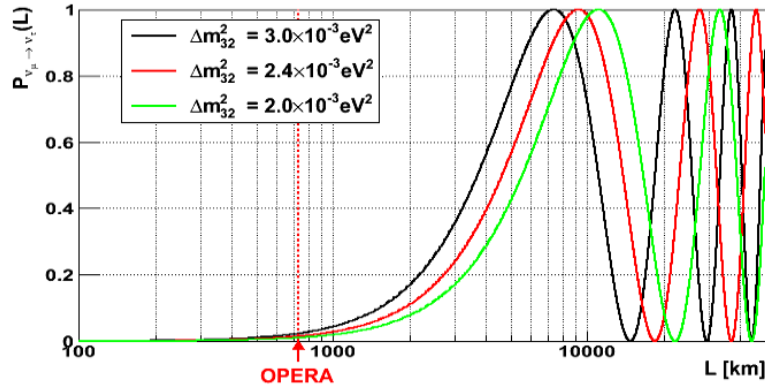


**Figure 4.3:** 2-flavour  $\nu_{\mu} \rightarrow \nu_{\tau}$  oscillation probability vs. baseline  $L$  for different values of  $\Delta m_{32}^2$ ,  $\sin^2(2\theta_{23}) = 1$ , and a neutrino energy of  $E_{\nu} = 17.9 \text{ GeV}$ . With  $L = 730 \text{ km}$ , the OPERA detector is at an off-peak position.

<sup>1</sup>With the OPERA detector positioned at the center of the widened beam at the LNGS,  $E_{\nu}$  follows a broad distribution. Due to the kinematics of parent particles, off-axis-beams allow for a more distinct selection, but also result in much lower average neutrino energies.

<sup>2</sup>The LNGS laboratory provides convenient infrastructure and a shielding against cosmic particles of  $\sim 3800 \text{ m.w.e.}$

## 4.2 Predecessors to OPERA

OPERA is neither the first experiment to search for  $\nu_\mu \rightarrow \nu_\tau$  oscillations, nor the only one able to directly detect  $\nu_\tau$  CC interactions. The most notable predecessors - namely DONuT, CHORUS, and NOMAD - will be briefly described in the following.

### 4.2.1 DONuT

Since the observation of the  $\tau$  lepton in 1975 [142], the  $\tau$  neutrino had been searched for. In 2001, the Direct Observation of Nu Tau (DONuT) experiment was finally able to provide the first direct evidence for  $\nu_\tau$  CC interactions [119].

Figure 4.4 shows a schematic drawing of the experimental setup. The neutrino beam is created using 800 GeV protons from the FermiLab TeVatron accelerator directed onto a 1 m-long tungsten beam dump. Absorbers and magnetic shielding decrease the rate of hadrons and muons. The neutrino target, made from a sandwich structure of nuclear emulsions and sheets of stainless steel, is located 36 m downstream. It is interleaved with planes of scintillating fibers and followed by drift chambers, a calorimeter, and a spectrometer.

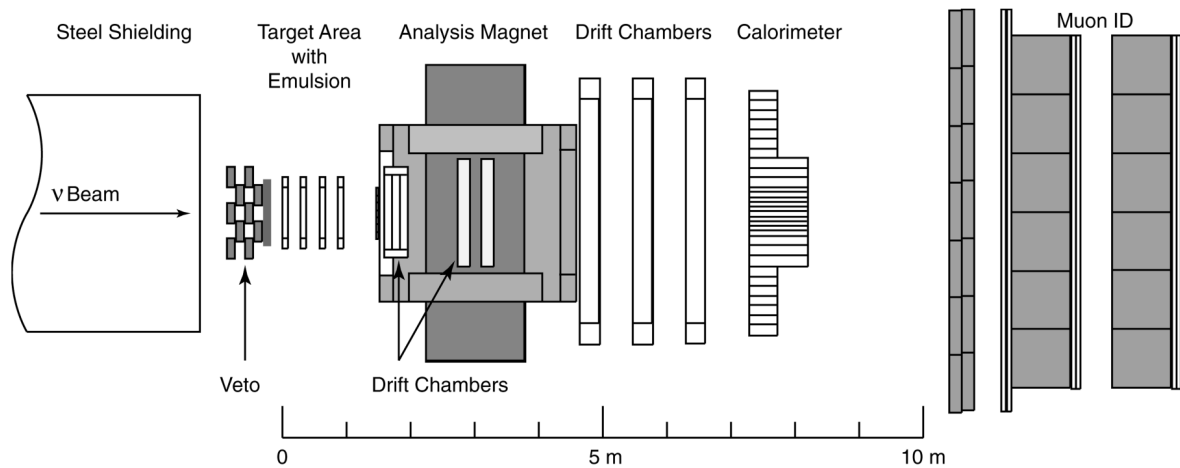


**Figure 4.4:** Schematic drawing of the DONuT experiment [120]. The detector is located 36 m downstream from the W beam dump and consists of ECC modules and electronic detector elements. Much of the employed technology has been adopted for OPERA.

A closeup of the Emulsion Cloud Chamber (ECC) neutrino target structure used by DONuT can be seen in Figure 4.5. Different modules are combined to create walls of 3.0 or 2.0  $X_0$  in thickness, with an area of  $50 \text{ cm} \times 50 \text{ cm}$  perpendicular to the beam direction.

$\nu_\tau$  and  $\bar{\nu}_\tau$  are produced by the leptonic decays of  $D_S^\pm$  mesons inside the beam dump. Just as for OPERA (see Chapter 4.7), the identification of  $\nu_\tau$  CC interactions within the DONuT ECC target is conducted via detection of the created  $\tau$  leptons and their subsequent decay after  $\sim 1 \text{ mm}$ . With a spatial resolution of better than  $0.6 \mu\text{m}$ , the nuclear emulsions act as tracking detectors and are well suited for the study of short-lived particle decays. The main background (BG) arises from the decay of charmed mesons produced in  $\nu_\mu$  or  $\nu_e$  CC interactions.

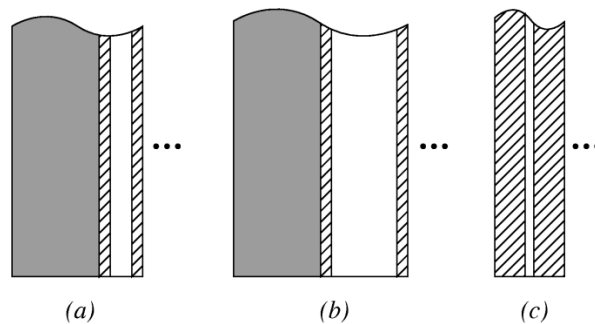


**Figure 4.5:** DONuT neutrino target structure [119]. **(a)**, **(b)** ECC modules using 1 mm-thick stainless steel plates as the passive neutrino interaction target are alternated with 100  $\mu\text{m}$  layers of nuclear emulsion coated on plastic bases of either 200  $\mu\text{m}$  or 800  $\mu\text{m}$  thickness. **(c)** Bulk emulsion target consisting of 350  $\mu\text{m}$ -thick emulsion layers on 90  $\mu\text{m}$  plastic bases.

Analysing the full data sample of 578 detected neutrino interactions corresponding to  $3.6 \times 10^{17}$  p.o.t., 9  $\nu_\tau$  candidates are observed, with an expected BG of 1.5 events [120]. Without being able to distinguish between  $\nu_\tau$  and  $\bar{\nu}_\tau$  interactions, the total  $\nu_\tau$  CC cross section is estimated as  $\sigma_{CC}^{\nu_\tau} = (0.39 \pm 0.13 \pm 0.13) \times 10^{-38} \text{cm}^2/\text{GeV}$ .

#### 4.2.2 CHORUS & NOMAD

Even before the existence of the  $\tau$  neutrino had been proven via the direct measurement conducted by DONuT (see previous Section 4.2.1), the NOMAD and CHORUS experiments started the search for  $\tau$  neutrino appearance in  $\nu_\mu \rightarrow \nu_\tau$  oscillations.

Using complementary techniques, both detectors studied the CERN West Area Neutrino Facility (WANF) wide-band  $\nu_\mu$  beam that was produced using 450 GeV protons from the SPS impinging on a beryllium target [156, 103]. With short baselines of 822 m (CHORUS) and 835 m (NOMAD), and given the average muon neutrino energy of 26 GeV, the experiments were sensitive to  $\Delta m^2 \gtrsim 1 \text{eV}^2$  in a two-flavour mixing scheme.

The search was motivated by the interpretation of the solar neutrino deficit (see Chapter 2.1.3) as due to  $\nu_e \rightarrow \nu_\mu$  oscillations that were enhanced by matter effects. According to the Seesaw Mechanism (see Chapter 2.5.5), neutrino masses of  $\sim 3 \times 10^{-3} \text{eV}$  ( $\nu_\mu$ ) and  $\gtrsim 1 \text{eV}$  ( $\nu_\tau$ ) were expected [48].

#### CHORUS

Similar to the DONuT experiment, the CERN Hybrid Oscillation Research apparatus (CHORUS) detector is a hybrid apparatus consisting of a nuclear emulsion target and electronic detector elements [153].

A drawing of the detector can be seen in Figure 4.6. The nuclear emulsion neutrino target is equipped with a scintillating fiber tracker. It is followed by a first magnetic spectrometer employing an air core magnet, scintillating fibre and drift tube detectors, a spaghetti calorimeter made from lead and scintillating fibers, and a second magnetic muon spectrometer consisting of magnetised iron interleaved with plastic scintillators.

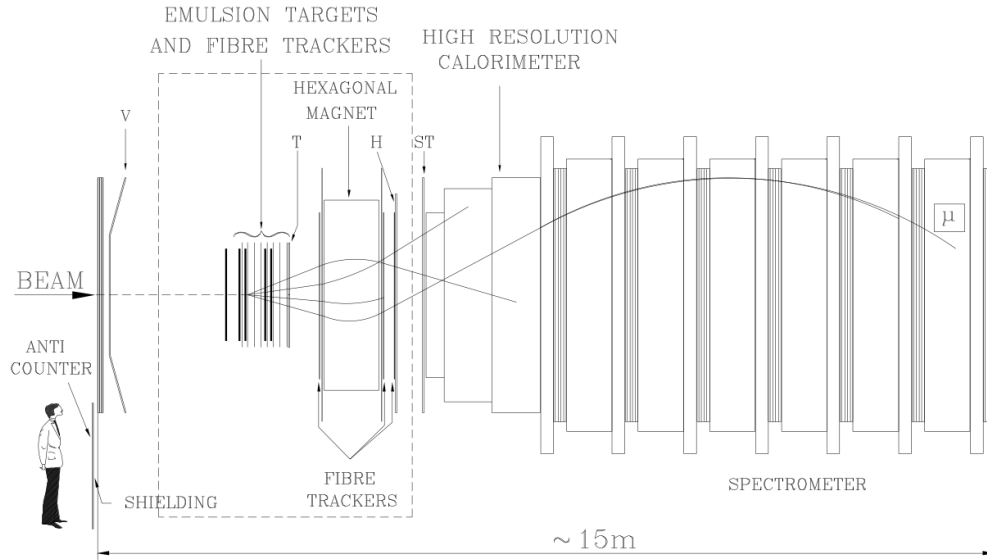


**Figure 4.6:** Schematic drawing of the CHORUS experiment [153]. The detector is located 822 m downstream from the Be target. Based on the design of DONuT, it consists of a nuclear emulsion neutrino target, followed by a calorimeter and magnetic spectrometers.

Figure 4.7 shows the structure of the CHORUS neutrino target. It is segmented into four stacks of nuclear emulsion modules, each followed by interface emulsion sheets and scintillating fiber target trackers. The overall target mass is 770 kg, with a spatial resolution of better than  $1 \mu\text{m}$ .

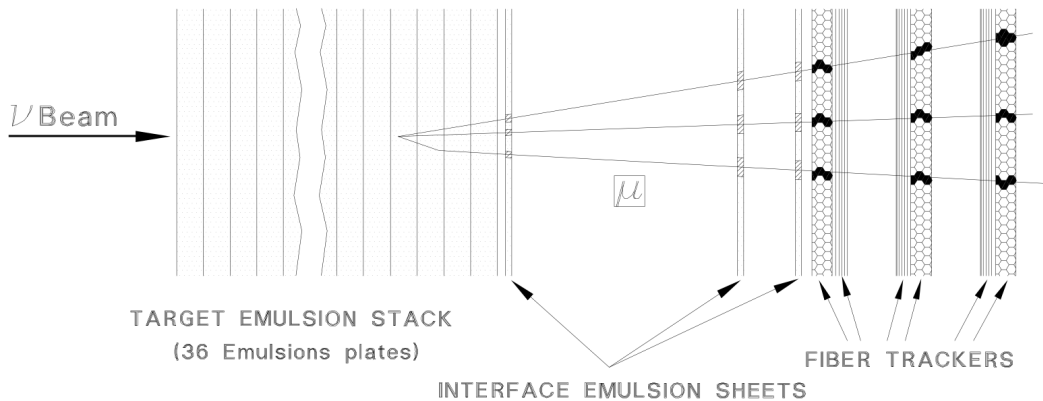


**Figure 4.7:** CHORUS neutrino target structure [153].  $350 \mu\text{m}$  layers of nuclear emulsion are coated on both sides of  $90 \mu\text{m}$ -thick plastic bases.  $8 \times 36$  emulsion sheets form a stack that is followed by three sheets of  $100 \mu\text{m}$  nuclear emulsion layers on  $800 \mu\text{m}$  plastic bases which provide an interface to the downstream scintillating fiber trackers. The area perpendicular to the beam is  $36 \text{ cm} \times 71 \text{ cm}$ .

The analysis of the nuclear emulsions occurs via automated scanning microscopes. Using CCD cameras, series of tomographic images are taken at different focusing depths in the emulsion layer. Predictions from the fiber trackers are then used to locate tracks in the digitised images.

As in DONuT,  $\nu_\tau$  CC interactions are identified by the detection of creation and decay of the  $\tau$  lepton. In the CHORUS emulsion target, the average  $\tau$  decay length is  $\sim 1.7 \text{ mm}$ .

After preselection of 600 000 candidate  $\nu_\tau$  interactions and application of fiducial volume cuts, more than 455 000 events were scanned and analysed [153]. In 12 152 fully reconstructed neutrino interactions, 107  $\nu_\tau$  candidate events remain, at an expected BG of  $100 \pm 14$  events that arises mainly from the decays of charmed particles [116].

Given the large BG and uncertainty, no observation of  $\nu_\tau$  appearance can be made. For large values of  $\Delta m^2$ , the derived upper limit on the mixing angle in a two-flavour scheme is  $\sin^2(2\theta_{\mu\tau}) < 4.4 \times 10^{-4}$  at 90% C.L. [153].

## NOMAD

Located directly downstream from the CHORUS experiment, the Neutrino Oscillation MAGnetic Detector (NOMAD) detector studies the WANF  $\nu_\mu$  beam at a baseline of 835 m. Contrary to the DONuT and CHORUS experiments, NOMAD does not employ high-resolution nuclear emulsions to resolve the creation and decay of  $\tau$  leptons, but relies on kinematical criteria to search for  $\nu_\mu \rightarrow \nu_\tau$  appearance [48].

Figure 4.8 shows a schematic drawing of the detector. The neutrino target is situated inside a large dipole magnet. It consists of drift chambers, has a length of 405 cm (corresponding to  $\sim 1X_0$ ), and a fiducial mass of  $\sim 2.7$  t. Also inside the magnetic field are a transition radiation detector providing electron identification, a preshower detector, and a high-resolution lead-glass electromagnetic calorimeter. The magnet is followed by a hadronic calorimeter and muon drift chambers.

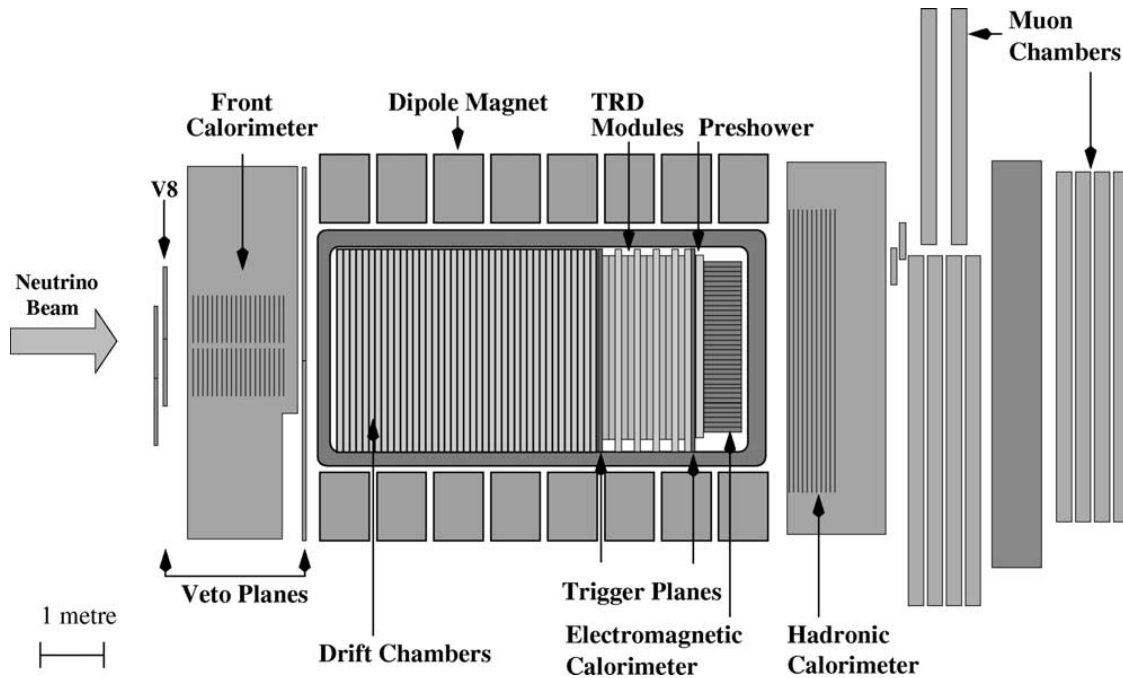


**Figure 4.8:** Schematic drawing of the NOMAD experiment [48]. The detector is located 835 m downstream from the Be target inside a 0.4 T magnetic field. The active neutrino target is followed by a transition radiation detector, a preshower detector, and an electromagnetic calorimeter. A hadronic calorimeter and muon chambers are situated further downstream outside the magnet.

Designed to identify leptons and measure  $\mu$ ,  $\pi$ ,  $e$ ,  $\gamma$  with good energy and momentum resolution, the detector provides a precise measurement of all visible final-state particles. A sophisticated analysis exploiting the kinematical variables can thus be employed to identify  $\nu_\tau$  CC interactions.

Signal and BG topologies for the  $\nu_\mu \rightarrow \nu_\tau$  appearance search in NOMAD are shown in Figure 4.9.  $\nu_\tau$  CC events can be discriminated against  $\nu_\mu / \nu_e$  NC and CC interactions via the transverse components of the total visible momenta, the absolute values of the visible decay products' kinematical variables, and their different correlations with the remaining hadronic system [48].

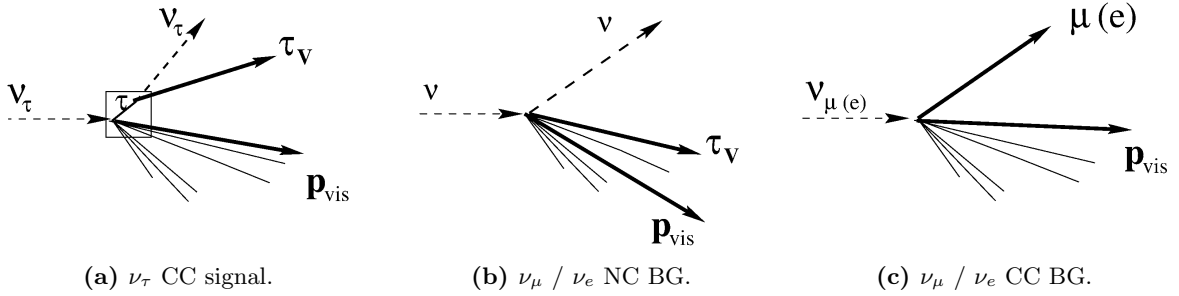


**Figure 4.9:** NOMAD signal and BG event topologies [48]. Via the presence of secondary visible charged  $\tau$  decay products,  $\nu_\tau$  CC interactions (a) can be distinguished from  $\nu_\mu / \nu_e$  NC events (b). On the other hand, the emission of secondary invisible neutrinos (a) provides discrimination against  $\nu_\mu / \nu_e$  CC interactions (c).

Analysing the full data sample of more than  $1.5 \times 10^6$  events, no statistically significant excess of  $\nu_\tau$  CC interactions w.r.t. the expected BG is found. In the two-flavour mixing scheme of  $\nu_\mu \rightarrow \nu_\tau$ , oscillations an upper limit of  $\sin^2(2\theta_{\mu\tau}) < 3.3 \times 10^{-4}$  is derived at 90% C.L. for values of  $\Delta m^2 \gtrsim 1$  eV.

Motivated by the LSND experiment's positive indications [24] (see Chapter 2.5.3), a search for  $\nu_\mu \rightarrow \nu_e$  oscillations is performed on the NOMAD data [50]. Optimised for the identification of electrons from  $\tau \rightarrow e$  decays, the experiment is also able to search for  $\nu_e$  appearance.

Given the oscillation parameter values favoured by LSND, a signal should be observed by NOMAD for  $\Delta m^2 \gtrsim 10$  eV<sup>2</sup>. Finding no evidence for  $\nu_\mu \rightarrow \nu_e$  appearance, a 90% C.L. upper limit of  $\sin^2(2\theta) < 1.4 \times 10^{-3}$  is derived for  $\Delta m^2 \gtrsim 10$  eV<sup>2</sup> (compare Figure 6.6) [50].



### 4.3 The CNGS Neutrino Beam

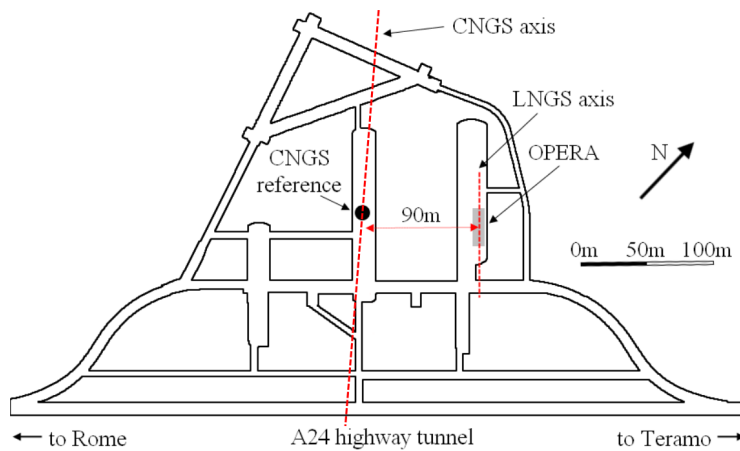
The neutrino beam studied by the OPERA experiment is created at the CERN Neutrinos to Gran Sasso (CNGS) facility [106]. It is designed to provide a high-energy, nearly-pure  $\nu_\mu$  beam with negligible contamination of  $\nu_\tau$  to enable a quasi background-free analysis of  $\nu_\mu \rightarrow \nu_\tau$  appearance.

Figure 4.10 shows an overview of the experiment facility locations. With the neutrino beam creation at the CERN North Area and the detector situated at the LNGS underground laboratory at a distance of  $L \sim 730$  km, OPERA is a long-baseline experiment.



**Figure 4.10:** OPERA experiment locations. (a) SPS extraction at the CERN North Area. (b) 730 km CNGS baseline from CERN to LNGS. (c) OPERA detector location at Hall C of the LNGS.

The relative alignment of the CNGS proton target focal point at CERN and a reference point within Hall B of the LNGS underground laboratory is conducted via GPS geodesy. The measured distance is  $L = (730520.3 \pm 0.2)$  m, with the neutrino flight path shortened by  $\sim 450$  m due to the average meson decay point downstream from the proton target (see Section 4.3.1) [63].



**Figure 4.11:** Top view of the LNGS laboratory. The CNGS beam axis reference point is located in LNGS Hall B,  $\sim 3$  m above the floor. Its coordinates within the OPERA reference frame w.r.t. the origin near the center of the detector are  $x_{CNGS} = -86.0$  m and  $y_{CNGS} = +2.6$  m [63].

Figure 4.11 shows a top view of the LNGS laboratory, indicating the CNGS beam axis crossing Hall B and the OPERA detector in Hall C. The coordinates of the CNGS reference point within the OPERA coordinate system are  $x_{CNGS} = -86.0$  m and  $y_{CNGS} = +2.6$  m [63].

Schematic drawings of the right-handed Cartesian OPERA coordinate system can be seen in Figure 4.12. The  $Z$  axis is roughly following the direction of the CNGS beam, the  $Y$  axis is vertical and pointing upwards, and the  $X$  axis is oriented horizontally, pointing from *corridor side* to *rock side* of LNGS Hall C.

The angles of the neutrino beam in the  $ZY$  and  $ZX$  projections are  $\theta_{CNGS} = +58.11$  mrad (as expected from Earth curvature) and  $\phi_{CNGS} = -4.48$  mrad, respectively [63].

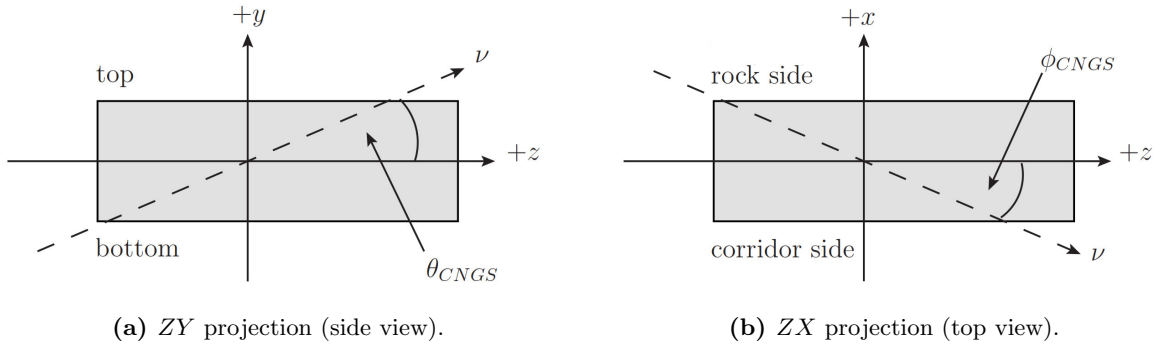


**Figure 4.12:** CNGS beam in the OPERA reference frame [91]. The neutrino beam angles are (a)  $\theta_{CNGS} = +58.11$  mrad in  $ZY$  projection and (b)  $\phi_{CNGS} = -4.48$  mrad in  $ZX$  projection [63].

### 4.3.1 CNGS Facility & Beam Properties

The high-energy and high-intensity CNGS neutrino beam is created at the CERN North Area using 400 GeV protons from the SPS accelerator.

Employing the same channel as used for the LHC  $p^+$  beam, two SPS fast extractions are made during a CNGS cycle of 6 s [101]. Separated by 50 ms, they each have a length of  $10.5 \mu\text{s}$  with a nominal intensity of  $2.4 \times 10^{13}$  protons on target (p.o.t.). Assuming a run time of 200 days, a maximum intensity of  $4.5 \times 10^{19}$  p.o.t. can be attained per year [106].

The extracted protons are focused and directed at an inclination of 5.6% onto a graphite target<sup>1</sup>, producing secondary pions and kaons at a maximum beam power of 0.5 MW. Inside a helium tube kept at 20 mbar, a system of water-cooled magnetic horn and reflector lenses then performs an energy-selection of the positively charged mesons, guiding them into a vacuum decay tube.

Remaining hadrons are stopped in the downstream hadron absorbers, consisting of 18 m of water-cooled graphite and iron, which are followed by muon detectors for beam monitoring. After 500 m of rock, the muons will too be absorbed, leaving a beam of neutrinos to travel into the direction of the LNGS with a time-of-flight of  $\sim 2.44$  ms.

<sup>1</sup>Made from 13 consecutive air-cooled graphite rods, each being 10 cm in length with diameters of 5 mm (first two rods) or 4 mm and distances of 9 cm or 0.1 cm (last five rods), the target geometry is optimised for the creation of secondary mesons at small angles w.r.t. the beam axis [93]. The total target length is  $\sim 2$  m.

The layout of secondary CNGS beamline is shown in Figure 4.13.

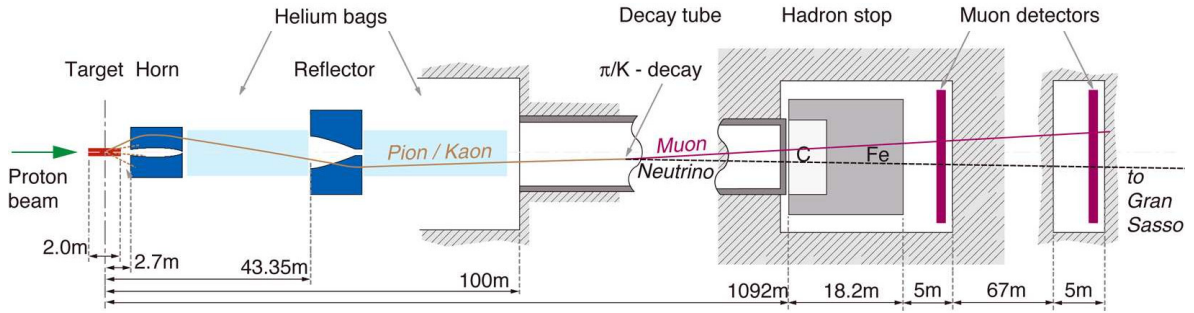


**Figure 4.13:** CNGS facility at the CERN North Area.[93]. The 400 GeV proton beam impinges on a graphite target. Created mesons enter a magnetic focusing system followed by a  $\sim 1$  km-long decay tube. After a hadron stop, downstream muon detectors are used for beam monitoring.

With 989.5 m, the length of the evacuated volume is optimised for the decay of  $\pi^+ \rightarrow \mu^+ + \nu_\mu$  that accounts for  $\sim 97\%$  of the resulting  $\nu_\mu$  flux (see Section 4.3.2). Further  $\nu_\mu$  contributions arise from  $K^+ \rightarrow \mu^+ + \nu_\mu$ . While the contamination with prompt  $\nu_\tau$  is negligible, contributions of  $\bar{\nu}_\mu$  (mainly from underdeflected high-energy  $\pi^-$ ),  $\nu_e$  ( $\mu^+$  and  $K^+$  decays), and  $\bar{\nu}_e$  ( $K^0$  and  $K^-$  decays) have to be taken into account.

Table 4.1 lists the most important decay modes and their relative contribution to the respective neutrino flavour. The average muon neutrino energy is  $\langle E_{\nu_\mu} \rangle = 17.9$  GeV.

**Table 4.1:** Meson and muon decay modes sorted by their flavour contribution to the CNGS beam [140, 91]. Relative contributions to the respective neutrino flux and average energies are calculated for  $E_\nu \leq 100$  GeV, using unoscillated spectra and integrating within the default CNGS limits of  $r \leq 120$  m ( $\nu_\mu$  and  $\bar{\nu}_\mu$ ) or  $r \leq 400$  m ( $\nu_e$  and  $\bar{\nu}_e$ ) (compare Figure 4.14, Section 4.3.2).

	Parent	Main decay mode	Contribution [%]	$\langle E_{\nu_l} \rangle$ [GeV]
$\nu_\mu$	$\pi^+$	$\rightarrow \mu^+ + \nu_\mu$	96.9	17.0
	$K^+$	$\rightarrow \mu^+ + \nu_\mu$	3.0	48.4
	$\mu^-$	$\rightarrow e^- + \bar{\nu}_e + \nu_\mu$	$< 0.1$	-
	$K^0$	$\rightarrow \pi^- + \mu^+ + \nu_\mu$	$< 0.1$	-
$\bar{\nu}_\mu$	$\pi^-$	$\rightarrow \mu^- + \bar{\nu}_\mu$	84.9	21.7
	$\mu^+$	$\rightarrow e^+ + \nu_e + \bar{\nu}_\mu$	7.5	17.6
	$K^-$	$\rightarrow \mu^- + \bar{\nu}_\mu$	6.6	33.6
	$K^0$	$\rightarrow \pi^+ + \mu^- + \bar{\nu}_\mu$	0.9	24.8
$\nu_e$	$\mu^+$	$\rightarrow e^+ + \bar{\nu}_\mu + \nu_e$	47.1	16.4
	$K^+$	$\rightarrow \pi^0 + e^+ + \nu_e$	39.2	33.6
	$K^0$	$\rightarrow \pi^- + e^+ + \nu_e$	9.5	25.6
	$\pi^+$	$\rightarrow e^+ + \nu_e$	4.0	30.7
$\bar{\nu}_e$	$K^0$	$\rightarrow \pi^+ + e^- + \bar{\nu}_e$	68.8	25.9
	$K^-$	$\rightarrow \pi^0 + e^- + \bar{\nu}_e$	21.6	23.3
	$\mu^-$	$\rightarrow e^- + \nu_\mu + \bar{\nu}_e$	8.3	16.9
	$\pi^-$	$\rightarrow e^- + \bar{\nu}_e$	$< 0.1$	-

Due to the long baseline of the experiment, the neutrino spectrum at the LNGS is dominated by well-focused meson decays with small opening angles. W.r.t. the WANF beam studied in short-baseline predecessor experiments CHORUS and NOMAD (see Section 4.2.2), the contamination of the CNGS  $\nu_\mu$  beam with neutrinos of other flavours is much lower [91].

To allow the reduction of cosmic backgrounds (or of beam-induced BG to other analyses), a CNGS timing synchronisation is performed. Two atomic clocks that are operated in common view mode [63], one at CERN, the other at the LNGS, provide timestamps for SPS kicker magnets and OPERA detector trigger. Taking into account corrections for cable delays at both locations and a neutrino time-of-flight (TOF) of  $\delta_t = 2394.4874 \mu\text{s}$ , both timestamps are then required to be within a window of  $\pm 20 \mu\text{s}$  for an event to be tagged as ONTIME with the CNGS [112].

### 4.3.2 Monte Carlo Simulation

Designed as a quasi BG-free  $\nu_\mu \rightarrow \nu_\tau$  appearance experiment, OPERA does not require a neutrino near detector for the CNGS beam. This however severely limits other analyses, such as  $\nu_\mu \rightarrow \nu_\mu$  disappearance [91] or  $\nu_\mu \rightarrow \nu_e$  appearance [16] measurements, which have to rely on Monte Carlo (MC) simulations for the unoscillated beam spectra.

Using the FLUKA framework<sup>1</sup> [87, 95], the CNGS beamline is simulated. Specific FLUKA routines have been developed for the CNGS calculations, including polarised particle decays and the implementation of correct matrix elements. The simulation has been compared with the performance of other frameworks GHEISHA and GFLUKA, and successfully benchmarked against experimental data from WANF-beam experiments NOMAD and NA56/SPY [75, 49, 31].

The FLUKA CNGS simulation includes the target chamber, focusing system, decay volume, absorbers, beam monitors, and all supports and infrastructure. The same geometry file is used for studies of energy deposition, beam monitor response, and the neutrino propagation to the LNGS [93].

In the simulation, the 400 GeV CNGS proton beam is centered on the target surface with Gaussian spacial and angular distributions of  $\sigma_X = 0.53 \text{ mm}$  and  $\sigma_\theta = 0.053 \text{ mrad}$ . The nominal parameters assume two fast extractions per 6 s with  $2.4 \times 10^{13}$  p.o.t. that deliver a total of  $4.5 \times 10^{19}$  p.o.t. per year.

Encompassing  $10^7$  p.o.t., the generated sample provides unoscillated fluxes for  $\nu_\mu$  and  $\bar{\nu}_\mu$ ,  $\nu_e$  and  $\bar{\nu}_e$ . The resulting statistical uncertainty on energy-integrated quantities is  $< 1\%$  for  $\nu_\mu$  events and  $\mathcal{O}(\%)$  for the other flavours. Being below a fraction of  $10^{-6}$  and therefore negligible, the contamination of the beam with prompt  $\nu_\tau$  has not been simulated [93].

With the neutrinos propagating approximately parallel to the beam axis at the LNGS site, their double differential distribution can be reduced to an energy-dependent flux  $\Phi(E_\nu)$  that is normalised to a given number of p.o.t. and area. The default CNGS integration limits

<sup>1</sup>FLUKA offers the ability to simulate the interactions and transport of hadrons, heavy ions, and electromagnetic particles of energies  $\mathcal{O}(\text{keV} - \text{TeV})$  in any desired material.

encompass the neutrino flux in a radius of  $r \leq 120$  m (for  $\nu_\mu$  and  $\bar{\nu}_\mu$ ) or  $r \leq 400$  m (for  $\nu_e$  and  $\bar{\nu}_e$ ) around the beam axis, covering the whole LNGS underground laboratory and much of the surrounding rock. Inside these limits, the fluxes are constant within their statistical uncertainties, and the beam composition at the small displacement of  $\sim 90$  m of the OPERA detector (see Section 4.3) does not need to be corrected [91].

The resulting unoscillated spectra of  $\nu_\mu$ ,  $\bar{\nu}_\mu$ ,  $\nu_e$ , and  $\bar{\nu}_e$  at the LNGS site are shown in Figure 4.14, also indicating their parent particles (compare Table 4.1, Section 4.3.1).

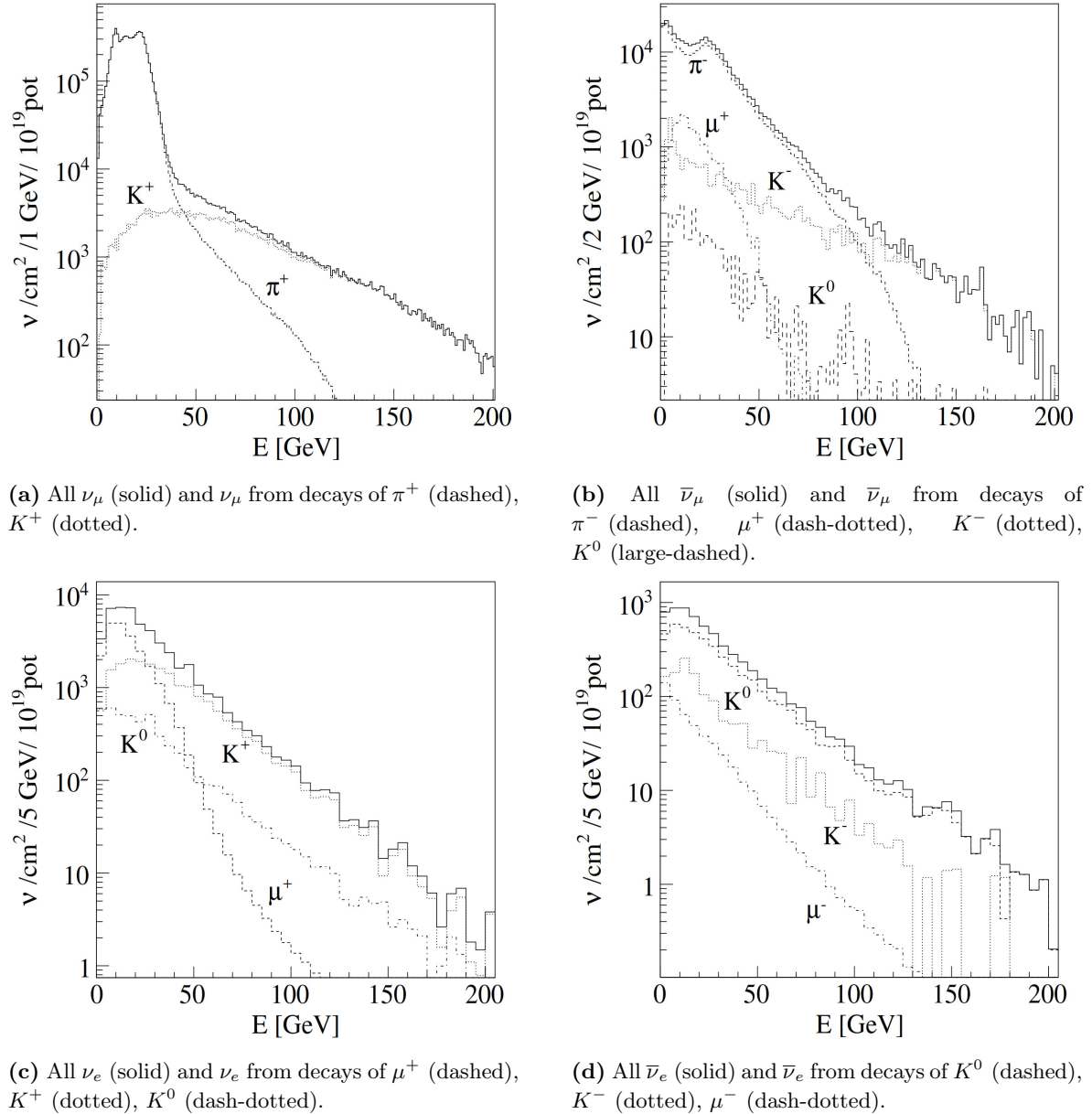


**Figure 4.14:** Unoscillated CNGS neutrino energy spectra at the LNGS and parent particles [91]. Fluxes are integrated within the default CNGS limits of  $r \leq 120$  m ( $\nu_\mu$  and  $\bar{\nu}_\mu$ ) or  $r \leq 400$  m ( $\nu_e$  and  $\bar{\nu}_e$ ) (compare Table 4.1, Section 4.3.1).

Integrated over a radius of  $r \leq 400$  m, the unoscillated flux of muon neutrinos per p.o.t. and its contamination with neutrinos of other flavours at the LNGS is listed in Table 4.2. Average

energies and contaminations have been calculated taking into account a maximum neutrino energy of  $E_\nu \leq 100$  GeV. The average muon neutrino energy is  $\langle E_{\nu_\mu} \rangle = 17.9$  GeV.

**Table 4.2:** Unoscillated CNGS  $\nu$  flux per p.o.t. at the LNGS, integrated within  $r \leq 400$  m [93]. Average energy and beam compositions are calculated for  $E_\nu \leq 100$  GeV.

	$\Phi^{\nu_i}$ [ $\nu/\text{cm}^2/\text{p.o.t.}$ ]		$\langle E_{\nu_i} \rangle$ [GeV]	$\Phi^{\nu_i}/\Phi^{\nu_\mu}$ [%]
	$E_\nu \leq 100$ GeV	$E_\nu \leq 400$ GeV		
$\nu_\mu$	$7.4 \times 10^{-13}$	$7.5 \times 10^{-13}$	17.9	
$\bar{\nu}_\mu$	$2.9 \times 10^{-14}$	$2.9 \times 10^{-14}$	21.8	3.9
$\nu_e$	$4.7 \times 10^{-15}$	$4.8 \times 10^{-15}$	24.5	0.65
$\bar{\nu}_e$	$6.0 \times 10^{-16}$	$6.2 \times 10^{-16}$	24.4	0.08

Assuming an isoscalar detector target, the expected CC neutrino interaction rates per  $10^{19}$  p.o.t. and kton of target material are given in Table 4.3. For maximal neutrino energies of  $E_\nu \leq 100$  GeV, the contamination with events from  $\bar{\nu}_\nu$ ,  $\nu_e$ , and  $\bar{\nu}_e$  CC interactions is 2.4%, 0.89%, and 0.06%, respectively.

**Table 4.3:** CNGS  $\nu$  CC event rates on an isoscalar target, normalised to  $10^{19}$  p.o.t. and 1 kton target mass, using the unoscillated fluxes listed in Table 4.2 [93]. The contaminations are calculated for  $E_\nu \leq 100$  GeV.

	$N_{CC}^{\nu_i}$ [events/kton/ $10^{19}$ p.o.t.]			$N_{CC}^{\nu_i}/N_{CC}^{\nu_\mu}$ [%]
	$E_\nu \leq 30$ GeV	$E_\nu \leq 100$ GeV	$E_\nu \leq 400$ GeV	
$\nu_\mu$	496	580	604	
$\bar{\nu}_\mu$	6.5	14.0	15.1	2.4
$\nu_e$	2.26	5.02	5.44	0.89
$\bar{\nu}_e$	0.13	0.33	0.38	0.06

The systematic uncertainty on the CNGS neutrino flux prediction is dominated by the extrapolation from the WANF target material (Be) to the CNGS target (C). Taking into account systematic and statistical uncertainties, the total uncertainty on the  $\nu_\mu$  flux is estimated as 5.5%, the respective values for  $\bar{\nu}_\mu$ ,  $\nu_e$ , and  $\bar{\nu}_e$  being 6.2%, 6.3%, and 8.5% [91].

As the  $\nu_\mu$  and  $\nu_e$  mainly originate from the same parent particles ( $\nu_\mu$  from  $\pi^+ \rightarrow \mu^+ + \nu_\mu$  decays,  $\nu_e$  from the subsequent decay of the  $\mu^+$ , see Table 4.1, Section 4.3.1), the ratio  $\Phi^{\nu_\mu}/\Phi^{\nu_e}$  of their fluxes has a reduced uncertainty of  $\sim 4.3\%$  [93].

### 4.3.3 CNGS Performance

After two years of commissioning in 2006 and 2007, the CNGS physics program encompassed 5 years of data taking from 2008 to 2012 [106]. A total of  $18.0 \times 10^{19}$  p.o.t. were delivered, corresponding to 80% of the nominally approved  $22.5 \times 10^{19}$  p.o.t.

The average beam intensity amounted to  $1.8 \times 10^{13}$  p.o.t., the reduction w.r.t. the nominal intensity of  $2.4 \times 10^{13}$  p.o.t. being mainly due to losses in the Proton Synchrotron (PS) injector. Sharing the beam with other SPS users, the average beam power reached 160 kW.

Figure 4.15 demonstrates the CNGS performance via the intensity per extraction (4.15a) and the integrated number of p.o.t. per year (4.15b). 2011 and 2012 profited from early run starts during which the SPS beam did not need to be shared with other users. The  $\sim 25\%$  decrease in proton intensity in run year 2012 that is visible in both plots arose from new radiation limits at the PS pre-accelerator.

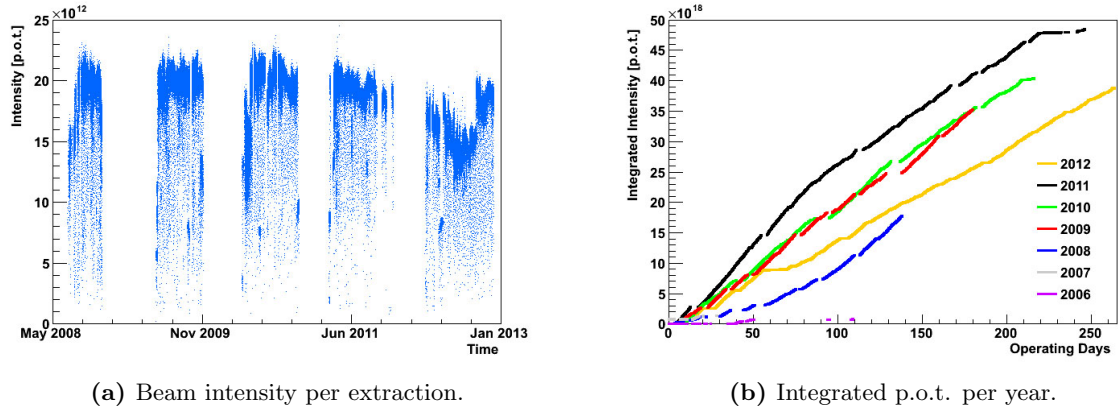


**Figure 4.15:** CNGS performance [106]. (a) P.o.t. per extraction during the physics runs of 2008 - 2012. (b) Integrated p.o.t. per year, including the commissioning runs of 2006 and 2007.

A dedicated *bunched beam* program in run years 2011 and 2012 addressed an anomaly observed in the measurement of the neutrino velocity with OPERA [63, 8]. For two weeks in October and November of 2011, the SPS extractions consisted of four bunches with an intensity of  $2.5 \times 10^{11}$  protons each and a separation of 524 ns. During the 2011 / 2012 shutdown, diamond timing detectors were installed in the CNGS muon pits to improve the timing system. A second bunched beam period in May 2012, providing 16 bunches of protons per batch at four batches per extraction with a bunch intensity of  $1.25 \times 10^{11}$  and a separation of 100 ns, helped in resolving the issue [9].

The final numbers of delivered p.o.t. per run year available to the OPERA oscillation analyses (including small inefficiencies from CNGS ONTIME tagging and OPERA detector uptime) are listed in Table 4.4 [20].

**Table 4.4:** P.o.t. delivered during the CNGS physics runs [20]. The numbers include inefficiencies from CNGS ONTIME tagging and detector uptime.

	p.o.t. [ $\times 10^{19}$ ]
2008	1.74
2009	3.53
2010	4.09
2011	4.75
2012	3.86
Total	17.97

## 4.4 The OPERA Detector

Specifically designed for the detection of  $\nu_\tau$  appearance [107], the OPERA detector needs to fulfill two conflicting requirements: A micrometric position accuracy to resolve the  $\tau$  decay topology (see Section 4.7.1) on the one hand, and on the other hand a large target mass to compensate the small neutrino cross sections (see Chapter 2.3).

The resulting detector is a hybrid apparatus with a modular design built from Electronic Detector (ED) elements and Emulsion Cloud Chamber (ECC) nuclear emulsion sheets, similar to the DONuT and CHORUS detectors (see Section 4.2) [6]. It is divided into two identical Super Modules (SMs), each consisting of an instrumented target area (see Section 4.4.1) followed by a magnetic spectrometer (see Section 4.4.2). The ED provides real-time event information and triggers the high-resolution ECC data acquisition (DAQ).

Figure 4.16 shows a side view of the OPERA detector where the different sections have been highlighted. Including support structures, the detector weighs about 4000 t, with overall dimensions of  $\sim 10\text{ m} \times 10\text{ m} \times 20\text{ m}$ .

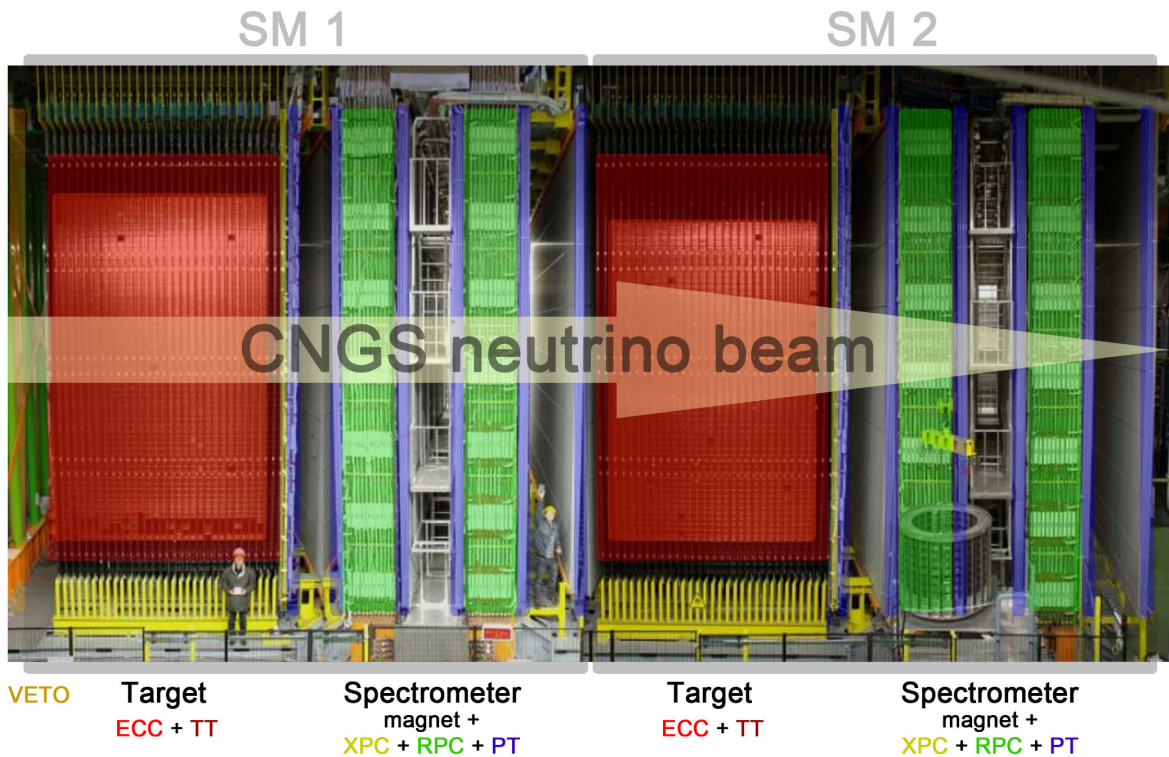


**Figure 4.16:** Side view of the OPERA detector [11]. The CNGS  $\nu_\mu$  beam arrives from the left, first entering the veto system. The detector is divided into two identical SMs, each consisting of a target area (walls of ECC bricks and TT scintillator strips) followed by a magnetic spectrometer (iron core magnets, RPC & XPC detectors, and PT drift tubes).

With the detector location in Hall C of the LNGS underground laboratory, the vertical rock coverage of  $\sim 1400\text{ m}$ , corresponding to 3800 meters water equivalent (m.w.e.), provides excellent shielding against cosmic rays. The rate of cosmic muons is reduced by a factor of  $10^{-6}$  to  $\sim 1/\text{m}^2/\text{h}$  [113].



#### 4.4.1 Target Area

The two target areas of the OPERA detector each comprise about 75 000 ECC units, called bricks, arranged in an ultra-light stainless steel shelf structure of 31 walls transverse to the neutrino beam direction [6]. Each wall is capable of holding  $52 \times 64$  bricks (columns  $\times$  rows) and is followed by a double layer of perpendicular Target Tracker (TT) scintillator strips that provide real-time information on outgoing particles and allow to pinpoint the brick containing a specific neutrino interaction. Two detachable extra-layers of nuclear emulsion, the so-called Changeable Sheets (CSs), are attached to the downstream side of each brick and provide an interface between the TT Electronic Detector and the ECC bricks [40].

Figure 4.17a shows a schematic drawing of the OPERA target area detectors, while in Figure 4.17b a side view photo of the empty brick support structure can be seen.

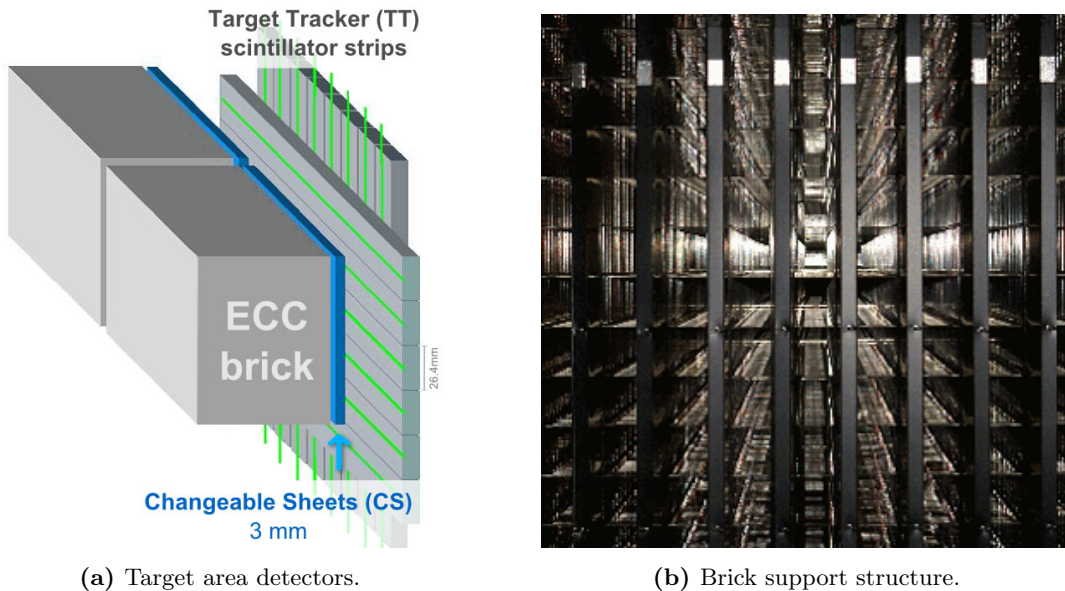


**Figure 4.17:** The OPERA target area [6]. (a) Schematic drawing of the target area detectors: ECC brick with attached CS, followed by two perpendicular layers of TT scintillator strips. (b) Side view of the empty stainless steel brick support structure with vertical TT walls.

#### Emulsion Cloud Chamber Bricks

The main detector units of the OPERA detector are the Emulsion Cloud Chamber (ECC) bricks. Each brick consists of alternating layers of nuclear emulsion sheets and low-radioactivity lead plates [41]. The lead acts as the neutrino interaction target material, with the emulsion sheets providing a high-resolution tracking detector.

Figure 4.18a shows the structure of an ECC brick, its outer dimensions being  $128 \text{ mm} \times 192 \text{ mm} \times 79 \text{ mm}$ . 57 nuclear emulsion sheets are alternated with 56 1 mm-thick lead plates<sup>1</sup>,

<sup>1</sup>For increased stability, a Pb – Ca alloy of 0.04% is used.

corresponding to about 10 radiation lengths  $X_0$  in beam direction<sup>1</sup> and resulting in a target mass of 8.3 kg per brick. The decay topologies of  $\tau$  leptons (see Section 4.7.1) created in  $\nu_\tau$  CC interactions, with characteristic decay lengths of  $\sim 1$  mm, can be resolved by reconstructing the associated particle tracks crossing consecutive emulsion sheets.

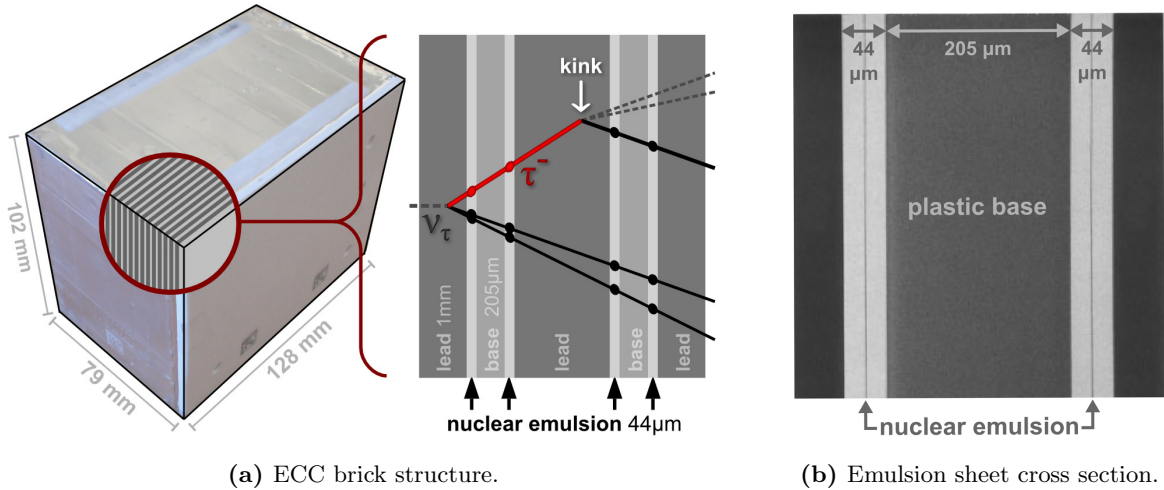


**Figure 4.18:** (a) Structure of an OPERA ECC brick, consisting of alternating layers of 1 mm-thick Pb plates (target material) and AgBr nuclear emulsion sheets (active detector). (b) Cross section of an OPERA emulsion sheet. A 205  $\mu\text{m}$ -thick plastic<sup>2</sup> base is coated on both sides with AgBr nuclear emulsion layers of 44  $\mu\text{m}$  thickness.

Figure 4.18b displays the cross section of an OPERA emulsion sheet. The transparent 205  $\mu\text{m}$ -thick plastic<sup>2</sup> base is coated on both sides with 44  $\mu\text{m}$ -thick layers of an emulsion of AgBr in gelatine binder. Excited electrons created by the passage of ionising particles are trapped in lattice defects and create Ag atoms that act as latent images. During chemical development, the number of Ag atoms is increased by a factor of  $10^8 - 10^{10}$ , resulting in grains of  $\sim 0.6 \mu\text{m}$  diameter which are visible under optical microscopes [6]. The surface area of a single emulsion sheet, transverse to the neutrino beam direction, measures  $124.6 \times 99.0 \text{ mm}^2$ .

Vacuum-sealed and wrapped light-tight in aluminium foil, each brick is equipped with a detachable module of CS on its downstream side. This double layer of separately packed emulsion sheets is no different from the nuclear emulsions used in the ECC bricks, but subject to an additional *refreshing* process<sup>3</sup> that reduces the single-film track density to  $< 100$  tracks/ $\text{cm}^2$  [40]. Acting as an interface between the TT ED signals and the ECC brick, the CS of bricks tagged for analysis are developed first, thus allowing a reinsertion of the respective brick into the detector if no positive signal is found (see Section 4.6.2).

Comprising a maximum of  $\sim 150\,000$  ECC bricks of 8.3 kg mass each, the total detector target mass amounts to about 1.25 kton, with a sensitive emulsion area of  $\sim 110\,000 \text{ m}^2$ .

<sup>1</sup>This provides a better momentum resolution and  $e^\pm/\pi^0$  identification efficiency w.r.t. the DONuT experiment's brick thickness of  $3 X_0$ .

<sup>2</sup>Cellulose triacetate.

<sup>3</sup>Prior to insertion into the detector, tracks accumulate in the nuclear emulsions due to cosmic ray exposure during storage and transport. Via exposing the emulsion films to an atmosphere of high humidity and warmth for a few days, such BG can be erased.

### Target Tracker

As the electronic target area detector, the main purpose of the OPERA Target Tracker (TT) is to locate the ECC bricks containing neutrino interactions by providing real-time information on the outgoing charged particles [7]. It furthermore acts as a sampling calorimeter for hadronic and electromagnetic showers.

To realise the required brick finding efficiency (see Section 4.6.2), the TT needs to provide a sufficiently high spatial resolution and track detection efficiency over a total sensitive surface of  $\mathcal{O}(600\text{ m}^2)$ . As replacement of detector elements would be extremely difficult, long-term stability for at least 5 years of OPERA data taking must be guaranteed.

The OPERA TT consists of 6.86 m-long plastic scintillator strips of 26.3 mm width and 10.6 mm thickness. Wavelength-shifting (WLS) fibres are glued into grooves along the strip length. A diffuse-reflective coating of 0.15 mm  $\text{TiO}_2$  improves light collection. See Figure 4.19 for a schematic picture.

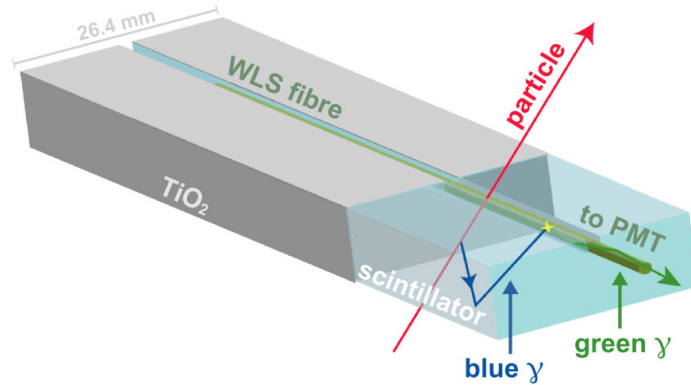


**Figure 4.19:** Schematic drawing of an OPERA TT scintillator strip with WLS fibre [7].

The scintillator strips are produced by polystyrene extrusion, with 2% p-Terphenyl and 0.02% POPOP acting as the primary and secondary fluors. Figure 4.20 shows the respective absorption and emission spectra.

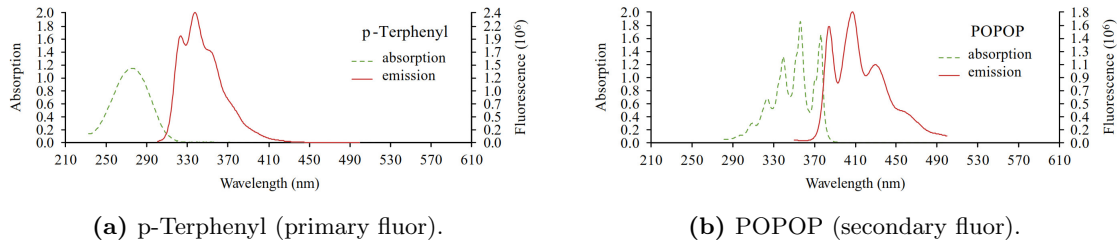


**Figure 4.20:** Absorption and emission spectra of the OPERA TT plastic scintillator primary and secondary fluors [7]. (a) p-Terphenyl, (b) POPOP.

The short and long attenuation lengths of the WLS fibre<sup>1</sup> are  $\lambda_s = 79\text{ cm}$  and  $\lambda_l = 573\text{ cm}$ , respectively<sup>2</sup>. The light signal is read out on both ends of the scintillator by multi-anode

<sup>1</sup>Kuraray Y11(175) MJ non-S.

<sup>2</sup>Obtained by fitting the sum of two exponential distributions to the measured data [7].

photo multiplier tubes (PMTs). For minimum ionising particles (m.i.p.s) crossing the middle of the scintillator strip (i.e. at the greatest distance from the two photosensors), a particle detection efficiency of better than 99% is achieved.

A basic TT module comprises 64 scintillator strips that are read out by WLS fibres directly coupled<sup>1</sup> to two 64-channel photodetectors<sup>2</sup>, Figure 4.21a shows a schematic drawing. Low rates of dark current (2.45 Hz mean per channel at 20°C) and crosstalk (1.43% mean for direct neighbours of PMT channels) allow the operation of the detector without an external trigger. To shield the PMTs from the spectrometer fringe magnetic fields, the module end-cap frames are built from 0.8 mm-thick soft steel<sup>3</sup>, preventing the modification of photo electron (p.e.) trajectories or secondary electron multiplication processes.

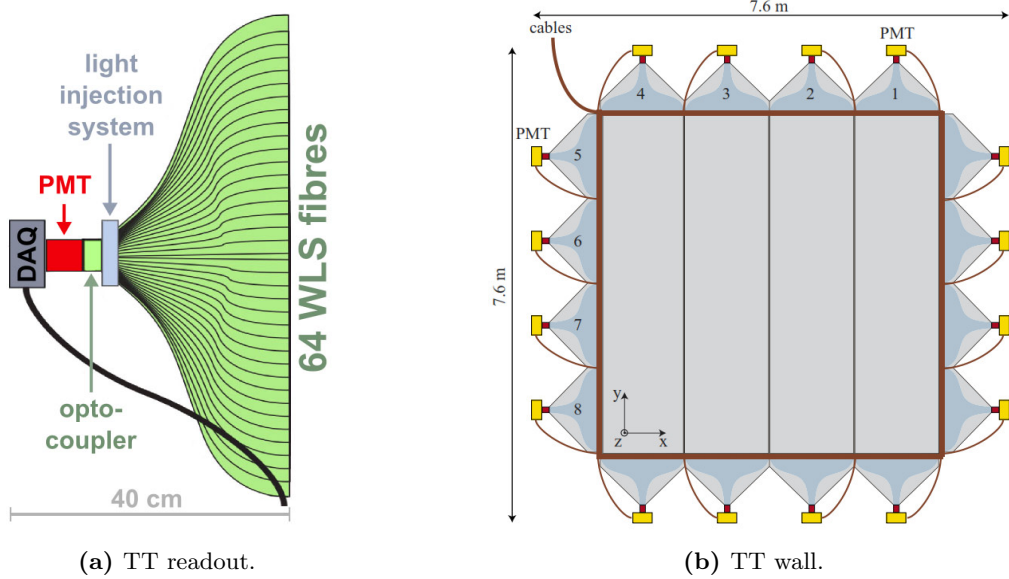


**Figure 4.21:** The OPERA TT detector [7]. (a) TT module readout structure. The light injection system, based on fast-pulsed LEDs, allows to test all electric channels and provides monitoring of WLS fibre ageing. (b) Schematic drawing of a TT wall consisting of horizontal and vertical modules.

A TT plane is assembled from four modules, two planes of horizontal and vertical modules form a TT wall (see Figure 4.21b). Suspended on a support structure in-between two walls of ECC bricks (shown in Figure 4.17b), the OPERA TT walls cover the sensitive brick area of  $6.7 \times 6.7 \text{ m}^2$ , providing 2D track information. A total of 496 TT modules are arranged to 62 walls, 31 per SM. Altogether, the OPERA TT comprises 31 744 scintillator strips and 63 488 electronic readout channels. It provides a spatial resolution of  $\sim 7.5 \text{ mm}$  and a time resolution  $\mathcal{O}(\text{ns})$  at 99% trigger efficiency [74].

The OPERA TT front-end board is an 8-layer PCB carrying two 32-channel ASIC ReadOut Chips (ROCs) which are directly plugged to the multi-anode PMTs and provide both charge measurement and time information. More detailed information on the readout can be found in [129].

<sup>1</sup>Causing a loss of  $\sim 15\%$  of absorbed photons. Optical grease was omitted to prevent possible ageing effects.

<sup>2</sup>Based on Hamamatsu H7546, also used for the MINOS near detector.

<sup>3</sup>STE37, 99.5%Fe.

### Brick Extraction / Insertion

The initial OPERA target filling, as well as brick removal, reinsertion, and reallocation during the CNGS runs, is conducted using the Brick Manipulator System (BMS) [6].

As each target area is symmetrically subdivided in  $X$  into two semi-walls, two independent BMS machines are installed on both sides<sup>1</sup> of the detector. Each machine features a moveable platform, a brick extraction / insertion vehicle, and a carousel able to store up to 32 bricks. In Figure 4.22, a photo of a BMS machine with attached brick storage drum can be seen. Capable of holding up to  $9 \times 26$  bricks, a drum can store the content of nine detector semi-walls.

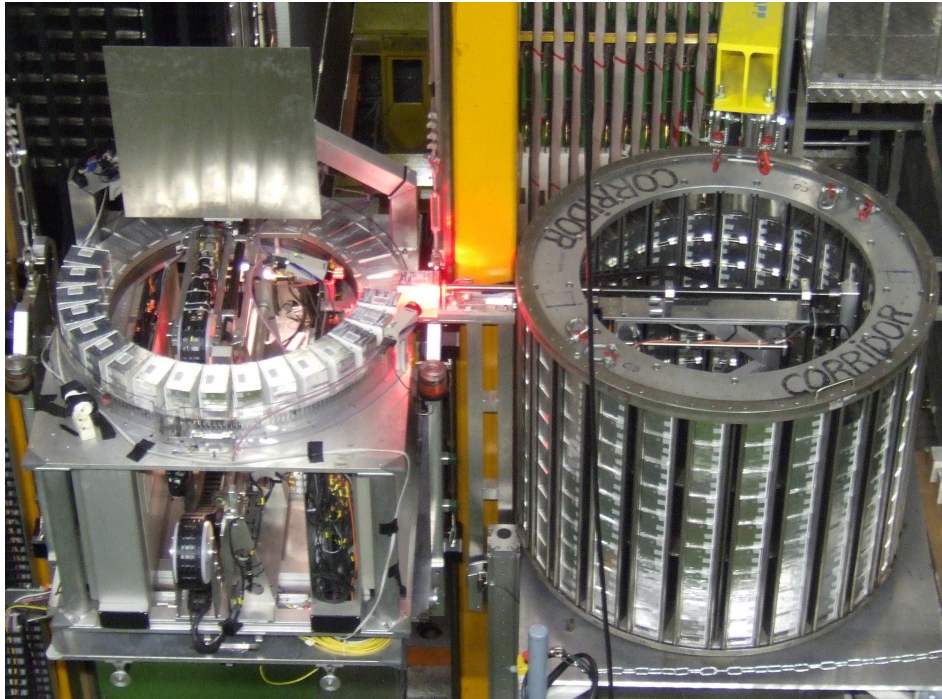


**Figure 4.22:** BMS machine (left) and brick storage drum (right) during loading / unloading process.

The modular structure of the OPERA target allows to extract only those bricks containing a specific neutrino interaction, the other ones being rearranged to keep the target both compact and symmetrical. This minimises the target mass loss during the CNGS beam exposure and enables a quasi online analysis of the selected bricks. While developed bricks will not be replaced with new ones, extracted bricks whose CS show no indication for the respective neutrino interaction are equipped with fresh CS and reinserted into the detector.

Figure 4.23 shows the target mass evolution of the OPERA detector from 2007 to 2016. The initial brick filling was completed in 2008, but due to high fog levels in the nuclear emulsions of the CS, more than 17 000 bricks of SM1 had to be extracted during the winter shutdown and equipped with new CS [154]. The steady, slow decrease during the CNGS run years of 2008 - 2012 illustrates the removal of  $\sim 15$  000 bricks for analysis, until detector decommissioning in 2015.

<sup>1</sup>Respectively labelled *rock side* and *corridor side*.

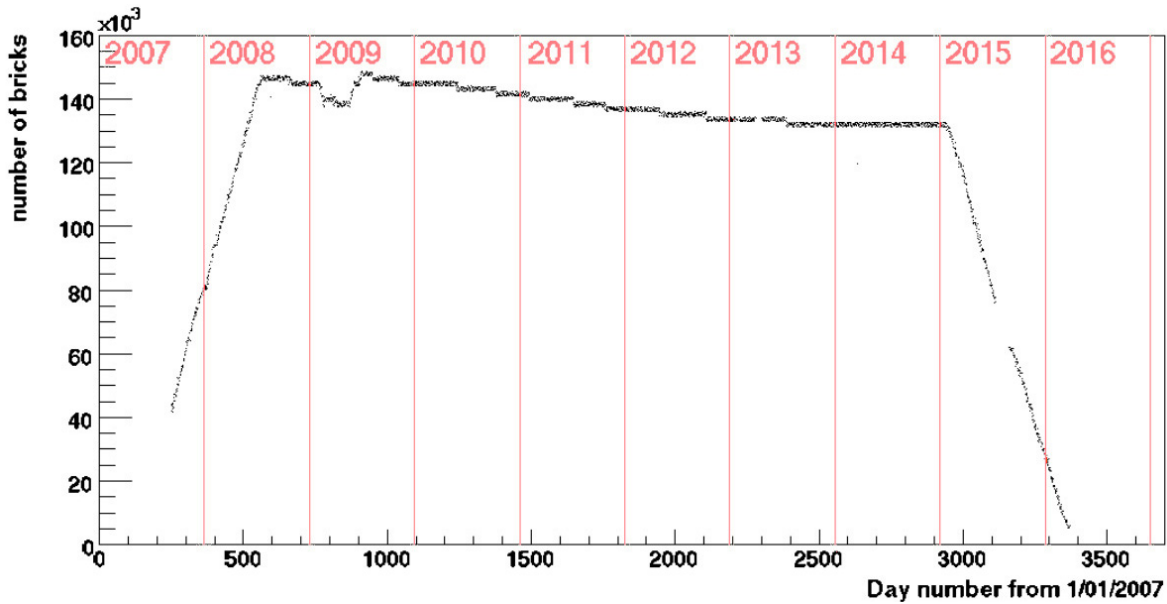


**Figure 4.23:** OPERA target mass evolution. The initial brick filling was completed in July 2008, decommissioning of the detector started in January 2015. The slow decrease in-between shows the loss of  $\sim 15\,000$  bricks caused by the standard analysis procedure. During the 2009 CNGS winter shutdown,  $> 17\,000$  bricks were equipped with new CS and reinserted into the detector.

The SM, wall, row, and column positions of each brick (identified via unique numbers and matrix code) are stored in a Brick Manipulation Manager (BMM) database along with the timestamp of its insertion. This allows to reconstruct the general brick filling status and location of individual bricks for any given time.

Figure 4.24 shows an example of the OPERA brick status on 2009-06-29. This date marks the maximum detector filling of 148 828 bricks<sup>1</sup>, corresponding to a total target mass<sup>2</sup> of 1 235 kt.

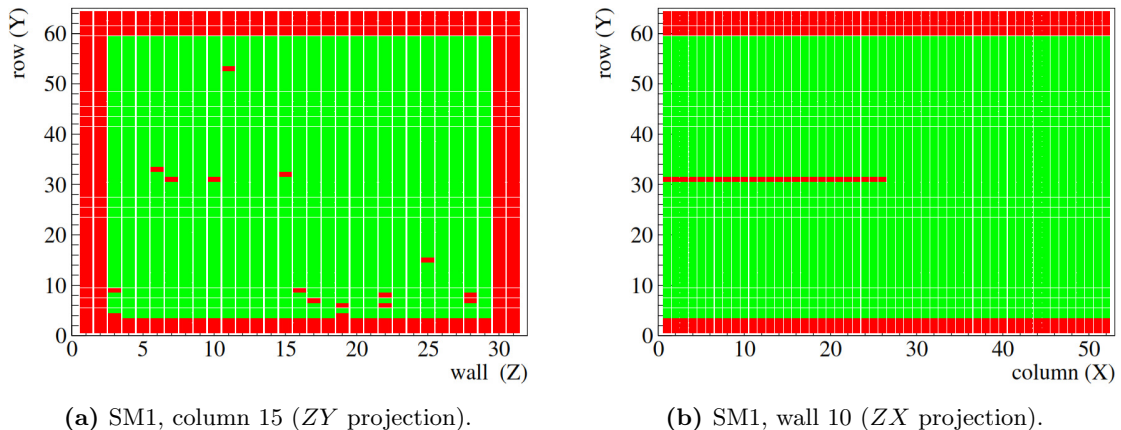


**Figure 4.24:** OPERA brick status on 2009-06-29 (date of maximum real brick filling) [91]. Rows filled with bricks are green, red marks empty spaces. (a) Side view of SM1, column 15. (b) Front view of SM1, wall 10.

<sup>1</sup>Rock side:  $38\,716(\text{SM1}) + 35\,504(\text{SM2}) = 74\,220$  bricks, corridor side:  $38\,899(\text{SM1}) + 35\,709(\text{SM2}) = 74\,608$  bricks.

<sup>2</sup>W.r.t. the experiment proposal, the OPERA target mass was reduced by  $\sim 25\%$  due to funding difficulties.

### 4.4.2 Spectrometer

Each OPERA target area (see Section 4.4.1) is followed by a magnetic spectrometer [32, 6]. A schematic cross section can be seen in Figure 4.25.

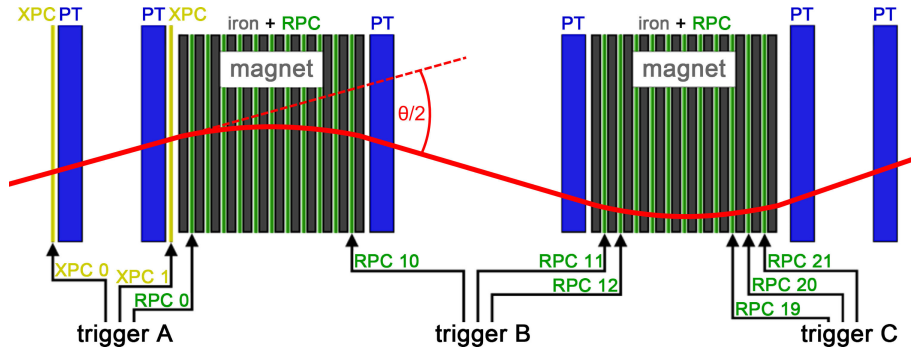


**Figure 4.25:** Top view of the OPERA spectrometer and PT trigger scheme [125]. The dipole magnet deflects charged particles whose tracks are then precisely measured by the PT drift tubes in front of and behind the magnet arms, and the RPC detectors within.

Designed to precisely measure their electric charge and momentum, the spectrometer employs a large dipole magnet to horizontally deflect charged particles (i.e. primarily muons) from their original path. The resulting track curvature is measured in Precision Tracker (PT) drift tube stations in front of and behind the two magnet arms, and the resistive plate chamber (RPC) detectors placed inside the gaps between the vertical slabs of magnetised iron.

### Dipole Magnets

Each of the two identical magnets consists of two vertical *arms* that are composed of twelve 5 cm-thick iron slabs and connected via top and bottom return yokes [68]. Water-cooled copper coils, wound around both yokes and connected in series, create a magnetic field of  $\sim 1.53$  T inside the iron that is uniform within 3% at an operating current of 1 600 A.

Figure 4.26 shows a schematic drawing of an OPERA dipole magnet.

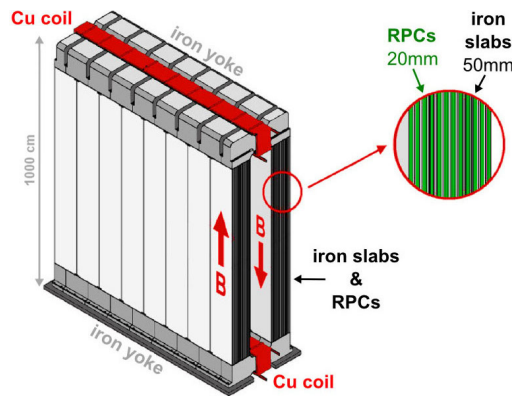


**Figure 4.26:** Isometric view of an OPERA dipole magnet. The Cu coils wound around top and bottom return yokes are connected in series. They create a uniform magnetic field within the iron slabs of  $\sim 1.53$  T.

Covering a magnetised area of  $875 \text{ cm} \times 820 \text{ cm}$  perpendicular to the neutrino beam direction, the iron slabs are interspaced by 2 cm-gaps that provide room for planes of RPC detectors. The nominal field polarisation is pointing upwards in the first magnet arm and pointing downwards in the second arm of the magnet, but may be reversed by changing the direction of the electrical current without loss of performance [90].

### Resistive Plate Chamber Detectors

For the reconstruction of charged particle tracks inside the magnet, OPERA uses a system of resistive plate chamber (RPC) detectors which are able to safely operate in magnetic fields of moderate strength [55, 6]. The RPC enable the measurement of stopping particles<sup>1</sup>, are taken into account for ED hadronic shower energy reconstruction (see Chapter 5.4.1), and provide the trigger signal for the PT readout.

With 11 planes of RPC (each covering an area of  $70 \text{ m}^2$ ) inside the 2 cm-gaps between the iron slabs of one magnet arm, the *inner tracker* consists of 22 planes per SM, 44 in total. To resolve ambiguities in the simultaneous  $XY$  reconstruction of multiple tracks, two planes of Crossed RPC (XPC) that are rotated around  $Z$  by  $\pm 42.6^\circ$  are added upstream of each magnet, directly in front of the first and after the second PT stations (see Figure 4.25).

A schematic cross section of an OPERA RPC is shown in Figure 4.27.

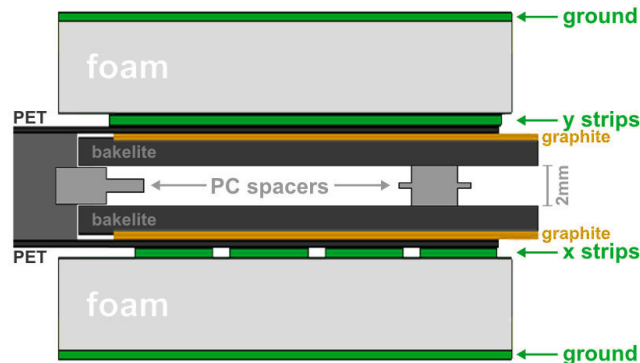


**Figure 4.27:** Cross section of an OPERA RPC. Two 2 mm-thick Bakelite electrodes coated with linseed oil are kept 2 mm apart by PC spacers, the cavity is flushed with a gas mixture of  $\text{Ar}/\text{C}_2\text{H}_2\text{F}_4/\text{iC}_4\text{H}_{10}/\text{SF}_6$ . The external electrode surface is painted with graphite and covered by an insulating film of  $190 \mu\text{m}$  PET. The readout occurs via horizontal and vertical Cu strips (3.5 cm and 2.6 cm wide) on both sides of the detector.

The OPERA RPC are gas amplification detectors that are flushed with a mixture of  $\text{Ar}/\text{C}_2\text{H}_2\text{F}_4/\text{iC}_4\text{H}_{10}/\text{SF}_6$  (75.4/20.0/4.0/0.6) at atmospheric pressure [133]. As the expected event rates are lower than  $20 \text{ Hz}/\text{m}^2$ , they can be operated in streamer mode<sup>2</sup> at a high voltage (HV) of 5.8 kV without additional electronic amplification.

<sup>1</sup>For particles not crossing a whole spectrometer, the momentum may still be inferred from range.

<sup>2</sup>In streamer mode, the electric field is high enough to induce a permanent discharge between the electrodes, resulting in large electric signals  $\mathcal{O}(100 \text{ mV})$ .



While the general structure of inner tracker RPC and XPC is the same, their dimensions and readout geometry slightly differ.

The inner tracker planes consist of RPC with a surface area of  $2.91\text{ m} \times 1.134\text{ m}$  that are arranged in seven rows and three columns, resulting in a total of 462 RPC per magnet. The 8.73 m-long horizontal readout strips have a width of 3.5 cm, while the width of the 8.06 m-long vertical strips is reduced to 2.6 cm to improve the position resolution in the bending plane. Vertical strips are directly glued onto the iron of the magnet, the horizontal ones are arranged in panels of 32 strips each, with 7 rows at a distance of 3 cm per RPC plane. The single-plane acceptance reaches 97%.

For the XPC, the width of all readout strips is 2.6 cm. They are of different lengths and arranged in one large panel per view, covering both sides of the 21-RPC planes. Due to limitations imposed by the OPERA target support structure, the first XPC plane per SM has a decreased size of  $7.50\text{ m} \times 8.06\text{ m}$ .

The digital signals of both RPC and XPC are read out using LVDS receivers as comparators [53]. The self-triggering front-end boards provide 64-channel discriminators, and a dedicated trigger board allows for the definition of special trigger conditions.

To further provide a trigger for the PT readout, three groups of RPC and XPC per SM are equipped with timing boards (TBs) (see Figure 4.25) that are operating in a 2-of-3 coincidence [76, 89, 125]. For nominal RPC thresholds, the PT trigger rate per SM is below 10 Hz.

Using the PT time-to-digital converter (TDC) boards, the excellent RPC time resolution  $\mathcal{O}(\text{ns})$  can also be used for TOF measurements.

As it will be impossible to replace any RPC after installation, a dedicated quality assessment was performed beforehand [54]. The average RPC efficiency was measured to be 98%, with non-uniformities smaller than 2% over the whole surface.

### Precision Tracker

The main task of the Precision Tracker (PT) is the reconstruction of the charge and momentum of particles passing through the OPERA spectrometer via measurement of their tracks both before and after deflection by the magnet [162]. It consists of altogether twelve walls of vertically oriented drift tubes, six per SM: Two upstream of each magnet, two in-between the magnet arms, and two walls downstream (see Figure 4.25).

The 8 m-long drift tubes are made of aluminium with an outer diameter of 38 mm and a wall thickness of 0.85 mm. A gold-coated tungsten sense wire with a diameter of  $45\text{ }\mu\text{m}$  is held at both ends of the tube, without additional supports and independent of the tube position. Its position accuracy is better than  $150\text{ }\mu\text{m}$ , resulting in a single-tube spatial resolution of  $\sim 300\text{ }\mu\text{m}$ .

As gas amplification detectors similar to the RPC, the drift tubes are flushed with a gas mixture of Ar/CO<sub>2</sub> (80/20) at  $1005 \pm 5\text{ mbar}$  [92]. They are operated in proportional mode<sup>1</sup>

<sup>1</sup>In proportional mode, the lower electric field prevents the continuous discharge between the electrodes.

at a HV of 2.45 kV and equipped with L3 preamplifiers. Custom temperature- and voltage-compensating TDC enable the measurement of the electron drift time<sup>1</sup> with a maximum value of  $\sim 1.6 \mu\text{s}$  and the rejection of short-width noise pulses. The single-tube hit efficiency is better than 98%.

The trigger signal is provided by the RPC / XPC TB (see Figure 4.25) [89] which also create the TDC stop for the drift time measurement. The regular trigger condition is given by a 2-of-3 coincidence per trigger station that is optimised for through-going tracks, stopping muons, and hadronic showers. For the measurement of cosmic particles with large incident angles, a special configuration prompts the readout of all drift tubes, even if only one station sends a trigger signal. The average PT trigger rate per SM is  $\sim 2 \text{ Hz}$ .

The PT encompasses nearly 10 000 drift tubes that are arranged in modules of 48 tubes. A PT wall is built from 17 modules, covering an area of  $8 \text{ m} \times 8 \text{ m}$  perpendicular to the neutrino beam direction. To allow for BMS movement and brick access, the walls directly adjacent to the OPERA target are reduced by one module on both sides.

A module is made of 4 staggered layers of 12 tubes each in hexagonal close packing with a relative shift of 11 mm (see Figure 4.28). The structure was optimised via MC simulations to provide maximal track efficiency and large angular acceptance for beam-induced events and cosmic muons.

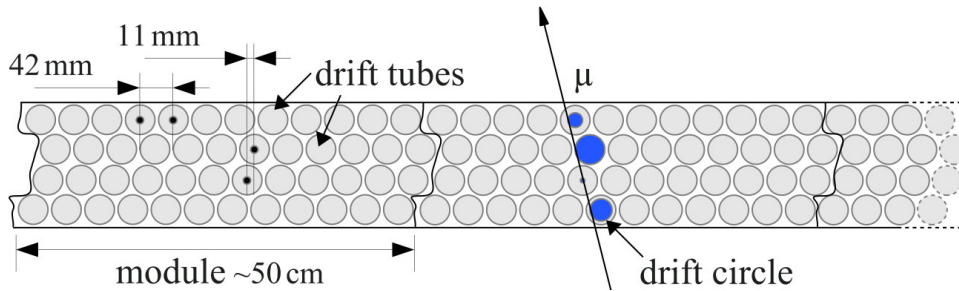


**Figure 4.28:** Top view of several PT drift tube modules [102]. A module consists of 48 drift tubes arranged in 4 staggered layers. Measured drift times are translated into drift circles, the tangent to which gives the reconstructed particle track.

When at least three drift tubes per module are hit by a crossing particle, its track can be unequivocally reconstructed by the tangent to the measured drift circles [161, 159]. With a single-tube track efficiency of  $\sim 90\%$ , for particles crossing a whole spectrometer a track reconstruction efficiency of  $> 98.5\%$  is attained. The total spatial resolution is better than  $600 \mu\text{m}$ , including geometrical misalignment [102].

In passing the spectrometer, charged particles are deflected by the OPERA magnet and will follow *S*-shaped paths (see Figure 4.25). Using the PT's high spatial resolution, the particles' charge and momenta can be inferred from the horizontal shift measured by the drift tubes. The momentum resolution is  $\Delta p/p \sim (20 - 25)\%$  for muon energies  $E_\mu \leq 30 \text{ GeV}$  [161].

<sup>1</sup>The drift time that the electrons need to reach the sense wire is translated to a drift circle radius which corresponds to distance of the crossing particle to the wire.

### 4.4.3 Veto System

To discriminate against CNGS beam-induced neutrino interactions upstream<sup>1</sup> of the OPERA target volume, two planes of glass RPC (GRPC) have been installed in front of the first detector SM [56].

A Veto plane consists of 32 GRPC that are arranged in eight rows of four chambers (measuring either  $2.60\text{ m} \times 1.14\text{ m}$  or  $2.40\text{ m} \times 1.14\text{ m}$ ). Each plane is equipped with 384 horizontal and 416 vertical copper readout strips of 2.5 cm width.

Contrary to the graphite-painted Bakelite electrodes of the OPERA spectrometer, the Veto system uses 3 mm-thick glass electrodes that are coated with metal oxide. As the RPC, they are operated in streamer mode [108], and the general design and readout are similar.

With a total area of  $10.04\text{ m} \times 9.23\text{ m}$ , the Veto covers the whole active detector in beam direction and reduces the number of false triggers for brick extraction.

The veto of external interactions is further supplemented by the TT planes of the two most upstream target walls of each SM, which due to the target mass reduction w.r.t. the experiment proposal (see Section 4.4.1) are not filled with bricks.

### 4.4.4 DAQ & Overall Event Trigger

The OPERA data acquisition (DAQ) system is based on 1 184 Ethernet Controller Mezzanines (ECMs) that provide a common interface for the various sub-detector front-end boards [131]. These small PCB collect the signals from more than 100 000 electronic channels of TT, RPC, XPC, Veto<sup>2</sup>, and PT<sup>3</sup> and transfer them to the global DAQ server via ethernet. As OPERA is a low-rate experiment<sup>4</sup>, a network connection of 100 MBit is sufficient.

The asynchronous readout of the sub-detectors necessitates a global timestamping at the level of the ECM which is provided by a dedicated 100 MHz clock distribution system.

Sensor data are grouped into one event until no further hits are received for 500 ns. Using a GPS link, the OPERA UTC timestamps are correlated with the SPS timestamps, and events are tagged as ONTIME with the neutrino beam if they occur within a window of  $\pm 20\text{ }\mu\text{s}$  (see Section 4.3.1).

The DAQ system runs continuously in triggerless mode. While TT and RPC are self-triggering, the PT receives its trigger signal from the RPC and XPC (see Section 4.4.2). A minimum bias filter, requiring at least 10 hits in the ED and the fulfillment of further quality criteria, is employed to reduce noise [91].

<sup>1</sup>I.e. in the rock and concrete surrounding LNGS Hall C, or the BOREXino detector and infrastructure.

<sup>2</sup>Employing analog-to-digital converters (ADCs).

<sup>3</sup>Using time-to-digital converters (TDCs).

<sup>4</sup>The overall data rate is dominated by cosmics and ambient radioactivity.

## 4.5 The OpRelease Software Framework

The `OpRelease` software framework is based on ROOT classes and written in C++ in a 64-bit architecture. It encompasses several official packages for event generation, detector simulation, and event reconstruction that will be briefly summarised in the following.

### 4.5.1 OpNegn

For the simulation of neutrino interactions in the detector, OPERA employs the NEGN event generator [51].

DIS interactions are described by a modified version of the LEPTO 6.1 generator, fragmentation is handled by JETSET 7.4. Sub-generators based on Llewellyn-Smith and Rein-Sehgal models are used for QE and RES processes. Nuclear re-interactions are simulated employing the DP-MJET II.4 generator FZIC code.

Originally developed for the NOMAD experiment (see Section 4.2.2), NEGN provides a complete kinematical simulation of  $\tau$  lepton production and decay, taking into account displaced secondary vertices and polarisation effects. It is thus suited for the generation of ECC event topologies and allows the introduction of kinematical cuts to determine detection efficiencies.

NEGN has been tuned using the large sample of neutrino interactions accumulated at NOMAD. For OPERA, it is adjusted for the CNGS beamline and graphite target, the slightly lower average neutrino energies, and the OPERA data format.

### 4.5.2 OpData & OpRData

The OPERA data structure is defined by two classes of similar structure with slight differences in object and function names [111]: `OpData` is a temporary format for processing by reconstruction and analysing algorithms, while the resistant `OpRData` is used for storage.

A `TreeManager` sub-package manages the data by reading and creating ROOT files of the OPERA format.

The data structure is identical for both simulated and real data, enabling the application of the same reconstruction and analysis algorithms. For MC-generated data, additional information on the simulation is saved in lists.

### 4.5.3 OpGeom

The OPERA geometry implementation is handled by the `OpGeom` package [72]. It is based on the ROOT `TGeoManager` geometry class and describes a full, idealised geometry of all detector parts, a map of the magnetic field, and major environment structures.

A box-shaped volume labelled `OPDY` contains the OPERA detector, including passive material and support structure. The cylindrical `WRLD` volume (measuring 400 m in length and 200 m in diameter) also encompasses the rock and concrete surrounding LNGS Hall C, as well as parts

of the BOREXino experiment. By selecting either OPERA mode (providing the OPDY volume) or FULL mode (WRLD volume), OpRelease programs can access the OpGeom description.

Materials and dimensions of detector components (such as PT drift tubes or TT scintillator strips) are defined in the OpDim sub-package. They are summarised to modules, the positions of which are saved in OpGeom.

The default OPERA coordinate system is Cartesian and right-handed with the  $Z$  axis pointing roughly into the direction of CNGS beam. The origin is near the center of the detector in LNGS Hall C (see Section 4.3, Figure 4.11).

A full 3D detector visualisation (see Chapter 5.3.2, Figure 5.5) inside the ROOT framework is offered by the sub-package OpDisplay.

#### 4.5.4 OpSim, OpDigit, OpEmuIO

The detector response is simulated using the OpSim, OpDigit, and OpEmuIO packages.

OpSim reproduces the particle propagation and generates *hits* in the various sub-detectors. It is based on the ROOT VMC and offers a choice of different transport generators<sup>1</sup>.

With OpDigit, the Electronic Detector response is simulated. The *digitisation* of signals uses parameterised response functions and detector efficiencies that are tuned to cosmic muon data [13]. The simulation includes electronic noise for the PT and crosstalk of the TT multi-channel PMT. Signal attenuation in cables and optical fibers is taken into account.

OpEmuIO simulates ECC data. It generates *micro tracks* in the nuclear emulsions, then applies smearing and the efficiencies of the OPERA scanning system.

#### 4.5.5 OpRec & OpEmuRec

The official reconstruction packages OpRec and OpEmuRec are used to process both simulated and real data.

OpRec performs the reconstruction of ED data, including ONTIME event tagging, crosstalk removal, ED track reconstruction, muon identification, and energy estimation.

After adjusting the perfect geometry implemented in OpGeom with real alignment files, 2D *track segments* are reconstructed from sub-detector digits. Those are connected to track elements in  $ZX$  and  $ZY$  projections and finally merged into *3D-tracks*. The highest-level output of the tracking algorithm is the result of a Kalman filter that provides the charge, momentum, vertex coordinates, and track slopes at the beginning of each 3D-track [66].

OpEmuRec is the package for emulsion data analysis [152]. It handles the reconstruction of micro tracks and their linking to *base tracks*, film alignment, vertex and shower reconstruction, and momentum estimation via MCS (see Section 4.6.3). Also providing sub-packages for simulating CS scanning and the automated ECC Scan Back procedure, OpEmuRec is used to estimate detection efficiencies for various neutrino interactions.

<sup>1</sup>I.e. GEANT 3.21 or GEANT 4 for ED simulation, and FLUKA for ECC bricks.

### 4.5.6 OpCarac

After reconstruction by `OpRec`, events are classified by the `OpCarac` package, assigning them one of the following tags [58]:

`CONTAINED` - Events with reconstructed neutrino interaction vertices inside the OPERA target.

`BORDERSOFTNC` - Low-energetic  $\nu_\mu$  NC-like interactions near the borders of the OPERA target.

`SPECTRO` - Interactions with tracks originating from one of the OPERA spectrometers.

`FRONTMUON / SIDEMUON` -  $\nu_\mu$  CC-like events with reconstructed vertices outside the OPERA active detector volume<sup>1</sup>.

`UNKOWNTYPE` - All events that cannot be classified due to insufficient data.

### 4.5.7 OpBrickFinder

Using the BMM database information (see Section 4.4.1), the `OpBrickFinder` package is employed to identify the most probable brick for each `CONTAINED` neutrino interaction [74].

Following an artificial neural network (ANN) approach, the algorithm takes into account ED reconstructed tracks and hadronic shower parameters. The resulting probability map lists the probability for each ECC brick to contain the respective interaction vertex, providing the basis for subsequent brick extraction and analysis.

---

<sup>1</sup>These are mainly muons entering from the front or sides that were created in CNGS  $\nu_\mu$  interactions in the upstream rock or BOREXino experiment.

## 4.6 Event Reconstruction in OPERA

Due to the hybrid structure of the detector, event reconstruction in OPERA is subdivided into separate procedures for the Electronic Detector and Emulsion Cloud Chamber bricks [13, 11]. The general analysis scheme is outlined in the following, while more details on the  $\nu_\tau$  search procedure will be given in Section 4.7.2.

### 4.6.1 Electronic Detector Event Reconstruction

The reconstruction of a  $\nu_\mu$  CC interaction in the Electronic Detector of OPERA is shown in Figure 4.29, easily identified by the long muon track passing both spectrometers.

Particle charge and momentum are inferred from the deflection inside the OPERA spectrometers, measured in  $ZX$  projection by the Precision Tracker drift tubes. The hadronic energy deposition in the first target area indicates where the neutrino interaction took place, and the OpCarac package characterises this event as CONTAINED. A coarse calorimetric measurement of the hadronic shower energy is conducted by the Target Tracker (see Chapter 5.4.1).

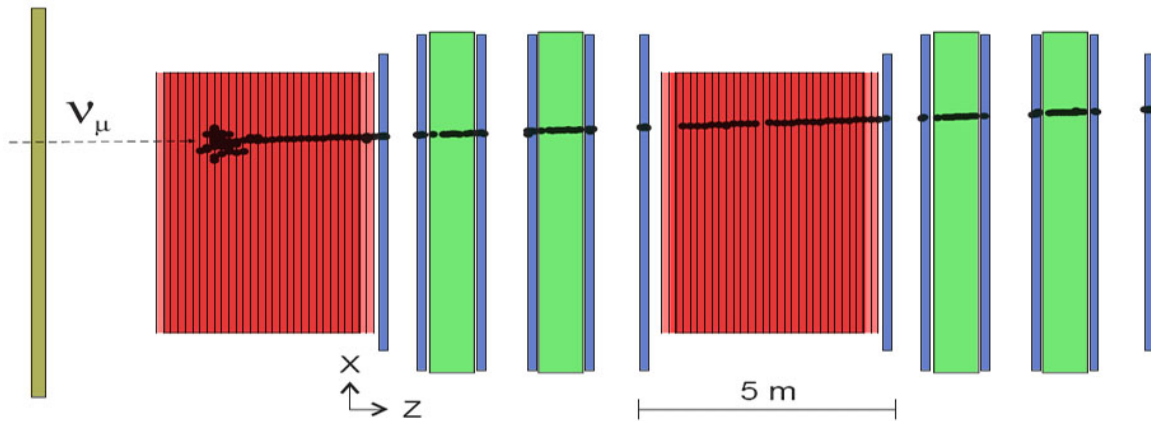


**Figure 4.29:** ED reconstruction of a CONTAINED CNGS  $\nu_\mu$  event in  $ZX$  projection (top view) [6]. The  $\nu_\mu$  CC interaction occurs in the target of the 1st OPERA SM. Hadronic products create a cluster of deposited energy in the TT, while the long track of the charged muon crosses both spectrometers. The Veto system does not register any signal.

With a time resolution  $\mathcal{O}(\text{ns})$ , the real-time ED reconstruction timestamps detector interactions and performs an ONTIME tagging of events occurring in sync with the CNGS beam.

The overall trigger efficiency for  $\nu_\tau$  CC interactions in the OPERA ED is better than 98%.

### 4.6.2 Electronic Detector - Emulsion Cloud Chamber Interface

The interface between the online ED readout and offline ECC analysis is provided by the Brick Finding (BF) algorithm and subsequent analysis of Changeable Sheets. The implementation minimises detector target mass loss and emulsion scanning load.

## Brick Finding

After the tagging of CONTAINED events by the OpCarac algorithm, the OpBrickFinder package performs a filtering of the reconstructed data [74]. Isolated hits that cannot be associated with any track are removed by a cellular automaton (CA) approach.

For  $1\mu$  ( $\nu_\mu$  CC-like) events, the prediction of the brick containing the neutrino interaction, as well as track slopes and positions in the CS is straightforward. Pattern recognition for high-energy muons is done via linear Hough transform, while lower-energy tracks are reconstructed using a tracing algorithm. The alignment between TT walls and brick positions is performed by analysing a sample of  $\sim 700$  reconstructed tracks of crossing muons and accordingly correcting the brick coordinates from the BMM database.

In the case of  $0\mu$  ( $\nu_\mu$  NC-like) events, there are no tracks in the ED that clearly point to the interaction vertex. By means of a modified least squares method (LSM) which employs line fitting and takes into account outliers and non-Gaussian errors, the hadronic shower axis is estimated (see Figure 4.30).

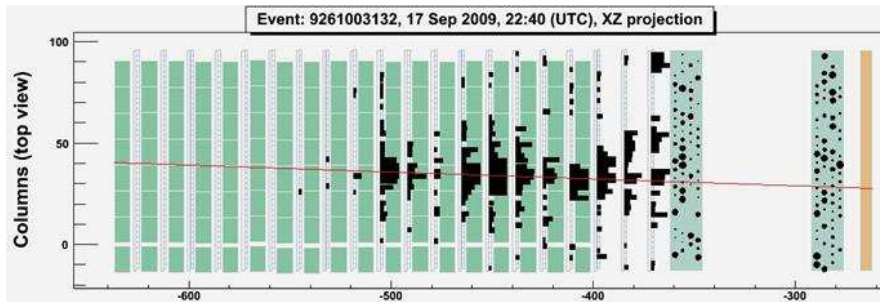


**Figure 4.30:** Reconstruction of the hadronic shower axis for an interaction occurring in the first SM of the OPERA ED using a modified LSM [74].

The determination of the target wall containing the neutrino interaction may be complicated by back-scattered particles. An ANN with Multi-Layer Perceptron (MLP) architecture trained on simulated data is used to estimate the probabilities for the three target walls most likely to contain the primary event vertex. The per-brick probability is then given by an integral of the PDF over the brick volume.

The attained Brick Finding efficiencies for  $\nu_\mu$  CC and NC events are estimated using a MC simulation. They are listed in Table 4.5, taking into account the four most probable bricks.

**Table 4.5:** Brick Finding efficiencies for  $\nu_\mu$  CC and  $\nu_\mu$  NC events, estimated via MC [74].

Number of extr. bricks	$\epsilon_{BF}^{CC}$ [%]	$\epsilon_{BF}^{NC}$ [%]	$\epsilon_{BF}^{total}$ [%]
1 brick	77.5	58.5	71.4
2 bricks	91.3	75.4	88.0
3 bricks	94.8	82.3	92.2
4 bricks	96.7	86.1	94.4



### Changeable Sheet Analysis

Following the Brick Finding procedure, the ECC brick most likely to contain a neutrino interaction is extracted from the OPERA target using the Brick Manipulator System [11].

Before the Changeable Sheet is detached from its downstream side, the brick is placed in an X-ray system to print marks at the four corners of the sheets [40]. With these, the CS can later be aligned between themselves, and to the emulsions of the brick<sup>1</sup>.

While the ECC brick is temporarily kept in a shielded area, its CS are developed underground. Using automated scanning microscopes (see Section 4.6.3), they are searched for tracks matching the predictions from the ED. In the case of  $1\mu$  events, a region of  $6\text{ cm} \times 4\text{ cm}$  around the predicted tracks is scanned<sup>2</sup>, while  $0\mu$  events require an increased area  $8\text{ cm} \times 6\text{ cm}$ . All micro-tracks (MTs), i.e. 3D sequences of grains found via combination of clusters at different depth in a single emulsion layer (see Figure 4.31a), within the scanned area are automatically reconstructed. Matching MTs in the top and bottom layer of an emulsion sheet are combined to base-tracks (BTs) (see Figure 4.31b), and coinciding BTs in both CS emulsion sheets form a double BT [152]. Combinations of matching BTs with a single MT are reconstructed as 3/4-tracks to recover inefficiencies of the MT reconstruction.

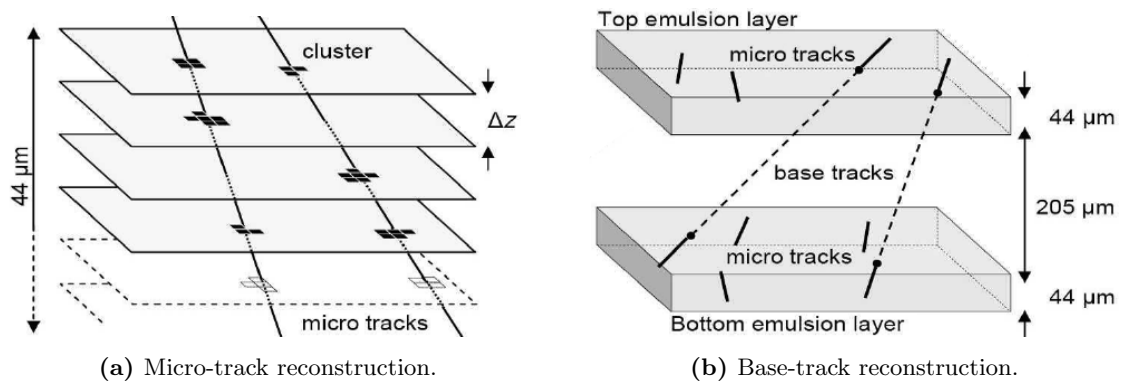


**Figure 4.31:** OPERA nuclear emulsion track reconstruction [83]. (a) Combination of grain clusters at different depth in a single emulsion layer to micro-tracks. (b) Matching of micro-tracks in both layers of an emulsion sheet to base-tracks.

If the indication for the brick to contain the respective neutrino interaction cannot be validated by tracks matching the TT predictions, a second (then third, and forth) brick will be extracted and analysed, following the probability map provided by the BF algorithm. To minimise target mass loss, bricks with negative CS analysis results are equipped with new CS and reinserted into the detector.

The efficiency of the CS validation procedure strongly depends on the type of neutrino interaction and topology. For  $\nu_\tau$  CC interactions, it ranges from  $\sim 37\%$  (QE interactions with  $\tau \rightarrow e$  long decays) to  $> 95\%$  (DIS interactions with  $\tau \rightarrow 3h$  decays) [83].

<sup>1</sup>The X-ray marks only provide a coarse alignment of  $\mathcal{O}(10\mu\text{m})$  precision. The subsequent micrometric alignment between the emulsion sheets is performed using low-energetic electrons from radioactive isotopes contained in the nuclear emulsions [40].

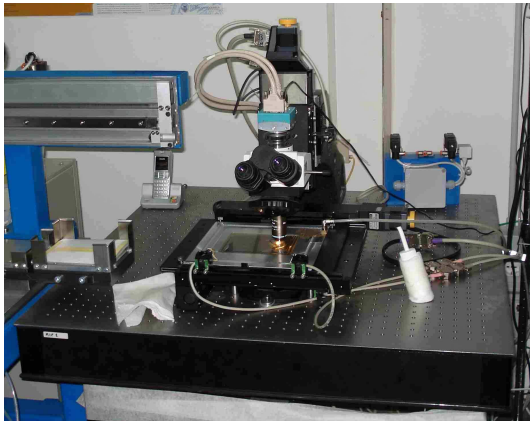
<sup>2</sup>During exposure inside the OPERA detector, the vertical alignment of the bricks is guaranteed by the rails they are loaded on, while the horizontal positioning is less accurate.

### 4.6.3 Emulsion Cloud Chamber Event Reconstruction

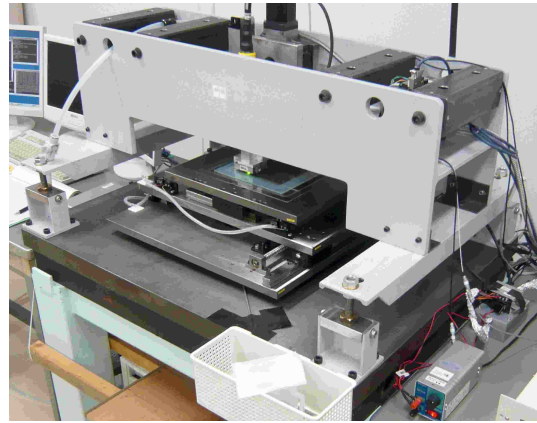
After a neutrino interaction has been validated by the analysis of the CS, a second X-ray exposure of the respective brick is conducted, creating lateral reference marks on all of its sheets [11]. It is subsequently placed within a specifically designed muon pit and exposed for 12 hours to cosmic rays, accumulating  $\sim 1$  through-going track/mm which can later be used for sub-micrometric film-to-film alignment. The brick is afterwards disassembled, and its emulsion films are developed and shipped to scanning laboratories in Europe or Japan.

#### Automatic Scanning Systems

Though employing different strategies concerning hardware implementation and software architecture, the European and Japanese scanning systems (shown in Figure 4.32) provide comparable performance.



(a) European scanning system (ESS).



(b) Japanese scanning system (S-UTS).

**Figure 4.32:** European and Japanese scanning Systems [11]. (a) The ESS uses a moving stage and stop-and-go approach to take images with a CMOS camera. (b) In the S-UTS, stage and CCD camera move in sync.

The European Scanning System (ESS) consists of a software-based framework and commercial parts that can be easily updated with more performant components [148, 46, 124]. It uses a horizontally moving stage ( $XY$  plane) and a CMOS megapixel camera that takes images at different focal depth by moving in  $Z$  in a stop-and-go approach. Micro-tracks are reconstructed by the workstation CPU.

In the Japanese Super-Ultra Track Selector (S-UTS) system, both stage and objective lens move at the same constant speed in  $X$  and  $Y$ , preventing the mechanical bottleneck of the stop-and-go approach [136]. It employs a fast CCD camera and uses a dedicated processing board for micro-track reconstruction.

Both fully automatic microscope systems provide a scanning speed of  $20 \text{ cm}^2/\text{h}/\text{layer}$ , enabling the analysis of the  $\sim 200 \text{ cm}^2$  emulsion area required to be scanned per event in OPERA. New developments in hardware and programming give rise to a steady increase in scanning speed [160].

### Emulsion Cloud Chamber Track Reconstruction

Starting from the most downstream emulsion sheet of the ECC brick, an automatic Scan Back (SB) procedure is performed on base-tracks compatible with predictions from the CS [11]. Found tracks are followed upstream plate-by-plate until the position of the presumed interaction vertex is reached, around which a Volume Scan (VS) of  $\sim 1 \text{ cm}^3$  is performed (see Section 4.7.2).

Figure 4.33a shows the base-tracks found by the Volume Scan of a neutrino interaction in the OPERA ECC. Through-going tracks from cosmic muons or external interactions are rejected (Figure 4.33b), and the final vertex reconstruction can be seen in Figure 4.33c.

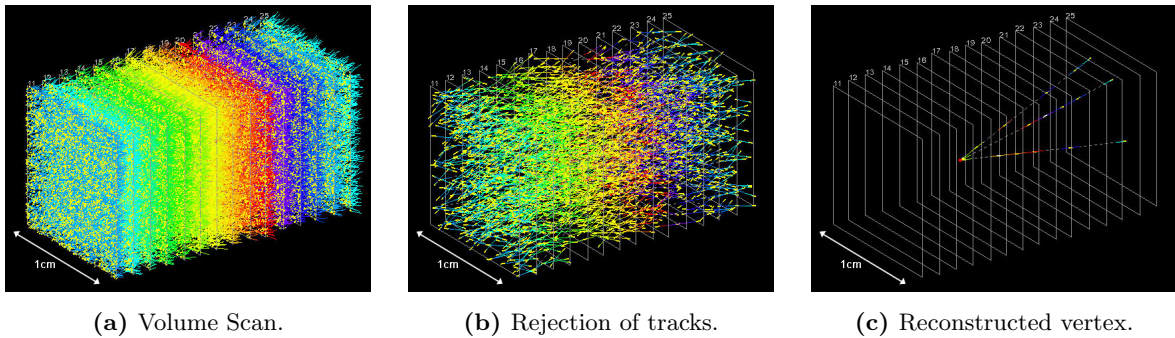


**Figure 4.33:** ECC reconstruction of a neutrino interaction in OPERA. **(a)** All base-tracks found in the VS. **(b)** Through-going muon tracks have been rejected. **(c)** Final vertex reconstruction.

Following Volume Scan and vertex location, the  $\tau$  Decay Search (DS) is conducted. This encompasses the search for kinks and possible extra tracks or parent particles and will be described in more detail in the following section.

A full kinematical analysis is afterwards performed for  $\nu_\tau$  candidate events.

## 4.7 $\nu_\mu \rightarrow \nu_\tau$ Appearance Search

The main goal of the OPERA experiment is the detection of  $\nu_\mu \rightarrow \nu_\tau$  oscillations via the appearance of  $\tau$  neutrinos in the nearly-pure CNGS  $\nu_\mu$  beam.

### 4.7.1 General Event Topology

$\nu_\tau$  CC interactions with target nucleons  $N$  will result in the production of  $\tau$  leptons, together with other leptonic and hadronic products  $X$ :

$$\nu_\tau + N \rightarrow \tau^- + X. \quad (4.3)$$

With a mean life of  $(290.3 \pm 0.5) \times 10^{-15}$  s [138], at OPERA energies the  $\tau$  leptons will decay after a distance of several  $100 \mu\text{m}$  under virtual  $W^-$  boson emission. These virtual  $W^-$  will then decay into a charged lepton and its corresponding anti-neutrino or pairs of  $\bar{u}/d$ -like quarks [91]. The resulting most important  $\tau$  decay modes (classified by the decay daughters as *electronic*, *muonic* or *hadronic*) and their respective branching ratios (BRs) are listed in Table 4.6.

**Table 4.6:** Most important  $\tau$  decay modes and BR [138]. The hadronic final states are dominated by the production of single  $\pi^-$  and the intermediate resonances  $\rho^-(770) \rightarrow \pi^- \pi^0$ ,  $a_1^-(1260) \rightarrow \pi^- 2\pi^0$ ,  $a_1^-(1260) \rightarrow 2\pi^- \pi^+$ .

	Decay mode	Branching ratio [%]
Electronic	$\tau^- \rightarrow e^- + \bar{\nu}_e + \nu_\tau$	$17.83 \pm 0.04$
Muonic	$\tau^- \rightarrow \mu^- + \bar{\nu}_\mu + \nu_\tau$	$17.41 \pm 0.04$
Hadronic (1-prong)	$\tau^- \rightarrow h^- + X^0 + \nu_\tau$	$52.30 \pm 0.19$
$\pi^-$	$\tau^- \rightarrow \pi^- + \nu_\tau$	$10.83 \pm 0.06$
$\rho^-$	$\tau^- \rightarrow \pi^- + \pi^0 + \nu_\tau$	$25.52 \pm 0.09$
$a_1^-$	$\tau^- \rightarrow \pi^- + 2\pi^0 + \nu_\tau$	$9.30 \pm 0.11$
Hadronic (3-prong)	$\tau^- \rightarrow 2h^- + h^+ + X^0 + \nu_\tau$	$12.34 \pm 0.11$
$a_1^-$	$\tau^- \rightarrow 2\pi^- + \pi^+ + \nu_\tau$	$8.99 \pm 0.06$
	$\tau^- \rightarrow 2\pi^- + \pi^+ + \pi^0 + \nu_\tau$	$2.70 \pm 0.08$

While different kinematical cuts have to be defined to identify the respective decay channel (see Section 4.7.4), the shared signature is a characteristic *kink* topology marking the decay of the  $\tau$  lepton. Due to the OPERA target ECC structure, the event reconstruction has to discriminate between  $\tau$  *long decays* and  $\tau$  *short decays*, see Figure 4.34.

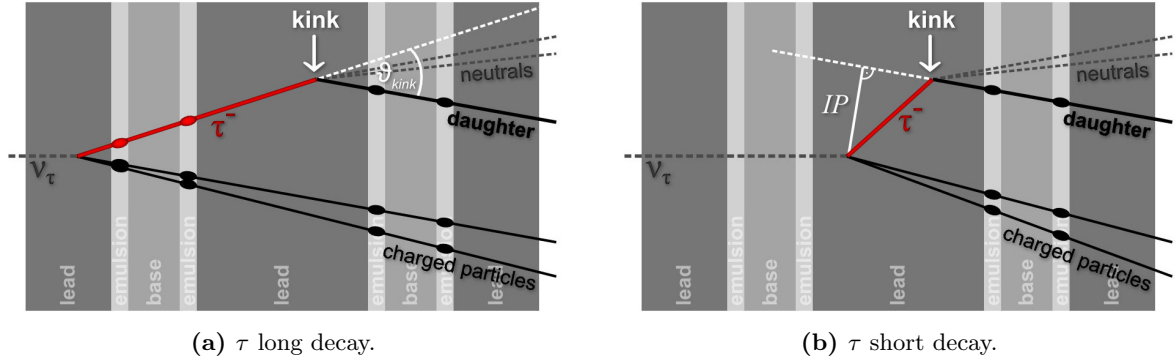


**Figure 4.34:**  $\tau$  decay topologies. For  $\tau$  long decays (a) the kink angle  $\theta_{kink}$  is measured, for  $\tau$  short decays (b) the impact parameter  $IP$  is used.

In  $\tau$  long decays (Figure 4.34a), the  $\tau$  lepton decays in the Pb plate downstream of the plate where the primary  $\nu_\tau$  CC interaction took place. The  $\tau$  lepton track is reconstructed in the nuclear emulsions, as is the daughter particle track, thus exhibiting a visible kink whose angle  $\theta_{kink}$  can be measured.

If the  $\tau$  lepton decays inside the same Pb plate it was produced in, no primary  $\tau$  track can be reconstructed inside the emulsions, and no kink angle will be visible (Figure 4.34b). In such short decays, the decay daughter track will however exhibit a measurable impact parameter  $IP$  w.r.t. the primary neutrino interaction, indicating that it originated from a secondary vertex.

About 46% of the  $\tau$  decays registered in the OPERA emulsions are expected to be short decays [15]. Due to strong kinematical cuts for BG rejection, the general kink detection efficiency is lower than for  $\tau$  long decays. In  $\nu_\tau$  CC QE interactions where no charged particles other than the  $\tau$  lepton are produced at the primary vertex,  $\tau$  short decays cannot be observed at all.

### 4.7.2 Standard Analysis Chain

The analysis procedure and kinematical cuts for the  $\nu_\mu \rightarrow \nu_\tau$  oscillation search in OPERA were already defined at the time of the experiment proposal [107].

#### Electronic Detector Trigger

The standard analysis chain for  $\nu_\tau$  candidate events starts with the Electronic Detector (ED) classification of CONTAINED or BORDERSOFTNC CNGS ONTIME events as either  $1\mu$  or  $0\mu$  events: If a 3D-track with a length  $\times$  density value of  $> 660 \text{ g/cm}^2$  is reconstructed in the ED or at least 20 planes of TT and RPC are hit, the event is tagged as  $1\mu$  ( $\nu_\mu$  CC-like), otherwise as  $0\mu$  ( $\nu_\mu$  NC-like) [15]. The  $\tau$  decay search procedure is then applied to

$$0\mu \text{ events} \quad \text{and} \quad (4.4)$$

$$1\mu \text{ events} \quad \text{with} \quad p_\mu < 15 \text{ GeV}/c, \quad (4.5)$$

with  $p_\mu$  being the momentum of the longest reconstructed 3D-track.

The BF algorithm provides a probability map for the bricks most likely to contain the neutrino interaction. Furthermore, a prediction is made for slope and position in the CSs of the candidate muon track in  $1\mu$  events, or the hadronic shower center in  $0\mu$  events.

### Changeable Sheet Validation

Starting with the most probable brick, up to 4 ECC bricks are extracted from the detector in search for the primary neutrino interaction. After development of the Changeable Sheets (CSs), for

$$0\mu \text{ events} \quad \text{an area of } 8 \times 6 \text{ cm}^2 \text{ around the hadronic shower center, and for} \quad (4.6)$$

$$1\mu \text{ events} \quad \text{an area of } 4 \times 3 \text{ cm}^2 \text{ around the muon prediction} \quad (4.7)$$

is scanned [83]. The double base-tracks (BTs) and 3/4-tracks (see Section 4.6.2) reconstructed within the scanned area are then compared to the ED prediction. If in

$$0\mu \text{ events} \quad \text{a track compatible with an isolated ED 3D-track, or in} \quad (4.8)$$

$$1\mu \text{ events} \quad \text{the muon candidate track, or} \quad (4.9)$$

a pattern of at least two converging tracks is found, the event is validated [15].

### ECC Track Scan Back

After successful CS validation, the corresponding ECC brick is developed and scanned. BT compatible with the tracks found during CS validation are searched for in the most downstream emulsion sheet and followed plate-by-plate upstream until they cannot be detected in three consecutive emulsion sheets. The Pb plate upstream of the most upstream emulsion sheet where a Scan Back (SB) track could be found is then defined as the vertex plate.

### ECC Volume Scan and Vertex Location

After track SB, a Volume Scan (VS) is performed: An area of  $1 \times 1 \text{ cm}^2$ , centered in  $x$  and  $y$  on the predicted neutrino interaction vertex position, is scanned in 5 emulsion sheets upstream and 10 emulsion sheets downstream of the vertex Pb plate [15], thus corresponding to a distance in  $z$  of 19.5 mm. The most upstream emulsion sheet is then used as a veto for passing-through tracks.

If the scanned volume is large enough to contain the decay topology, i.e. if the vertex plate is at least three emulsion sheets upstream from the downstream end of the ECC brick, the event is *located*, and the Decay Search (DS) will be performed.

### Decay Search Procedure

To improve the resolution on the primary neutrino interaction vertex, a visual inspection of the emulsion film downstream of the Pb vertex plate is conducted. Thus, missing track segments may be recovered, and  $e^+e^-$  pairs as well as low-momentum particles can be identified and removed [15].

In the Decay Search (DS) procedure, reconstructed tracks with large  $IP > 10 \mu\text{m}$  w.r.t. the primary vertex are then studied, looking for possible decays.

An extra-track search aims to find tracks that have already been reconstructed in the VS but, due to larger  $IP$ , were not associated with the primary vertex. This is followed by the parent search, where tracks connecting the extra-track to the primary vertex are searched for.

Finally, an in-track DS is performed, studying the tracks originating from the primary vertex for small kinks occurring within the 4 emulsion films downstream of the vertex Pb plate. In  $1\mu$  events, only the muon candidate track is examined.

### Track Follow-Down & Kinematical Analysis

Once a decay topology has been confirmed, a high-resolution scanning that may follow primary tracks also into neighboring bricks, called Track Follow-Down (TFD), is conducted. The subsequent full kinematical analysis of all involved particle tracks allows to discriminate against the various BGs [15].

#### 4.7.3 Backgrounds

A possible contamination of the  $\nu_\mu$  beam with prompt  $\tau$  neutrinos might constitute a general BG to the oscillation search, as does the decay of charmed particles. Furthermore, depending on the respective  $\tau$  decay mode (see Table 4.6), other interactions may mimick the expected topologies:  $e^\pm$  scattering or electronic decay of  $\pi^0$ , the large-angle scattering of  $\mu^\pm$ , or hadronic re-interactions.

W.r.t. the experiment proposal [107], the knowledge of several of these BGs has greatly improved.

#### Prompt $\nu_\tau$ Background (All $\tau$ Decay Modes)

A prompt contamination of  $\tau$  neutrinos in the CNGS  $\nu_\mu$  beam may arise from the decay of  $D_s^\pm$  mesons.

For the CHORUS and NOMAD experiments in the CERN wide-band WANF neutrino beam, this background has been estimated in [156, 103]. Scaling from the WANF Be target to the CNGS graphite target and taking into account the differences in proton energy and beam geometry, the rate of prompt  $\nu_\tau$  interactions per  $\nu_\mu$  CC interaction is expected to be

$$f_{\nu_\tau}^{\text{prompt}} = \mathcal{O}(10^{-6}) \times \nu_\mu^{\text{CC}} \quad (4.10)$$

in the OPERA experiment [107]. Furthermore given the low  $\tau$  detection efficiency, the prompt  $\nu_\tau$  BG becomes completely negligible for all  $\tau$  decay channels..

### Charmed Particle Decays (All $\tau$ Decay Modes)

With masses and lifetimes comparable to those of the  $\tau$  lepton, the decay of charmed hadrons created in  $\nu_\mu$  CC DIS interactions with nuclei in the OPERA target (see Chapter 2.3.3) is a major BG for all  $\tau$  decay channels. Table 4.7 lists charm production processes in OPERA.

**Table 4.7:**  $\nu_\mu$  interactions resulting in charmed hadrons.  $N$  denotes the target nucleus,  $c$  ( $\bar{c}$ ) are the charm (anti-charm) quarks,  $X$  is the system of outgoing hadrons.

		Decay mode
Single-charm production	(CC)	$\nu_\mu + N \rightarrow \mu^- + c + X$
Associated charm production	(CC)	$\nu_\mu + N \rightarrow \mu^- + c + \bar{c} + X$
Associated charm production	(NC)	$\nu_\mu + N \rightarrow \nu_\mu + c + \bar{c} + X$

The total single-charm production rate in OPERA, relative to the  $\nu_\mu$ CC interaction rate, is

$$f_{charm} = (4.49 \pm 0.26) \times 10^{-2} \times \nu_\mu^{CC}, \quad (4.11)$$

using the hadronic fractions  $f_{D^0} = (43.8 \pm 3.0)\%$ ,  $f_{D^+} = (21.7 \pm 3.4)\%$ ,  $f_{D_s^+} = (9.2 \pm 3.8)\%$ ,  $f_{\Lambda_c^+} = (25.3 \pm 4.9)\%$  for the creation of  $D^0$ ,  $D^+$ ,  $D_s^+$  mesons and  $\Lambda_c^+$  [19, 116]. The associated production rates of  $c\bar{c}$  pairs (via boson-gluon fusion or bremsstrahlung), resulting in two charmed hadrons in the final state, are more than one order of magnitude lower than the single-charm production rate [91].

Figure 4.35 shows the ECC reconstruction of a  $D^0$  candidate event in OPERA.

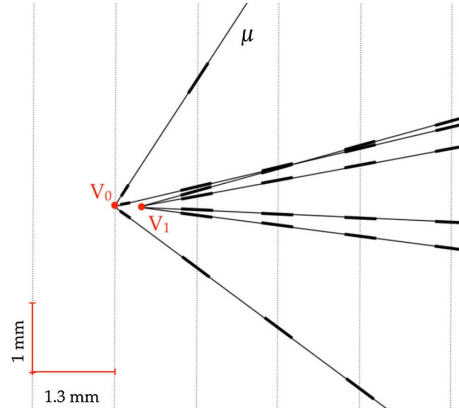


**Figure 4.35:** ECC reconstruction of a charm candidate event:  $\nu_\mu$  CC interaction at the primary vertex and a 4-prong decay at the secondary vertex after a distance of  $310 \mu\text{m}$  [19]. With  $m_{inv} \geq (1.7 \pm 0.4) \text{ GeV}/c^2$ , the invariant mass is consistent with that of a  $D^0$  meson,  $m_{D^0} = (1864.84 \pm 0.07) \text{ MeV}/c^2$  [138].

If the primary  $\mu^-$  (single-charm production) or one of the two charmed hadrons (associated charm production) remains undetected, charmed particle reactions may constitute a BG for the  $\nu_\tau$  search.

Due to CP conservation, the hadrons created in single-charm production will predominantly decay into muons of positive sign [138]. Given the charge-reconstruction performance of the OPERA spectrometer (see Section 4.4.2), the muonic  $\tau^-$  decay channel is thus less affected by charm BG.



As the topologies and decay lengths of charmed hadrons are very similar to those of the  $\tau$  lepton, these interactions can also be used for checking the detector's performance and validating the analysis chain for  $\nu_\tau$  detection. In [19], this was done using the 2008 – 2010 CNGS beam data of 2925 fully analysed events: 50 charm decay candidates are observed, at an expectation of  $54 \pm 4$  events (including BG). Table 4.8 lists the numbers for different topologies.

**Table 4.8:** Comparison of expected and observed charm event numbers for various topologies (possible migration in-between taken into account) for the 2008 – 2010 data sample [19]. The expected charm event numbers were calculated using the default OPERA neutrino interaction generator NEGN with the FLUKA simulation of the CNGS beam tuned to CHORUS data [116].

Topology	Expected events			Observed events
	charm	BG	total	
1-prong	21 $\pm$ 2	9 $\pm$ 3	30 $\pm$ 4	19
2-prong	14 $\pm$ 1	4 $\pm$ 1	18 $\pm$ 1	22
3-prong	4 $\pm$ 1	1.0 $\pm$ 0.3	5 $\pm$ 1	5
4-prong	0.9 $\pm$ 0.2	-	0.9 $\pm$ 0.2	4
Total	40 $\pm$ 3	14 $\pm$ 3	54 $\pm$ 4	50

### Prompt $\nu_e$ , Pion Charge Exchange, $\gamma$ Conversion ( $\tau \rightarrow e$ )

CC interactions of prompt  $\nu_e$  ( $\bar{\nu}_e$ ) from the CNGS beam contamination will result in  $e^\pm$ . The scattering of these particles might then mimic the electronic decay of a  $\tau$  lepton. However, a full MC simulation showed the kinematical cuts for the  $\tau \rightarrow e$  channel to very efficiently remove such events [107].

Taking into account a combined beam contamination of  $\nu_e$  and  $\bar{\nu}_e$  below 1%, the BG from prompt  $\nu_e + \bar{\nu}_e$ , relative to the  $\nu_\mu$  CC interaction rate, can safely be assumed as

$$f_{\nu_e \bar{\nu}_e}^{prompt} < 1.0 \times 10^{-6} \times \nu_\mu^{CC}. \quad (4.12)$$

A further  $\nu_\mu$  NC BG to the  $\tau \rightarrow e$  channel arises from  $\pi^0$  created in RES interactions (see Chapter 2.3.2) or  $\pi^-$  that undergo charge exchange ( $\pi^- + p^+ \rightarrow \pi^0 + n$ ). The subsequent decay of the  $\pi^0$  into a  $\gamma e^+ e^-$  Dalitz pair (or  $2\gamma$  creating  $e^+ e^-$  pairs) may then be mistaken for an electronic  $\tau$  decay, resulting in an expected BG rate of

$$f_{\pi^0} \sim 0.2 \times 10^{-6} \times \nu_\mu^{CC}. \quad (4.13)$$

The conversion of  $\gamma$  produced at the primary interaction vertex to  $e^+ e^-$  pairs gives an additional BG of

$$f_\gamma \sim 0.1 \times 10^{-6} \times \nu_\mu^{CC}. \quad (4.14)$$

Altogether, compared to the BG from charmed particle decays (see above), the contributions to the  $\tau \rightarrow e$  channel from prompt  $\nu_e$  ( $\bar{\nu}_e$ ), pion charge exchange, or  $\gamma$  conversion are negligible [15].

### Large-Angle $\mu$ Scattering ( $\tau \rightarrow \mu$ )

$\mu^-$  produced in  $\nu_\mu$  CC reactions and scattering in the lead plate downstream of the interaction vertex may be mistaken for muonic  $\tau$  decays.

In [127], the large-angle MCS of muons with energies  $\mathcal{O}(10 \text{ GeV})$  is studied, comparing theoretical calculations, simulation, and experimental data. Using a mixed approach based on GEANT 4 libraries [23, 30] and a realistic Woods-Saxon nuclear charge density, the scattering of muons in targets of 1 mm lead was simulated. This new implementation achieves far better reproduction of the available experimental data - the scattering of 7.3 GeV and 11.7 GeV  $\mu^-$  on Cu [29], 2 GeV  $\mu^-$  on C and Pb [132], and 502 MeV  $e^-$  on Pb [97] - than older simulations. Taking into account the kinematical selection cuts for the muonic  $\tau$  decay channel (see Table 4.10), the BG from large-angle MCS of muons is conservatively estimated as

$$f_{\mu\text{Pb}}^{LAS} = (1.2 \pm 0.1) \times 10^{-7} \times \nu_\mu^{CC}, \quad (4.15)$$

relative to the  $\nu_\mu$  CC interaction rate, with detection efficiencies not yet taken into account. While muon photo-nuclear interactions with high energy transfer may give an additional contribution of

$$f_{\mu N}^\gamma < 2.7 \times 10^{-7} \times \nu_\mu^{CC}, \quad (4.16)$$

the BG arising from hard muon bremsstrahlung can even more efficiently be discriminated in the emulsions.

### Hadronic Re-Interactions ( $\tau \rightarrow h$ )

The 1-prong and 3-prong hadronic  $\tau$  decay channels are subject to further BG from hadronic re-interactions: Primary hadrons created in  $\nu_\mu$  NC interactions (or  $\nu_\mu$  CC interactions with undetected primary  $\mu^-$ ) may scatter off Pb nuclei, thus mimicking  $\tau \rightarrow 1h$  or  $\tau \rightarrow 3h$  decays.

The kinematical cuts for the hadronic  $\tau$  decay channels strongly reduce this BG. By requiring the absence of nuclear fragments or m.i.p.s pointing to the secondary vertex, it is further lowered by about 30%.

Using a FLUKA-based MC simulation including event reconstruction up to the location level, the remaining BG rate from hadronic re-interactions is expected to be

$$f_{re-int}^{1h} = (3.9 \pm 0.2) \times 10^{-5} \times N_{0\mu}^{loc} \quad (4.17)$$

per located  $0\mu$  event for the  $\tau \rightarrow h$  channel and

$$f_{re-int}^{3h} = (1.5 \pm 0.2) \times 10^{-5} \times N_{0\mu}^{loc}, \quad (4.18)$$

for  $\tau \rightarrow 3h$  decays [15]. The associated decay search efficiencies are assumed to be similar to those of real  $\nu_\tau$  events [83]. A dedicated study using test beams of 2, 4, and 10 GeV hadrons shows the simulation to be consistent with the measurements at the level of 30% [114].

#### 4.7.4 Decay Channels & Kinematical Cuts

To reduce the BGs mentioned in Section 4.7.3, various kinematical cuts have been defined, optimising the signal-over-noise ratio of the respective  $\tau$  decay channel for a quasi BG-free analysis.

Of these, the kink angle  $\theta_{kink}$  and the decay length  $z_{dec}$  (the distance in  $z$  between the downstream edge of the primary vertex Pb plate and the secondary vertex), are the most important, defining the general *kink* topology of all  $\nu_\tau$  events. For  $\tau$  long decay candidate events, it is required that

$$\theta_{kink} > 20 \text{ mrad} \quad (4.19)$$

and

$$44 \mu\text{m} < z_{dec} < 2600 \mu\text{m}, \quad (4.20)$$

the latter implying the decay vertex to lie within the two Pb plates downstream of the primary neutrino interaction vertex. If the kink angle is not directly accessible, as in  $\tau$  short decays, an impact parameter  $IP$  is measured instead.

Further kinematical cuts are defined on the momenta of the secondary particles -  $p^e$  and  $p^\mu$  for the electronic and muonic  $\tau$  decay channels, and  $p^{2ry}$  for the (scalar sum of) momenta in 1-prong or 3-prong hadronic  $\tau$  decays. The total transverse momentum of the secondary particles  $p_T^{2ry}$  plays another important role, as do the missing transverse momentum at the primary vertex  $p_T^{miss}$  and the transverse angle between  $\tau$  candidate track and hadronic shower  $\Delta\phi_{\tau h}$ . The kinematical cuts for the above-mentioned parameters have already been defined at the time of the experiment proposal [107]. For the  $\tau \rightarrow 3h$  channel, additional limits on the invariant mass of the daughter particles  $m^{inv}$  and the minimum invariant mass  $m_{min}^{inv}$  need to be considered [15].

In the following, the kinematical parameters and cut values for the respective  $\tau$  decay mode will be listed, along with the detected  $\nu_\tau$  candidate events and their measured parameter values.

##### Electronic $\tau$ Decays

The kinematical cuts predefined for the electronic  $\tau$  decay channel are listed in Table 4.9. A lower cut of  $p_T^{2ry} > 100 \text{ MeV}/c$  on the total transverse momentum of the secondary particles very efficiently reduces the BG from prompt  $\nu_e$  CC events, as does the upper limit of  $p^e < 15.0 \text{ GeV}/c$  on the electron candidate momentum. Low-energy  $e^+e^-$  pairs from  $\gamma$  conversion are removed by a lower cut of  $p^e > 1.0 \text{ GeV}/c$  [107].

No  $\tau \rightarrow e$  candidate events have been found in the analysed data sample.

**Table 4.9:** Kinematical cuts applied to the  $\tau \rightarrow e$  decay channel [15, 107]. No candidate events have been found in this decay mode.

	$\theta_{kink}$ [mrad]	$z_{dec}$ [ $\mu\text{m}$ ]	$p^e$ [GeV/c]	$p_T^{2ry}$ [MeV/c]
Selection cut	> 20	> 2600	[1.0, 15.0]	> 100

### Muonic $\tau$ Decays

Table 4.10 lists the kinematical cuts for the  $\tau \rightarrow \mu$  decay channel, in comparison to the measured values of the muonic  $\tau$  decay candidate event that was reported in [17].

The upper limit of  $p^\mu < 15.0 \text{ GeV}/c$  on the muon candidate momentum removes a large amount of BG from  $\nu_\mu$  CC interactions, while the lower cut of  $p^\mu > 1.0 \text{ GeV}/c$  ensures good muon identification and rejection of low-energy hadrons [107]. The lower cut on  $p_T^{2ry} > 250 \text{ MeV}/c$  very efficiently discriminates against the BG from large-angle scattering of muons [127].

**Table 4.10:** Kinematical cuts applied to the  $\tau \rightarrow \mu$  decay channel [15, 107] and measured parameter values for the 3rd  $\nu_\tau$  candidate event [17].

	$\theta_{kink}$ [mrad]	$z_{dec}$ [ $\mu\text{m}$ ]	$p^\mu$ [GeV/c]	$p_T^{2ry}$ [MeV/c]
Selection cut	> 20	[44, 2600]	[1.0, 15.0]	> 250
Meas. value (3rd)	$245 \pm 5$	$151 \pm 10$	$2.8 \pm 0.2$	$690 \pm 50$

### Hadronic $\tau$ Decays

The kinematical cuts for the  $\tau \rightarrow 1h$  decay mode are listed in Table 4.11, along with the measured values for the 1st, 4th, and 5th  $\nu_\tau$  candidate events reported by OPERA [12, 18, 20] that were found in this channel.

The hard lower cut on  $p_T^{2ry} > 0.3 \text{ GeV}/c$  or  $p_T^{2ry} > 0.6 \text{ GeV}/c$  (with or without  $\gamma$  emission at the secondary vertex) very efficiently reduces BG from elastic and inelastic pion interactions. Other low-energetic hadron reinteractions are removed by the lower limit on  $p^{2ry} > 2.0 \text{ GeV}/c$ . A maximum missing transverse momentum at the primary vertex of  $p_T^{miss} < 1.0 \text{ GeV}/c$  discriminates against the outgoing neutrinos in  $\nu_\mu$  NC interactions.  $\Delta\phi_{\tau h} > 90^\circ$  describes a lower limit on the transverse angle between the decay parent candidate track and the hadronic shower at the primary vertex. For  $\tau \rightarrow h$  events, the  $\tau$  lepton and hadronic showers are produced back-to-back in the transverse plane ( $\Delta\phi_{\tau h}$  peaking at  $180^\circ$ ), while for hadronic reinteractions mimicking a  $\tau \rightarrow h$  decay, the hadron is part of the hadronic shower ( $\Delta\phi_{\tau h}$  peaking at  $0^\circ$ ) [107]. In charmed particle decays with unidentified primary  $\mu^-$ ,  $\Delta\phi$  is nearly evenly distributed [83].

**Table 4.11:** Kinematical cuts applied to the  $\tau \rightarrow 1h$  decay channel [15, 107] and measured parameter values for the 1st, 4th, and 5th  $\nu_\tau$  candidate events [12, 18, 20]. The  $p_T^{2ry}$  selection reflects the predefined value for a hadronic decay with (without)  $\gamma$  emission at the secondary vertex.

	$\theta_{kink}$ [mrad]	$z_{dec}$ [ $\mu\text{m}$ ]	$\Delta\phi_{\tau h}$ [ $^\circ$ ]	$p_T^{miss}$ [GeV/c]	$p^{2ry}$ [GeV/c]	$p_T^{2ry} \gamma (0\gamma)$ [GeV/c]
Selection cut	$> 20$	[44, 2600]	$> 90$	$< 1.0$	$> 2.0$	$> 0.3 (0.6)$
Meas. value (1st)	$41 \pm 2$	$1335 \pm 35$	$172.5 \pm 1.7$	$0.57^{+0.32}_{-0.17}$	$12^{+6}_{-3}$	$0.47^{+0.24}_{-0.12}$
Meas. value (4th)	$137 \pm 4$	$406 \pm 30$	$166^{+2}_{-31}$	$0.55^{+0.55}_{-0.20}$	$6.0^{+2.2}_{-1.2}$	$0.82^{+0.30}_{-0.16}$
Meas. value (5th)	$90 \pm 2$	$630 \pm 30$	$151 \pm 1$	$0.3 \pm 0.1$	$11^{+14}_{-4}$	$(1.0^{+1.2}_{-0.4})$

In Table 4.12, the kinematical cuts for the 3-prong hadronic  $\tau$  decays are shown, compared to the parameter values measured for the 2nd  $\nu_\tau$  candidate event [15].

The same cuts on  $p_T^{miss}$  and  $\Delta\phi_{\tau h}$  are applied as for the  $\tau \rightarrow 1h$  channel, while the lower limit on the scalar sum of secondary particle momenta is adjusted to  $p^{2ry} > 3.0 \text{ GeV}/c$ . To further decrease BG, cuts on both the invariant mass and minimum invariant mass of the daughter system of  $0.5 \text{ GeV}/c^2 < m^{inv}, m_{min}^{inv} < 2.0 \text{ GeV}/c^2$  are introduced, and the average kink angle of the decay daughters w.r.t. the parent track is required to be  $\theta_{kink} < 500 \text{ mrad}$ .

**Table 4.12:** Kinematical cuts applied to the  $\tau \rightarrow 3h$  decay channel [15, 107] and measured parameter values for the 2nd  $\nu_\tau$  candidate event [15].

	$\theta_{kink}$ [mrad]	$z_{dec}$ [ $\mu\text{m}$ ]	$\Delta\phi_{\tau h}$ [ $^\circ$ ]	$p_T^{miss}$ [GeV/c]	$p^{2ry}$ [GeV/c]	$m^{inv}$ [GeV/c $^2$ ]	$m_{min}^{inv}$ [GeV/c $^2$ ]
Selection cut	$< 500$	$< 2600$	$> 90$	$< 1.0$	$> 3.0$	[0.5, 2.0]	[0.5, 2.0]
Meas. value (2nd)	$87.4 \pm 1.5$	$1446 \pm 10$	$167.8 \pm 1.1$	$0.31 \pm 0.11$	$8.4 \pm 1.7$	$0.80 \pm 0.12$	$0.96 \pm 0.13$

#### 4.7.5 Discovery of $\nu_\mu \rightarrow \nu_\tau$ Oscillations

The current analysis presents an update with an enlarged data sample and improved knowledge of expected backgrounds w.r.t. a previous study that reported the observation of  $\nu_\tau$  appearance with 4  $\nu_\tau$  candidate events [18]. Using the analysis procedure and kinematical cuts already defined at the time of the experiment proposal [107], it was possible to identify 5  $\nu_\tau$  candidate events in the data collected during the CNGS beam runs, giving a significance of  $5.1 \sigma$  [20].

The new  $\nu_\tau$  candidate event occurred on August 14th, 2012 in the 2nd SM of the OPERA detector. It was characterised as a  $0\mu$  event, as is evident from the ED reconstruction shown in Figure 4.36a. Figure 4.36b shows an ECC display of the event, where a 1-prong hadronic decay of the  $\tau$  lepton is reconstructed. Table 4.11 summarises the kinematical parameters of the  $\nu_\tau$  candidate, in comparison with the predefined selection cuts for the  $\tau \rightarrow 1h$  channel - the event survives all cuts for this channel. See [20] for further details.

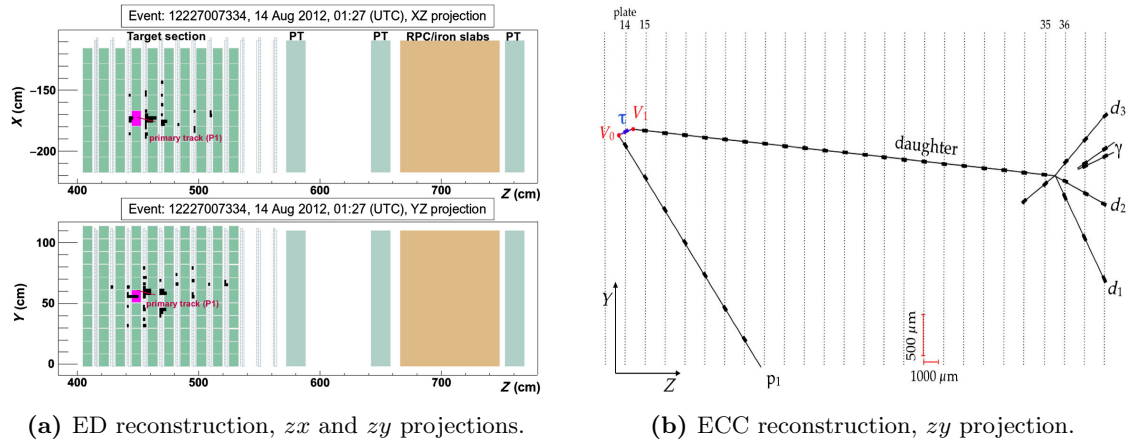


**Figure 4.36:** The 5th  $\nu_\tau$  candidate event [20]. (a) ED reconstruction, showing part of the 2nd SM target and spectrometer in both projections. The visible energy is  $(12 \pm 4)$  GeV. (b) ECC reconstruction, shown in  $zy$  projection. The  $\tau$  candidate decays after a flight length of  $(960 \pm 30)$   $\mu\text{m}$  into a charged hadron (daughter) that interacts after 22 plates, producing four charged particles and a photon. A second charged hadron ( $p_1$ ) is attached to the primary vertex. The scalar sum of measured momenta is  $12_{-4}^{+14}$  GeV/c.

The data sample analysed in [20] comprises the 2008 - 2012 CNGS beam data, with a total exposure of  $17.97 \times 10^{19}$  p.o.t. that resulted in 19 505 neutrino interactions in the OPERA target fiducial volume (FV). It includes all  $0\mu$  events, as well as  $1\mu$  events with reconstructed muon momenta below 15 GeV. See Table 4.13 for p.o.t. and event numbers for the respective run years.

**Table 4.13:** Number of events for each CNGS run year and identified  $\nu_\tau$  candidates [20].  $1\mu$  events with  $p_\mu < 15$  GeV/c were analysed.

	p.o.t. [ $\times 10^{19}$ ]	Events			$\nu_\tau$ candidates
		$0\mu$	$1\mu^{(*)}$	total	
2008	1.74	149	542	691	0
2009	3.53	253	1020	1273	1
2010	4.09	268	968	1236	0
2011	4.75	270	966	1236	1
2012	3.86	204	768	972	3
Total	17.97	1144	4264	5408	5

[18] gives a detailed description of the analysis procedure and likelihood-based statistical analysis. With the increased statistics and improved knowledge of BGs of the current analysis, the BG and signal expectation changes to the numbers listed in Table 4.14.

**Table 4.14:** Expected numbers of signal and BG events for the analysed data sample, assuming  $\Delta m_{23}^2 = 2.44 \times 10^{-3} \text{ eV}^2$  and  $\sin^2(2\theta_{23}) = 1$  [20].

Decay channel	Expected BG				Expected signal	Observed $\nu_\tau$
	charm	hadr. re-int.	large-angle $\mu$	total		
$\tau \rightarrow 1h$	$0.017 \pm 0.003$	$0.022 \pm 0.006$	-	$0.04 \pm 0.01$	$0.52 \pm 0.10$	3
$\tau \rightarrow 3h$	$0.17 \pm 0.03$	$0.003 \pm 0.001$	-	$0.17 \pm 0.03$	$0.73 \pm 0.14$	1
$\tau \rightarrow \mu$	$0.004 \pm 0.001$	-	$0.0002 \pm 0.0001$	$0.004 \pm 0.001$	$0.61 \pm 0.12$	1
$\tau \rightarrow e$	$0.03 \pm 0.01$	-	-	$0.03 \pm 0.01$	$0.78 \pm 0.16$	0
Total	$0.22 \pm 0.04$	$0.02 \pm 0.01$	$0.0002 \pm 0.0001$	$0.25 \pm 0.05$	$2.64 \pm 0.53$	5

Using the simulation of the CNGS neutrino flux (see Section 4.3.2), assuming  $\Delta m_{23}^2 = 2.44 \times 10^{-3} \text{ eV}^2$  and  $\sin^2(2\theta_{23}) = 1$ , and taking into account reconstruction efficiency [15] and uncertainties [20], the total expected signal is  $2.64 \pm 0.53$  events, at an expected total BG of  $0.25 \pm 0.05$ . With a measured signal of 5  $\nu_\tau$  events, a significance of  $5.1\sigma$  has been obtained [20]. The Fisher method and likelihood-based approaches give consistent results. Also, the first measurement of  $\Delta m_{23}^2$  in appearance mode could be performed with different statistical methods, all giving a 90% C.L. interval of  $[2.0, 5.0] \times 10^{-3} \text{ eV}^2$  and a best fit value of  $\Delta m_{23}^2 = 3.3 \times 10^{-3} \text{ eV}^2$  [20].

#### 4.7.6 Outlook: Final Analysis

The oscillation analysis summarised in the previous section follows the procedure and event selection predefined at the time of the experimental proposal [107]. It was optimised to maximise the signal-to-noise ratio and thus provide a quasi background-free measurement of  $\tau$  neutrino appearance.

An upcoming publication will present an updated study of the final CNGS data set of 2008 – 2012 [21]. While the number of neutrino target interactions does not change w.r.t. [20], the completed analysis of 3rd and 4th ECC bricks increases the number of fully analysed events by nearly 200.

A multivariate approach based on Boosted Decision Trees allows to loosen the kinematical cuts, resulting in ten new  $\nu_\tau$  candidate events, thereby reducing statistical uncertainties and increasing the statistical significance of the oscillation analysis. The measurement of  $\Delta m_{23}^2$  in appearance mode will likewise benefit from the increased statistics. A measurement of the  $\nu_\tau$  CC cross section will be provided, as well as the first direct measurement of the  $\nu_\tau$  lepton number.





# Chapter 5

## $\nu_e$ Event Reconstruction

The reconstruction of  $\nu_e$  candidate events, including their energy estimation and subsequent discrimination against backgrounds, is crucial to any  $\nu_\mu \rightarrow \nu_e$  appearance search.

This chapter will start with an overview of the general event topology (Section 5.1), after which Section 5.2 will give more information on the reconstruction of electromagnetic showers in OPERA and the identification of  $\nu_e$  events. A summary of the MC simulation used to study the detector response to  $\nu_e$  CC interactions is then provided in Section 5.3. Section 5.4 gives a detailed description of the energy reconstruction employed for electron neutrino events, followed by a brief outlook on future developments (Section 5.5).

### 5.1 General Event Topology

At the high neutrino energies provided by the CNGS beam,  $\nu_e$  CC interactions with target nuclei  $N$  in OPERA will predominantly occur via deep-inelastic scattering:

$$\nu_e + N \rightarrow e^- + X \tag{5.1}$$

resulting in the production of electrons, together with other hadronic products  $X$ .

The created electromagnetic (e.m.) shower (see Chapter 3) is used to identify the electron during ECC event reconstruction.

Acting as high-resolution sampling calorimeters, the OPERA bricks should in principle enable the exploitation of longitudinal and transversal shower parameters to reconstruct its energy. With an overall extension of no more than ten radiation lengths in beam direction, however, most e.m. showers will leak out of the brick volume.

To obtain an estimate of the original  $\nu_e$  energy, the Electronic Detector event reconstruction has to be employed.

## 5.2 Electromagnetic Showers in OPERA

With the high granularity of its ECC emulsion sheet detector, the OPERA experiment is capable of reconstructing the electromagnetic showers created by electrons. This enables the identification of  $\nu_e$  CC interactions, and with it the search for  $\nu_\mu \rightarrow \nu_e$  oscillations in appearance mode.

### 5.2.1 ED Reconstruction

In the Electronic Detector (ED) of OPERA, the topology of  $\nu_e$  CC interactions is that of  $0\mu$  ( $\nu_\mu$  NC-like) events, and as such they will be subjected to the  $\tau$  decay search procedure described in Section 4.7.2.

Figure 5.1 shows the ED reconstruction of a  $\nu_e$  candidate event that occurred in the target section of Super Module (SM) 1.

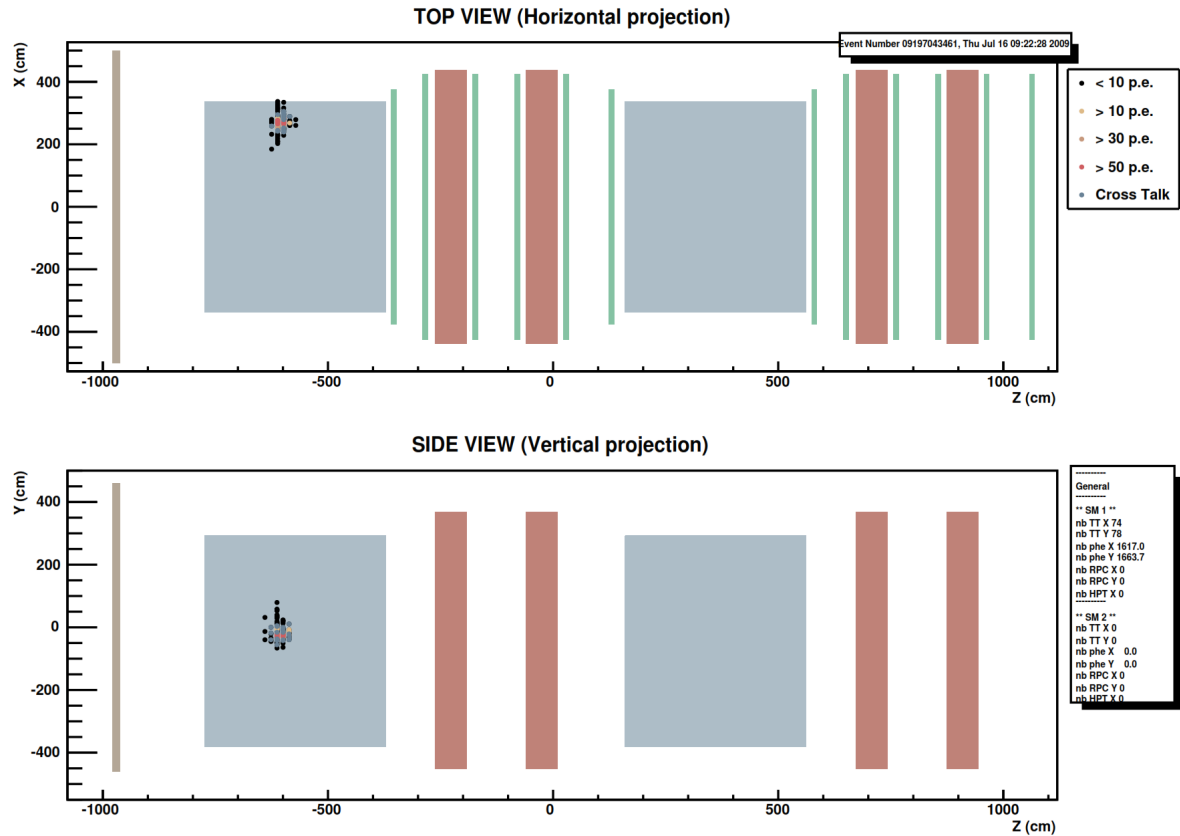


**Figure 5.1:**  $\nu_e$  candidate event 9197043461, as reconstructed in the ED of OPERA. Exhibiting no long muon track, the event topology is  $0\mu$  ( $\nu_\mu$  NC-like), and the event will be subjected to the  $\tau$  decay search procedure.

The hadronic shower from the hadronic products of the  $\nu_e$  CC interaction and the electromagnetic shower created by the electron are overlapping in the detector and cannot be easily separated. If certain corrections are applied (see Section 5.4), the hadronic energy  $E_{had,rec}$  reconstructed in the OPERA ED can however be used to estimate the original neutrino energy.

### 5.2.2 CS Shower Hints & Extended Scanning Volume

The general procedure applied in the search for  $\tau$  neutrino candidate events (see Section 4.7.2) can also identify electrons, and thus  $\nu_e$  CC interactions. Comprising only 10 plates (corresponding to  $\sim 1.8 X_0$ ) downstream from the primary interaction vertex, the extension of the standard scanned volume for event location will however be too short to contain the e.m. shower (see Chapter 3.4).

A systematic shower search is thus defined, opening up an extended scanning volume for  $\nu_e$  candidate events [16]. It is schematically outlined in Figure 5.2.

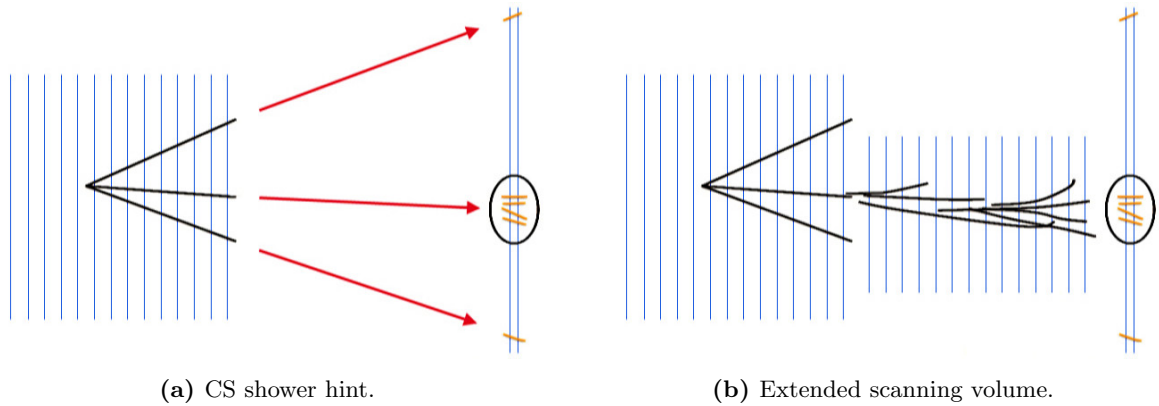


**Figure 5.2:** Systematic  $\nu_e$  search using CS shower hints. **(a)** After event location in the standard scanned volume, all tracks connected to the primary neutrino interaction vertex are extrapolated to the CS, where a search for additional tracks is performed. **(b)** If CS shower hints are found, an extended volume along the full track length is scanned to reconstruct the e.m. shower.

After the primary neutrino interaction vertex has been located in the standard scanned volume, all tracks connected to it are extrapolated to the CS. If at least 3 tracks of angles similar to that of the corresponding primary track ( $\Delta\theta < 150$  mrad) are found within 2 mm of the projected point, an extended volume along the full track length will be scanned and analysed. Should an e.m. shower be reconstructed in this volume, the corresponding primary vertex track becomes an electron candidate.

In the  $\tau$  decay search procedure, further shower hints are provided by clusters of tracks found in the Changeable Sheets during CS validation, or a converging pattern of several tracks merging into one during ECC track Scan Back (SB) (see Chapter 4.7.2) [122].

### 5.2.3 ECC Reconstruction & Rejection of Backgrounds

The ECC reconstruction of a  $\nu_e$  candidate event can be seen in Figure 5.3. The main characteristic of the topology is an electromagnetic shower originating from a charged particle track which is connected to the primary neutrino interaction vertex.

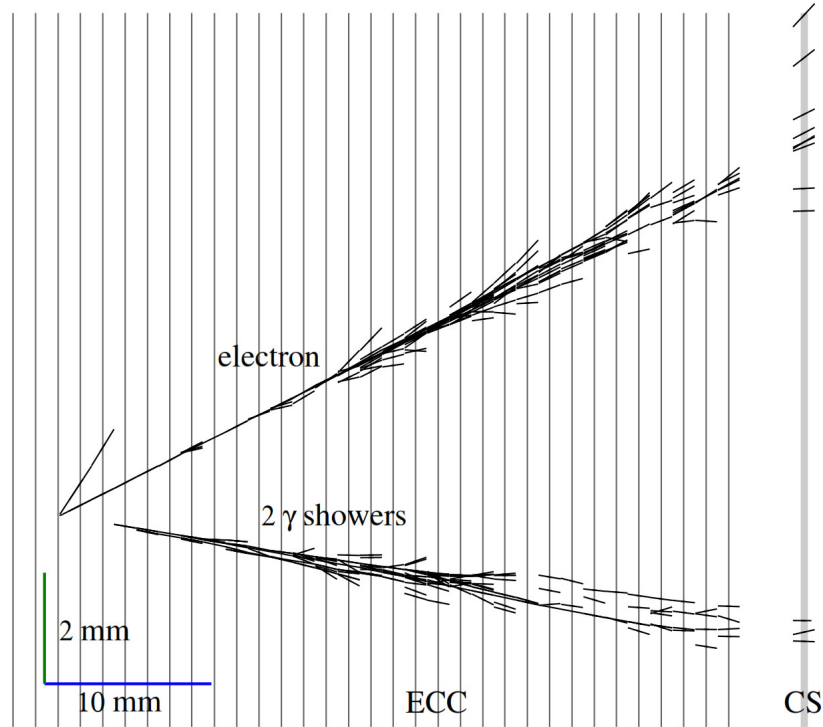


**Figure 5.3:** ECC reconstruction of  $\nu_e$  candidate event 9197043461 [16]. The primary neutrino interaction vertex shows a two-prong decay with an e.m. shower identified as an electron. Two additional showers from  $\gamma$  conversion are reconstructed, starting 2 and 3 emulsion films downstream (overlapping in this projection).

An additional SB procedure that was originally defined to improve the location efficiency for the  $\tau \rightarrow e$  decay channel in QE  $\nu_\tau$  interactions [107] also helps in the identification of  $\nu_e$  events: E.m. showers, detected by their signature in the CS, are followed in the brick upstream. There, a scan of the volume around the shower stopping point will be performed to detect possible parent particles.

After the rejection of backgrounds (see below), an event will be classified as a  $\nu_e$  interaction once the presence of an electron at the primary vertex has been confirmed.

### Electromagnetic Showers from $\pi^0$ $\gamma$ Conversion

If the primary muon cannot be reconstructed, the decay of  $\pi^0$  from  $\nu_\mu$  NC RES scattering (see Chapter 2.3.2) or  $\nu_\mu$  CC interactions with pion charge exchange may constitute a significant BG to the  $\nu_e$  search: Early  $\gamma$  conversion of the  $\pi^0$  will result in pairs of  $e^+e^-$ , creating e.m. showers.

To discriminate against this kind of events, electron candidate tracks are carefully investigated in the two emulsion sheets downstream from the primary neutrino interaction vertex. If the track can be separated into two nearly parallel segments that are least  $1\ \mu\text{m}$  apart, the e.m. shower is proven to not originate from a single electron but an  $e^+e^-$  pair, and the event will be rejected.

Figure 5.4 shows the tracks left by such an  $e^+e^-$  pair in an OPERA emulsion sheet.

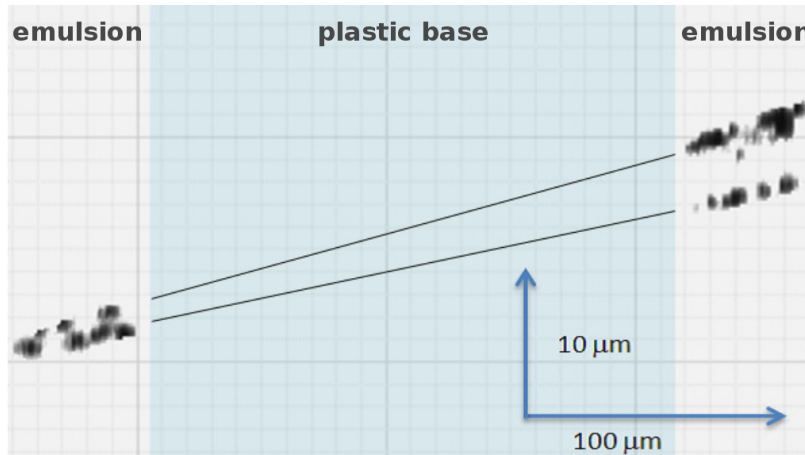


**Figure 5.4:** Reconstruction of an  $e^+e^-$  pair from  $\pi^0$   $\gamma$  conversion in an OPERA emulsion sheet [16]. The clear separation of the track segments in the downstream emulsion layer allows the rejection of this BG.

### $\tau \rightarrow e$ Decays

Another important background to the search for  $\nu_e$  candidates originates from  $\nu_\tau$  CC interactions with subsequent  $\tau$  decay in the electronic channel (see Chapter 4.7.1).

By requesting an impact parameter of the electron candidate track of less than  $10\ \mu\text{m}$  w.r.t. the primary interaction vertex (short  $\tau$  decays) or a kink angle smaller than  $\theta_{kink} < 20\ \text{mrad}$  (long  $\tau$  decays), most of these events can be rejected.

### 5.3 Monte Carlo Simulation

The response of the OPERA Electronic Detector to  $\nu_e$  interactions has been investigated using a large sample of MC-generated data. Event generator, detector simulation, and the applied quality cuts will be described in the following.

#### 5.3.1 Neutrino Event Generator

In the scope of a dedicated search for  $\nu_\mu$  disappearance [91], an OPERA-specific neutrino event generator using GENIE [37, 36] has been developed, along with the implementation of necessary adjustments to the official OPERA software.

The electron neutrino events studied in this thesis are generated employing the above-mentioned framework, i.e. using GENIE version 2.6.2 and its default set of interactions and physics parameters. The neutrino flux is given by the CNGS FLUKA simulation [93] described in Chapter 4.3.2 and propagated through the OPERA ROOT geometry.

CNGS beam neutrinos are simulated with a random starting point  $\mathbf{x}_0$  on the surface of a disk of radius  $R = 20.0$  m, the center of which is displaced by  $\mathbf{s} = (0, 0, -20.0)$  m w.r.t. the OPERA geometry origin at  $(0, 0, 0)$ . The relative angles between the CNGS beam direction and the OPERA coordinate system in the  $ZY$  and  $ZX$  projections are  $\theta_{CNGS} = +58.11$  mrad and  $\phi_{CNGS} = -4.48$  mrad, respectively (see Figure 4.12).

With  $\sigma$  being the interaction cross section,  $\rho$  the material density, and  $\mathbf{x}$  the position within the geometry, the integrated neutrino interaction probability is

$$P_{int} \propto \int_{\mathbf{x}_0}^{\mathbf{x}_1} \sigma(\mathbf{x}) \cdot \rho(\mathbf{x}) \cdot \mathbf{x} \, d\mathbf{x} \quad (5.2)$$

For neutrinos travelling along the beam direction of  $\mathbf{d} = (\tan(\phi_{CNGS}), \tan(\theta_{CNGS}), 1)$ , the endpoint  $\mathbf{x}_1$  is given by the border of the OPERA ROOT geometry.

The simulated sample consists of 500 000  $\nu_e$  interactions, with equal statistics of electron neutrinos from beam contamination and from  $\nu_\mu \rightarrow \nu_e$  oscillations. For prompt  $\nu_e$ , the unoscillated CNGS  $\nu_e$  flux is used (Figure 4.14c), while the oscillated  $\nu_e$  are simulated following the unoscillated CNGS  $\nu_\mu$  spectrum (Figure 4.14a). Parameter- and model-dependent oscillation probabilities are not yet applied.

Using GENIE, the events are generated inside the OPERA volume and weighted by the respective cross sections for the different event classes. The simulation does not take into account the displaced secondary vertices for decays of  $\tau$  leptons, charmed particles or neutral pions. All outgoing particles are produced at generator level and originate from the same primary pseudo-vertex. While this is not suitable for emulsion analysis, the lifetimes  $c\tau$  of the decayed particles are  $\mathcal{O}(1mm)$  and thus far below the OPERA ED spatial resolution.

More details on the event generator can be found in [91].

### 5.3.2 Detector Geometry Description

A detailed geometry description of the OPERA detector and support structure (shown in Figure 5.5) is provided by the `OpGeom` geometry model which is used in both simulation and reconstruction of neutrino interactions. It is based on a ROOT `TGeoManager` and included in the `OpRelease` software framework (see Chapter 4.5).

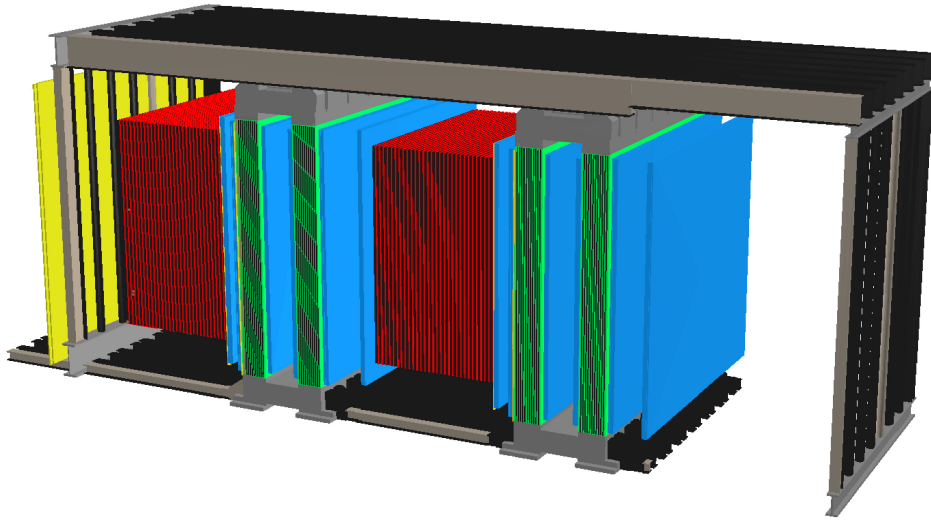


**Figure 5.5:** OpGeom implementation of the OPERA detector and support structure [91]. Active detector elements are highlighted by colour.

In the line of [91], adjustments were made to the default OPERA geometry model to enable GENIE event generation. Material definitions were changed from average element mixtures to isotope mixtures, and material compositions were updated with new information [68, 41].

Table 5.1 lists the material budget of the implemented OPERA geometry.

**Table 5.1:** Material composition of the simulated OPERA geometry using the maximum real brick filling of 2009-06-29 [91].

Material	Mass [kt]
Iron	2.202
Lead	1.156
Aluminium	0.066
Plastic scintillator	0.058
ECC plastic base	0.032
ECC nuclear emulsion	0.029
Bakelite	0.021
Nylon	0.020
Total other	< 0.035

For the MC simulation of  $\nu_e$  events in the OPERA detector, the variable brick configuration (see Chapter 4.4.1) is set to the maximum real brick filling of 2009-06-29.

### 5.3.3 Detector Simulation

The official OPERA Electronic Detector simulation is based on GEANT 3.21 [61] and included in the `OpRelease` package `OpSim`. While the OPERA ECC simulation relies on standalone FLUKA, it is possible to choose between three generators (GHEISHA, GFLUKA, GCALOR) [94] for the simulation of hadronic interactions in the ED.

Using calibrations obtained with cosmic muon data [13] and parameterised response functions, detector signals are digitised by the `OpDigit` package. The simulation further comprises electronic noise for PT and TT, as well as crosstalk in the multi-channel PMTs.

#### Hadronic Showers

Affecting deposited energy, shower length, and shower profile, the hadronic interaction generator will have a direct impact on the energy reconstruction of simulated data.

The default GEANT 3.21 generator GHEISHA produces the weakest hadronic activity, while GFLUKA generates the largest energy depositions [91]. GCALOR results lie in-between, with shower lengths and longitudinal profiles being very similar to the GFLUKA simulation. Calibration measurements performed with the MINOS-CalDet using charged hadrons from the CERN-PS showed the best compatibility with the GCALOR simulation [121].

While being the preferred generator for hadronic interactions also in OPERA, GCALOR is limited to 32-bit architectures and incompatible with the 64-bit `OpRelease` environment. Thus, GFLUKA has been chosen as the default generator for the OPERA ED.

#### Electromagnetic Showers

Contrary to the hadronic shower generation, the GEANT 3.21 simulation of electromagnetic showers follows well-understood models, and the differences in simulated detector response are negligible for the different generators [91].

With a brick wall thickness of  $\sim 10X_0$  however, most showers originating from  $e^\pm$  or  $\pi^0$  of low energies  $\mathcal{O}(\text{GeV})$  will be stopped within a few walls, thus limiting their reconstruction with the ED of OPERA.

### 5.3.4 Quality Cuts

Not all of the 500 000  $\nu_e$  interactions generated in the OPERA geometry using above-mentioned procedures are suitable for further analysis. The applied quality cuts and their impact on the data sample will be briefly summarised.



### OpRec4.1 Reconstruction

Any event that is to be further studied must be reconstructed by the OpRec4.1 algorithms.

Figure 5.6 shows the MC true vertex locations of all prompt and oscillated  $\nu_e$  interactions that generated signals which could be reconstructed by OpRec4.1. Most neutrino interactions occur outside the bricks (brick plate number "0", compare right panel), and their vertex distribution visualises not only active detector parts, but also the OPERA magnets and support structure.

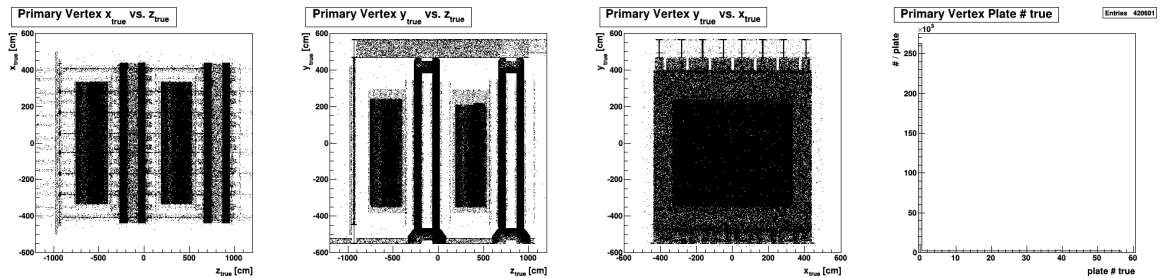


**Figure 5.6:** True vertex distribution in the OPERA detector and support structure of all MC  $\nu_e$  events that were reconstructed by OpRec4.1. Shown is the full ED in  $ZX$ ,  $ZY$ , and  $XY$  projections, as well as brick plate numbers.

About 420 000 events are remaining after this selection which naturally includes the ED reconstruction efficiency.

### True $\nu_e$ CC Events

Intended to select only true  $\nu_e$  CC interactions by discarding NC events, the next cut excludes all primary vertices with  $\neq 1$  outgoing  $e^-$ .

The resulting true vertex distributions are shown in Figure 5.7.

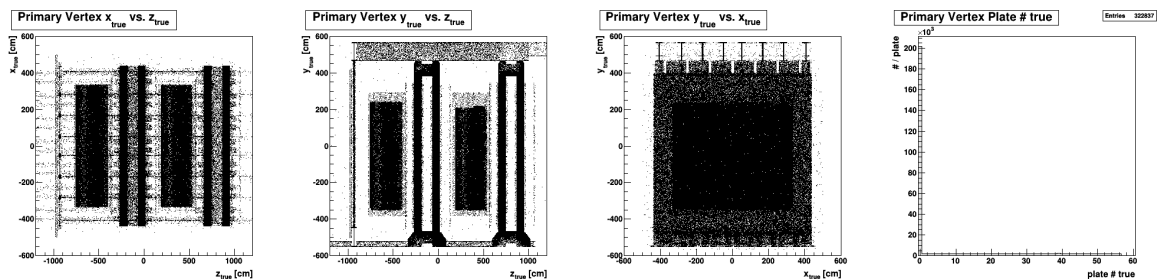


**Figure 5.7:** True vertex distribution in the OPERA detector and support structure of MC  $\nu_e$  CC interactions that were reconstructed by OpRec4.1. Shown is the full ED in  $ZX$ ,  $ZY$ , and  $XY$  projections, as well as brick plate numbers.

While reducing the number of remaining events to  $\sim 320\,000$ , the qualitative shape of the distributions does not change.

### Interaction Vertex Inside Brick

The last selection discards all generated events whose true interaction vertex lies outside the brick. This cut retains only true  $\nu_e$  CC interactions that could, in principle, be reconstructed in ECC analysis.

Figure 5.8 shows the resulting true  $\nu_e$  vertex distributions. In the ED projections, only the OPERA target regions are visible, and the brick plate number histogram (see right panel) now exhibits a flat distribution.

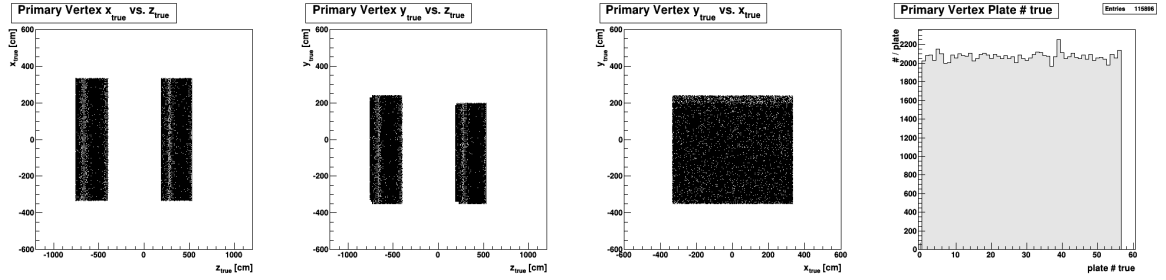


**Figure 5.8:** True vertex distribution of MC  $\nu_e$  CC interactions with primary vertices inside the brick that were reconstructed by OpRec4.1. Shown is the full ED in  $ZX$ ,  $ZY$ , and  $XY$  projections, as well as brick plate numbers.

After this final cut, a total of about 115 000  $\nu_e$  CC events remain that will be used for the energy estimation discussed in Section 5.4.

### 5.3.5 Location of $\nu_e$ Candidate Bricks

The locations within the OPERA ED volume of the 19  $\nu_e$  candidate events found in the CNGS data of 2008 - 2009 used in the oscillation analysis (see Chapter 6) are shown in Figure 5.9. They are superimposed on the distribution of MC-simulated  $\nu_e$  events after the application of all the above-described quality cuts.

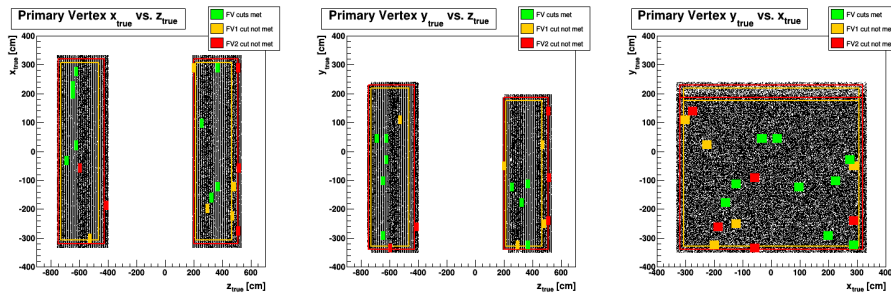


**Figure 5.9:** Location of  $\nu_e$  candidate bricks in the OPERA target in  $ZX$ ,  $ZY$ , and  $XY$  projections, overlaid on the MC  $\nu_e$  true vertex distribution. Colours indicate possible severe (orange) and less severe (red) FV cuts, along with the  $\nu_e$  candidate bricks they would exclude.

Various fiducial volume (FV) definitions, intended to guarantee a better containment of hadronic and e.m. showers within the active detector volume, were discussed. They would have decreased the uncertainty on the estimated  $\nu_e$  energy (see Section 5.4) but were ultimately discarded, as the sample of real  $\nu_e$  events would have been severely diminished.

## 5.4 Energy Estimation for $\nu_e$ Events

Contrary to the nearly background-free OPERA main  $\nu_\mu \rightarrow \nu_\tau$  oscillation analysis, the electron neutrino appearance search has to deal with a combined  $\nu_e$  and  $\bar{\nu}_e$  beam contamination of  $\sim 1\%$  (see Chapter 4.3.2). Given the different energy spectra of prompt and oscillated  $\nu_e$  however, the introduction of cuts on the reconstructed neutrino energy  $E_{\nu,rec}$  may provide a separation of these events and thus improve the signal-to-noise ratio.

In the following, a correction function  $E_{\nu,rec}(E_{had,rec})$  will be derived to provide an estimate of the initial  $\nu_e$  energy. It relies on the MC simulation described in the previous section by taking into account the hadronic energy  $E_{had,rec}$  reconstructed in the ED of OPERA and the true neutrino energy  $E_{\nu,true}$ .

For real data, the ECC analysis enables identification of  $\nu_e$  events and outgoing particles and provides information on the primary interaction vertex location in the brick. The knowledge gained from the `OpRelease4.1` ED reconstruction encompasses the position of the interaction brick within the detector, muon identification and spectroscopy, as well as the reconstructed hadronic energy  $E_{had,rec}$  in the TT and RPC subdetectors.

### 5.4.1 Energy Reconstruction in the OPERA TT

The estimation of the energy of  $\nu_e$  candidates is based on the hadronic energy reconstructed for these events in the OPERA Target Tracker (TT) (see Section 4.4.1) which will be summarised in the following.

According to the PMT channel gain (see Figure 5.10), the ADC count signals measured at both ends of the OPERA TT scintillator strips are converted into numbers of photo electrons (p.e.s) [7].

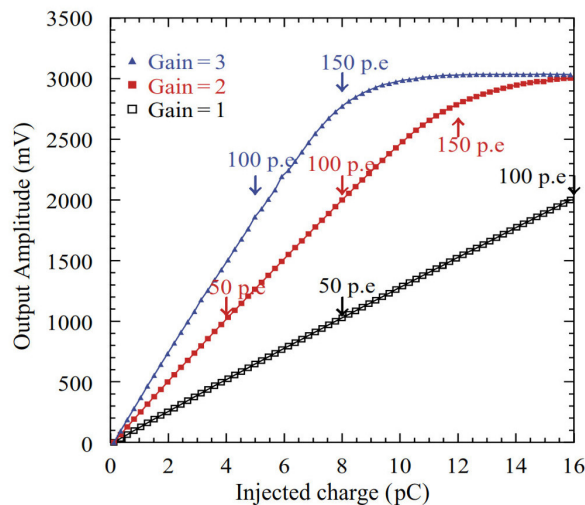


**Figure 5.10:** TT ROC individual channel charge measurement [7]. For a preamplifier gain of 1, the charge measurement is linear over the range of 1 – 16 pC (corresponding to 0 – 100 p.e.), with an uncertainty of less than 2%.

Calibrations were performed both before detector assembly and during its running (see Figure 5.11) [7, 13]. Depending on the reconstructed position of the particle crossing the TT strip and taking into account signal attenuation in the WLS fibre, the sum of p.e. measured on both ends of the strip is converted into a MeV-deposit of visible energy  $E_{TT,vis}$ .

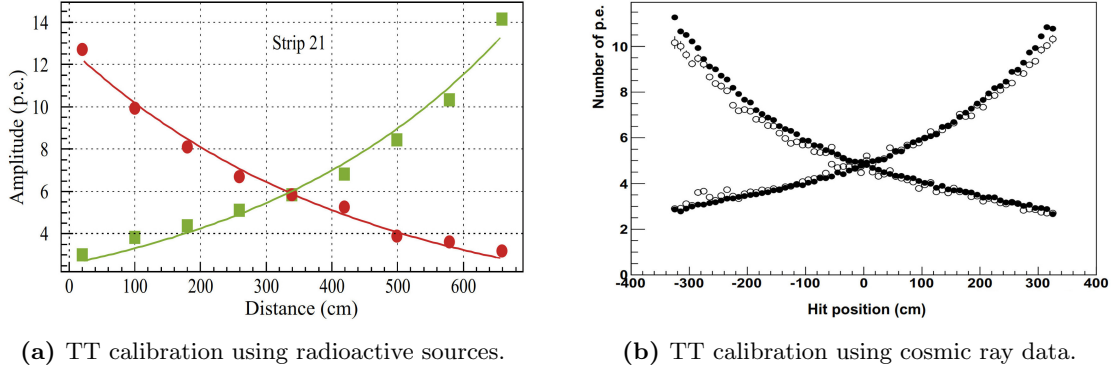


**Figure 5.11:** Number of p.e. observed at the ends of a TT scintillator strip WLS fibre vs. position of crossing m.i.p. (a) TT calibration before detector assembly using radioactive sources, fit with a double exponential function [7]. (b) TT calibration after detector assembly using cosmic ray data (full circles) and compared to MC expectation (empty circles), the discrepancy is within 10% [13].

Based on a simulation of MC-generated  $\nu_\mu$  events following the CNGS energy spectrum in the OPERA ED [13], the visible energy  $E_{TT,vis}$  is then translated into the total hadronic energy  $E_{had,rec}$ . In the case of hadronic shower leakage into the spectrometer, energy deposits in the RPC are also taken into account. Figure 5.12 shows the resulting energy resolution

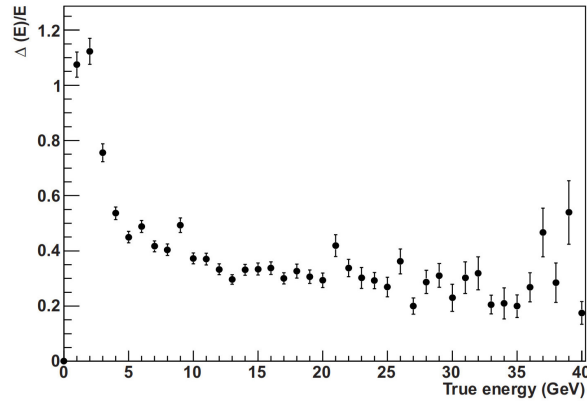


**Figure 5.12:** Energy resolution for correlating the visible energy reconstructed in the OPERA TT  $E_{TT,vis}$  with the hadronic reconstructed energy  $E_{had,rec}$  vs. the incoming neutrino energy  $E_{\nu,true}$  [13]. MC-generated  $\nu_\mu$  events using the CNGS energy spectrum.

The performance of this calibration was verified by comparing the distributions of reconstructed visible energy in the TT  $E_{TT,vis}$  in data and MC for  $\nu_\mu$  CC and  $\nu_\mu$  NC events. For  $\nu_\mu$  CC events, also the total reconstructed energy<sup>1</sup>  $E_{\nu,rec} = E_{had,rec} + E_{\mu,rec}$  and Bjorken- $y$ <sup>2</sup> were studied. The distributions are in good agreement, discrepancies are seen only for soft  $\nu_\mu$  NC events at very low energies [13].

<sup>1</sup>Taking into account the muon energy reconstructed in the spectrometer  $E_{\mu,rec}$ .

<sup>2</sup>The Bjorken- $y$  variable describes the fraction of outgoing hadronic energy w.r.t. the incoming neutrino energy.

### 5.4.2 ED $\nu_e$ Energy Estimation

For  $\nu_\mu$  CC events, the total incoming neutrino energy  $E_{\nu,rec}$  can be estimated by adding up the reconstructed hadronic energy  $E_{had,rec}$  and the energy measured for the muon in the spectrometer  $E_{\mu,rec}$  (see Section 5.4.1). Unfortunately, the reconstruction of the outgoing electron's energy in  $\nu_e$  CC events is not as straightforward.

While the standard scanned volume of 10 emulsion plates downstream from the primary vertex (see Section 4.7.2) is sufficient for electron identification, a reconstruction of the e.m. shower over at least 20 plates of Pb (corresponding to  $3X_0 - 4X_0$ ) is needed for a reliable energy estimation [62].

Depending on the position of the  $\nu_e$  interaction inside the ECC volume and the electron's energy, some e.m. showers may be contained within the brick where the  $\nu_e$  CC interaction occurred (see Chapter 3.4). Other showers will leak out, overlapping with the hadronic shower in the TT and possibly continuing into further downstream bricks. This complicates the reconstruction of the e.m. shower's energy based on ECC data.

Consequently, a new calibration for estimating the total energy of  $\nu_e$  CC events from the available ED data is needed which will be described in the following.

### Reconstructed Hadronic Energy in the ED for $\nu_e$ Events

Using MC-generated data of  $\nu_e$  events in the OPERA detector (described in Section 5.3), the dependence of the hadronic reconstructed energy in the ED  $E_{had,rec}$  (see Section 5.4.1) on the true neutrino energy  $E_{\nu,true}$  has been parameterised.

Figure 5.13 shows the distribution of  $E_{had,rec}$  vs.  $E_{\nu,true}$ .

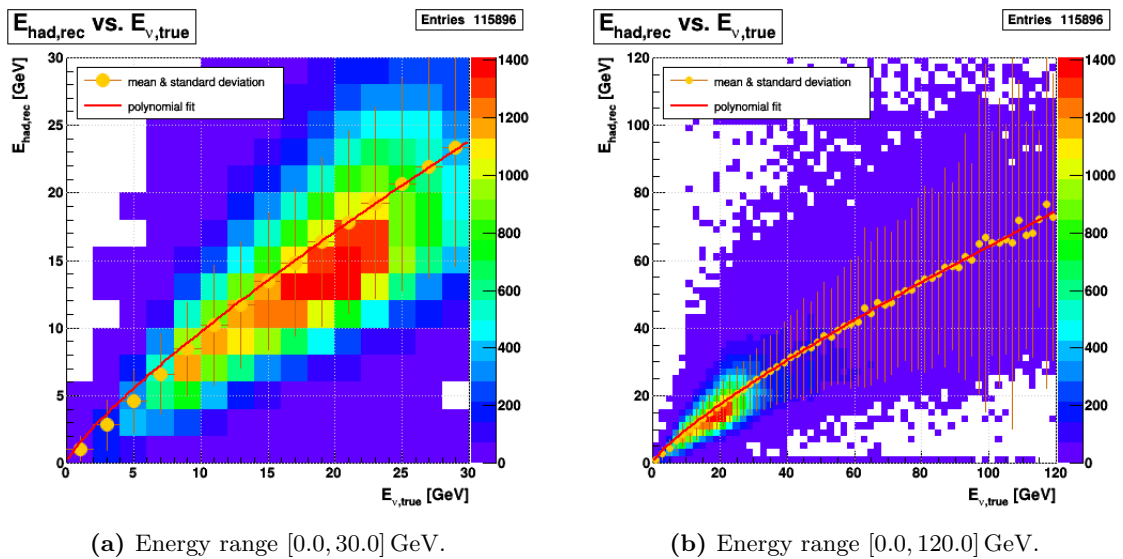


**Figure 5.13:**  $E_{had,rec}$  vs.  $E_{\nu,true}$  in bins of 2 GeV. Arithmetic mean and standard deviation of  $E_{had,rec}$  per 2 GeV-bin of  $E_{\nu,true}$  shown in orange, polynomial fit to mean in range [5.0, 60.0] GeV shown in red.

Using MINUIT and the invertible fit function:

$$E_{had,rec}(E_{\nu,rec}) = c_1 \cdot (E_{\nu,true})^{c_2} \quad (5.3)$$

a fit to the mean of  $E_{had,rec}$  per 2 GeV-bin of  $E_{\nu,true}$  has been performed in the relevant energy range of [5.0, 60.0] GeV. It yields:

$$E_{had,rec}(E_{\nu,rec}) = 1.45 \cdot (E_{\nu,true})^{0.822} \quad (5.4)$$

as a result, the fitted constants determined to  $c_1 = 1.45$  and  $c_2 = 0.822$ .

The inverse relation:

$$E_{\nu,rec}(E_{had,rec}) = (0.694 \cdot E_{had,rec})^{1.21} \quad \text{if } E_{had,rec} \geq 1.45 \text{ GeV} \quad (5.5)$$

can then be used to estimate the reconstructed  $\nu_e$  energy  $E_{\nu,rec}$ .

A low-energy fix of:

$$E_{\nu,rec}(E_{had,rec}) = E_{had,rec} \quad \text{if } E_{had,rec} < 1.45 \text{ GeV} \quad (5.6)$$

is applied to prevent unphysical values of  $E_{\nu,rec}(E_{had,rec}) < E_{had,rec}$ .

### $E_{\nu,rec}$ Overflow Fix for Poorly Contained Showers

In the ED reconstruction of the hadronic energy  $E_{had,rec}$ , RPC data is taken into account if the shower is leaking out of the brick-filled target area. An example of such a  $\nu_e$  event as seen by the ED is given in Figure 5.14.

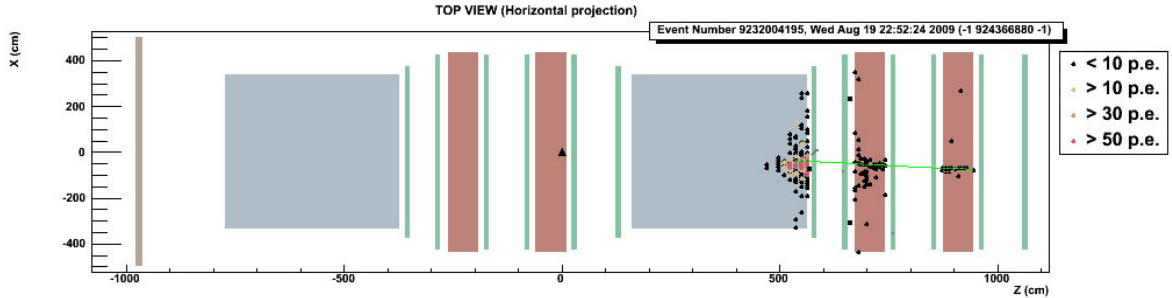


**Figure 5.14:** ED reconstruction of a  $\nu_e$  event with showers poorly contained in the target area. The reconstructed hadronic energy  $E_{had,rec}$  will be overestimated.

For well-developed but poorly contained hadronic and e.m. showers, less particles are absorbed in the passive lead sheets of the ECC bricks, leading to a larger energy deposition in the downstream ED elements. In these cases, the energy calibration will fail, severely overestimating the reconstructed hadronic energy  $E_{had,rec}$  and consequently the neutrino energy  $E_{\nu,rec}$ . An overflow fix of:

$$E_{\nu,rec}(E_{had,rec}) = 165 \text{ GeV} \quad \text{if } E_{had,rec} > 160 \text{ GeV} \quad (5.7)$$

is thus applied to prevent unreasonably large values of  $E_{\nu,rec}$ .

### Performance of the $\nu_e$ Energy Estimation

The performance of the energy estimation of  $\nu_e$  events using the parameterisation derived above (Equations 5.5 - 5.7) is studied by comparing true and reconstructed energy of MC-generated  $\nu_e$  events. The quality cuts on the MC data applied here are the same as used for the  $\nu_e$  energy calibration (see Section 5.3.4).

In Figure 5.15, the reconstructed  $\nu_e$  energy  $E_{\nu,rec}$  is plotted against the true neutrino energy  $E_{\nu,true}$ . Arithmetic mean and standard deviation of  $E_{\nu,rec}$  are calculated for 2 GeV-bins of  $E_{\nu,true}$ . Figure 5.15a shows the reconstructed  $\nu_e$  energy without the 165 GeV-overflow fix described in the previous section, while in Figure 5.15b, the overflow fix is applied. In both cases, the behaviour of  $E_{\nu,rec}$  vs.  $E_{\nu,true}$  is approximately linear over the energy range of [0.0, 120.0] GeV. At high energies, the application of the overflow fix results in much lower uncertainties.

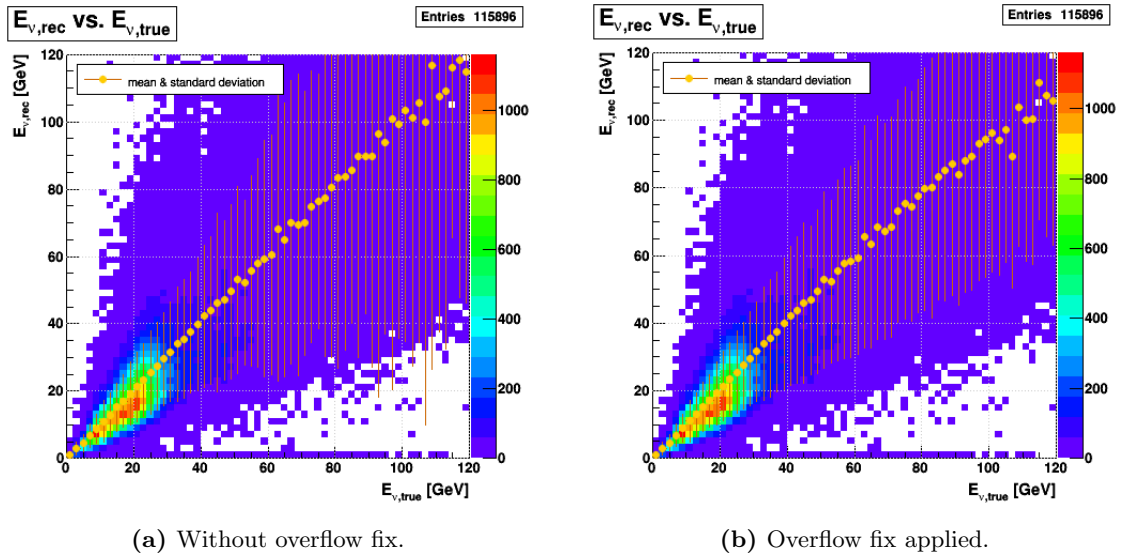


**Figure 5.15:**  $E_{\nu,rec}$  vs.  $E_{\nu,true}$  in bins of 2 GeV. Arithmetic mean and standard deviation of  $E_{\nu,rec}$  per 2 GeV-bin of  $E_{\nu,true}$  shown in orange.

Figure 5.16 shows the deviation  $E_{\nu,rec} - E_{\nu,true}$  of the reconstructed neutrino energy from the true MC energy, plotted against  $E_{\nu,true}$ . Arithmetic mean of  $E_{\nu,rec} - E_{\nu,true}$  and standard deviation are calculated per 2 GeV-bin of  $E_{\nu,true}$ . In Figure 5.16a, the overflow fix is not used, while in Figure 5.16b it is applied. The overflow fix greatly reduces the uncertainties at higher energies, but also results in a slight underestimation of  $E_{\nu,rec}$ .

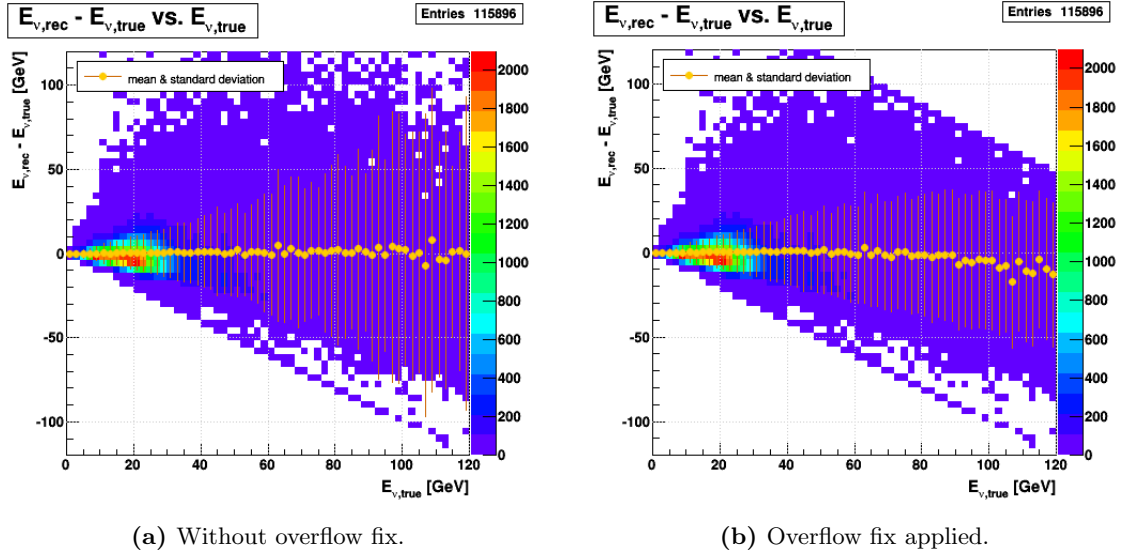


**Figure 5.16:**  $E_{\nu,rec} - E_{\nu,true}$  vs.  $E_{\nu,true}$ . Arithmetic mean and standard deviation of  $E_{\nu,rec} - E_{\nu,true}$  per 2 GeV-bin of  $E_{\nu,true}$  shown in orange.

Other calibrations and cuts on the MC data have been studied but resulted in worse performance.

### Reconstructed $\nu_e$ Energy Resolution

The uncertainty of the electron neutrino energy, reconstructed as described above (Equations 5.5 - 5.7), is given by its resolution  $\Delta E/E$ . It is calculated as:

$$\frac{\Delta E}{E} = \frac{\sqrt{\frac{\sum_{i=1}^n (E_{\nu,rec,i} - E_{\nu,true,i})^2}{n}}}{E_{\nu,true}} \quad (5.8)$$

with  $n$  being the number of entries per energy bin of  $E_{\nu,true}$ .

Figure 5.17 shows the reconstructed energy resolution  $\Delta E/E$  per 2 GeV-bin of  $E_{\nu,true}$ . Applying the overflow fix (Figure 5.17a) results in a better and much more stable behaviour at high energies than omitting the overflow fix (Figure 5.17a).



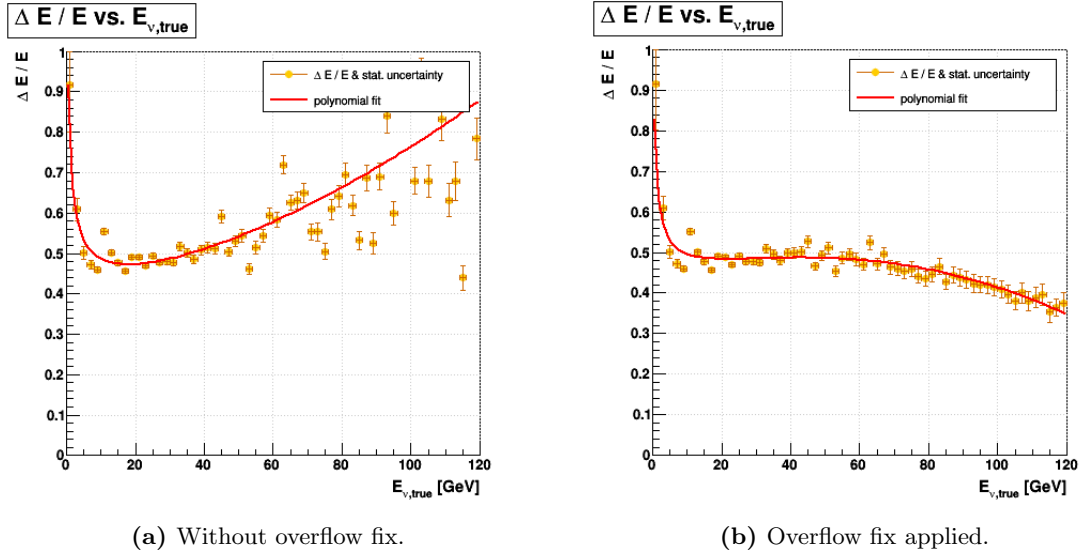


**Figure 5.17:** Resolution of  $E_{\nu,rec}$  vs.  $E_{\nu,true}$  calculated per 2 GeV-bin of  $E_{\nu,true}$ , the statistical uncertainty is given by the RMSD. Polynomial fits in range [2.0, 120.0] GeV shown in red.

In the relevant energy range of [5.0, 50.0] GeV, the resolution can be approximated as:

$$\frac{\Delta E}{E} \sim 0.5 \quad (5.9)$$

if the overflow fix is used.

To better match the binning used in the lower statistics of real data, the energy resolution  $\Delta E/E$  has also been re-evaluated in 10 GeV-bins of  $E_{\nu,true}$ , as shown in Figure 5.18.

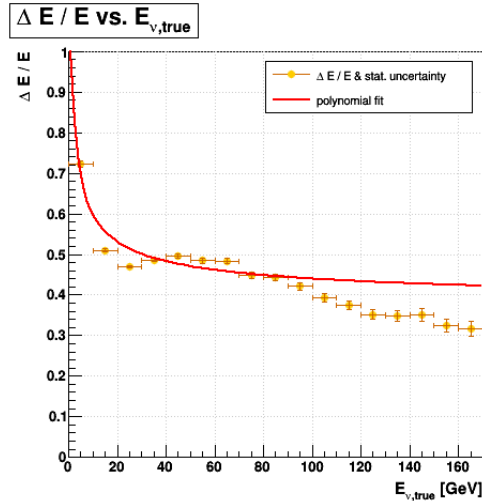


**Figure 5.18:** Resolution of  $E_{\nu,rec}$  vs.  $E_{\nu,true}$  per 10 GeV-bin of  $E_{\nu,true}$ , as used for [16]. The statistical uncertainty is given by the RMSD. Polynomial fit in range [0.0, 80.0] GeV shown in red.

A polynomial fit to the data in the energy range of [0.0, 80.0] GeV using a typical calorimeter resolution function:

$$\frac{\Delta E}{E} = c_1 + c_2 \cdot \frac{1}{\sqrt{E}} \quad (E \text{ in GeV}) \quad (5.10)$$

yields:

$$\frac{\Delta E}{E} = 0.366 + 0.736 \cdot \frac{1}{\sqrt{E}} \quad (E \text{ in GeV}) \quad (5.11)$$

with the fitted constants determined to  $c_1 = 0.366$  and  $c_2 = 0.736$ .

As can be seen in Figure 5.18, this parameterisation is valid for energies  $E \lesssim 100$  GeV.

### Application to Real $\nu_e$ Candidate Events

The energy calibration described above has been applied to the 19  $\nu_e$  candidate events observed by OPERA in the CNGS data of 2008 - 2009 (see Chapter 6.1). The reconstructed  $\nu_e$  energies are listed in Table 5.2.

**Table 5.2:** Reconstructed energy of real  $\nu_e$  candidate events using the calibration described by Equations 5.5 - 5.7. For events 236878897 and 9232004195, the overflow fix results in the maximum reconstructed  $\nu_e$  energy of 165 GeV. The uncertainties of  $E_{\nu,rec}$  are given by Equation 5.11.

Event number	Brick number	$E_{had,rec}$ [GeV]	$E_{\nu,rec}$ [GeV]
218200851	1005538	31.1	41.2
226195054	1079239	76.7	122.7
226395185	1048483	18.3	21.6
235990918	1111165	78.8	126.7
236878897	1093347	104.5	165.0
9162064902	1121872	39.6	55.1
9173042169	1142415	12.2	13.2
9177016997	1098472	40.4	56.4
9197043461	1040009	25.6	32.5
9201065192	1123715	43.6	61.8
9203100936	1004249	34.3	46.4
9218038732	1057098	19.3	23.2
9232004195	1112293	104.5	165.0
9263028113	1030202	66.4	103.0
9290026555	1084000	12.4	13.5
9296074371	1154798	39.6	55.2
9301040593	1096038	35.5	48.3
9302000526	1106972	15.3	17.5
9322059646	1090377	15.0	17.1

Figure 5.19a displays the spectrum of reconstructed hadronic energy  $E_{had,rec}$  for these events, while in Figure 5.19b Equations 5.5 - 5.7 were used to compute the reconstructed neutrino energy  $E_{\nu,rec}$ . The overlaid spectra of MC-generated  $\nu_e$  events from beam contamination and  $\nu_\mu \rightarrow \nu_e$  oscillations are the same as used for the calibration of  $E_{\nu,rec}$ , normalised to the number of detected  $\nu_e$  candidate events. They do not yet include oscillation probabilities or ECC detection efficiency.

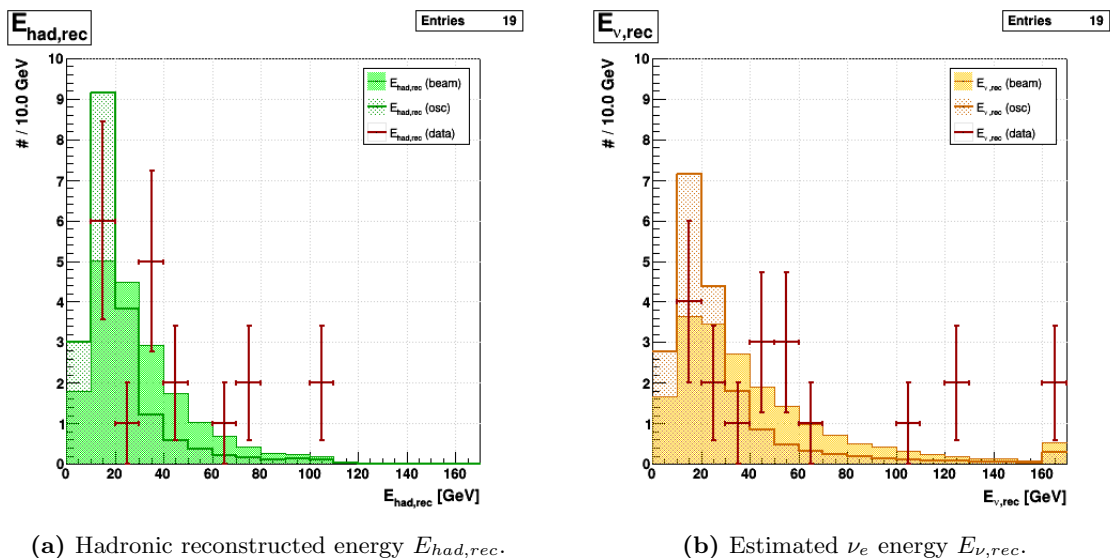


**Figure 5.19:** Reconstructed energy of the 19  $\nu_e$  candidate events (data) in bins of 10 GeV, including simple statistic uncertainties. The overlaid spectra of MC-generated  $\nu_e$  events from beam contamination (beam) and  $\nu_\mu \rightarrow \nu_e$  oscillations (osc) do not include oscillation probabilities or ECC detection efficiency.

The  $\nu_e$  energy estimation described in this section has been applied in the  $\nu_\mu \rightarrow \nu_e$  oscillation analysis performed in [16]. More details on this will be given in Chapter 6.

## 5.5 Outlook

On the Electronic Detector side, the reconstruction of the  $\nu_e$  energy may be improved by introducing further cuts on the data and refining the shower reconstruction.

Similar to the FV selection briefly presented in Section 5.3.5, the official `OpCarac` classification algorithm [58] can be employed to only select events that are fully CONTAINED in the ED of OPERA. With showers no longer leaking out of the instrumented volume, the overflow fix (see Section 5.4.2) can then be omitted. In addition, a separation of the hadronic and e.m. showers may be attempted by using parameterisations of their longitudinal and transverse profiles in comparison to the measured shower shape.

To improve ECC analysis, dedicated test beam measurements at the CERN PS using standard OPERA bricks, as well as custom 'two-brick' modules were performed. Reconstruction methods for connecting e.m. showers leaking out of the interaction brick and into the downstream one are in development.

Furthermore, in cooperation with the Yandex School of Data Analysis, machine learning techniques are trained on  $\nu_e$  interactions in OPERA ECC bricks. They will be used not only to provide a more accurate reconstruction of the electromagnetic showers and their energy, but also for the automated detection of  $\nu_e$  CC events in large volumes of emulsion data.

While not yet ready to be implemented for the OPERA analyses, future experiments such as SHiP [38] will benefit from these methods.



# Chapter 6

## $\nu_\mu \rightarrow \nu_e$ Oscillation Analysis

The relatively large<sup>1</sup>, nonzero value of  $\theta_{13}$  that was first measured in 2012 by reactor experiments [5, 35, 28] creates the opportunity for measurements of the neutrino mass ordering and CP violation (see Chapters 2.5.1 and 2.5.2).

It enables the OPERA experiment to do an electron neutrino appearance search, despite the CNGS beam contamination with  $\nu_e$  and  $\bar{\nu}_e$ . Sharing the high-energy CNGS beam and long baseline, both OPERA and the ICARUS experiment<sup>2</sup> also have good sensitivity to nonstandard oscillations with  $\Delta m^2 > 0.01 \text{ eV}^2$  and the regions of parameter space hinted to by measurements of the LSND [24] and MiniBooNE [25] collaborations.

For increasing the signal-to-noise ratio of oscillation signal  $\nu_e$  events and beam contamination, the analysis that was published in [16] relies on the Electronic Detector (ED)  $\nu_e$  energy reconstruction developed within the framework of this thesis (see Chapter 5). It furthermore requires a good knowledge of reconstruction and detection efficiencies for which several cross checks, both on simulated and real data, were conducted.

First, a brief overview of the analysed data sample and involved backgrounds will be given (Section 6.1). Apart from a standard 3-flavour  $\nu_\mu \rightarrow \nu_e$  oscillation analysis, Section 6.2 will then put special focus on nonstandard oscillations. The chapter is concluded in Section 6.3 with an outlook on a future analysis.

### 6.1 Data Sample

The data sample analysed in this  $\nu_\mu \rightarrow \nu_e$  oscillation study comprises the CNGS beam data collected in run years 2008 and 2009. It is the same data set in which OPERA's first  $\nu_\tau$  candidate event was detected [14] and corresponds to  $5.25 \times 10^{19}$  p.o.t. with 5255 neutrino interactions recorded in the OPERA target.

The 2008 data, encompassing  $1.73 \times 10^{19}$  p.o.t. and 1698 neutrino target interactions, were selected by visual inspection of the 10 121 **ONTIME** events registered in the ED and manually

---

<sup>1</sup>A global best fit using the data of 2016 yields  $\theta_{13} = (8.46 \pm 0.15)^\circ$  or  $\theta_{13} = (8.49 \pm 0.15)^\circ$  for normal and inverted mass orderings, respectively [86].

<sup>2</sup>In [42], ICARUS already provided severe limits on the nonstandard  $\nu_\mu \rightarrow \nu_e$  parameter space.

discarding external events and low-energy  $n$  or  $\gamma$  interactions [14]. For the 2009 sample of  $3.52 \times 10^{19}$  p.o.t., the `OpCarac` algorithm [58] was employed. It was optimised based on experience with the 2008 data and, after subsequent visual inspection, resulted in the selection of 3557 events.

Experimental event rates and position distributions are well reproduced by a MC simulation of the OPERA ED [13].

After ED event reconstruction (see Chapter 4.6.1), the first and second most probable bricks were studied following the  $\nu_\tau$  analysis chain described in Chapter 4.7.2. If hints for electromagnetic (e.m.) showers were found, the interactions were analysed according to the procedure defined for  $\nu_e$  candidate events (see Chapter 5.2).

### 6.1.1 $\nu_e$ Detection Efficiency

To estimate the overall detection efficiency for electron neutrino events, the propagation of a sample of MC-generated  $\nu_e$  interactions was simulated in both ECC and ED of OPERA [122].

Using GEANT 3.21, outgoing particles and e.m. showers are propagated in lead and emulsions of the OPERA bricks, followed by the ED TT scintillators and spectrometer detectors. The subsequent event reconstruction by the official `OpRec` and `OpEmuRec` packages (see Chapter 4.5.5) incorporates the full data analysis chain and employs the same algorithms as applied for real data.

The performance of the event reconstruction is evaluated separately for interaction location<sup>1</sup>  $\epsilon_{loc}^{\nu_e}$  and electron identification  $\epsilon_{id}^e$  efficiencies [122]. Both can be parameterised as exponential functions of the true neutrino energy  $E_{\nu,true}$ :

$$\epsilon = c_0 \cdot (1 - e^{-E_{\nu,true}/c_1}) \quad (6.1)$$

with fit constants  $c_0$  and  $c_1$ .

In order to optimise the experimental performance, scanning and analysis strategies were tuned during data taking. Their deviations are likewise studied in simulation, and the differences taken as systematic uncertainties on the detection efficiency. For  $\nu_e$  energies above 10 GeV, the resulting uncertainty is 10%, while at lower energies it is estimated as 20% due to the decreased number of tracks found in the CS [16].

Figure 6.1 shows the overall  $\nu_e$  detection efficiency  $\epsilon_{det}^{\nu_e}$  in 10 GeV-bins of  $E_{\nu,true}$ , including systematic uncertainties.

---

<sup>1</sup>Including ED characterisation by `OpCarac`, brick finding, CS analysis, track SB, brick-to-brick connection for penetrating tracks, vertex location.

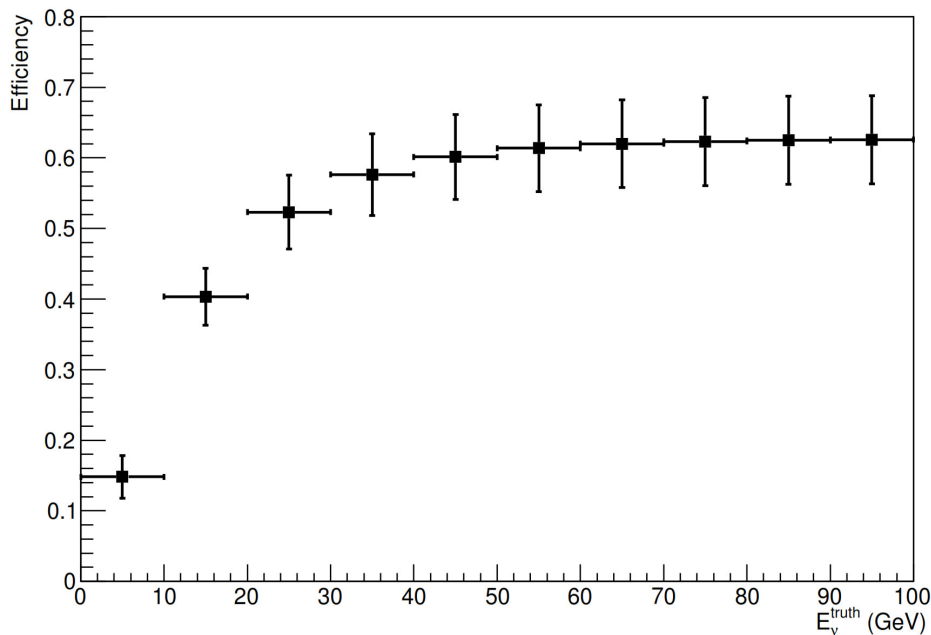


**Figure 6.1:**  $\nu_e$  detection efficiency  $\epsilon_{det}^{\nu_e}$  and systematic uncertainty per 10 GeV-bin of  $E_{\nu, true}$  [16]. The numbers are obtained using a GEANT 3.21-based MC simulation of  $\nu_e$  interactions in the OPERA detector, taking into account the complete data analysis chain.

### 6.1.2 $\nu_e$ Event Selection & Backgrounds

From the 2008 - 2009 data of 5 255 candidate neutrino interactions in the OPERA target, 2 853 events could be located with vertices reconstructed inside the bricks. With no long muon tracks reconstructed in the ED, 505 of these interactions are tagged as  $0\mu$  ( $\nu_\mu$  NC-like) and further analysed.

In this sample, 2 electron neutrino events were found during the standard  $\nu_\tau$  analysis by observing hints for e.m. showers in the Scan Back procedure. The dedicated CS shower search (see Chapter 5.2.2) led to the detection of another 17  $\nu_e$  candidate events, resulting in a total of 19 electron neutrino events.

#### Background from $\pi^0\gamma$ Conversion

The  $\nu_\mu$  CC background created by the decay of  $\pi^0 \rightarrow \gamma\gamma$  has been described in Chapter 5.2.3. To evaluate it, a real data sample of 1 106 neutrino interactions has been studied, including both  $\nu_\mu$  CC-like events and such without a reconstructed muon track [16]. Appropriate normalisation factors are introduced to take into account the different vertex location efficiencies (see Chapter 4.7.2) for  $1\mu$  and  $0\mu$  events.

E.m. showers are detected using the same strategies as utilised in the systematic  $\nu_e$  search. The interactions are then examined for  $\pi^0\gamma$  conversions and resulting  $e^+e^-$  pairs occurring in the three emulsion plates downstream from the primary neutrino interaction vertex (see Chapter 5.2.3).

Thus extended to the second and third emulsion sheet, the application of the  $\nu_e$  BG rejection leads to 1 out of 1106 background events surviving those cuts. Based on the radiation length, further normalisations are then employed to take into account the probability of the  $\gamma$  conversions occurring in the first lead plate downstream from the interaction vertex and their subsequent misidentification as signal events.

The resulting final  $\nu_\mu$  CC background expectation for the  $\nu_e$  search in the analysed sample of 505  $0\mu$  events is  $0.2 \pm 0.2$  events, which is compatible with earlier MC simulations [16]. Further BG from  $\pi^0$  Dalitz pair conversion can be neglected, as its contribution is expected to be an order of magnitude lower.

### Background from Electronic $\tau$ Decays

The BG from electronic decays of oscillated  $\tau$  neutrinos (see Chapter 4.7.1) to the  $\nu_e$  appearance search has been estimated using a MC simulation taking into account the full OPERA ECC data analysis chain. It assumes 3-flavour  $\nu_\mu \rightarrow \nu_\tau$  oscillations with  $\Delta m_{23}^2 = 2.32 \times 10^{-3} \text{ eV}^2$  and maximal mixing  $\sin^2(2\theta_{23}) = 1$ . The same strategy was also employed in the  $\nu_\tau$  appearance analysis published in [15].

Neutrino fluxes are given by the CNGS FLUKA simulation [93] described in Chapter 4.3.2. The generation of neutrino interactions in the detector is handled by the NEGN generator tuned to NOMAD data [51], followed by their propagation in the detector using OpEmuRec (see Chapter 4.5.5).

Simulated  $\nu_\tau$  events are weighted by the respective cross sections for DIS and QE interactions using the default GENIE 2.6.2 implementation [37] and normalised to the number of p.o.t. of the 2008 - 2009 data sample. Isoscalar corrections to account for the correct number of protons and neutrons in the  $^{208}\text{Pb}$  target nuclei are applied.

The resulting background expectation for the electron neutrino search is  $0.3 \pm 0.1$  events [16]. It mainly stems from short  $\tau$  decays with small impact parameters  $IP < 10 \mu\text{m}$  of the daughter electron w.r.t. the primary vertex that cannot be rejected by the  $\nu_e$  selection. A minor contribution is due to long  $\tau$  decays with undetected kink  $\theta_{kink} < 20 \text{ mrad}$  (see Chapter 5.2.3).

### Total BG to $\nu_e$ Search

Combining the two aforementioned sources of  $\pi^0\gamma$  conversion and  $\tau \rightarrow e$  decays, the total expected background to the search for  $\nu_e$  CC interactions in the analysed sample of 2008 - 2009 CNGS data is  $0.4 \pm 0.2$  events.



## 6.2 $\nu_e$ Appearance Search

Given the contamination of the CNGS beam with prompt  $\nu_e$  and  $\bar{\nu}_e$ , as well as the nonexistence of a near detector, the OPERA  $\nu_\mu \rightarrow \nu_e$  oscillation search requires a precise MC simulation of both neutrino beam and detector.

Details on the FLUKA simulation of the CNGS beam [93] are given in Chapter 4.3.2. The resulting unoscillated CNGS  $\nu_\mu$  energy spectrum at the LNGS site is shown in Figure 6.2, including the contaminations by other neutrino flavours. While the  $\nu_\mu$  flux visibly peaks between 10 GeV and 30 GeV, the distributions for  $\bar{\nu}_\mu$ ,  $\nu_e$ , and  $\bar{\nu}_e$  are more flat over the whole energy range.

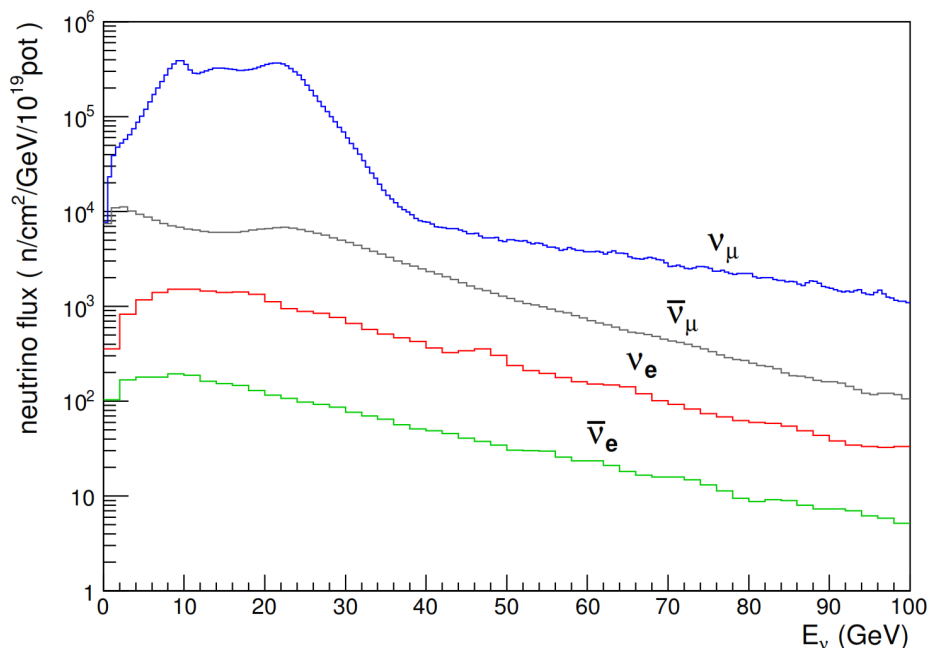


**Figure 6.2:** Unoscillated CNGS neutrino spectrum at the LNGS site, showing the contamination with  $\bar{\nu}_\mu$ ,  $\nu_e$ , and  $\bar{\nu}_e$  [16]. The distributions have been obtained from a FLUKA simulation of the CNGS target and beamline [93].

The neutrino fluxes are weighted by the respective CC cross sections (see Chapter 2.3) and energy-dependent detection efficiencies. For the 2008 - 2009 data sample, additional inefficiencies of 6% (2008) and 3% (2009) need to be taken into account to reflect a lower film quality of a small fraction of ECC bricks [16].

While the uncertainty on the  $\nu_e$  and  $\bar{\nu}_e$  beam contamination is conservatively estimated as 10%, the measurement sensitivity will be ultimately dominated by the small statistics of the data sample.

### 6.2.1 Background from Beam Contamination

The  $\nu_e$  and  $\bar{\nu}_e$  CNGS beam contamination constitutes the dominating BG to the  $\nu_\mu \rightarrow \nu_e$  appearance search with OPERA.

Taking into account the exposure of  $N_{p.o.t.} = 1.73 \times 10^{19}$  protons on target during the CNGS runs of 2008 - 2009 and an average detector target mass of  $M = 1.179$  kton, the expected number of observed  $\nu_e$  and  $\bar{\nu}_e$  events from beam contamination is calculated as [122]:

$$N_{beam}^{\nu_e, \bar{\nu}_e} = N_A \cdot N_{p.o.t.} \cdot M \cdot \int \Phi^{\nu_e, \bar{\nu}_e}(E) \cdot \sigma_{CC}^{\nu_e, \bar{\nu}_e}(E) \cdot \epsilon_{det}^{\nu_e}(E) dE \quad (6.2)$$

with  $N_A$  being the Avogadro constant,  $\Phi^{\nu_e, \bar{\nu}_e}$  the neutrino fluxes, and  $\sigma_{CC}^{\nu_e, \bar{\nu}_e}$  the respective energy-dependent CC cross sections in lead (see Chapter 2.3).  $\epsilon_{det}^{\nu_e}$  is the overall detection efficiency for electron neutrino events discussed in Section 6.1.1.

The integrated contaminations of  $\nu_e$  and  $\bar{\nu}_e$  in terms of neutrino CC interactions w.r.t. the rate of  $\nu_\mu$  are:

$$R_{CC}^{\nu_e/\nu_\mu} = 0.88\% \quad (6.3)$$

$$R_{CC}^{\bar{\nu}_e/\nu_\mu} = 0.05\% \quad (6.4)$$

Taking into account the energy-dependent detection efficiency and the spectral shape of the CNGS  $\nu_e$  and  $\bar{\nu}_e$  beam contaminations, and considering the additional above-mentioned inefficiencies of 6% and 3% for lower-quality emulsions (see Section 6.2), the energy-averaged detection efficiency is [16]:

$$\langle \epsilon_{det}^{\nu_e} \rangle = (53 \pm 5)\% \quad (6.5)$$

Limiting the range to energies smaller than 30 GeV or 20 GeV, it decreases accordingly:

$$\langle \epsilon_{det}^{\nu_e} \rangle = (43 \pm 5)\% \quad \text{for } E_\nu \leq 30 \text{ GeV} \quad (6.6)$$

$$\langle \epsilon_{det}^{\nu_e} \rangle = (35 \pm 4)\% \quad \text{for } E_\nu \leq 20 \text{ GeV} \quad (6.7)$$

Over the whole energy range, a number of  $19.4 \pm 2.8$   $\nu_e$  and  $\bar{\nu}_e$  events from CNGS beam contamination are expected to be observed in the analysed data sample.

Including the backgrounds from  $\pi^0\gamma$  conversion and electronic  $\tau$  decays (see Section 6.1.2), the total BG expectation increases to  $19.8 \pm 2.8$  events.

### 6.2.2 Reconstructed Energy

Considering the different spectra of unoscillated electron neutrinos from beam contamination and  $\nu_\mu \rightarrow \nu_e$  oscillations, a selection based on the neutrino energy will enhance the sensitivity of the  $\nu_e$  appearance search.

Figure 6.3 displays the energy spectrum of the 19  $\nu_e$  candidate events that was reconstructed according to the procedure outlined in Chapter 5.4. The measured values of  $E_{\nu,rec}$  are overlaid on stack histograms of the expected backgrounds from beam contamination,  $\pi^0\gamma$  conversion, and  $\tau \rightarrow e$  decays, normalised to the statistics of the 2008 - 2009 data sample. Also shown is the expectation for events from standard 3-flavour  $\nu_\mu \rightarrow \nu_e$  oscillations (see Section 6.2.3).

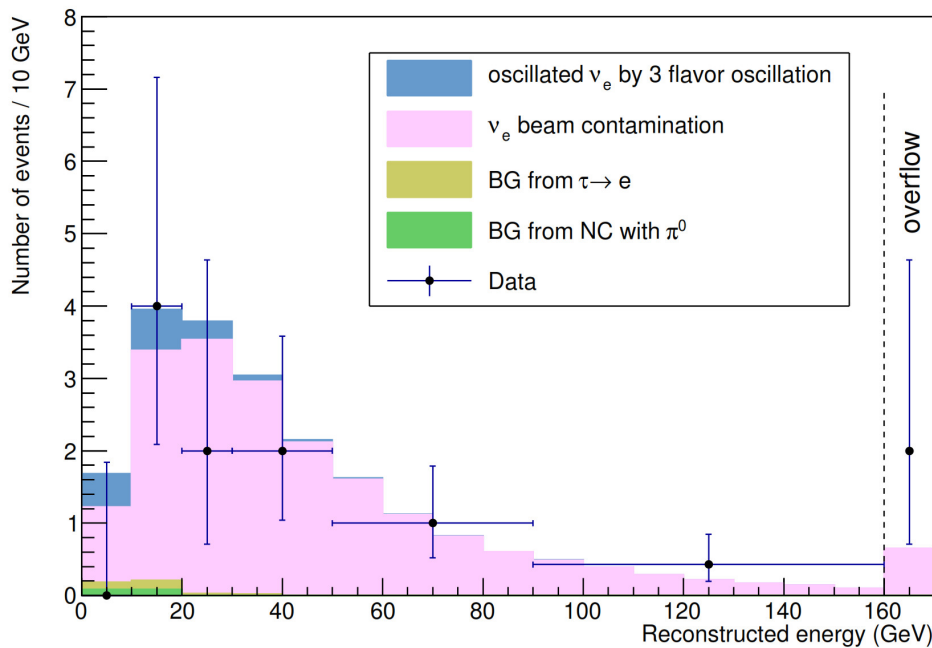


**Figure 6.3:** Reconstructed energy  $E_{\nu,rec}$  of the 19  $\nu_e$  candidate events detected in the 2008 - 2009 data sample, using the correction derived in Chapter 5.4 [16]. The overlaid spectra of MC-generated signal and BG events include oscillation probabilities (see Sections 6.1.2 and 6.2.3) and detection efficiencies taking into account the complete OPERA data analysis chain (see Section 6.1.1).

As is evident from the spectra, the exclusion of  $\nu_e$  candidates with higher reconstructed energies will have a positive impact on the signal-to noise ratio by mainly removing beam contamination events.

The expected detection rates for signal and BG events using no energy cut or possible selections of  $E_{\nu,rec} \leq 20$  GeV and  $E_{\nu,rec} \leq 30$  GeV are listed in Table 6.1, compared to the number of observed  $\nu_e$  candidates. These cuts will be of benefit to the oscillation analyses discussed in the next sections.

**Table 6.1:** Expected and observed  $\nu_e$  event numbers in the analysed sample of 2008 - 2009 data for different cuts on the reconstructed energy  $E_{\nu,rec}$  [16]. Listed are the BG contributions from  $\pi^0\gamma$  conversion,  $\tau \rightarrow e$  decays, and  $\nu_e$  and  $\bar{\nu}_e$  from beam contamination. The expected signal of standard 3-flavour  $\nu_\mu \rightarrow \nu_e$  oscillations was calculated according to Section 6.2.3. It constitutes an additional source of BG to the nonstandard oscillation search (see Section 6.2.4).

$E_{\nu,rec}$ [GeV]	Expected BG			Total BG	Signal	Total BG	Observed events
	$\pi^0$	$\tau \rightarrow e$	$\nu_e$ beam	3-flavour	3-flavour	nonst.	
$\leq 20$	0.2	0.2	4.2	4.6	1.0	5.6	4
$\leq 30$	0.2	0.3	7.7	8.2	1.3	9.4	6
No cut	0.2	0.3	19.4	19.8	1.4	21.3	19

### 6.2.3 $\nu_e$ Appearance Search: Standard 3-Flavour Scenario

Being the subdominant neutrino oscillation channel at the OPERA experiment,  $\nu_\mu \rightarrow \nu_e$  oscillations cannot be described using the 2-flavour approximation of Equation 2.67 (see Chapter 2.4.1).

The full 3-flavour parameterisation for  $\nu_\mu \rightarrow \nu_e$  oscillations in vacuum is given by Equation A.4 in Appendix A.1.3. For  $\delta_{CP} = 0$ , it can be approximated as [140]:

$$P_{\nu_\mu \rightarrow \nu_e}^{3flavour}(E) \simeq \sin^2(\theta_{13}) \cdot \sin^2(2\theta_{23}) \cdot \sin^2\left(1.27 \cdot \Delta m_{31}^2 [\text{eV}^2] \cdot \frac{L[\text{km}]}{E[\text{GeV}]}\right) \quad (6.8)$$

with  $L = 730$  km being the CNGS baseline and  $E$  the neutrino energy.

In analogy to Equation 6.2, the number of detected  $\nu_e$  events from 3-flavour  $\nu_\mu \rightarrow \nu_e$  oscillations is then calculated as:

$$N_{osc}^{\nu_e} = N_A \cdot N_{p.o.t.} \cdot M \cdot \int \Phi^{\nu_\mu}(E) \cdot P_{\nu_\mu \rightarrow \nu_e}^{3flavour}(E) \cdot \sigma_{CC}^{\nu_e}(E) \cdot \epsilon_{det}^{\nu_e}(E) dE \quad (6.9)$$

using the unoscillated CNGS  $\nu_\mu$  flux  $\Phi^{\nu_\mu}$  (see Chapter 4.3.2), the respective  $\nu_e$  CC interaction cross sections  $\sigma_{CC}^{\nu_e}$  (see Chapter 2.3), and the parameterisation for the  $\nu_e$  detection efficiency  $\epsilon_{det}^{\nu_e}$  described in Section 6.1.1.

Figure 6.4 shows the 3-flavour  $\nu_\mu \rightarrow \nu_e$  oscillation probability for different values of  $\theta_{13}$ , superimposed on the total  $\nu_e$  CC cross section in lead. The oscillation probability shows a maximum at low energies  $E_\nu < 10$  GeV, while the cross section rises with increasing energy.

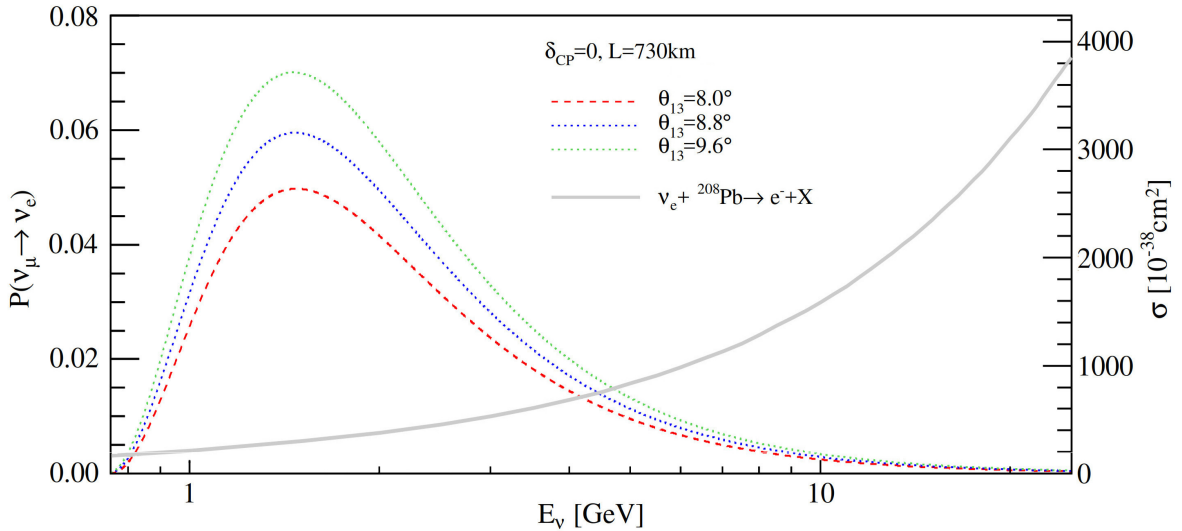


**Figure 6.4:** 3-flavour  $\nu_\mu \rightarrow \nu_e$  oscillation probability vs.  $E_\nu$  for different values of  $\theta_{13}$ ,  $\Delta m_{31}^2 = 2.5 \times 10^{-3} \text{ eV}^2$ ,  $\delta_{CP} = 0$ , and the OPERA baseline of  $L = 730$  km [91]. The total  $\nu_e$  CC cross section in lead is superimposed.

### Parameters & Prediction

The number of expected  $\nu_e$  interactions is estimated according to Equation 6.9 using the world best fit parameters of 2012 [57]:

$$\Delta m_{31}^2 \simeq \Delta m_{32}^2 = (2.32_{-0.08}^{+0.12}) \times 10^{-3} \text{ eV}^2 \quad (6.10)$$

$$\sin^2(2\theta_{13}) = 0.098 \pm 0.013 \quad (6.11)$$

and neglecting matter effects (see Chapter 2.4.2), assuming maximal mixing in  $\theta_{23}$ , normal mass ordering (see Chapter 2.5.1), and CP conservation (see Chapter 2.5.2):

$$\sin^2(2\theta_{23}) = 1 \quad (6.12)$$

$$\delta_{CP} = 0 \quad (6.13)$$

Over the whole energy range,  $1.4 \pm 0.2$  oscillated  $\nu_e$  CC events are thus expected to be detected, with a total BG from beam contamination,  $\tau \rightarrow e$ , and  $\pi^0\gamma$  events of  $19.8 \pm 2.8$ , and 19 observed  $\nu_e$  candidate events (compare Table 6.1).

### Energy Selection & Results

The best sensitivity to  $\theta_{13}$  for OPERA is attained by introducing a cut on the reconstructed neutrino energy of  $E_{\nu,rec} \leq 20$  GeV that improves the signal-to-noise ratio by removing most of the  $\nu_e$  beam contamination.

4 real data candidate events survive this selection, with an expectation of  $4.6 \pm 0.7$  events from BG and  $1.0 \pm 0.2$  signal events (see Table 6.1). Given the large uncertainties, the number of observed  $\nu_e$  interactions is compatible with the no-oscillation hypothesis.

To derive limits on the neutrino oscillation parameter space, the statistical method developed by Feldman & Cousins (FC) [88] is used. While based on the Neyman classical frequentist approach, it is able to provide two-sided limits, allows for complicated structures, and avoids unphysical confidence intervals. Contrary to the Bayesian method [78], no reliance on subjective or uniform priors exists.

The resulting 90% C.L. exclusion plot in  $\sin^2(2\theta_{13})$  and  $\Delta m_{31}^2$  is shown in Figure 6.5.

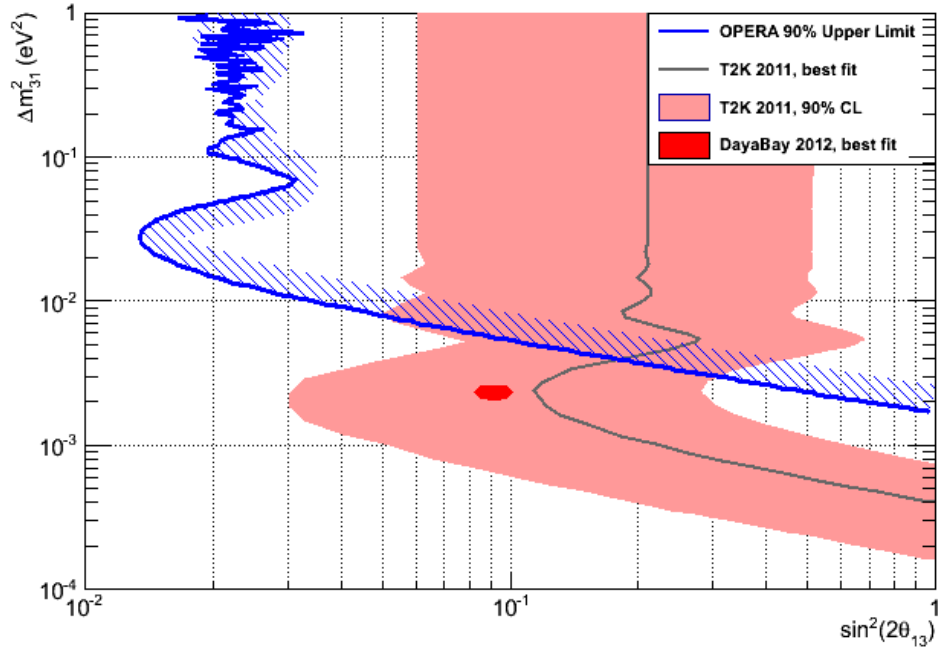


**Figure 6.5:**  $\nu_\mu \rightarrow \nu_e$  3-flavour oscillations exclusion plot in the  $\sin^2(2\theta_{13})$  and  $\Delta m_{31}^2$  parameter space. 90% C.L. limits for OPERA are derived using the FC method and overlaid on previous results from T2K [3] and DayaBay [35].

For the global best fit value of  $\Delta m_{31}^2 = 2.32 \times 10^{-3} \text{ eV}^2$ , the upper limit on the mixing angle is  $\sin^2(2\theta_{13}) < 0.44$  at 90% C.L. [16].

The ratio  $L/E$  of an experiment's baseline and average neutrino energy defines its sensitivity w.r.t. different values of  $\Delta m^2$  (see Equation 6.8).

With its long baseline of  $L = 730 \text{ km}$  and high CNGS  $\nu_\mu$  energy of  $\langle E \rangle = 17.9 \text{ GeV}$  (see Figure 6.2), the OPERA experiment provides good coverage for  $\Delta m_{31}^2 \gtrsim 0.01 \text{ eV}^2$  [140]. Considering the world best fit parameters for 3-flavour neutrino oscillations, however, OPERA is less suited for measuring the  $\nu_\mu \rightarrow \nu_e$  transitions expected to occur at lower energies (compare Figure 6.4).

Operating at energies  $\mathcal{O}(\text{MeV})$ , reactor  $\bar{\nu}_e$  experiments with baselines of  $1 \text{ km} - 100 \text{ km}$  are able to provide better sensitivity on small parameter values down to  $\Delta m_{31}^2 \gtrsim 10^{-5} \text{ eV}^2$ .

### 6.2.4 $\nu_e$ Appearance Search: Nonstandard Oscillations

Positive indications for nonstandard neutrino oscillations arise from measurements conducted by the LSND ( $\bar{\nu}_\mu \rightarrow \bar{\nu}_e$ ) [24] and MiniBooNE ( $\nu_\mu \rightarrow \nu_e, \bar{\nu}_\mu \rightarrow \bar{\nu}_e$ ) [25] experiments (see Chapter 2.5.3). A 4th sterile neutrino state with a mass  $\mathcal{O}(\text{eV})$  might also explain the anomalies measured in reactor [134] and radioactive source experiments [115, 2].

With favoured large values of the new squared mass difference w.r.t. the standard 3-flavour oscillation parameters (i.e.  $\Delta m_{new}^2 \gg \Delta m_{32}^2 \simeq \Delta m_{31}^2$ ) an effective 2-flavour approximation (compare Equation 2.67, Chapter 2.4.1) may be used to describe the dominant oscillation probability:

$$P_{\nu_\mu \rightarrow \nu_e}^{nonst.}(E) \simeq \sin^2(2\theta_{new}) \cdot \sin^2\left(1.27\Delta m_{new}^2[\text{eV}^2] \frac{L[\text{km}]}{E[\text{GeV}]}\right) \quad (6.14)$$

at the baseline of OPERA ( $L = 730 \text{ km}$ ) and assuming  $\delta_{CP} = 0$ . The results will however be not directly comparable to the different  $L/E$  ratios of short-baseline experiments [59].

The number of expected  $\nu_e$  events from nonstandard  $\nu_\mu \rightarrow \nu_e$  oscillations is then given by:

$$N_{osc}^{\nu_e} = N_A \cdot N_{p.o.t.} \cdot M \cdot \int \Phi^{\nu_\mu}(E) \cdot P_{\nu_\mu \rightarrow \nu_e}^{nonst.}(E) \cdot \sigma_{CC}^{\nu_e}(E) \cdot \epsilon_{det}^{\nu_e}(E) dE \quad (6.15)$$

with  $N_A$ ,  $N_{p.o.t.}$ ,  $M$ ,  $\Phi^{\nu_\mu}$ ,  $\sigma_{CC}^{\nu_e}$ , and  $\epsilon_{det}^{\nu_e}$  defined analogue to Equations 6.2 and 6.9.

At large  $\Delta m_{new}^2$ , the spectrum of oscillated  $\nu_e$  will basically be following that of the CNGS  $\nu_\mu$  flux (see Figure 6.2) and thus mostly vanish for  $E_\nu > 40 \text{ GeV}$  [16].

### Parameters & Prediction

In addition to the BGs from  $\nu_e$  beam contamination,  $\tau \rightarrow e$  decays, and  $\pi^0\gamma$  conversion (see Table 6.1), also the  $\nu_e$  events from standard 3-flavour oscillations now have to be treated as a source of background.

Using the same parameters and equations as in Section 6.2.3 for the estimation of this contribution, the total expected BG to the nonstandard  $\nu_\mu \rightarrow \nu_e$  oscillation search is  $21.3 \pm 3.0$  events.

### Energy Selection & Results

To improve the signal-to-noise ratio and sensitivity, a cut on the reconstructed energy of  $\nu_e$  events is conducted. The best figure of merit was found for a selection of  $E_{\nu,rec} \leq 30$  GeV (compare Table 6.2). This reduces the total background to  $9.4 \pm 1.3$  events (see Table 6.1), while keeping  $\sim 69\%$  of the expected signal for large  $\Delta m_{new}^2$  [16].

The number of 6 observed  $\nu_e$  events surviving this energy cut in the real data sample is lower than the background expectation. To render the upper limit on  $\sin^2(2\theta_{new})$  independent of the expected background, not only FC confidence intervals [88] on the parameter space of  $\sin^2(2\theta_{new})$  and  $\Delta m_{new}^2$  are calculated, but also Bayesian credible intervals [78]. In the latter case, the prior is set to 0 in the unphysical region and to a constant in the physical region. BG uncertainties are treated according to [57].

Table 6.2 lists the results of both methods for different cuts on  $E_{\nu,rec}$  assuming large values of  $\Delta m_{new}^2$ . FC 90% C.L. upper limits are obtained by comparing the number of observed events with the expectation from BGs and signal. The sensitivity is calculated for an assumed number of 9 observed events<sup>1</sup>. It represents the average upper limit that would be obtained by experiments observing the expected background in the presence of no signal.

**Table 6.2:** 90% upper limits and sensitivities on  $\sin^2(2\theta_{new})$  for  $\Delta m_{new}^2 \sim 1 \text{ eV}^2$  obtained by the FC and Bayes methods for different cuts on the reconstructed neutrino energy  $E_{\nu,rec}$  [16].

$E_{\nu,rec}$ [GeV]	Upper limit		Sensitivity	
	FC	Bayes	FC	Bayes
$\leq 20$	$8.5 \times 10^{-3}$	$10.4 \times 10^{-3}$	$14.2 \times 10^{-3}$	$14.2 \times 10^{-3}$
$\leq 30$	$5.0 \times 10^{-3}$	$7.2 \times 10^{-3}$	$9.7 \times 10^{-3}$	$10.4 \times 10^{-3}$
No cut	$8.6 \times 10^{-3}$	$9.5 \times 10^{-3}$	$10.8 \times 10^{-3}$	$11.0 \times 10^{-3}$

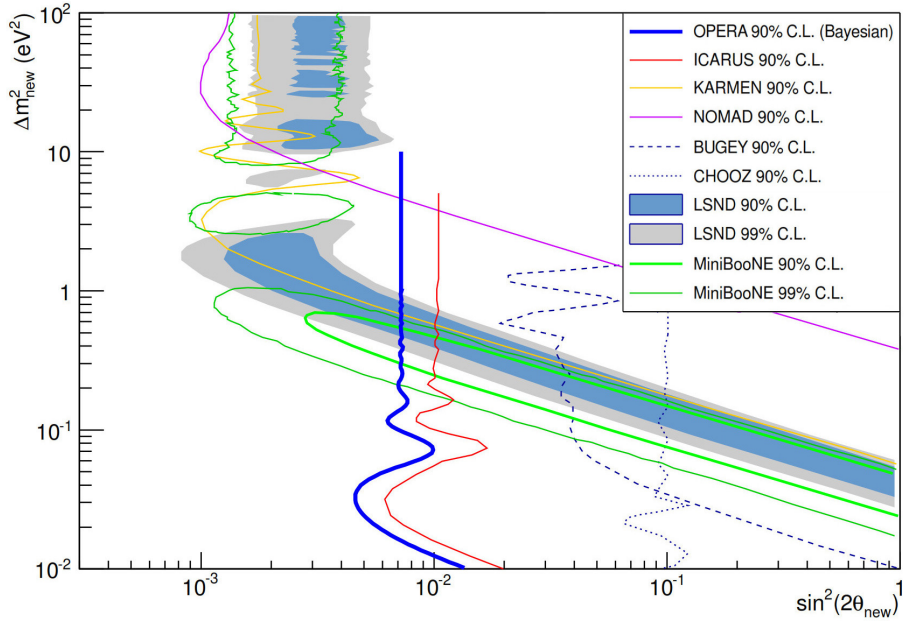
With the present underfluctuation of the data w.r.t. the expected BG in the selected region of  $E_{\nu,rec}$ , the Bayes method is considered to provide the most reliable results. Over the whole energy range, the deficit is less pronounced (compare Table 6.1), and the differences between the FC and Bayes results decrease.

Figure 6.6 shows the resulting 90% C.L. exclusion plot in the  $\sin^2(2\theta_{new})$  and  $\Delta m_{new}^2$  parameter space, together with previous limits from ICARUS<sup>2</sup>. Though not directly comparable in this 2-flavour approximation due to their different ratios of  $L/E$ , limits and indications from short-baseline experiments are superimposed for illustrative purposes.

<sup>1</sup>9 being the closest integer to the BG expectation of 9.4 events.

<sup>2</sup>Sharing the CNGS beam and baseline (and even using the same cut on the reconstructed neutrino energy), the results from ICARUS and OPERA would have been directly comparable but for the fact that the ICARUS collaboration chose to employ the FC method in [42].





**Figure 6.6:**  $\nu_\mu \rightarrow \nu_e$  nonstandard oscillations exclusion plot in the  $\sin^2(2\theta_{new})$  and  $\Delta m_{new}^2$  parameter space [16]. 90% C.L. limits for OPERA are derived using the Bayes method and overlaid on previous (mostly frequentist) limits from ICARUS ( $\nu_\mu \rightarrow \nu_e$ ) [42], KARMEN ( $\bar{\nu}_\mu \rightarrow \bar{\nu}_e$ ) [45], NOMAD ( $\nu_\mu \rightarrow \nu_e$ ) [50], BUGEY ( $\bar{\nu}_e \rightarrow \bar{\nu}_e$ ) [82], and CHOOZ ( $\bar{\nu}_e \rightarrow \bar{\nu}_e$ ) [43]. Also shown are the positive indications by LSND ( $\bar{\nu}_\mu \rightarrow \bar{\nu}_e$ ) [24] and MiniBooNE ( $\nu_\mu \rightarrow \nu_e, \bar{\nu}_\mu \rightarrow \bar{\nu}_e$ ) [25].

For large values of  $\Delta m_{new}^2 \sim 1 \text{ eV}^2$ , the present  $\nu_\mu \rightarrow \nu_e$  nonstandard oscillation analysis studying the 2008 - 2009 CNGS data sample thus allows to exclude values of  $\sin^2(2\theta_{new}) > 7.2 \times 10^{-3}$  at 90% C.L.

Given the analysed number of  $5.25 \times 10^{19}$  p.o.t., the sensitivity of OPERA to the new mixing angle extends down to  $\sin^2(2\theta_{new}) > 10.4 \times 10^{-3}$ .

## 6.3 Outlook

An upcoming analysis of the full 2008 - 2012 CNGS beam data collected by OPERA will comprise a total of 18 941 neutrino detector interactions, corresponding to  $17.97 \times 10^{19}$  p.o.t.

The factor 3.4 increase in statistics will allow the introduction of FV cuts that guarantee a better ED containment of e.m. and hadronic showers. Based on their different longitudinal and transversal profiles, and the information gained by the  $\nu_e$  interaction vertex reconstruction in the ECC bricks, a separation of both shower types is then conducted [22]. This will decrease the uncertainty on the reconstructed  $\nu_e$  energy in the OPERA ED, where a calorimetric measurement can be performed for the hadronic shower part in the TT, while the electron's energy is estimated by the e.m. shower shape.

Rather than applying a cut on the reconstructed energy of  $\nu_e$  events to decrease background contributions, a spectral shape analysis will then be performed on the larger data sample to provide limits on the parameter space for nonstandard  $\nu_\mu \rightarrow \nu_e$  oscillations.

### Global Picture in 2018

The current global knowledge on neutrino oscillations, comprising the search for light sterile neutrinos, is summarised in Figure 6.7 [140]. It includes the limits on  $\nu_\mu \rightarrow \nu_e$  nonstandard oscillations obtained by OPERA in the present analysis.

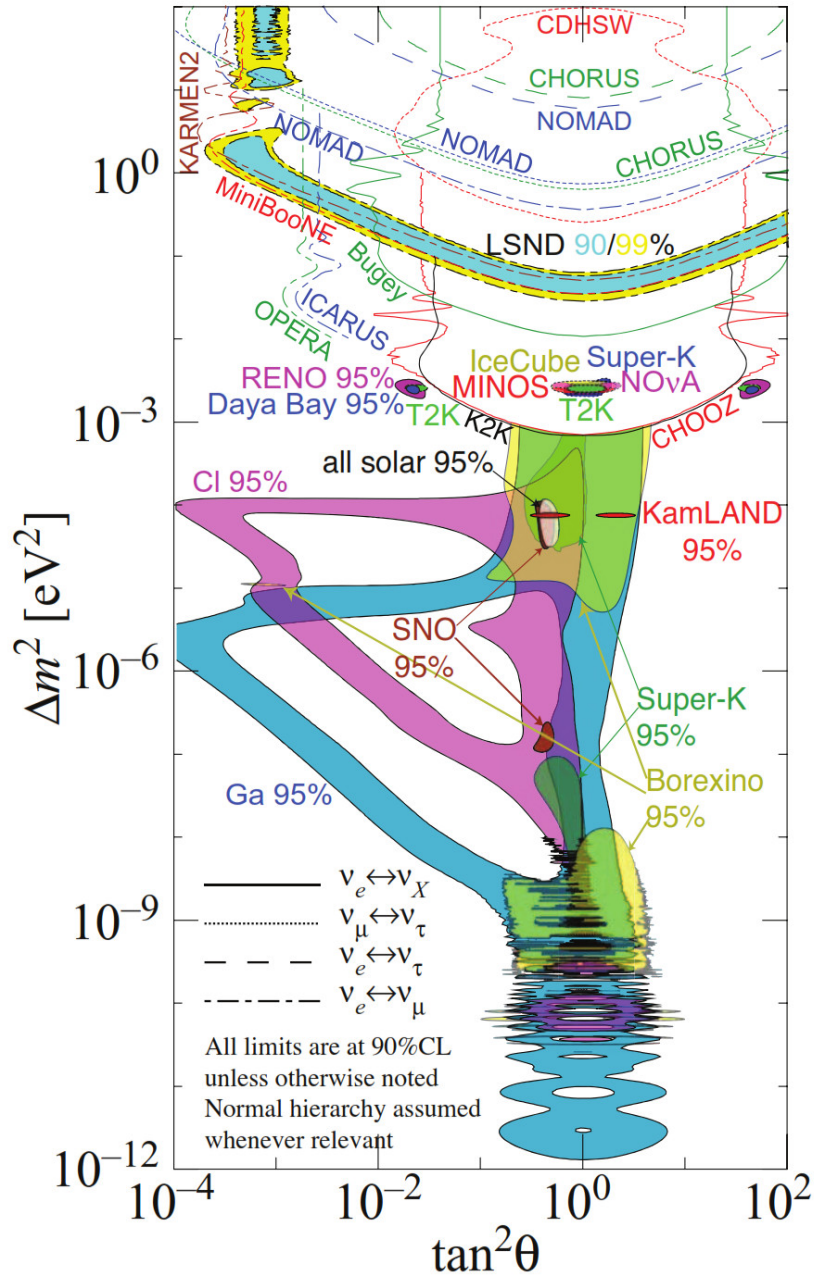


**Figure 6.7:** Global picture of neutrino oscillations in 2018, showing excluded regions and indications from various neutrino oscillation experiments [140].

Global fits using '3+1' or '3+2' models are trying to reconcile all experimental results (see e.g. [99]), and data from future experiments should soon be able to provide definite answers to the contemporary 'sterile neutrino' anomalies.

# Chapter 7

## Conclusion

OPERA is a neutrino oscillation experiment with the main goal of detecting  $\nu_\mu \rightarrow \nu_\tau$  oscillations by studying the CNGS high-energy  $\nu_\mu$  beam at a baseline of 730 km. It is designed to provide a measurement of  $\tau$  neutrino appearance on an event-by-event basis. Able to resolve the topology of  $\tau$  lepton creation in  $\nu_\tau$  CC interactions and their subsequent decay, the realised detector is a complex hybrid apparatus:

150 000 Emulsion Cloud Chamber bricks, made from lead and nuclear emulsions, provide both target mass and high-resolution tracking. Using automatic scanning microscopes, neutrino interactions can be reconstructed at micrometric precision. With an overall sensitive emulsion area of  $\sim 110\,000\text{ m}^2$ , OPERA relies on electronic detector components to timestamp and locate neutrino interactions within the bricks. Target Tracker scintillator strips instrumenting the ECC target are used to reconstruct hadronic showers, and a downstream magnetic spectrometer provides muon identification and momentum measurement.

The principal  $\nu_\mu \rightarrow \nu_\tau$  oscillation analysis is quasi background-free [20]. Concerning the search for electron neutrino appearance from the sub-leading channel of  $\nu_\mu \rightarrow \nu_e$  oscillations, the CNGS beam contamination with prompt  $\nu_e$  and  $\bar{\nu}_e$  however provides a background that has to be taken into account. As the experiment does not feature a near detector for measuring the original neutrino fluxes, a crucial part of the oscillation search is a reliable MC simulation of both beam and detector. Neutrino interactions and cross sections need to be well understood, and the efficiencies of all sub-detectors and analysis steps must be known.

Within the scope of this thesis, several cross checks on reconstructed events and detector efficiencies were conducted, using both real and simulated data. A calibration was developed that provides an estimation of the original electron neutrino's energy based on the OPERA Electronic Detector data.  $\nu_e$  CC interactions within the OPERA detector were generated using a GENIE simulation and the FLUKA CNGS beam spectra. The Electronic Detector response was simulated in the official OPERA software framework, taking into account the complete data analysis chain.

The resulting energy estimation for  $\nu_e$  events was successfully applied in the first search for  $\nu_\mu \rightarrow \nu_e$  appearance with OPERA, using the CNGS data of 2008 - 2009 [16]. Cuts on the reconstructed neutrino energy, improving the signal-to-noise ratio for both the 3-flavour and the nonstandard oscillation analysis by removing beam-induced background, could be performed.

While being less sensitive to the 3-flavour oscillation scenario, the OPERA nonstandard  $\nu_\mu \rightarrow \nu_e$  analysis was able to provide improved limits on the parameter space of  $\sin^2(2\theta_{new})$  and  $\Delta m_{new}^2$ . For large values of  $\Delta m_{new}^2 \sim 1 \text{ eV}^2$ , values of  $\sin^2(2\theta_{new}) > 7.2 \times 10^{-3}$  are excluded at 90% C.L.

An upcoming publication describes a  $\nu_\mu \rightarrow \nu_e$  analysis within the complete OPERA data set of 2008 - 2012 [22]. With larger available statistics, FV cuts are introduced that had to be discarded in the present analysis due to low event numbers. Given the better containment of the events, kinematical variables related to the e.m. shower shape can be used to improve the energy resolution.

The detailed reconstruction of the event topology in the OPERA ECC analysis allows to identify  $\nu_e$  CC interactions and reject backgrounds. Due to the electromagnetic showers leaking out of the brick, it however cannot provide a reliable energy measurement for  $\nu_e$  CC interactions. Test beam measurements at the CERN PS EA using electron-enriched pion beams of 2 GeV and 4 GeV were conducted to analyse and reconstruct the development of electromagnetic showers in custom 2-brick ECC modules. Their study provides valuable insight for the automated reconstruction of such interactions in ECC detectors, but the algorithms were not yet ready to be implemented in the present analyses.

Though OPERA finished data taking in 2012 and the final analyses are now concluding [21, 22], future experiments will benefit from its technologies and expertise:

Parts of the OPERA Target Tracker will directly be used as a cosmic muon veto for the JUNO experiment, and the development of improved nuclear emulsion films and automated scanning methods enables several low-background and tomographic experiments. As a direct successor, the neutrino detector of the proposed SHiP experiment at the CERN SPS [38] will make use of OPERA-like ECC bricks to study an expected number of  $\mathcal{O}(1000)$   $\tau$  neutrino CC interactions.

# Appendix A

## Appendix

### A.1 3-Flavour Neutrino Oscillations in Vacuum

The full 3-flavour oscillation probabilities for  $\nu_\mu \rightarrow \nu_\mu$ ,  $\nu_\mu \rightarrow \nu_\tau$ , and  $\nu_\mu \rightarrow \nu_e$  transitions in vacuum (see Chapter 2.4.1) are listed in the following [155].

Approximations are commonly introduced by assuming  $\delta_{CP} = 0$ , and the dominance of one transition over the other at a given experiment's ratio of baseline  $L$  and neutrino energy  $E$ .

The equations make use of the Jarlskog invariant  $J$ :

$$J = \frac{1}{8} \cdot \sin(2\theta_{12}) \cdot \sin(2\theta_{23}) \cdot \sin(2\theta_{13}) \cdot \cos(\theta_{13}) \cdot \sin(\delta_{CP}) \quad (\text{A.1})$$

#### A.1.1 $\nu_\mu \rightarrow \nu_\mu$ Survival Probability

$$\begin{aligned} P_{\nu_\mu \rightarrow \nu_\mu}(L, E) = & 1 - \left( \sin^2(2\theta_{23}) \sin^2(\theta_{13}) \cdot \left( 1 - \frac{1}{2} \sin^2(2\theta_{12}) \right) \right. \\ & + \sin^2(2\theta_{12}) \cdot \left( \cos^4(\theta_{23}) + \sin^4(\theta_{23}) \sin^2(\theta_{13}) \right) \\ & + \sin(4\theta_{12}) \sin(2\theta_{23}) \sin(\theta_{13}) \cdot \left( \cos^2(\theta_{23}) - \sin^2(\theta_{23}) \sin^2(\theta_{13}) \right) \cdot \cos(\delta_{CP}) \\ & \left. - \sin^2(2\theta_{12}) \sin^2(2\theta_{23}) \sin^2(\theta_{13}) \cos^2(\delta_{CP}) \right) \cdot \sin^2 \left( \frac{\Delta m_{21}^2 L}{4E} \right) \\ & - 4 \left( \sin^2(\theta_{23}) \cos^2(\theta_{13}) \cdot \left( \cos^2(\theta_{12}) \cos^2(\theta_{23}) + \sin^2(\theta_{12}) \sin^2(\theta_{23}) \sin^2(\theta_{13}) \right) \right. \\ & \left. - \frac{1}{2} \sin(2\theta_{12}) \sin(2\theta_{23}) \sin(\theta_{13}) \cos(\delta_{CP}) \right) \cdot \sin^2 \left( \frac{\Delta m_{32}^2 L}{4E} \right) \\ & - 4 \left( \sin^2(\theta_{23}) \cos^2(\theta_{13}) \cdot \left( \sin^2(\theta_{12}) \cos^2(\theta_{23}) + \cos^2(\theta_{12}) \sin^2(\theta_{23}) \sin^2(\theta_{13}) \right) \right. \\ & \left. + \frac{1}{2} \sin(2\theta_{12}) \sin(2\theta_{23}) \sin(\theta_{13}) \cos(\delta_{CP}) \right) \cdot \sin^2 \left( \frac{\Delta m_{31}^2 L}{4E} \right) \end{aligned} \quad (\text{A.2})$$

### A.1.2 $\nu_\mu \rightarrow \nu_\tau$ Appearance Probability

$$\begin{aligned}
P_{\nu_\mu \rightarrow \nu_\tau}(L, E) = & \left( -\frac{1}{4} \sin^2(2\theta_{12}) \sin^2(2\theta_{23}) \cdot \left(1 + \sin^2(\theta_{13})\right)^2 \right. \\
& + \sin^2(\theta_{13}) \cdot \left( \sin^2(2\theta_{12}) + \sin^2(2\theta_{23}) \right) \\
& + \frac{1}{4} \sin(4\theta_{12}) \sin(4\theta_{23}) \sin(\theta_{13}) \cdot \left(1 + \sin^2(\theta_{13})\right) \cdot \cos(\delta_{CP}) \\
& \left. - \sin^2(2\theta_{12}) \sin^2(2\theta_{23}) \sin^2(\theta_{13}) \cos^2(\delta_{CP}) \right) \cdot \sin^2\left(\frac{\Delta m_{21}^2 L}{4E}\right) \\
& + \sin(2\theta_{23}) \cos^2(\theta_{13}) \cdot \left( \sin(2\theta_{23}) \cdot \left( \cos^2(\theta_{12}) - \sin^2(\theta_{12}) \sin^2(\theta_{13}) \right) \right. \\
& \left. + \sin(2\theta_{12}) \cos(2\theta_{23}) \sin(\theta_{13}) \cos(\delta_{CP}) \right) \cdot \sin^2\left(\frac{\Delta m_{32}^2 L}{4E}\right) \\
& - \sin(2\theta_{23}) \cos^2(\theta_{13}) \cdot \left( \sin(2\theta_{23}) \cdot \left( \cos^2(\theta_{12}) \sin^2(\theta_{13}) - \sin^2(\theta_{12}) \right) \right. \\
& \left. + \sin(2\theta_{12}) \cos(2\theta_{23}) \sin(\theta_{13}) \cos(\delta_{CP}) \right) \cdot \sin^2\left(\frac{\Delta m_{31}^2 L}{4E}\right) \\
& \pm 2J \left( \sin\left(\frac{\Delta m_{21}^2 L}{2E}\right) + \sin\left(\frac{\Delta m_{32}^2 L}{2E}\right) - \sin\left(\frac{\Delta m_{31}^2 L}{2E}\right) \right) \quad (\text{A.3})
\end{aligned}$$

with the + sign in the last line referring to neutrinos, the – sign to anti-neutrinos.

The 2-flavour approximation assumed for the OPERA  $\nu_\mu \rightarrow \nu_\tau$  oscillation analysis is given by Equation 4.2, Chapter 4.1.

**A.1.3  $\nu_\mu \rightarrow \nu_e$  Appearance Probability**

$$\begin{aligned}
P_{\nu_\mu \rightarrow \nu_e}(L, E) = & \left( \sin^2(2\theta_{12}) \cos^2(\theta_{13}) \cdot \left( \sin^2(2\theta_{12}) \cdot \left( \cos^2(\theta_{23}) - \sin^2(\theta_{23}) \sin^2(\theta_{13}) \right) \right. \right. \\
& \left. \left. + \cos(2\theta_{12}) \sin(2\theta_{23}) \sin(\theta_{13}) \cos(\delta_{CP}) \right) \right) \cdot \sin^2 \left( \frac{\Delta m_{21}^2 L}{4E} \right) \\
& + 4 \left( \sin(\theta_{12}) \sin(\theta_{23}) \sin(\theta_{13}) \cos^2(\theta_{13}) \cdot \left( \sin(\theta_{12}) \sin(\theta_{23}) \sin(\theta_{13}) \right. \right. \\
& \left. \left. - \cos(\theta_{12}) \cos(\theta_{23}) \cos(\delta_{CP}) \right) \right) \cdot \sin^2 \left( \frac{\Delta m_{32}^2 L}{4E} \right) \\
& + 4 \left( \cos(\theta_{12}) \sin(\theta_{23}) \sin(\theta_{13}) \cos^2(\theta_{13}) \cdot \left( \cos(\theta_{12}) \sin(\theta_{23}) \sin(\theta_{13}) \right. \right. \\
& \left. \left. + \sin(\theta_{12}) \cos(\theta_{23}) \cos(\delta_{CP}) \right) \right) \cdot \sin^2 \left( \frac{\Delta m_{31}^2 L}{4E} \right) \\
& \pm 2J \left( \sin \left( \frac{\Delta m_{21}^2 L}{2E} \right) + \sin \left( \frac{\Delta m_{32}^2 L}{2E} \right) - \sin \left( \frac{\Delta m_{31}^2 L}{2E} \right) \right) \quad (\text{A.4})
\end{aligned}$$

with the + sign in the last line referring to neutrinos, the – sign to anti-neutrinos.

The approximation assumed for the OPERA  $\nu_\mu \rightarrow \nu_e$  oscillation analysis is given by Equation 6.8, Chapter 6.2.3.





# List of Abbreviations

$\nu$ MSM	Neutrino Minimal Standard Model
ADC	analog-to-digital converter
ALEPH	Apparatus for LEP Physics
ANN	artificial neural network
ASIC	application-specific integrated circuit
ATLAS	A Toroidal LHC ApparatuS
BDT	Boosted Decision Tree
BF	Brick Finding
BG	background
BMM	Brick Manipulation Manager
BMS	Brick Manipulator System
BNL	Brookhaven National Laboratory
BOREXino	named after BORon solar neutrino EXperiment
BR	branching ratio
BT	base-track
BUGEY	Bugey reactor neutrino experiment
c.c.	charge conjugate
C.L.	Confidence Level
C0BRA	Cadmium Zinc Telluride 0-Neutrino Double-Beta Research Apparatus
CA	cellular automaton
CC	Charged Current
CCD	charge-coupled device
CERN	Conseil Européen pour la Recherche Nucléaire
CHOOZ	Chooz reactor neutrino experiment
CHORUS	CERN Hybrid Oscillation Research apparatus
CMOS	complementary metal-oxide-semiconductor
CMS	Compact Muon Solenoid
CNGS	CERN Neutrinos to Gran Sasso
CP	Charge-Parity
CPT	Charge-Parity-Time
CPU	central processing unit
CS	Changeable Sheet

---

DAQ	data acquisition
DIS	deep-inelastic scattering
DONuT	Direct Observation of Nu Tau
DS	Decay Search
e.m.	electromagnetic
EA	East Area
ECC	Emulsion Cloud Chamber
ECHo	Electron Capture in $^{163}\text{Ho}$
ECM	Ethernet Controller Mezzanine
ED	Electronic Detector
EL	elastic
ESS	European Scanning System
FC	Feldman & Cousins
FermiLab	Fermi National Accelerator Laboratory
FLUKA	FLUktierende KAskade
FSI	final state interactions
FV	fiducial volume
GALLEX	Gallium Experiment
GEANT	GEometry ANd Tracking
GENIE	Generates Events for Neutrino Interaction Experiments
GERDA	GERmanium Detector Array
GPS	Global Positioning System
GRPC	glass RPC
GWS	Glashow Weinberg Salam
HV	high voltage
ICARUS	Imaging Cosmic And Rare Underground Signals
IMB	Irvine-Michigan-Brookhaven
IO	Inverted Ordering
JUNO	Jiangmen Underground Neutrino Observatory
KARMEN	KARlsruhe Rutherford Medium Energy Neutrino experiment
KATRIN	KARlsruhe TRItium Neutrino
LED	light-emitting diode
LEP	Large Electron Positron Collider
LHC	Large Hadron Collider
LNGS	Laboratori Nazionali del Gran Sasso
LSM	least squares method
LSND	Liquid Scintillator Neutrino Detector
LVDS	Low Voltage Differential Signaling
m.i.p.	minimum ionising particle
m.w.e.	meters water equivalent

---

MC	Monte Carlo
MCS	Multiple Coulomb Scattering
MiniBooNE	Mini Booster Neutrino Experiment
MINOS	Main Injector Neutrino Oscillation Search
MLP	Multi-Layer Perceptron
MO	Mass Ordering
MSW	Mikheyev Smirnov Wolfenstein
MT	micro-track
NA56/SPY	NA56 / Secondary Particle Yield
NC	Neutral Current
NEGN	Neutrino Event Generator for NOMAD
NO	Normal Ordering
NOMAD	Neutrino Oscillation MAgnetic Detector
NO $\nu$ A	NuMI Off-Axis $\nu_e$ Appearance
OPERA	Oscillation Project with Emulsion tRacking Apparatus
ORCA	Oscillation Research with Cosmics in the Abyss
p.e.	photo electron
p.o.t.	protons on target
PC	polycarbonate
PCB	printed circuit board
PDF	probability density function
PET	polyethylene terephthalate
PINGU	Precision IceCube Next Generation Upgrade
PMNS	Pontecorvo Maki Nakagawa Sakata
PMT	photo multiplier tube
PS	Proton Synchrotron
PT	Precision Tracker
PTOLEMY	Princeton Tritium Observatory for Light, Early-Universe, Massive-Neutrino Yield
QCD	Quantum Chromo Dynamics
QE	quasi-elastic
QFD	Quantum Flavour Dynamics
RES	resonant
RMSD	root-mean-square deviation
ROC	ReadOut Chip
ROOT	ROOT Data Analysis Framework
RPC	resistive plate chamber
S-UTS	Super-Ultra Track Selector
SAGE	Soviet-American Gallium Experiment
SB	Scan Back

SHiP	Search for Hidden Particles
SK	Super-Kamiokande
SLAC	Stanford Linear Accelerator Center
SM	Super Module
SNO	Sudbury Neutrino Observatory
SPEAR	Stanford Positron Electron Accelerating Ring
SPS	Super Proton Synchrotron
SSM	Standard Solar Model
T2K	Tokai to Kamioka
TB	timing board
TDC	time-to-digital converter
TFD	Track Follow-Down
TOF	time-of-flight
TT	Target Tracker
UTC	Coordinated Universal Time
VMC	Virtual Monte Carlo
VS	Volume Scan
WANF	West Area Neutrino Facility
WLS	wavelength-shifting
XPC	Crossed RPC

# List of Tables

2.1	Properties of quarks and leptons. . . . .	8
2.2	Potentials for neutrino oscillations in matter . . . . .	23
2.3	Global best fit parameters for 3-flavour neutrino oscillations . . . . .	24
4.1	CNGS meson and muon decay modes . . . . .	43
4.2	CNGS $\nu$ flux per p.o.t. at the LNGS . . . . .	46
4.3	CNGS $\nu$ CC event rates on an isoscalar target . . . . .	46
4.4	P.o.t. delivered during the CNGS physics runs . . . . .	47
4.5	Brick Finding efficiencies for $\nu_\mu$ CC and NC events . . . . .	64
4.6	$\tau$ decay modes . . . . .	68
4.7	$\nu_\mu$ interactions resulting in charmed hadrons . . . . .	72
4.8	Numbers of expected and observed charm events, 2008 – 2010 data . . . . .	73
4.9	Kinematical cuts for the $\tau \rightarrow e$ decay channel . . . . .	76
4.10	Kinematical cuts for the $\tau \rightarrow \mu$ decay channel and measured values for the 3rd $\nu_\tau$ candidate event . . . . .	76
4.11	Kinematical cuts for the $\tau \rightarrow 1h$ decay channel and measured values for the $\nu_\tau$ candidate events . . . . .	77
4.12	Kinematical cuts for the $\tau \rightarrow 3h$ decay channel and measured values for the 2nd $\nu_\tau$ candidate event . . . . .	77
4.13	Number of events for each CNGS run year and identified $\nu_\tau$ candidates . . . . .	78
4.14	Expected numbers of signal and BG events for the analysed data sample . . . . .	79
5.1	Material composition of the simulated OPERA geometry . . . . .	87
5.2	Reconstructed energy of real $\nu_e$ candidate events . . . . .	98
6.1	Expected and observed $\nu_e$ event numbers . . . . .	107
6.2	Limits and sensitivities on $\sin^2(2\theta_{new})$ . . . . .	112



# List of Figures

2.1	Continuous $\beta$ decay spectrum . . . . .	3
2.2	$^8\text{B}$ solar neutrino flux measured by SNO . . . . .	6
2.3	Asymmetry of atmospheric $\nu$ events in SK . . . . .	7
2.4	$\nu_e + n^0$ CC QE scattering . . . . .	12
2.5	$\nu_\mu + n^0$ NC RES scattering . . . . .	13
2.6	$\nu_e + p^+$ CC RES scattering . . . . .	14
2.7	$\nu_e + N$ CC DIS scattering . . . . .	15
2.8	NC and CC DIS charm production . . . . .	15
2.9	Total $\nu_\mu + N$ CC cross section . . . . .	17
2.10	Total $\bar{\nu}_\mu + N$ CC cross section . . . . .	17
2.11	Total $\nu_e + N$ CC cross section . . . . .	18
2.12	Total average ( $\nu_\tau + \bar{\nu}_\tau$ ) CC cross section . . . . .	18
2.13	Neutrino Mass Ordering . . . . .	24
2.14	Measurement of the neutrino MO at JUNO . . . . .	25
2.15	Indications for nonstandard neutrino oscillations . . . . .	26
2.16	Effective Majorana mass $ \langle m \rangle $ as a function $m_{min}$ . . . . .	28
3.1	Fractional energy loss of $e^\pm$ in Pb. . . . .	29
3.2	Total cross section of $\gamma$ in Pb . . . . .	30
3.3	Probability of $e^+e^-$ pair production for $\gamma$ in different target materials . . . . .	30
3.4	Longitudinal profile of an e.m. cascade in iron . . . . .	32
4.1	$P_{\nu_\mu \rightarrow \nu_\tau}^{3flavour}(E)$ for different values of $\theta_{13}$ and $\sigma_{CC}^{\nu_\tau}(E)$ . . . . .	34
4.2	$P_{\nu_\mu \rightarrow \nu_\tau}^{2flavour}(E) \times \sigma_{CC}^{\nu_\tau}(E)$ for different values of $\Delta m_{32}^2$ . . . . .	35
4.3	$P_{\nu_\mu \rightarrow \nu_\tau}^{2flavour}(L)$ for different values of $\Delta m_{32}^2$ . . . . .	35
4.4	The DONuT detector . . . . .	36
4.5	DONuT ECC structure . . . . .	37
4.6	The CHORUS detector . . . . .	38
4.7	CHORUS neutrino target structure . . . . .	38
4.8	The NOMAD detector . . . . .	39
4.9	NOMAD event topologies . . . . .	40
4.10	OPERA facility locations. . . . .	41
4.11	LNGS laboratory . . . . .	41
4.12	CNGS beam angles in the OPERA reference frame . . . . .	42
4.13	CNGS facility layout . . . . .	43

4.14	Unoscillated CNGS neutrino energy spectra at the LNGS . . . . .	45
4.15	CNGS performance . . . . .	47
4.16	The OPERA detector . . . . .	48
4.17	OPERA target area . . . . .	49
4.18	Structure of an OPERA ECC brick . . . . .	50
4.19	TT scintillator strip . . . . .	51
4.20	TT scintillator absorption and emission spectra . . . . .	51
4.21	The OPERA TT . . . . .	52
4.22	BMS machine and brick storage drum . . . . .	53
4.23	OPERA target mass evolution . . . . .	54
4.24	Brick status on 2009-06-29 . . . . .	54
4.25	OPERA spectrometer and PT trigger scheme . . . . .	55
4.26	OPERA dipole magnet . . . . .	55
4.27	Cross section of an OPERA RPC . . . . .	56
4.28	OPERA PT drift tube modules . . . . .	58
4.29	ED reconstruction of a $\nu_\mu$ event . . . . .	63
4.30	Reconstruction of the hadronic shower axis in the OPERA ED . . . . .	64
4.31	OPERA nuclear emulsion track reconstruction . . . . .	65
4.32	European and Japanese scanning Systems . . . . .	66
4.33	ECC reconstruction of a neutrino interaction in OPERA . . . . .	67
4.34	$\tau$ decay topologies . . . . .	69
4.35	ECC reconstruction of a charm candidate event . . . . .	72
4.36	The 5th $\nu_\tau$ candidate event . . . . .	78
5.1	$\nu_e$ candidate event 9197043461 (ED reconstruction) . . . . .	82
5.2	Systematic $\nu_e$ search using CS shower hints . . . . .	83
5.3	$\nu_e$ candidate event 9197043461 (ECC reconstruction) . . . . .	84
5.4	$e^+e^-$ pair from $\pi^0$ $\gamma$ conversion . . . . .	85
5.5	OpGeom implementation of the OPERA detector . . . . .	87
5.6	MC $\nu_e$ events vertex distribution (OpRec4.1) . . . . .	89
5.7	MC $\nu_e$ events vertex distribution (true $\nu_e$ CC interactions) . . . . .	89
5.8	MC $\nu_e$ events vertex distribution (interaction inside brick) . . . . .	90
5.9	Location of $\nu_e$ candidate bricks . . . . .	90
5.10	TT charge measurement . . . . .	91
5.11	TT calibration . . . . .	92
5.12	$E_{had,rec}$ energy resolution . . . . .	92
5.13	$E_{had,rec}$ vs. $E_{\nu,true}$ . . . . .	93
5.14	$\nu_e$ event with poorly contained showers . . . . .	94
5.15	$E_{\nu,rec}$ vs. $E_{\nu,true}$ . . . . .	95
5.16	$E_{\nu,rec} - E_{\nu,true}$ vs. $E_{\nu,true}$ . . . . .	96
5.17	Resolution of $E_{\nu,rec}$ vs. $E_{\nu,true}$ (2 GeV-bins) . . . . .	97
5.18	Resolution of $E_{\nu,rec}$ vs. $E_{\nu,true}$ (10 GeV-bins) . . . . .	97
5.19	Reconstructed energy of $\nu_e$ candidates . . . . .	99
6.1	$\nu_e$ detection efficiency . . . . .	103



---

6.2	Unoscillated CNGS neutrino spectrum at LNGS . . . . .	105
6.3	Reconstructed energy of $\nu_e$ candidates and expectation of signal and BG . . .	107
6.4	3-flavour $\nu_\mu \rightarrow \nu_e$ oscillation probability for different values of $\theta_{13}$ . . . . .	108
6.5	$\nu_\mu \rightarrow \nu_e$ 3-flavour oscillations exclusion plot . . . . .	110
6.6	$\nu_\mu \rightarrow \nu_e$ nonstandard oscillations exclusion plot . . . . .	113
6.7	Global picture of neutrino oscillations in 2018 . . . . .	114



# Bibliography

- [1] G. Aad et al. Observation of a new particle in the search for the Standard Model Higgs boson with the ATLAS detector at the LHC. *Phys. Lett.*, B716:1–29, 2012, 1207.7214. doi:10.1016/j.physletb.2012.08.020.
- [2] J. N. Abdurashitov et al. Measurement of the response of a Ga solar neutrino experiment to neutrinos from an Ar-37 source. *Phys. Rev.*, C73:045805, 2006, nucl-ex/0512041. doi:10.1103/PhysRevC.73.045805.
- [3] K. Abe et al. Indication of Electron Neutrino Appearance from an Accelerator-produced Off-axis Muon Neutrino Beam. *Phys. Rev. Lett.*, 107:041801, 2011, 1106.2822. doi:10.1103/PhysRevLett.107.041801.
- [4] K. Abe et al. Measurement of the Inclusive Electron Neutrino Charged Current Cross Section on Carbon with the T2K Near Detector. *Phys. Rev. Lett.*, 113(24):241803, 2014, 1407.7389. doi:10.1103/PhysRevLett.113.241803.
- [5] Y. Abe et al. Indication of Reactor  $\bar{\nu}_e$  Disappearance in the Double Chooz Experiment. *Phys. Rev. Lett.*, 108:131801, 2012, 1112.6353. doi:10.1103/PhysRevLett.108.131801.
- [6] R. Acquafredda et al. The OPERA experiment in the CERN to Gran Sasso neutrino beam. *JINST*, 4:P04018, 2009. doi:10.1088/1748-0221/4/04/P04018.
- [7] T. Adam et al. The OPERA experiment target tracker. *Nucl. Instrum. Meth.*, A577:523–539, 2007, physics/0701153. doi:10.1016/j.nima.2007.04.147.
- [8] T. Adam et al. Measurement of the neutrino velocity with the OPERA detector in the CNGS beam. *arXiv e-prints*, 2011, 1109.4897v1.
- [9] T. Adam et al. Measurement of the neutrino velocity with the OPERA detector in the CNGS beam. *JHEP*, 10:093, 2012, 1109.4897. doi:10.1007/JHEP10(2012)093.
- [10] P. A. R. Ade et al. Planck 2015 results. XIII. Cosmological parameters. *Astron. Astrophys.*, 594:A13, 2016, 1502.01589. doi:10.1051/0004-6361/201525830.
- [11] N. Agafonova et al. The Detection of neutrino interactions in the emulsion/lead target of the OPERA experiment. *JINST*, 4:P06020, 2009, 0903.2973. doi:10.1088/1748-0221/4/06/P06020.
- [12] N. Agafonova et al. Observation of a first  $\nu_\tau$  candidate in the OPERA experiment in the CNGS beam. *Phys. Lett.*, B691:138–145, 2010, 1006.1623. doi:10.1016/j.physletb.2010.06.022.

- [13] N. Agafonova et al. Study of neutrino interactions with the electronic detectors of the OPERA experiment. *New J.Phys.*, 13:053051, 2011, 1102.1882. doi:10.1088/1367-2630/13/5/053051.
- [14] N. Agafonova et al. Search for  $\nu_\mu \rightarrow \nu_\tau$  oscillation with the OPERA experiment in the CNGS beam. *New J. Phys.*, 14:033017, 2012. doi:10.1088/1367-2630/14/3/033017.
- [15] N. Agafonova et al. New results on  $\nu_\mu \rightarrow \nu_\tau$  appearance with the OPERA experiment in the CNGS beam. *JHEP*, 11:036, 2013, 1308.2553. doi:10.1007/JHEP11(2013)036, 10.1007/JHEP04(2014)014. [Erratum: JHEP04,014(2014)].
- [16] N. Agafonova et al. Search for  $\nu_\mu \rightarrow \nu_e$  oscillations with the OPERA experiment in the CNGS beam. *JHEP*, 07:004, 2013, 1303.3953. doi:10.1007/JHEP07(2013)004, 10.1007/JHEP07(2013)085. [Addendum: JHEP07,085(2013)].
- [17] N. Agafonova et al. Evidence for  $\nu_\mu \rightarrow \nu_\tau$  appearance in the CNGS neutrino beam with the OPERA experiment. *Phys. Rev. D*, 89:051102, Mar 2014. doi:10.1103/PhysRevD.89.051102.
- [18] N. Agafonova et al. Observation of tau neutrino appearance in the CNGS beam with the OPERA experiment. *PTEP*, 2014(10):101C01, 2014, 1407.3513. doi:10.1093/ptep/ptu132.
- [19] N. Agafonova et al. Procedure for short-lived particle detection in the OPERA experiment and its application to charm decays. *Eur. Phys. J.*, C74(8):2986, 2014, 1404.4357. doi:10.1140/epjc/s10052-014-2986-0.
- [20] N. Agafonova et al. Discovery of  $\tau$  neutrino appearance in the cngs neutrino beam with the opera experiment. *Phys. Rev. Lett.*, 115:121802, Sep 2015. doi:10.1103/PhysRevLett.115.121802.
- [21] N. Agafonova et al. Final results of the OPERA experiment on  $\nu_\tau$  appearance in the CNGS beam. *arXiv e-prints*, 2018, 1804.04912.
- [22] N. Agafonova et al. Final results of the search for  $\nu_\mu \rightarrow \nu_e$  oscillations with the OPERA detector in the CNGS beam. *arXiv e-prints*, 2018, 1803.11400.
- [23] S. Agostinelli et al. GEANT4: A Simulation toolkit. *Nucl. Instrum. Meth.*, A506:250–303, 2003. doi:10.1016/S0168-9002(03)01368-8.
- [24] A. Aguilar-Arevalo et al. Evidence for neutrino oscillations from the observation of anti-neutrino(electron) appearance in a anti-neutrino(muon) beam. *Phys. Rev.*, D64:112007, 2001, hep-ex/0104049. doi:10.1103/PhysRevD.64.112007.
- [25] A. Aguilar-Arevalo et al. A Combined  $\nu_\mu \rightarrow \nu_e$  and  $\bar{\nu}_\mu \rightarrow \bar{\nu}_e$  Oscillation Analysis of the MiniBooNE Excesses. *arXiv e-prints*, 2012, 1207.4809. URL <http://lss.fnal.gov/archive/2012/pub/fermilab-pub-12-394-ad-ppd.pdf>.
- [26] Q. R. Ahmad et al. Measurement of the rate of  $\nu_e + d \rightarrow p + p + e^-$  interactions produced by  $^8B$  solar neutrinos at the Sudbury Neutrino Observatory. *Phys. Rev. Lett.*, 87:071301, 2001, nucl-ex/0106015. doi:10.1103/PhysRevLett.87.071301.

- [27] Q. R. Ahmad et al. Direct evidence for neutrino flavor transformation from neutral current interactions in the Sudbury Neutrino Observatory. *Phys. Rev. Lett.*, 89:011301, 2002, nucl-ex/0204008. doi:10.1103/PhysRevLett.89.011301.
- [28] J. K. Ahn et al. Observation of Reactor Electron Antineutrino Disappearance in the RENO Experiment. *Phys. Rev. Lett.*, 108:191802, 2012, 1204.0626. doi:10.1103/PhysRevLett.108.191802.
- [29] S. A. Akimenko, V. I. Belousov, A. M. Blik, G. I. Britvich, V. N. Kolosov, V. M. Kutin, B. N. Lebedev, V. N. Peleshko, Ya. N. Rastsvetalov, and A. S. Solovev. Multiple Coulomb Scattering of 7.3-GeV/c and 11.7-GeV/c Muons on Cu Target. *Nucl. Instrum. Meth.*, A243:518, 1986. doi:10.1016/0168-9002(86)90990-3.
- [30] J. Allison et al. Geant4 developments and applications. *IEEE Trans. Nucl. Sci.*, 53:270, 2006. doi:10.1109/TNS.2006.869826.
- [31] G. Ambrosini et al. Measurement of charged particle production from 450-GeV/c protons on beryllium. *Eur. Phys. J.*, C10:605–627, 1999. doi:10.1007/s100520050601.
- [32] M. Ambrosio, R. Brugnera, S. Dusini, B. Dulach, C. Fanin, et al. The OPERA magnetic spectrometer. *IEEE Trans.Nucl.Sci.*, 51:975–979, 2004, physics/0409137. doi:10.1109/TNS.2004.829659.
- [33] C. Amsler et al. Review of Particle Physics. *Phys. Lett.*, B667:1–1340, 2008. doi:10.1016/j.physletb.2008.07.018.
- [34] F. An et al. Neutrino Physics with JUNO. *J. Phys.*, G43(3):030401, 2016, 1507.05613. doi:10.1088/0954-3899/43/3/030401.
- [35] F. P. An et al. Observation of electron-antineutrino disappearance at Daya Bay. *Phys. Rev. Lett.*, 108:171803, 2012, 1203.1669. doi:10.1103/PhysRevLett.108.171803.
- [36] C. Andreopoulos, C. Barry, S. Dytman, H. Gallagher, T. Golan, R. Hatcher, G. Perdue, and J. Yarba. The GENIE Neutrino Monte Carlo Generator: Physics and User Manual. *arXiv e-prints*, 2015, 1510.05494.
- [37] C. Andreopoulos et al. The GENIE Neutrino Monte Carlo Generator. *Nucl. Instrum. Meth.*, A614:87–104, 2010, 0905.2517. doi:10.1016/j.nima.2009.12.009.
- [38] M. Anelli et al. A facility to Search for Hidden Particles (SHiP) at the CERN SPS. Technical Report CERN-SPSC-2015-016, SPSC-P-350, CERN, Geneva, Apr 2015.
- [39] J. Angrik et al. KATRIN design report 2004. 2005.
- [40] A. Anokhina et al. Emulsion sheet doublets as interface trackers for the OPERA experiment. *JINST*, 3:P07005, 2008, 0804.1985. doi:10.1088/1748-0221/3/07/P07005.
- [41] A. Anokhina et al. Study of the effects induced by lead on the emulsion films of the OPERA experiment. *JINST*, 3:P07002, 2008, 0805.0123. doi:10.1088/1748-0221/3/07/P07002.

- [42] M. Antonello et al. Experimental search for the LSND anomaly with the ICARUS detector in the CNGS neutrino beam. *Eur. Phys. J.*, C73(3):2345, 2013, 1209.0122. doi:10.1140/epjc/s10052-013-2345-6.
- [43] M. Apollonio et al. Limits on neutrino oscillations from the CHOOZ experiment. *Phys. Lett.*, B466:415–430, 1999, hep-ex/9907037. doi:10.1016/S0370-2693(99)01072-2.
- [44] M. Apollonio et al. Accelerator design concept for future neutrino facilities. *JINST*, 4:P07001, 2009, 0802.4023. doi:10.1088/1748-0221/4/07/P07001.
- [45] B. Armbruster et al. Upper limits for neutrino oscillations muon-anti-neutrino  $\rightarrow$  electron-anti-neutrino from muon decay at rest. *Phys. Rev.*, D65:112001, 2002, hep-ex/0203021. doi:10.1103/PhysRevD.65.112001.
- [46] L. Arrabito et al. Track reconstruction in the emulsion-lead target of the OPERA experiment using the ESS microscope. *JINST*, 2:P05004, 2007, 0705.3102. doi:10.1088/1748-0221/2/05/P05004.
- [47] V. N. Aseev et al. An upper limit on electron antineutrino mass from Troitsk experiment. *Phys. Rev.*, D84:112003, 2011, 1108.5034. doi:10.1103/PhysRevD.84.112003.
- [48] P. Astier et al. Final NOMAD results on muon-neutrino  $\rightarrow$  tau-neutrino and electron-neutrino  $\rightarrow$  tau-neutrino oscillations including a new search for tau-neutrino appearance using hadronic tau decays. *Nucl. Phys.*, B611:3–39, 2001, hep-ex/0106102. doi:10.1016/S0550-3213(01)00339-X.
- [49] P. Astier et al. Prediction of neutrino fluxes in the NOMAD experiment. *Nucl. Instrum. Meth.*, A515:800–828, 2003, hep-ex/0306022. doi:10.1016/j.nima.2003.07.054.
- [50] P. Astier et al. Search for  $\nu(\mu) \rightarrow \nu(e)$  oscillations in the NOMAD experiment. *Phys. Lett.*, B570:19–31, 2003, hep-ex/0306037. doi:10.1016/j.physletb.2003.07.029.
- [51] D. Autiero. The OPERA event generator and the data tuning of nuclear re-interactions. *Nucl. Phys. Proc. Suppl.*, 139:253–259, 2005. doi:10.1016/j.nuclphysbps.2004.11.168. [253(2005)].
- [52] J. N. Bahcall, M. H. Pinsonneault, and S. Basu. Solar models: Current epoch and time dependences, neutrinos, and helioseismological properties. *Astrophys. J.*, 555:990–1012, 2001, astro-ph/0010346. doi:10.1086/321493.
- [53] E. Balsamo et al. The OPERA RPCs front end electronics A novel application of LVDS line receiver as low cost discriminator. *JINST*, 7:P11007, 2012. doi:10.1088/1748-0221/7/11/P11007.
- [54] A. Bergnoli et al. The quality control tests for the RPCs of the OPERA experiment. *Nucl. Instrum. Meth.*, A533:203–207, 2004. doi:10.1016/j.nima.2004.07.028.
- [55] A. Bergnoli et al. Tests of OPERA RPC Detectors. *IEEE Trans. Nucl. Sci.*, 52:2963–2970, 2005. doi:10.1109/TNS.2005.862902.

- [56] A. Bergnoli et al. The OPERA VETO system. *Nucl. Instrum. Meth.*, A602:653–657, 2009. doi:10.1016/j.nima.2008.12.076.
- [57] J. Beringer et al. Review of Particle Physics (RPP). *Phys. Rev.*, D86:010001, 2012. doi:10.1103/PhysRevD.86.010001.
- [58] A. Bertolin and N. T. Tran. OpCarac: an algorithm for the classification of the neutrino interactions recorded by the OPERA experiment. OPERA public note 100, 2009.
- [59] B. Bhattacharya, A. M. Thalapillil, and C. E. M. Wagner. Implications of sterile neutrinos for medium/long-baseline neutrino experiments and the determination of  $\theta_{13}$ . *Phys. Rev.*, D85:073004, 2012, 1111.4225. doi:10.1103/PhysRevD.85.073004.
- [60] J. Blietschau et al. Total Cross-Sections for electron-neutrino and anti-electron-neutrino Interactions and Search for Neutrino Oscillations and Decay. *Nucl. Phys.*, B133:205–219, 1978. doi:10.1016/0550-3213(78)90299-7.
- [61] R. Brun, F. Bruyant, F. Carminati, S. Giani, M. Maire, A. McPherson, G. Patrick, and L. Urban. GEANT Detector Description and Simulation Tool. *CERN notes*, 501(CERN-W5013, CERN-W-5013, W5013, W-5013), 1994. doi:10.17181/CERN.MUHF.DMJ1.
- [62] F. Brunet and A. Zghiche. Electromagnetic shower reconstruction in the opera experiment for the  $\nu_{\mu} \rightarrow \nu_e$  and  $\nu_{\mu} \rightarrow \nu_{\tau}(\tau \rightarrow e)$  oscillation analysis. OPERA internal note 149, 2012.
- [63] G. Brunetti. *Neutrino velocity measurement with the OPERA experiment in the CNGS beam*. PhD thesis, Lyon, IPN, 2011. URL [http://inspirehep.net/record/1296901/files/TH2011\\_Brunetti\\_Giulia.pdf](http://inspirehep.net/record/1296901/files/TH2011_Brunetti_Giulia.pdf).
- [64] X. Bu. Measurement of Electron Neutrino Charged-Current Inclusive Cross Section in 1-3 GeV energy region with the NOvA Near Detector. In *Proceedings, 10th International Workshop on Neutrino-Nucleus Interactions in the Few GeV Region (NuInt15): Osaka, Japan, November 16-21, 2015*, 2016, 1601.01213. URL <https://inspirehep.net/record/1413749/files/arXiv:1601.01213.pdf>.
- [65] N. Cabibbo. Unitary Symmetry and Leptonic Decays. *Phys. Rev. Lett.*, 10:531–533, 1963. doi:10.1103/PhysRevLett.10.531. [648(1963)].
- [66] J. E. Campagne. Muon tracking in heterogeneous structure. OPERA internal note 6, 1999.
- [67] F. Capozzi, E. Di Valentino, E. Lisi, A. Marrone, A. Melchiorri, and A. Palazzo. Global constraints on absolute neutrino masses and their ordering. *Phys. Rev.*, D95(9):096014, 2017, 1703.04471. doi:10.1103/PhysRevD.95.096014.
- [68] A. Cazes, A. Cecchetti, B. Dulach, F. Iungo, M. Incurvati, D. Orecchini, C. Sanelli, F. Terranova, M. Ventura, and G. Peiro. Electromagnetic characterization of the 990-ton gapless magnets for the OPERA experiment. *JINST*, 2:T03001, 2007. doi:10.1088/1748-0221/2/03/T03001.

- [69] CERN. CNGS website. Accessed: 2017.
- [70] J. Chadwick. Intensitätsverteilung im magnetischen Spectrum der  $\beta$ -Strahlen von radium B + C. *Verhandl. Dtsc. Phys. Ges.*, 16:383, 1914. URL <http://cds.cern.ch/record/262756>.
- [71] S. Chatrchyan et al. Observation of a new boson at a mass of 125 GeV with the CMS experiment at the LHC. *Phys. Lett.*, B716:30–61, 2012, 1207.7235. doi:10.1016/j.physletb.2012.08.021.
- [72] L. Chaussard. OpGeom, software model of the OPERA detector. OPERA internal note 69, 2005.
- [73] J. H. Christenson, J. W. Cronin, V. L. Fitch, and R. Turlay. Evidence for the  $2\pi$  Decay of the  $K_2^0$  Meson. *Phys. Rev. Lett.*, 13:138–140, 1964. doi:10.1103/PhysRevLett.13.138.
- [74] A. Chukanov, S. Dmitrievsky, and Y. Gornushkin. Neutrino interaction vertex location with the OPERA electronic detectors (Brick Finding). OPERA public note 162, 2013.
- [75] G. Collazuol, A. Ferrari, A. Guglielmi, and P. R. Sala. Hadronic models and experimental data for the neutrino beam production. *Nucl. Instrum. Meth.*, A449:609–623, 2000. doi:10.1016/S0168-9002(00)00152-2.
- [76] G. Corradi et al. A 16 channels timing board for the opera rpcs. OPERA public note 70, 2009.
- [77] C. Cowan, F. Reines, F. Harrison, H. Kruse, and A. McGuire. Detection of the free neutrino: A Confirmation. *Science*, 124:103–104, 1956. doi:10.1126/science.124.3212.103.
- [78] G. Cowan. *Statistical Data Analysis*. Clarendon Press, Oxford, 1998.
- [79] G. Danby, J. M. Gaillard, K. A. Goulianos, L. M. Lederman, N. B. Mistry, M. Schwartz, and J. Steinberger. Observation of High-Energy Neutrino Reactions and the Existence of Two Kinds of Neutrinos. *Phys. Rev. Lett.*, 9:36–44, 1962. doi:10.1103/PhysRevLett.9.36.
- [80] R. Davis, Jr., D. S. Harmer, and K. C. Hoffman. Search for neutrinos from the sun. *Phys. Rev. Lett.*, 20:1205–1209, 1968. doi:10.1103/PhysRevLett.20.1205.
- [81] D. Decamp et al. Determination of the Number of Light Neutrino Species. *Phys. Lett.*, B231:519–529, 1989. doi:10.1016/0370-2693(89)90704-1.
- [82] Y. Declais et al. Search for neutrino oscillations at 15-meters, 40-meters, and 95-meters from a nuclear power reactor at Bugey. *Nucl. Phys.*, B434:503–534, 1995. doi:10.1016/0550-3213(94)00513-E.
- [83] A. Di Crescenzo. *Search for  $\nu_\mu \rightarrow \nu_\tau$  oscillations in the OPERA experiment*. PhD thesis, Naples U., 2013. URL <http://www.fedoa.unina.it/id/eprint/9501>.
- [84] C. D. Ellis and W. A. Wooster. The average energy of disintegration of radium e. *Proceedings of the Royal Society of London A: Mathematical, Physical and Engineering Sciences*, 117(776):109–123,



- 1927, <http://rspa.royalsocietypublishing.org/content/117/776/109.full.pdf>. doi:10.1098/rspa.1927.0168.
- [85] F. Englert and R. Brout. Broken Symmetry and the Mass of Gauge Vector Mesons. *Phys. Rev. Lett.*, 13:321–323, 1964. doi:10.1103/PhysRevLett.13.321.
- [86] I. Esteban, M. C. Gonzalez-Garcia, M. Maltoni, I. Martinez-Soler, and T. Schwetz. Updated fit to three neutrino mixing: exploring the accelerator-reactor complementarity. *JHEP*, 01:087, 2017, 1611.01514. doi:10.1007/JHEP01(2017)087.
- [87] A. Fasso et al. The Physics models of FLUKA: Status and recent developments. *eConf*, C0303241:MOMT005, 2003, hep-ph/0306267.
- [88] G. J. Feldman and R. D. Cousins. A Unified approach to the classical statistical analysis of small signals. *Phys. Rev.*, D57:3873–3889, 1998, physics/9711021. doi:10.1103/PhysRevD.57.3873.
- [89] G. Felici et al. The trigger system of the opera precision tracker. OPERA public note 71, 2009.
- [90] T. Ferber. Monte Carlo Studies on Different Magnetic Field Polarities of the OPERA Spectrometers. OPERA internal note 117, 2010.
- [91] T. Ferber. *Limits on neutrino oscillations in the CNGS neutrino beam and event classification with the OPERA detector*. PhD thesis, Hamburg U., 2012. URL <http://www-library.desy.de/cgi-bin/showprep.pl?thesis12-036>.
- [92] T. Ferber, D. Bick, J. Ebert, C. Hagner, M. Hierholzer, et al. The gas system of the drift tube detector of the neutrino experiment OPERA. *Nucl.Instrum.Meth.*, A592:493–497, 2008. doi:10.1016/j.nima.2008.04.040.
- [93] A. Ferrari, A. M. Guglielmi, M. Lorenzo-Sentis, S. Roesler, P. R. Sala, and L. Sarchiapone. An updated Monte Carlo calculation of the CNGS neutrino beam. Technical Report AB-Note-2006-038. CERN-AB-Note-2006-038, CERN, Geneva, Aug 2007. URL <http://cds.cern.ch/record/979037>.
- [94] A. Ferrari and P. Sala. GEANT Hadronic Event Generators: a comparison at the single interaction level. Technical Report ATL-PHYS-96-086. ATLGE-PN-86, CERN, CERN, 1996.
- [95] A. Ferrari, P. R. Sala, A. Fasso, and J. Ranft. FLUKA: A multi-particle transport code (Program version 2005). *arXiv e-prints*, 2005.
- [96] J. A. Formaggio and G. P. Zeller. From eV to EeV: Neutrino Cross Sections Across Energy Scales. *Rev. Mod. Phys.*, 84:1307–1341, 2012, 1305.7513. doi:10.1103/RevModPhys.84.1307.
- [97] B. Frois, J. B. Bellicard, J. M. Cavedon, M. Huet, P. Leconte, P. Ludeau, A. Nakada, X. H. Phan, and I. Sick. High Momentum Transfer electron Scattering from Pb-208. *Phys. Rev. Lett.*, 38:152–155, 1977. doi:10.1103/PhysRevLett.38.152.

- [98] Y. Fukuda et al. Evidence for oscillation of atmospheric neutrinos. *Phys. Rev. Lett.*, 81:1562–1567, 1998, hep-ex/9807003. doi:10.1103/PhysRevLett.81.1562.
- [99] S. Gariazzo, C. Giunti, M. Laveder, and Y. F. Li. Updated Global 3+1 Analysis of Short-BaseLine Neutrino Oscillations. *JHEP*, 06:135, 2017, 1703.00860. doi:10.1007/JHEP06(2017)135.
- [100] S. L. Glashow. Partial Symmetries of Weak Interactions. *Nucl. Phys.*, 22:579–588, 1961. doi:10.1016/0029-5582(61)90469-2.
- [101] B. Goddard, P. Knaus, G. Schroder, W. Weterings, and J. A. Uythoven. The new SPS extraction channel for LHC and CNGS. In *Particle accelerator. Proceedings, 7th European Conference, EPAC 2000, Vienna, Austria, June 26-30, 2000. Vol. 1-3*, pages 2240–2242, 2000. URL <http://weplib.cern.ch/abstract?CERN-SL-2000-036-BT>.
- [102] C. Göllnitz. *Alignment des Driftröhrendetektors am Neutrino-Oszillationsexperiment OPERA*. PhD thesis, Hamburg U., 2012. URL <http://www-library.desy.de/cgi-bin/showprep.pl?thesis12-035>.
- [103] M. C. Gonzalez-Garcia and J. J. Gomez-Cadenas. Prompt tau-neutrino fluxes in present and future tau-neutrino experiments. *Phys. Rev.*, D55:1297–1306, 1997. doi:10.1103/PhysRevD.55.1297.
- [104] V. N. Gribov and B. Pontecorvo. Neutrino astronomy and lepton charge. *Phys. Lett.*, 28B:493, 1969. doi:10.1016/0370-2693(69)90525-5.
- [105] D. Griffiths. *Introduction to elementary particles*. Wiley, 2008.
- [106] E. Gschwendtner, K. Cornelis, I. Efthymiopoulos, I. Kratschmer, A. Pardons, H. Vincke, and J. Wenninger. CNGS, CERN Neutrinos to Gran Sasso, Five Years of Running a 500 Kilowatt Neutrino Beam Facility at CERN. *Conf. Proc.*, C130512(CERN-ACC-2013-0266):MOPEA058. 4 p, May 2013. URL <https://cds.cern.ch/record/1635954>.
- [107] M. Güler et al. An appearance experiment to search for  $\nu_\mu \rightarrow \nu_\tau$  oscillations in the CNGS beam. Technical Report CERN-SPSC-2000-028. LNGS-2000-25. SPSC-P-318, CERN, Geneva, Jul 2000. URL <https://cds.cern.ch/record/456523>.
- [108] C. Gustavino, A. Candela, M. De Deo, M. D’Incecco, and R. Moro. Performance of glass RPC operated in streamer mode with four-fold gas mixtures containing SF-6. *Nucl. Instrum. Meth.*, A517:101–108, 2004. doi:10.1016/j.nima.2003.09.059.
- [109] T. J. Haines et al. Calculation of Atmospheric Neutrino Induced Backgrounds in a Nucleon Decay Search. *Phys. Rev. Lett.*, 57:1986–1989, 1986. doi:10.1103/PhysRevLett.57.1986.
- [110] P. W. Higgs. Broken symmetries, massless particles and gauge fields. *Phys. Lett.*, 12:132–133, 1964. doi:10.1016/0031-9163(64)91136-9.
- [111] A. Hollnagel. Separation of Muons and Pions in the Electronic Detector of OPERA by Applying Classical Cuts. Hamburg U., 2010.

- [112] A. Hollnagel and T. Ferber. Opera event - proton waveform matching. OPERA internal note 146, 2012.
- [113] INFN. LNGS website. <http://www.lngs.infn.it/>. Accessed: 2016.
- [114] H. Ishida et al. Study of hadron interactions in a lead-emulsion target. *PTEP*, 2014(9):093C01, 2014, 1408.0386. doi:10.1093/ptep/ptu119.
- [115] F. Kaether, W. Hampel, G. Heusser, J. Kiko, and T. Kirsten. Reanalysis of the GALLEX solar neutrino flux and source experiments. *Phys. Lett.*, B685:47–54, 2010, 1001.2731. doi:10.1016/j.physletb.2010.01.030.
- [116] A. Kayis-Topaksu et al. Measurement of charm production in neutrino charged-current interactions. *New J. Phys.*, 13:093002, 2011, 1107.0613. doi:10.1088/1367-2630/13/9/093002.
- [117] B. Kayser. Neutrino physics. *eConf*, C040802:L004, 2004, hep-ph/0506165.
- [118] M. Kobayashi and T. Maskawa. CP Violation in the Renormalizable Theory of Weak Interaction. *Prog. Theor. Phys.*, 49:652–657, 1973. doi:10.1143/PTP.49.652.
- [119] K. Kodama et al. Observation of tau neutrino interactions. *Phys. Lett.*, B504:218–224, 2001, hep-ex/0012035. doi:10.1016/S0370-2693(01)00307-0.
- [120] K. Kodama et al. Final tau-neutrino results from the DONuT experiment. *Phys. Rev.*, D78:052002, 2008, 0711.0728. doi:10.1103/PhysRevD.78.052002.
- [121] M. Kordosky. Hadronic interaction modelling in MINOS. *AIP Conf. Proc.*, 896:185–194, 2007, hep-ex/0701009. doi:10.1063/1.2720469. [185(2007)].
- [122] U. Kose, M. Sioli, and M. Tenti. Study of the  $\nu_\mu \rightarrow \nu_e$  oscillation channel in the opera experiment. OPERA internal note 160, 2013.
- [123] C. Kraus et al. Final results from phase II of the Mainz neutrino mass search in tritium beta decay. *Eur. Phys. J.*, C40:447–468, 2005, hep-ex/0412056. doi:10.1140/epjc/s2005-02139-7.
- [124] I. Kreslo et al. High-speed analysis of nuclear emulsion films with the use of dry objective lenses. *JINST*, 3:P04006, 2008. doi:10.1088/1748-0221/3/04/P04006.
- [125] J. Lenkeit. *Timing Calibration of the Trigger System for the Drift Tube Detector of the OPERA Neutrino Oscillation Experiment*. PhD thesis, Hamburg U., Hamburg, 2015. URL <http://bib-pubdb1.desy.de/search?cc=Publication+Database&of=hd&p=reportnumber:DESY-THESIS-2015-048>.
- [126] J. Linder. Derivation of neutrino matter potentials induced by earth. *Submitted to: Am. J. Phys.*, 2005, hep-ph/0504264.
- [127] A. Longhin, A. Paoloni, and F. Pupilli. Large-angle scattering of multi-GeV muons on thin Lead targets. *arXiv e-prints*, 2015, 1506.08759. doi:10.1109/TNS.2015.2473674.

- [128] S. Lorenz. *Topological Track Reconstruction in Liquid Scintillator and LENA as a Far-Detector in an LBNO Experiment*. PhD thesis, U. Hamburg, Dept. Phys., Hamburg, 2016. doi:10.3204/PUBDB-2016-06366.
- [129] A. Lucotte, S. Bondil, K. Borer, J.-E. Campagne, A. Cazes, M. Hess, C. de La Taille, G. Martin-Chassard, L. Raux, and J. P. Repellin. A front-end read out chip for the OPERA scintillator tracker. *Nucl. Instrum. Meth.*, A521:378–392, 2004. doi:10.1016/j.nima.2003.10.104.
- [130] Z. Maki, M. Nakagawa, and S. Sakata. Remarks on the unified model of elementary particles. *Prog. Theor. Phys.*, 28:870–880, 1962. doi:10.1143/PTP.28.870.
- [131] J. Marteau. The OPERA global readout and GPS distribution system. *Nucl. Instrum. Meth.*, A617:291–293, 2010, 0906.1494. doi:10.1016/j.nima.2009.10.095.
- [132] G. E. Masek, L. D. Heggie, Y. B. Kim, and R. W. Williams. Scattering of 2-Bev/c Muons in Carbon and Lead. *Phys. Rev.*, 122:937–948, 1961. doi:10.1103/PhysRev.122.937.
- [133] A. Mengucci, A. Paoloni, M. Spinetti, and L. Votano. Gas mixture studies for streamer operation of Resistive Plate Chambers at low rate. *Nucl. Instrum. Meth.*, A583:264–269, 2007. doi:10.1016/j.nima.2007.09.030.
- [134] G. Mention, M. Fechner, T. Lasserre, T. A. Mueller, D. Lhuillier, M. Cribier, and A. Letourneau. The Reactor Antineutrino Anomaly. *Phys. Rev.*, D83:073006, 2011, 1101.2755. doi:10.1103/PhysRevD.83.073006.
- [135] S. P. Mikheev and A. Yu. Smirnov. Resonant amplification of neutrino oscillations in matter and solar neutrino spectroscopy. *Nuovo Cim.*, C9:17–26, 1986. doi:10.1007/BF02508049.
- [136] K. Morishima and T. Nakano. Development of a new automatic nuclear emulsion scanning system, S-UTS, with continuous 3D tomographic image read-out. *JINST*, 5:P04011, 2010. doi:10.1088/1748-0221/5/04/P04011.
- [137] U. Mosel. Neutrino Interactions with Nucleons and Nuclei: Importance for Long-Baseline Experiments. *Ann. Rev. Nucl. Part. Sci.*, 66:171–195, 2016, 1602.00696. doi:10.1146/annurev-nucl-102115-044720.
- [138] K. Olive et al. Review of Particle Physics. *Chin. Phys.*, C38:090001, 2014 and 2015 update. doi:10.1088/1674-1137/38/9/090001.
- [139] E. A. Paschos and J. Y. Yu. Neutrino interactions in oscillation experiments. *Phys. Rev.*, D65:033002, 2002, hep-ph/0107261. doi:10.1103/PhysRevD.65.033002.
- [140] C. Patrignani et al. Review of Particle Physics. *Chin. Phys.*, C40(10):100001, 2016 and 2017 update. doi:10.1088/1674-1137/40/10/100001.
- [141] W. Pauli. Dear radioactive ladies and gentlemen. *Phys. Today*, 31N9:27, 1978.
- [142] M. L. Perl et al. Evidence for Anomalous Lepton Production in  $e^+e^-$  Annihilation. *Phys. Rev. Lett.*, 35:1489–1492, 1975. doi:10.1103/PhysRevLett.35.1489.

- [143] B. Pontecorvo. Inverse beta processes and nonconservation of lepton charge. *Sov. Phys. JETP*, 7:172–173, 1958. [Zh. Eksp. Teor. Fiz.34,247(1957)].
- [144] B. Pontecorvo. Neutrino Experiments and the Problem of Conservation of Leptonic Charge. *Sov. Phys. JETP*, 26:984–988, 1968. [Zh. Eksp. Teor. Fiz.53,1717(1967)].
- [145] D. Rein and L. M. Sehgal. Neutrino Excitation of Baryon Resonances and Single Pion Production. *Annals Phys.*, 133:79–153, 1981. doi:10.1016/0003-4916(81)90242-6.
- [146] F. Reines and C. Cowan. Detection of the free neutrino. *Phys.Rev.*, 92:830–831, 1953. doi:10.1103/PhysRev.92.830.
- [147] F. Reines and C. L. Cowan. The neutrino. *Nature*, 178:446–449, 1956. doi:10.1038/178446a0.
- [148] G. Rosa, A. Di Bartolomeo, G. Grella, and G. Romano. Automatic analysis of digitized TV images by a computer driven optical microscope. *Nucl. Instrum. Meth.*, A394:357–367, 1997. doi:10.1016/S0168-9002(97)00660-8.
- [149] A. Salam and J. C. Ward. Electromagnetic and weak interactions. *Phys. Lett.*, 13:168–171, 1964. doi:10.1016/0031-9163(64)90711-5.
- [150] A. Yu. Smirnov. Solar neutrinos: Oscillations or No-oscillations? *arXiv e-prints*, 2016, 1609.02386.
- [151] P. T. Springer, C. L. Bennett, and P. A. Baisden. Measurement of the Neutrino Mass Using the Inner Bremsstrahlung Emitted in the Electron-Capture Decay of  $^{163}\text{Ho}$ . *Phys. Rev.*, A35:679–689, 1987. doi:10.1103/PhysRevA.35.679.
- [152] M. Tenti. *Electron identification and reconstruction with the OPERA ECC bricks and search for  $\nu_\mu \rightarrow \nu_e$  oscillations*. PhD thesis, OCEM, Bologna, 2012-03-16. URL [http://www.infn.it/thesis/thesis\\_dettaglio.php?tid=7789](http://www.infn.it/thesis/thesis_dettaglio.php?tid=7789).
- [153] R. Tsenov. Final Results on  $\nu_\mu \rightarrow \nu_\tau$  Oscillation from the CHORUS Experiment. *Balk. Phys. Lett.*, 17:191–200, 2009.
- [154] S. Tufanli.  $D^0$  Background to Neutrino Oscillations in the OPERA Experiment. Middle East Technical University, 2009.
- [155] A. Upadhyay and M. Batra. Phenomenology of Neutrino Mixing in Vacuum and Matter. *ISRN High Energy Phys.*, 2013:206516, 2013, 1112.0445. doi:10.1155/2013/206516.
- [156] B. Van de Vyver and P. Zucchelli. Prompt tau-neutrino background in wide band muon-neutrino beams. *Nucl. Instrum. Meth.*, A385:91–99, 1997. doi:10.1016/S0168-9002(96)00940-0.
- [157] S. Weinberg. A Model of Leptons. *Phys. Rev. Lett.*, 19:1264–1266, 1967. doi:10.1103/PhysRevLett.19.1264.
- [158] L. Wolfenstein. Neutrino Oscillations in Matter. *Phys. Rev.*, D17:2369–2374, 1978. doi:10.1103/PhysRevD.17.2369.

- 
- [159] B. S. Wonsak. *Die Spurrekonstruktion für das Driftröhren-Myon-Spektrometer des Neutrino-Experiments OPERA*. PhD thesis, DESY, 2007. doi:10.3204/DESY-THESIS-2007-035.
- [160] M. Yoshimoto, T. Nakano, R. Komatani, and H. Kawahara. Hyper-track selector nuclear emulsion readout system aimed at scanning an area of one thousand square meters. *PTEP*, 2017(10):103H01, 2017, 1704.06814. doi:10.1093/ptep/ptx131.
- [161] R. Zimmermann. A General track reconstruction scheme and its application to the OPERA drift tubes. *arXiv e-prints*, 2007, 0706.0800. OPERA public note 70.
- [162] R. Zimmermann, J. Ebert, C. Hagner, B. Koppitz, V. Savelev, W. Schmidt-Parzefall, J. Sewing, and Y. Zaitsev. The precision tracker of the OPERA detector. *Nucl. Instrum. Meth.*, A555:435–450, 2005. doi:10.1016/j.nima.2005.12.039, 10.1016/j.nima.2005.09.003. [Erratum: *Nucl. Instrum. Meth.*A557,690(2006)].
- [163] K. Zuber. *Neutrino physics; 2nd ed.* Series in high energy physics, cosmology, and gravitation. CRC Press, Boca Raton, FL, 2012. URL <https://cds.cern.ch/record/1418160>.

# Acknowledgements

The writing of this thesis would not have been possible without the support and advice of many people.

First of all, I would like to express my gratitude to Prof. Dr. Caren Hagner for inciting my interest in neutrino physics and giving me the opportunity of doing research in her working group. I furthermore want to thank Prof. Dr. Walter Schmidt-Parzefall, Prof. Dr. Michael Wurm, Dr. Torben Ferber, and Dr. Björn Wonsak for being inspiring examples and for many enlightening discussions.

I am grateful to all my OPERA colleagues for their collaboration and company during many electron working group and collaboration meetings, detector operation shifts, test beam measurements, and conferences.

I want to thank my colleagues from Hamburg, working on either OPERA or other projects, for discussions and conversations, sharing insight and offices. In particular, I have to thank Dr. Joachim Ebert for his support and help concerning contracts.

Special thanks to Prof. Dr. Michael Wurm and Dr. Christoph Göllnitz for not only being great colleagues but also their lasting support during the final stages of my thesis.

I am grateful to n3w and all my friends for their company over the years.

Last but not least, I want to thank my parents and grandparents for their unconditional support and making me who I am.

